NATIONAL AERONAUTICS AND SPACE ADMINISTRATION

Technical Report 32-1526

Volume XVIII

The Deep Space Network

Progress Report
For September and October 1973

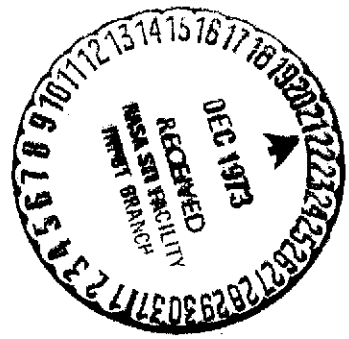

JET PROPULSION LABORATORY
CALIFORNIA INSTITUTE OF TECHNOLOGY
PASADENA, CALIFORNIA

December 15, 1973

NATIONAL AERONAUTICS AND SPACE ADMINISTRATION

Technical Report 32-1526

Volume XVIII

The Deep Space Network

Progress Report
For September and October 1973

JET PROPULSION LABORATORY
CALIFORNIA INSTITUTE OF TECHNOLOGY
PASADENA, CALIFORNIA

December 15, 1973

I

Prepared Under Contract No. NAS 7-100
National Aeronautics and Space Administration

Preface

This report presents DSN progress in flight project support, TDA research and technology, network engineering, hardware and software implementation, and operations. Each issue presents material in some, but not all, of the following categories in the order indicated:

Description of the DSN

Mission Support
- Interplanetary Flight Projects
- Planetary Flight Projects
- Manned Space Flight Projects
- Advanced Flight Projects

Radio Science

Supporting Research and Technology
- Tracking and Ground-Based Navigation
- Communications, Spacecraft/Ground
- Station Control and Operations Technology
- Network Control and Data Processing

Network Engineering and Implementation
- Network Control System
- Ground Communications
- Deep Space Stations

Operations and Facilities
- Network Operations
- Network Control System Operations
- Ground Communications
- Deep Space Stations
- Facility Engineering

In each issue, the part entitled "Description of the DSN" describes the functions and facilities of the DSN and may report the current configuration of one of the five DSN systems (Tracking, Telemetry, Command, Monitor and Control, and Test and Training).

The work described in this report series is either performed or managed by the Tracking and Data Acquisition organization of JPL for NASA.

Contents

DESCRIPTION OF THE DSN

MISSION SUPPORT

Planetary Flight Projects

RADIO SCIENCE

SUPPORTING RESEARCH AND NAVIGATION

Tracking and Ground-Based Navigation

Contents (contd)

Communications, Spacecraft/Ground

Station Control and Operations Technology

NETWORK ENGINEERING AND IMPLEMENTATION

Ground Communications

Deep Space Stations

Contents (contd)

DSN Functions and Facilities

N. A. Renzetti
Mission Support Office

The objectives, functions, and organization of the Deep Space Network are summarized. The Deep Space Instrumentation Facility, the Ground Communications Facility, and the Network Control System are described.

The Deep Space Network (DSN), established by the National Aeronautics and Space Administration (NASA) Office of Tracking and Data Acquisition under the system management and technical direction of the Jet Propulsion Laboratory (JPL), is designed for two-way communications with unmanned spacecraft traveling approximately 16,000 km (10,000 mi) from Earth to planetary distances. It supports or has supported, the following NASA deep space exploration projects: Ranger, Surveyor, Mariner Venus 1962, Mariner Mars 1964, Mariner Venus 67, Mariner Mars 1969, Mariner Mars 1971, Mariner Venus–Mercury 1973 (JPL); Lunar Orbiter and Viking (Langley Research Center); Pioneer (Ames Research Center); Helios (West Germany); and Apollo (Manned Spacecraft Center), to supplement the Spaceflight Tracking and Data Network (STDN).

The Deep Space Network is one of two NASA networks. The other, STDN, is under the system management and technical direction of the Goddard Space Flight Center. Its function is to support manned and unmanned Earth-orbiting and lunar scientific and communications satellites. Although the DSN was concerned with unmanned lunar spacecraft in its early years, its primary objective now and into the future is to continue its support of planetary and interplanetary flight projects.

A development objective has been to keep the network capability at the state of the art of telecommunications and data handling and to support as many flight projects as possible with a minimum of mission-dependent hardware and software. The DSN provides direct support of each flight project through that project's tracking and

data system. This management element is responsible for the design and operation of the hardware and software in the DSN which are required for the conduct of flight operations.

Beginning in FY 1973 a modified DSN interface has been established with the flight projects. In lieu of the SFOF, a multimission Mission Control and Computing Center (MCCC) has been activated as a separate functional and management element within JPL. This function, as negotiated with each flight project, will provide all computing and mission operations support for missions controlled from JPL. DSN computing support will be provided separately by the DSN. Radio metric, telemetry, and command data interfaces with the DSN are a joint DSN, MCCC, and flight project responsibility. The organization and procedures necessary to carry out these new activities will be reported in this document in the near future.

The DSN function, in supporting a flight project by tracking the spacecraft, is characterized by five network systems:

(1) DSN Tracking System. Generates radio metric data; i.e., angles, one- and two-way doppler and range, and transmits raw data to mission control.

(2) DSN Telemetry System. Receives, decodes, records, and retransmits engineering and scientific data generated in the spacecraft to Mission Control.

(3) DSN Command System. Accepts coded signals from mission control via the GCF and transmits them to the spacecraft in order to initiate spacecraft functions in flight.

(4) DSN Monitor and Control System. Instruments, transmits, records, and displays those parameters of the DSN necessary to verify configuration and validate the network. Provides operational direction and configuration control of the network and primary interface with flight project Mission Control personnel.

(5) DSN Test and Training System. Generates and controls simulated data to support development, test, training and fault isolation within the DSN. Participates in mission simulation with flight projects.

The facilities needed to carry out these functions have evolved in three technical areas: (1) the Deep Space Stations (DSSs) and the telecommunications interface through the RF link with the spacecraft is known as the Deep Space Instrumentation Facility (DSIF); (2) the Earth-based point-to-point voice and data communications from the stations to Mission Control is known as the Ground Communications Facility (GCF); (3) the network monitor and control function is known as the Network Control System (NCS).

I. Deep Space Instrumentation Facility

A. Tracking and Data Acquisition Facilities

A world-wide set of Deep Space Stations with large antennas, low-noise phase-lock receiving systems, and high-power transmitters provide radio communications with spacecraft. The DSSs and the deep space communications complexes (DSCCs) they comprise are given in Table 1.

Radio contact with a spacecraft usually begins when the spacecraft is on the launch vehicle at Cape Kennedy, and it is maintained throughout the mission. The early part of the trajectory is covered by selected network stations of the Air Force Eastern Test Range (AFETR) and the STDN of the Goddard Space Flight Center.[1] Normally, two-way communications are established between the spacecraft and the DSN within 30 min after the spacecraft has been injected into lunar, planetary, or interplanetary flight. A compatibility test station at Cape Kennedy (discussed later) tests and monitors the spacecraft continuously during the launch checkout phase. The deep space phase begins with acquisition by 26-m DSSs. These and the remaining DSSs listed in Table 1 provide radio communications until the end of the mission.

To enable continuous radio contact with spacecraft, the DSSs are located approximately 120 deg apart in longitude; thus a spacecraft in deep space flight is always within the field-of-view of at least one DSS, and for several hours each day may be seen by two DSSs. Furthermore, since most spacecraft on deep space missions travel within 30 deg of the equatorial plane, the DSSs are located within latitudes of 45 deg north and south of the equator. All DSSs operate at S-band frequencies: 2110-2120 MHz for Earth-to-spacecraft transmission and 2290-2300 MHz for spacecraft-to-Earth transmission. An X-band capability is being readied for future missions beginning in 1973.

[1]The 9-m (30-ft) diam antenna station established by the DSN on Ascension Island during 1965 to act in conjunction with the STDN orbital support 9-m (30-ft) diam antenna station was transferred to the STDN in July 1968.

To provide sufficient tracking capability to enable returns of useful data from around the planets and from the edge of the solar system, a 64-m (210-ft) diam antenna subnet will be required. Two additional 64-m (210-ft) diam antenna DSSs are under construction at Madrid and Canberra and will operate in conjunction with DSS 14 to provide this capability. These stations are scheduled to be operational by the middle of 1973.

B. Compatibility Test Facilities

In 1959, a mobile L-band compatibility test station was established at Cape Kennedy to verify flight-spacecraft/DSN compatibility prior to the launch of the Ranger and Mariner Venus 1962 spacecraft. Experience revealed the need for a permanent facility at Cape Kennedy for this function. An S-band compatibility test station with a 1.2-m (4-ft) diameter antenna became operational in 1965. In addition to supporting the preflight compatibility tests, this station monitors the spacecraft continuously during the launch phase until it passes over the local horizon.

Spacecraft telecommunications compatibility in the design and prototype development phases was formerly verified by tests at the Goldstone DSCC. To provide a more economical means for conducting such work and because of the increasing use of multiple-mission telemetry and command equipment by the DSN, a Compatibility Test Area (CTA) was established at JPL in 1968. In all essential characteristics, the configuration of this facility is identical to that of the 26-m (85-ft) and 64-m (210-ft) diameter antenna stations.

The JPL CTA is used during spacecraft system tests to establish the compatibility with the DSN of the proof test model and development models of spacecraft, and the Cape Kennedy compatibility test station is used for final flight spacecraft compatibility validation testing prior to launch.

II. Ground Communications Facility

The GCF provides voice, high-speed data, wideband data, and teletype communications between the Mission Operations Center and the DSSs. In providing these capabilities, the GCF uses the facilities of the worldwide NASA Communications Network (NASCOM)[2] for all long distance circuits, except those between the Mission Operations Center and the Goldstone DSCC. Communications between the Goldstone DSCC and the Mission Operations Center are provided by a microwave link directly leased by the DSN from a common carrier.

Early missions were supported by voice and teletype circuits only, but increased data rates necessitated the use of high-speed and wideband circuits for DSSs. Data are transmitted to flight projects via the GCF using standard GCF/NASCOM formats. The DSN also supports remote mission operations centers using the GCF/NASCOM interface.

III. Network Control System

The DSN Network Control System is comprised of hardware, software, and operations personnel to provide centralized, real-time control of the DSN and to monitor and validate the network performance. These functions are provided during all phases of DSN support to flight projects. The Network Operations Control Area is located in JPL Building 230, adjacent to the local Mission Operations Center. The NCS, in accomplishing the monitor and control function does not alter, delay, or serially process any inbound or outbound data between the flight project and tracking stations. Hence NCS outages do not have a direct impact on flight project support. Voice communications are maintained for operations control and coordination between the DSN and flight projects, and for minimization of the response time in locating and correcting system failures.

The NCS function will ultimately be performed in data processing equipment separate from flight project data processing and specifically dedicated to the NCS function. During FY 1973, however, DSN operations control and monitor data will be processed in the JPL 360/75 and in the 1108. In FY 1974 the NCS data processing function will be partly phased over to an interim NCS processor, and finally, in FY 1975, the dedicated NCS data processing capability will be operational. The final Network Data Processing Area will be located remote from the Network Operations Control Area so as to provide a contingency operating location to minimize single point of failure effects on the network control function. A preliminary description of the NCS appears elsewhere in this document.

[2]Managed and directed by the Goddard Space Flight Center.

Table 1. Tracking and data acquisition stations of the DSN

DSCC	Location	DSS	DSS serial designation	Antenna		Year of initial operation
				Diameter, m (ft)	Type of mounting	
Goldstone	California	Pioneer	11	26(85)	Polar	1958
		Echo	12	26(85)	Polar	1962
		(Venus)[a]	13	26(85)	Az-El	1962
		Mars	14	64(210)	Az-El	1966
Tidbinbilla	Australia	Weemala (formerly Tidbinbilla)	42	26(85)	Polar	1965
		Ballima (formerly Booroomba)	43	64(210)	Az-El	1973
–	Australia	Honeysuckle Creek[b]	44	26(85)	X-Y	1973
–	South Africa	Hartebeesthoek	51	26(85)	Polar	1961
Madrid	Spain	Robledo	61	26(85)	Polar	1965
		Cebreros	62	26(85)	Polar	1967
		Robledo	63	64(210)	Az-El	Under construction

[a]A maintenance facility. Besides the 26-m (85-ft) diam Az-El mounted antenna, DSS 13 has a 9-m (30-ft) diam Az-El mounted antenna that is used for interstation time correlation using lunar reflection techniques, for testing the design of new equipment, and for support of ground-based radio science.

[b]To be shared with STDN until January 1974.

Mariner Venus-Mercury 1973 Mission Support

E. K. Davis
DSN Systems Engineering Office

During September and October 1973, priority was given to support of Project Mission Operations System tests. DSN performance during these tests was less than satisfactory in many cases. Therefore, a significant level of effort was devoted to DSN problem isolation and resolution. Progress on open implementation tasks also continued.

I. Planning Activities

A. NASA Support Plan

The NASA Support Plan (NSP) for MVM'73 has been revised and resubmitted to NASA Headquarters for approval. This revision is consistent with current requirements, plans, and agreements. Update of the NSP at this time followed recent DSN Operational Readiness and Status Reviews. Therefore, the NSP contains actual, final support plans for the primary mission. Publication and distribution will be accomplished upon receipt of the signed approval page from NASA.

B. DSN Operations Plan

The final approved version of the DSN Operations Plan for MVM'73 was distributed in late September 1973. Any future changes required will be accomplished via Special Instruction Message to the appropriate operational area.

II. Program Control

A. DSN Operational Readiness Review

The DSN Operational Readiness Review for MVM'73 was conducted on September 26, 1973, as scheduled. This was the last in a series of DSN-sponsored reviews for the MVM'73 Project. The purpose was to review and evaluate the state of DSN readiness to support MVM'73 mission operations, and to determine and assign actions needed to meet readiness objectives. Achievement of DSN operational readiness included:

(1) Completion and verification of required data system configurations.

(2) Verification of proper system performance.

(3) Verification of interface compatibility between the DSN and the spacecraft, Mission Operations System (MOS), and Mission Control and Computing Center (MCCC).

(4) Publication and verification of mission dependent procedures.

(5) Completion of training of DSN operators and crews.

(6) Failure, discrepancy and problem analysis, and corrective action.

The scope of the review encompassed all committed DSN capabilities, including NASA communications services that support the DSN and Project. Presentations were made in accordance with the agenda given in Table 1. The Review Board, shown in Table 2, met in closed session following the presentations to assess problem areas and assign action items. Particular attention was given to continuing DSN implementation tasks (S/X-band and planetary ranging) and to problem areas wherein the quality of DSN system performance does not meet specifications (telemetry data records). Meetings have been held twice weekly to review progress and the closure of action items.

B. JPL Director's Review

On October 19, 1973, the MVM'73 Project Systems, including the spacecraft, Mission Operations, Mission Control and Computing Center, and the DSN, presented reports on the status of MVM'73 preparations to the JPL Director and Deputy. Emphasis was placed on problem areas and their potential impact on launch readiness. The DSN input to this review consisted of an update and summarization of pertinent material from the DSN Operational Readiness Review. The major area of concern in the DSN remained the quality of DSS telemetry original data records.

Of primary concern on a broader scale was the question of ability to achieve objectives and provide satisfactory support in the face of severe loading of JPL resources by Pioneer 10 encounter, MVM'73 launch/encounters, Pioneer 11 support, and Helios/Viking development. Figures 1 and 2 illustrate the DSN plan for subnetwork and Deep Space Station (DSN) sharing required to meet Pioneer 10 and MVM'73 objectives. Operationally this is a difficult plan to execute, and it alters standard practices regarding DSN configuration control and configuration freezes for critical phases.

C. MVM'73 Launch Readiness Review

The MVM'73 Project conducted the Launch Readiness Review on October 26, 1973. The Tracking and Data System (TDS) presentation included status of both the near-Earth and DSN elements. Material presented included planned launch/near-Earth support, support readiness status, problem areas and constraints, and DSN-spacecraft compatibility final report. Although work continues on certain DSN problem areas, it was concluded that required capabilities have been demonstrated and are green for launch (see Table 3).

D. Status Reviews and Reports

Each morning at 7:30 a.m. during October 1973, the Project, Mission Control and Computing Center, and DSN met to review the status of items on the "Critical Lien List." Troubleshooting and test activities within the DSN have concentrated on items in this list. As a result, only one item remains open: telemetry original data record quality has not been satisfactorily demonstrated at all DSSs.

At launch minus 30 days, the DSN initiated weekly status reports via teletype to NASA Headquarters. This was changed to daily reports at launch minus 10 days. These reports will continue through completion of the first trajectory correction maneuver (TCM) at launch plus 10 days.

III. Implementation Activities

A. Ground Communications

During this report period, installation of 28.5-kilobits/s wideband capabilities was completed, including CTA 21. Activation of the wideband circuit to DSS 43 was accomplished earlier than planned to permit transmission of high-rate data during Project operational demonstration tests in early October 1973. In many early tests the quality of wideband data was poor. This was first thought to be due to degraded circuit performance; however, later tests isolated the trouble to a phasing problem between the wideband coded multiplexer transmit and receive clocks. With two clocks (receive and transmit) running at each end of the circuit, phase crossings introduced errors resulting in frequent invalid wideband data blocks. This produced severe data dropouts in the long-loop simulation mode. A work-around was devised for test support purposes wherein the central communications terminal receive clock was slaved to the transmit clock and one clock was inhibited in each coded multiplexer at the DSS. This problem only affects operations in the long-loop simulation mode and has no impact on normal mission operations. A permanent fix is being designed to resolve the clock problem.

During October 1973, an additional high-speed data terminal was added at the central communications terminal making a total of twelve. This should ease the cir-

cuit scheduling difficulties caused by the heavy MVM'73 and Pioneer loads.

All communications implementation for MVM'73 is completed, and all subsystems are green for launch/mission support.

B. Deep Space Stations

Implementation of capabilities planned to be available prior to launch have been completed. However, hardware failures have precluded accomplishment of all objectives during test activities. Most hardware problems are associated with assemblies in the DSS telemetry string, particularly Data Decoder Assemblies and digital recorders. Actions being taken to resolve these problems are discussed below. Significant progress was also made toward completion of other capabilities (S/X-band and planetary ranging) committed to be operational at later dates.

1. Telemetry and command data subsystem (TCD). Revision A of the TCD software program completed the acceptance test and was transferred to operations on September 14, 1973 as scheduled. System performance tests with this version are essentially complete at all DSSs at this time.

Data Decoder Assemblies (DDAs) have experienced frequent faults and long mean time to repair. Also, improper performance introduces errors into the real-time and recorded telemetry data. The major cause was determined to be faulty selector channels. New selector channels have been installed in the DDA at each 64-m DSS, and installation has been initiated at 26-m DSSs. The replacement of selector channels will continue through November 1973. Capacitors have been added to the old selector channels at all DSSs to change and correct the address counter timing. This upgrade has significantly improved data quality and appears to have significantly increased the DDA reliability.

Poor quality of TCD telemetry digital original data records (ODRs) is the most serious DSN problem at this time. The telemetry ODR is the prime source of data for MVM'73 data records production. The problem is that the ODR does not meet the $\geq$99% good data criterion due to various error sources. Tape deck misalignment is a major source of error and causes incompatibilities with Mission test computer read capabilities. Faulty DDA selector channels are a major source of tape read/write error indications. Insufficient maintenance and operator errors have been contributors. Improper operation of the recorder write/read/rewrite error detection circuitry logic appears to be a minor source of errors. In addition, infrequent but serious time-tag errors have been observed.

Each of these ODR problems is being worked and a comprehensive validation program is in process wherein each recorder supporting MVM'73 is being verified. Tape decks at all DSSs have been aligned in accordance with a special procedure. Telemetry system performance tests have been run following alignment to verify results on-site. Tapes produced at the DSS are being shipped to JPL for content and compatibility verification. The DSS prepass countdown now includes items for tape recorder checks and minor maintenance. DDA selector channels are being replaced. Training continues to reduce operator errors. A fix is being designed for the error detection circuitry logic and will be implemented in November 1973. A special diagnostic program has been prepared and distributed for DSS use in detecting suspected erroneous counts in the DDA binary time of day counter. Each DSS is examining the 100-pulses/s input to the binary counter for noise and the source of extraneous counts that can be corrected with appropriate impedance. Additional operational procedures are being considered and developed to assure continued production of high quality ODRs throughout the mission. Results to date are very encouraging in that most ODRs have shown a 20% improvement in data quality and are within specification.

2. Tracking data handling subsystem (TDH). Significant progress was made on implementation of planetary ranging capabilities during September–October 1973. Installation at DSS 71 was completed in October, and planetary ranging tests were conducted with the flight spacecraft on October 23, 1973. Compatibility was verified and range numbers were as expected. Installation was completed at DSS 12 and final system tests are in process to verify planetary ranging end-to-end performance. Planetary ranging assemblies were shipped to DSSs 43 and 63 ahead of schedule. Implementation at these stations must work around the configuration freeze for Pioneer 10 encounter in December 1973. It is expected that planetary ranging overseas will be operational by January 1, 1974, as planned.

3. S/X-Band Equipment. Installation of the MU_2 ranging assembly at DSS 14 on October 22, 1973, marked completion of all installation required for S/X-band. This includes the Block IV Receiver/Exciter Assembly, Dual Doppler Assembly, and zero-delay device. However, the Command Modulation Switch Assembly was not installed for reasons stated below. S/X-band subsystem level test-

ing has been initiated. Testing, training, calibration, and evaluation for S/X will be carried out according to the baseline schedule shown in Fig. 3. This plan and schedule were negotiated between the Project and DSN.

The Command Modulator Assembly (CMA) switch was required as a part of the S/X implementation to provide for uplink commanding capabilities through either the Block III or the Block IV exciter. Figure 4 illustrates the current DSS 14 configuration for operational S-band uplink commanding. This configuration is under strict control for Pioneer 10 encounter critical command operations. Figure 5 illustrates the planned DSS 14 Block III/Block IV uplink configuration after addition of R&D assemblies having S/X-band capabilities. The CMA switch is a key component in providing for MVM'73 simultaneous commanding and ranging modulation via the Block IV exciter.

Alteration of DSS 14's command configuration at this time was challenged. Therefore, prior to installation approval, the appropriate people met on September 28 to review the switch design, operational characteristics, and proposed configuration. A number of factors were discussed (design, quality assurance, spares, documentation, test plans, reliability, operational procedures, and monitoring), resulting in a definite indication that the switch should not be installed at this time. Again, on September 28, the issue was discussed with the Assistant Laboratory Director (ALD) for Tracking and Data Acquisition, the Tracking and Data System (TDS) Manager, and the DSS 14 Station Manager, resulting in the decision to delay installation until completion of Pioneer 10 encounter operations. This decision would have required MVM'73 S/X operations to be handled via the configuration illustrated in Fig. 6.

The MVM'73 Project was informed of this decision on September 28. A more detailed briefing was given to the Project staff on October 1, 1973, wherein some possible work-arounds were suggested. Later on October 1, the appropriate Project and DSN people met to pursue the feasibility of alternative configurations. The recommendations from this working group were as follows:

(1) Until completion of Pioneer 10 critical encounter operations in mid-December 1973, the DSN should establish and use a configuration for DSS 14 as shown in Fig. 7. In this configuration, the MU_2 ranging assembly would interface with the Block III rather than Block IV exciter, the Block IV exciter is not used, and the commanding configuration is not changed.

(2) In mid-November 1973, the CMA switch status will again be reviewed and plans will be made for its installation per Fig. 5, or DSS 14 will be configured as illustrated in Fig. 8 in the absence of a CMA switch following Pioneer 10 encounter.

IV. Test and Training Activities

September and October 1973 were to have been devoted primarily to Mission Operations System tests and the support thereof. However, ground data system problems and their resolution were given priority. As a result, many of the planned Project operational demonstration tests and operational readiness tests were converted to data system tests. Critical problems were cleared and satisfactory support was provided for the Project launch/near-Earth operational readiness test during the week of October 22, 1973. A final operational readiness test is planned during the week of October 29 just prior to launch. DSN testing and training for MVM'73 standard capabilities have been completed. A continuation is, however, required to achieve performance verification and operations proficiency in the areas of planetary ranging and S/X-band operations.

Final DSN-spacecraft compatibility tests were conducted at DSS 71 on October 23, 1973. All telemetry modes, commanding, and ranging were verified. Compatibility has been demonstrated; however, detailed analysis of test results is still in process.

Table 1. Agenda for Operational Readiness Review for MVM'73

Topic	Speaker
Opening comments	N. A. Renzetti, Chairman
Introduction	E. K. Davis
Path to DSN readiness	
Review Board introduction	
Review purpose and scope	
Review procedure	
Review agenda	
Overview material	
Configuration diagrams	
Implementation identification	
DSN implementation status	
DSN equipment delivery and problem resolution	
DSS equipment	P. T. Westmoreland
GCF equipment	R. H. Evans
DSS 14 S/X-band	R. L. Weber
DSN equipment installation/ ECO status	C. W. Harris
DSN test and training	
Overview	
DSS system performance tests	
Tracking	G. D. Barnes
Telemetry	R. D. Rey
Command	B. Falin
Monitor	A. Caticchio
Network level test/training	C. W. Harris
OVT/PDT	
Training	
Interface testing	
DSN-spacecraft compatibility	A. I. Bryan
Ground data system	R. G. Polansky
Network operations status	C. W. Harris
Review Board Session	

Table 2. Review Board for Operational Readiness Review

Board title	Name, position
Chairman	N. A. Renzetti, TDS Manager for MVM'73
Member	V. C. Clarke, Mission Analysis and Engineering Manager for MVM'73
	E. K. Davis, DSN Manager for MVM'73, Review Coordinator
	E. C. Gatz, DSN Systems Engineer
	C. W. Johnson, DSN Representative for the Applied Mechanics Division
	R. K. Mallis, DSN Operations Manager R. G. Polansky, Ground Data System Engineer for MVM'73
	M. J. Sander, MCCC Manager for MVM'73 N. Sirri, MOS Manager for MVM'73
Secretary	Billie J. Weir

Table 3. DSN planned launch/near-Earth support

DSS	Event
42	Initial acquisition; Real-Time Computing System predicts prime
	Telemetry: 2450 bits/s; receive, record, real-time transmission
	Command: as soon as possible after two-way lock; automatic/manual backup
	Radio metric: doppler, angles, Mark IA lunar ranging Communications: one high-speed data line (HSDL), two teletypes (TTY), one voice
62	Normal support, no critical events
	Telemetry: 2450 bits/s; receive, record, real-time transmission
	Command: automatic/manual for contingency
	Radio metric: doppler, angles, Mark IA lunar ranging
	Communications: one HSDL, two TTY, one voice
14	Prime, real-time 117 kilobits/s Earth/Moon TV and 2450 bits/s
	Telemetry: 117 kilobits/s and 2450 bits/s; receive, record, real-time transmission
	Command: automatic required, high activity TV sequence
	Radio metric: doppler and angles
	Communications: one wide-band data line (WBDL) at 230 kilobits/s, one WBDL at 28.5 kilobits/s, one HSDL, two TTY, one voice
12	Backup to DSS 14 for command and 2450 bits/s telemetry
	Telemetry: 2450 bits/s; receive, record, real-time transmission
	Command: on-line backup to DSS 14
	Radio metric: doppler, angles; planetary ranging if used prime two-way
	Communications: one HSDL, two TTY, one voice

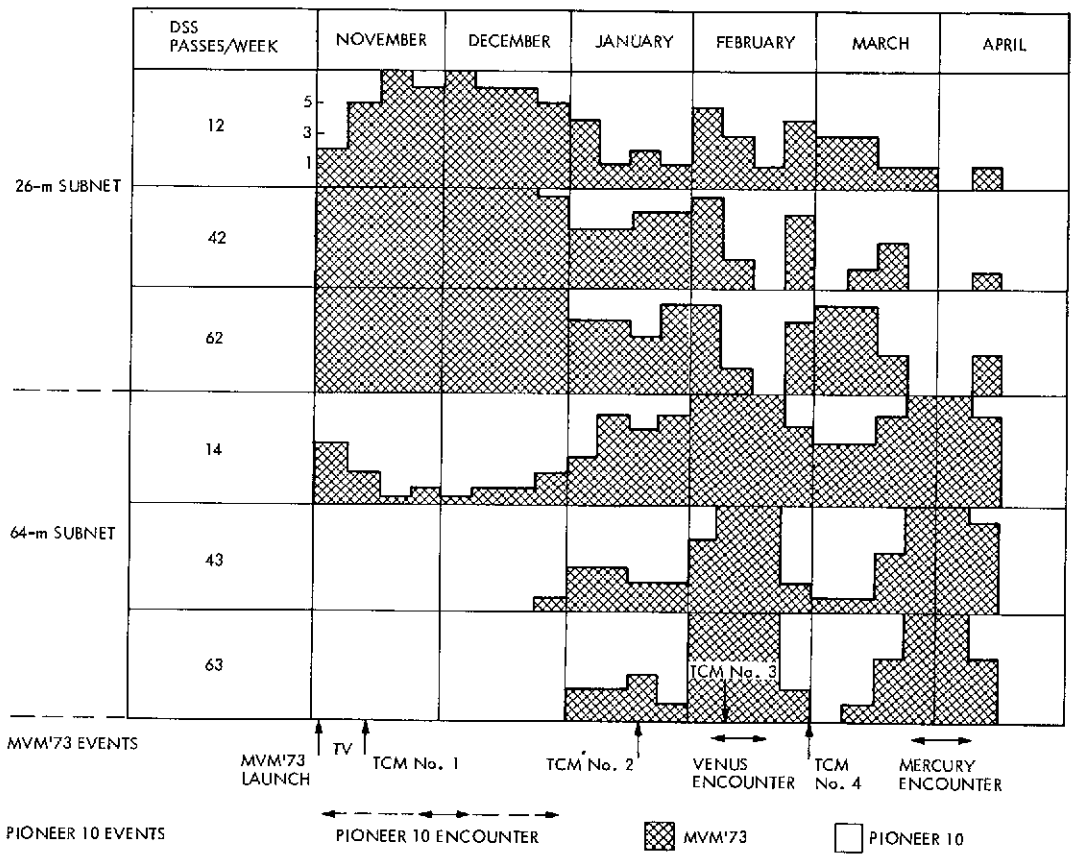

Fig. 1. MVM'73/Pioneer 10 subnet use schedule

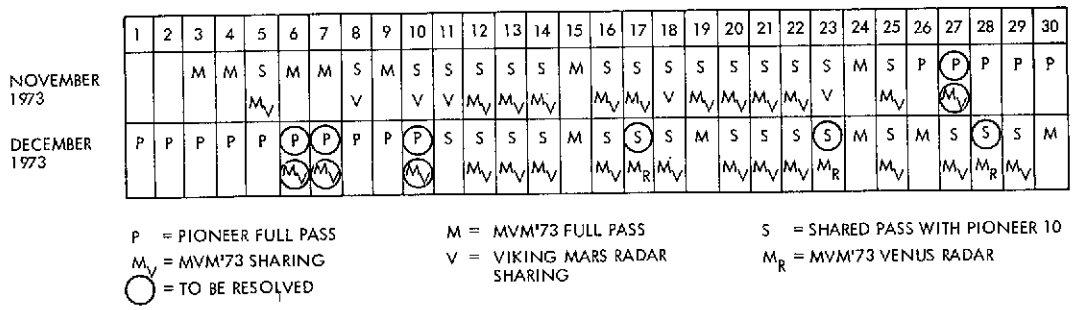

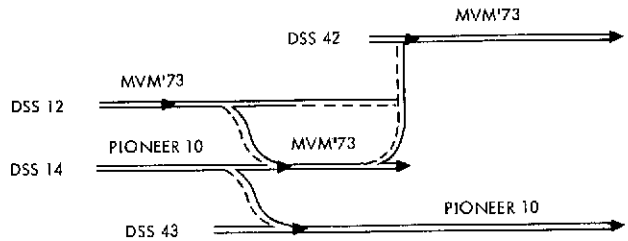

TYPICAL SHARING SEQUENCE FOR A DAY

Fig. 2. Pioneer 10/MVM'73 sharing plan for DSS 14

EVENT	OCTOBER	NOVEMBER	DECEMBER	JANUARY	FEBRUARY	MARCH
BLOCK IV INSTALLATION SUBSYSTEM CHECK	17					
MU_2 RANGING INSTALLATION SUBSYSTEM CHECK	22					
S/X SYSTEM CHECKOUT						
INFLIGHT SYSTEM CHECKOUT, EVALUATION, TRAINING						
REQUIRED SCIENTIFIC DATA						
DESIRED TECHNOLOGY DATA (TURN-AROUND TELEMETRY)		9				
PIONEER CONFIGURATION CONTROL	24					

Fig. 3. DSS 14 S/X-band implementation schedule

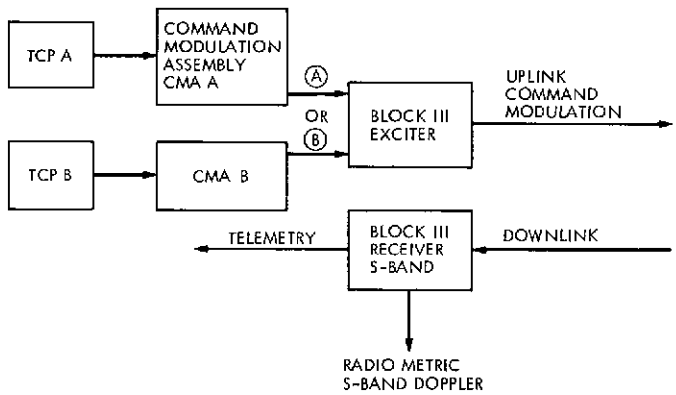

Fig. 4. Current DSS 14 Block III configuration

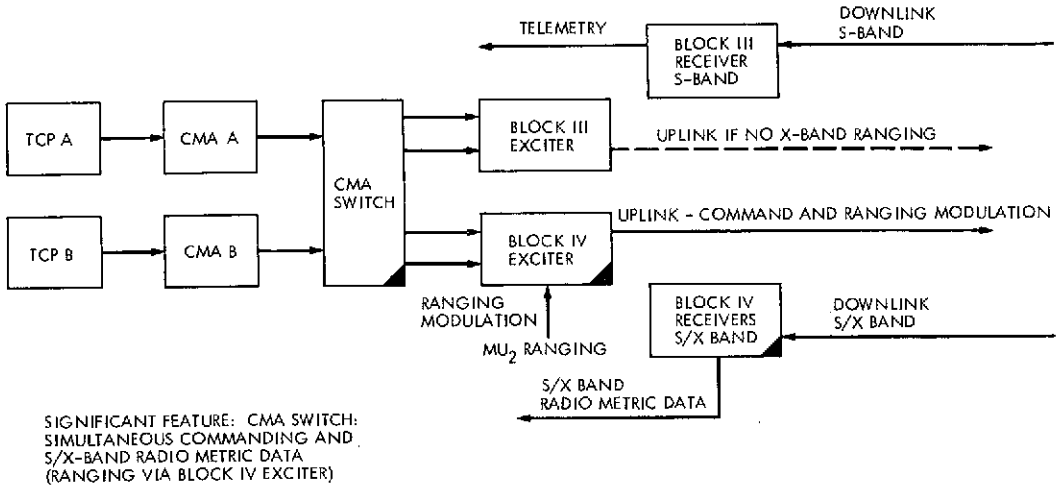

Fig. 5. Planned DSS 14 joint Block III/Block IV S/X-band R&D configuration for MVM'73

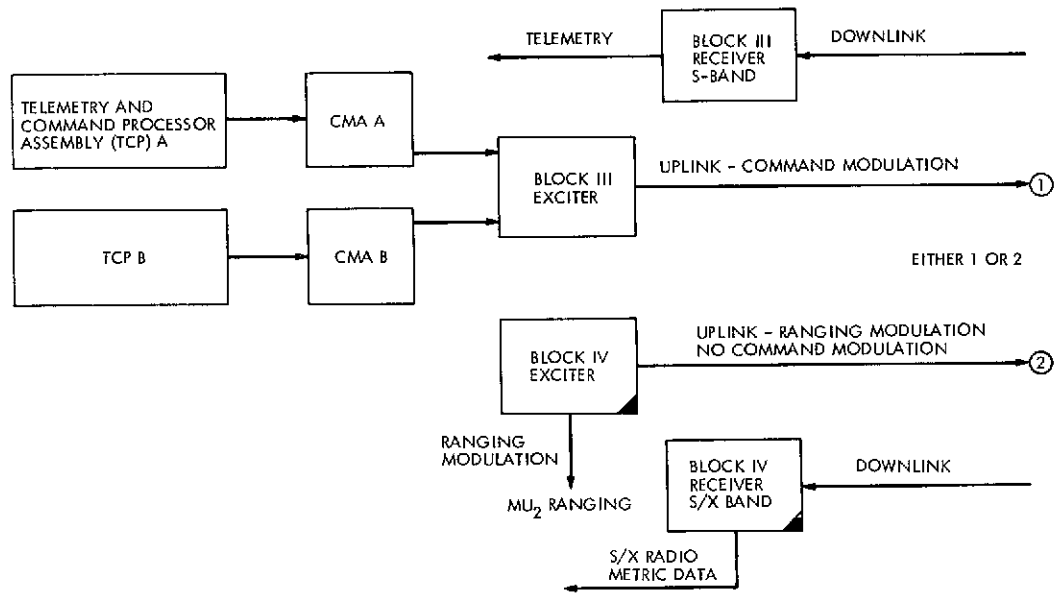

KEY CHARACTERISTICS:

NO CMA SWITCH
ALL COMMANDING THROUGH BLOCK III EXCITER
NO SIMULTANEOUS COMMANDING AND S/X RADIO METRIC (RANGING) DATA

Fig. 6. DSS 14 Block III/Block IV configuration as result of CMA switch decision

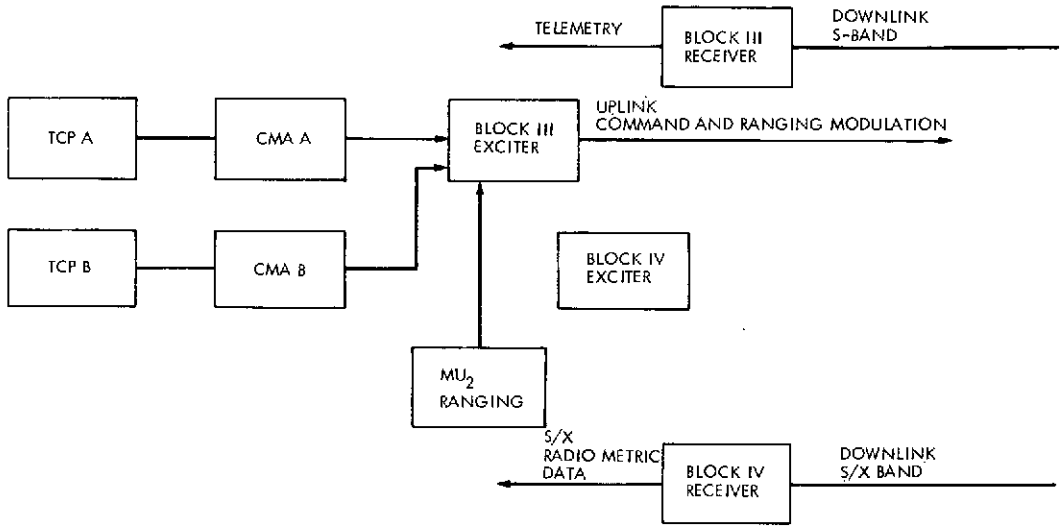

Fig. 7. Alternate DSS 14 configuration recommended through Pioneer 10 encounter

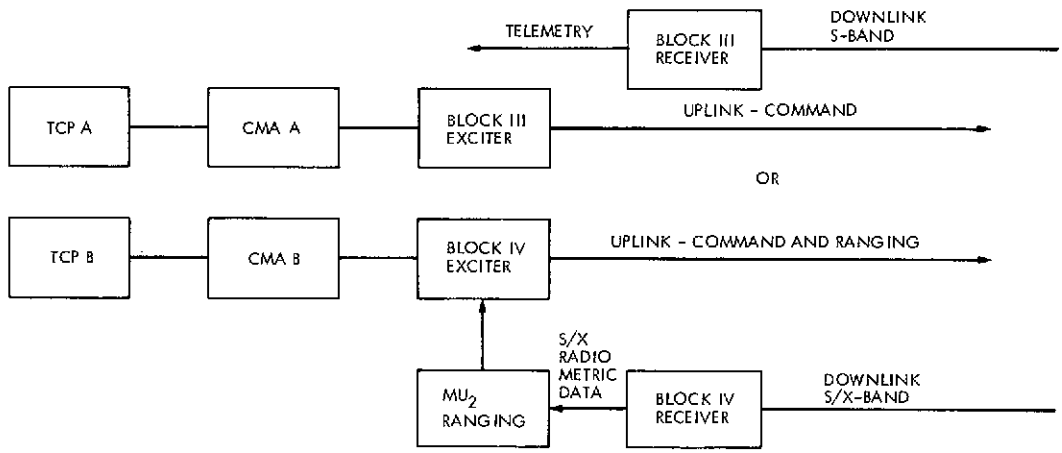

Fig. 8. Alternate DSS 14 configuration, after Pioneer 10 encounter without CMA switch

Pioneer 10 and 11 Mission Support

R. B. Miller
DSN Systems Engineering

This article describes the major elements involved in the total Ground Data System which supports the Pioneer 10 and 11 missions as it exists during the Pioneer 10 Jupiter encounter time frame.

I. Introduction

An additional unique aspect of the Pioneer 10 Jupiter encounter is that it will be the first major unmanned mission event the Jet Propulsion Laboratory has supported involving a remote control center. This means that this is the first unmanned mission supported by JPL where the mission operations control did not reside within JPL facilities located in Pasadena, California. This article describes the major elements involved in the total Ground Data System which supports the Pioneer 10 and 11 missions as it exists during the Pioneer 10 Jupiter encounter time frame.

Figure 1 depicts the major elements that comprise the total Ground Data System. The next three section headings correspond to the three major sections in the Ground Data System which are geographically separated. Paragraph headings within the three sections correspond to the elements portrayed in Fig. 1 within the three geographic locations. The following discussion concentrates on the data flow through the Ground Data System. The operations control, or "people" interface, will be shown on a separate chart and described in a subsequent article. Note that Fig. 1 is not necessarily a logical breakdown to a uniform level of detail in all elements of the Ground Data System, but rather a convenient construction for this discussion.

II. Deep Space Station

The station configuration is essentially identical for the encounter phase as for Pioneer 10 and 11 cruise support, except that a higher level of redundancy is provided for

critical mission periods. There are four major elements within the Deep Space Station (DSS) and within the DSN: the Telemetry, Command, Tracking, and Monitor Systems.

The Monitor System collects status and performance information in real time for transmission by high-speed data line (HSDL) and further processing for use by DSN Operations Control. The monitor data are not used by the Project. The ground communications form an additional DSN system and is comprised of voice, high-speed data, and teletype transmission equipment.

Telemetry. The DSS Telemetry Subsystem detects the telemetry subcarrier, acquires bit (or symbol in coded mode) synchronization, decodes coded data, and produces a Digital Original Data Record for recovery of data lost during real-time transmission. The Telemetry Subsystem formats the telemetry data for high-speed data transmission and provides an off-line capability for performing data recalls.

Command. The Command Subsystem receives command instructions via high-speed data, stores a number of commands for later transmission either when enabled or at pre-selected times, sends the commands to the modulator in the exciter, and performs various self-checking functions to assure that commands are transmitted without error.

Tracking. The Tracking Subsystem receives predictions via high-speed data for controlling the transmitter and ground reference frequency, and for pointing the antenna. The Tracking Subsystem also generates and samples doppler and angle information, and formats this information, called radio metric data (RMD), for high-speed data transmission.

III. Mission Control and Computing Center

The Mission Control and Computing Center (MCCC) currently provides real-time engineering processing for the Project, navigation processing, and the processing for DSN Operations Control functions. Telemetry data can be processed directly by the Ames Research Center (ARC), which is currently used as a backup mode of operations.

360/75 Real-Time System. The real-time system provides real-time engineering data processing including production of Project telemetry formats for local display and transmission to ARC, radio metric data processing including pseudo-residuals, and a Master Data Record (MDR) for processing by the Navigation Team. DSN Operations Control processing, including the generation of predicts and Monitor System data displays, resides in the 360/75. The telemetry and command Master Data Records are produced in this system and shipped to ARC. Extensive command processing, including command file creation and manipulation is also provided.

DSN Operations Control. The DSN Operations Control area resides in the MCCC and is the location where all DSS real-time activities are monitored and controlled.

MCCC Operations Control. MCCC self-monitoring and control functions are carried out in the MCCC.

Pioneer Mission Support Area. A limited Pioneer Project staff mans the Pioneer Mission Support Area (PMSA), which is an area provided in the MCCC. Most of the 360/75 displays are available only to the few Project operators located in this area. This area supplements the Pioneer Project real-time operations and serves as a backup mission operations center in the event of a failure in ARC equipment or the communications between JPL and ARC.

Navigation. The Navigation Team is a JPL-supported function for the Pioneer Project which utilizes the 1108 computer system for orbit determination and maneuver analysis by processing the radio metric data.

360/75 Off-Line. An off-line 360/75 (not shown in Fig. 1) will be utilized for limited time periods to support special tracking predict generation necessary for the special use of digitally controlled oscillators during the Pioneer 10 encounter.

IV. Pioneer Mission Control Center

The Pioneer Mission Control Center (PMCC) is located at the Ames Research Center and the principle real-time processing is performed on a Sigma 5. There are three Sigma 5's at ARC with one ordinarily processing Pioneer 10 data, one processing Pioneer 11 data, and the third serving as a backup and performing off-line processing. During critical encounter periods, Pioneer 11 data will be processed in the direct mode to relieve 360/75 loading.

Sigma 5 Real-Time System. This system does some limited engineering telemetry processing plus all of the science telemetry processing, and it produces listings for use by the experimenters. In addition, it accepts command instructions and interfaces with the 360/75 command software via high-speed data in standard NASA Communications (NASCOM) blocks.

Sigma 5 Off-Line System. The off-line system serves as a backup to the on-line and processes the received MDRs to produce the Experimenters' Data Record (EDR).

V. Summary

The Ground Data System is complex for the support of Pioneers 10 and 11. This complexity is particularly evident in command operations. During Pioneer 10 and 11 operations, including encounter, all commands will be entered by operators at ARC into the Sigma 5 for high-speed transmission to the 360/75 at JPL, extensive processing in the 360/75, then high-speed transmission to the Telemetry and Command Processor in the Deep Space Station, and finally through the transmitter link and radiated to the spacecraft. There is then a large number of individual elements in the command path which must all be working properly to assure command flow. Fortunately, backup plans exist to continue command operations in the event of failures in specific areas of the total Ground Data System. For example, commanding could be performed from the PMSA in the event of a failure in the PMCC, and a small number of commands can be entered directly by station personnel at the DSS when necessary.

Recognizing the complexity of the Ground Data System for Pioneers 10 and 11, ARC intends to implement a direct interface between the PMCC and the DSS after Pioneer 11 encounter some time in early 1975.

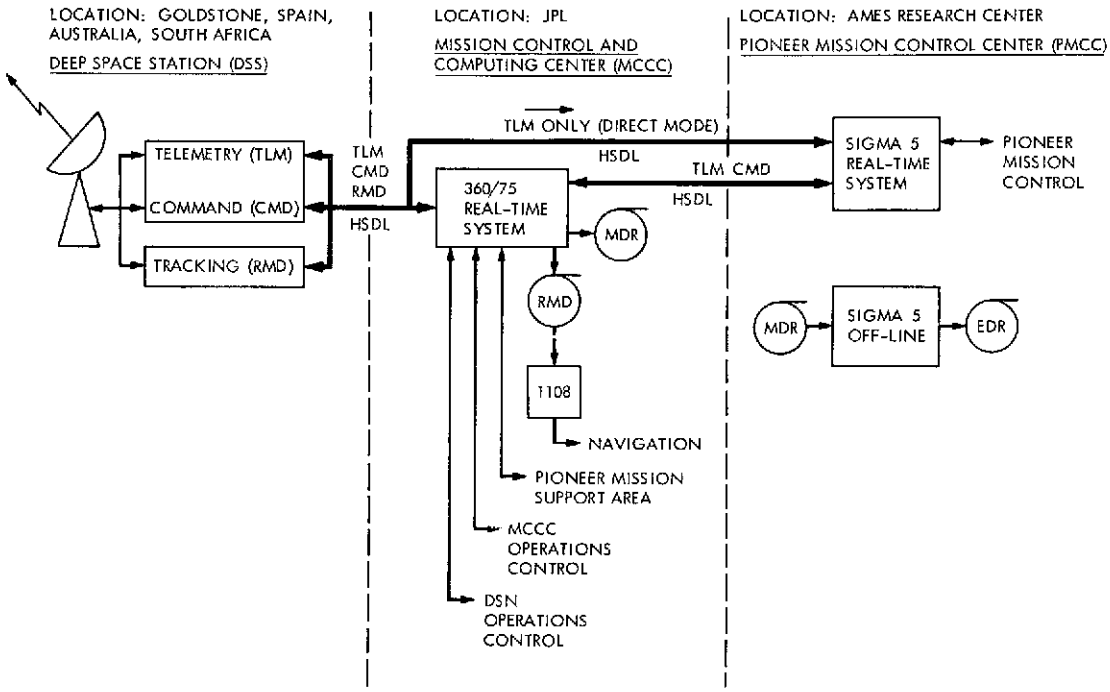

Fig. 1. Pioneer 10 Ground Data System during Jupiter encounter

Radio Science Support

K. W. Linnes
DSN Systems Engineering Office

Support provided by the DSN to radio science experiments is summarized for the period of January–October 1973. The 26-m and 64-m antennas were used to conduct Very Long Baseline Interferometry (VLBI) observations of pulsars, quasars, and radio galaxies. Radio astronomy scientists used the 64-m antenna at Goldstone, California, at 2.3 and 8.4 GHz to measure the confusion distribution of weak radio sources, to determine the population of radio sources near certain spiral galaxies, and to study emissions from various pulsars. This radio telescope was also used at 14 GHz to search for interstellar molecules and to study radio emission from Jupiter and Uranus; pulsar observations were also conducted at this frequency. The high-power transmitter capability of the Goldstone 64-m antenna was also used for radar ranging to the planets Venus, Mercury, and Mars for the purpose of improving the ephemerides of Venus and Mercury in support of the Mariner Venus/Mercury 1973 Project and to obtain surface height and roughness data of Mars in support of the Viking Mars 1975 Project. Some radio science-related DSN development activities were also carried on; these included attempts to obtain radar return from Saturn and/or its rings and to search for radar reflection from Jupiter or its moon Ganymede. In addition, VLBI techniques were used to make measurements between California and Spain to determine Deep Space Station locations, Earth polar motion, and Universal Time to higher precision. A bibliography of papers published by radio scientists using data obtained with DSN facilities is included.

I. Introduction

The 26- and 64-m antenna stations of the DSN have been used for several years to support radio science experiments. NASA, JPL, and university scientists have used key DSN facilities whose particular and unique capabilities were required for the performance of the experiments. A Radio Astronomy Experiment Selection (RAES) Panel was formed in 1969 in order to formalize the method of selecting the experiments of non-NASA experimenters. No charge is made for use of the standard DSN facilities and equipment; any special equipment required must be provided by the experimenters. A summary of all previous activity is reported in Refs. 1–10.

II. Radio Science Operations

Radio science support provided by the DSN during FY 1973 is summarized in Table 1. The total support, 1378 hours, represents 15.6% of the available antenna time. Most of the time shown for support of RAES Panel experiments was devoted to support of the Quasar Patrol (287 hours). The largest user of time among experiments sponsored by the Office of Space Science (OSS) was the radar ranging on Venus and Mercury in support of the Mariner Venus/Mercury 1973 Project (331 hours). Interstellar microwave spectroscopy (a search for interstellar molecules) received 232 hours; the remainder of the time was devoted to observations of Jupiter and Uranus and of pulsars. The

activity sponsored by the Office of Tracking and Data Acquisition (OTDA) consists only of the radio science-related elements of DSN Development.

Seventy-five hours were devoted to the application of VLBI techniques to the determination with higher precision of the Deep Space Station locations, Earth polar motion, and Universal Time. The remainder of the time was devoted to the development of weak signal processing techniques in observations of Jupiter, Saturn, and asteroids. Those months in which RAES experiments received fewer or no hours of support are those in which either the time was preempted by the Mariner 9 project or DSS 14 was out of service during major upgrading operations. During the former periods, other radio science experiments were scheduled outside the MM'71 view periods.

The experiments supported since the last report (Ref. 10) are shown in Table 2. A 24-h Quasar Patrol has been scheduled at least once per month, the observations generally being made every other month by one of the groups of investigators. Other RAES Panel experiments were scheduled as time was available. These included some VLBI observations as well as radiometer-type measurements from DSS 14 alone, such as measurement of confusion distribution and mapping of spiral galaxies. In April, the first use was made of the 64-m antenna in Australia in a VLBI observation with the 26-m antenna at Goldstone. In July, radar observations of Mars were resumed in support of the Viking Mars 1975 Project. The purpose of the measurements is to obtain surface height and roughness data of the planet to assist in the determination of landing sites. The radar observations resulted in a detection of the rings of Saturn (Ref. 41).

III. Publication of Results

As the radio science experiments have been evaluated and results have been published, the various papers resulting have been collected (identified in this report as Refs. 2–10). A few older papers previously not identified, and many new papers published since the last report, are shown in Refs. 11–41. References 11–23 set forth results of VLBI observations up to about the time the Quasar Patrol was formally established. Initially these observations were made on the California–Australia baseline at 2.3 GHz (Refs. 14 and 15).

The VLBI observations between Goldstone and the National Radio Astronomy Observatory (NRAO) antennas in West Virginia and the Haystack antenna in Massachusetts were employed in the first transcontinental uses of the DSN facility, first at 2.3 GHz, and later at 8.4 GHz (Refs. 11–13, 16, and 17). In 1971, these baselines were augmented by cooperative, simultaneous observations with the Crimean Astrophysical Observatory (Refs. 18–21). Early in 1972, the Quasar Patrol was established to provide a systematic approach in the use of DSN facilities to observe quasars and radio galaxies. The Patrol consists nominally of a regular, 24-h observation period, approximately once per month. The observations are made by the various investigating groups indicated in Table 2. A summary of the results obtained by that time was presented in December of 1972 (Ref. 24).

Reference 26 is an overall view of the subject of extragalactic radio sources with an indication of the role played by DSN-type instrumentation and investigation of compact radio sources. References 27–29 report on the measured apparent changes of some sources and verify what had been the anticipated need for the regular observations provided by the Quasar Patrol in order to detect such changes properly.

Additional investigations into the scientific questions posed by these radio sources are indicated in Refs. 30–32. These observations do not use VLBI techniques, but rather depend upon the extreme sensitivity of the 64-m antenna and the noise-adding radiometer to search for very weak radio sources in certain regions. References 33 and 34 are also papers resulting from RAES Panel–supported experiments. Reference 35 results from the OSS-supported investigation in the search for interstellar molecules. References 36–40 result from planetary astronomy observations supported by OSS. Detection of the rings of Saturn by radar (Ref. 41) results from a DSN development activity in detecting and processing weak signals.

References

1. Stevens, R., "Use of NASA/JPL Deep Space Network Facilities for Radio Astronomy," *Bulletin of the American Astronomical Society*, Vol. 4, No. 2, 1972, p. 305.

2. Linnes, K. W., Sato, T., and Spitzmesser, D., "Radio Science Support," in *The Deep Space Network Progress Report*, Technical Report 32-1526, Vol. III, pp. 46–51, Jet Propulsion Laboratory, Pasadena, Calif., June 15, 1971.

3. Linnes, K. W., "Radio Science Support," in *The Deep Space Network Progress Report*, Technical Report 32-1526, Vol. IV, pp. 47–48, Jet Propulsion Laboratory, Pasadena, Calif., Aug. 15, 1971.

4. Linnes, K. W., "Radio Science Support," in *The Deep Space Network Progress Report*, Technical Report 32-1526, Vol. V, pp. 42–44, Jet Propulsion Laboratory, Pasadena, Calif., Oct. 15, 1971.

5. Linnes, K. W., "Radio Science Support," in *The Deep Space Network Progress Report*, Technical Report 32-1526, Vol. VI, pp. 43–45. Jet Propulsion Laboratory, Pasadena, Calif., Dec. 15, 1971.

6. Linnes, K. W., "Radio Science Support," in *The Deep Space Network Progress Report*, Technical Report 32-1526, Vol. VII, pp. 29–31, Jet Propulsion Laboratory, Pasadena, Calif., Feb. 15, 1972.

7. Linnes, K. W., "Radio Science Support," in *The Deep Space Network Progress Report*, Technical Report 32-1526, Vol. VIII, pp. 24–28, Jet Propulsion Laboratory, Pasadena, Calif., Apr. 15, 1972.

8. Linnes, K. W., "Radio Science Support," in *The Deep Space Network Progress Report*, Technical Report 32-1526, Vol. X, pp. 52–58, Jet Propulsion Laboratory, Pasadena, Calif., Aug. 15, 1972.

9. Linnes, K. W., "Radio Science Support," in *The Deep Space Network Progress Report*, Technical Report 32-1526, Vol. XI, pp. 26–29, Jet Propulsion Laboratory, Pasadena, Calif., Oct. 15, 1972.

10. Linnes, K. W., "Radio Science Support," in *The Deep Space Network Progress Report*, Technical Report 32-1526, Vol. XIII, pp. 37–41, Jet Propulsion Laboratory, Pasadena, Calif., Feb. 15, 1973.

11. Cohen, M. H., et al., "Radio Interferometry at One-Thousandth Second-of-Arc," *Science*, Vol. 162, pp. 88–94, Oct. 4, 1968.

12. Kellermann, K. I., et al., "High-Resolution Observations of Compact Radio Sources at 13 Centimeters," *Astrophysical Journal*, Vol. 161, No. 3, pp. 803–809, Sept. 1970.

13. Broderick, J. J., et al., "High Resolution Observations of Compact Radio Sources at 13 Centimeters—II", *Astrophysical Journal*, Vol. 172, pp. 299–305, March 1, 1972.

14. Legg, A. J., et al., "Asymmetrics in Compact Sources at 2,298 MHz," *Nature*, Vol. 235, Feb. 21, 1972.

15. Robertson, D. S., et al., "Southern Hemisphere Very Long Baseline Interferometry," *Proceedings of the Astronomical Society of Australia*, Vol. II, No. 4 (in press).

References (contd)

16. Cohen, M. H., et al., "The Small Scale Structure of Radio Galaxies and Quasi-Stellar Sources at 3.8 Centimeters," *Astrophysical Journal*, Vol. 170, pp. 207–217, Dec. 1, 1971.

17. Cohen, M. H., "Accurate Positions for Radio Sources," *Astrophysical Letters*, Vol. 12, pp. 81–85, 1972.

18. Kellermann, K. I., "Joint Soviet-American Radio Interferometry," *Sky and Telescope*, pp. 132–133, Sept. 1971.

19. Kellermann, K. I., et al., "High Resolution Observations of Compact Radio Sources at 6 and 18 cm," *Astrophysical Journal*, Vol. 169, pp. 1–24, Oct. 1971.

20. Broderick, D. D., et al., "An Investigation of Compact Radio Emission Sources at a Wavelength of 3.55 cm," *Institute of Space Research*, Report No. Pr-117, Academy of Science, Moscow, USSR, 1972.

21. Clark, G. B., et al., "Observations of Compact Radio-Emitting Objects at 3.55 cm with Maximum Angular Resolution," *Soviet Astronomy—AJ*, Vol. 16, No. 4, Jan.–Feb. 1973.

22. Clark, B. G., et al., "Variations in the Radio Structure of VRO 42.22.01," *Astrophysical Journal Letters*, 182, L57, June 1, 1973.

23. Papers delivered at the Spring meeting of the International Union of Radio Science (URSI), Washington, D.C., 13–15 April 1972:

    1. Marandino, G., et al., "High Resolution Observations of Compact Radio Sources at Centimeter Wavelengths."

    2. Whiting, A. R., et al., "Astrometric Results from VLBI Observations of Extragalactic Radio Sources."

    3. Fanselow, J. L., et al., "Radio Interferometric Measurements of Universal Time Variations and Equatorial Components of an International Baseline."

    4. Cohen, M. H., "Source Positions and Baseline from Goldstack Observations."

24. Kellermann, K. I., "Very High Resolution Studies of Radio Galaxies and Quasars." Paper delivered at the Sixth Texas Symposium on Relativistic Astrophysics, December 18, 1972.

25. Arp, H., "Quasars." Paper delivered at Sixth Texas Symposium on Relativistic Astrophysics, December 18, 1972.

26. Kellermann, K. I., "Extragalactic Radio Sources," *Physics Today*, Vol. 26, pp. 38–47, October 1973.

27. Kellermann, K. I., et al., "VLB Observations of Apparent Changes in the Structure of Compact Radio Sources." Paper presented at the URSI meeting, Socorro, New Mexico, Jan. 8–9, 1973.

28. Shapiro, I., et al., "3C120: Intense Outburst(s) of Radio Radiation Detected with the Goldstone-Haystack Interferometer," *Astrophysical Journal Letters*, Vol. 183, No. 2, L47, 1973.

29. Kellermann, K. I., et al., "Observations of Further Outbursts in the Radio Galaxy 3C120," *Astrophysical Journal Letters*, Vol. 183, No. 2, L51, 1973.

References (contd)

30. Arp, H., "A Grouping of Radio Sources in the Area of NGC 7331 and Stephan's Quintet," *Astrophysical Journal*, Vol. 174, L111–L114, June 15, 1972.

31. Arp, H., "Stephan's Quintet of Interacting Galaxies," *Astrophysical Journal*, Vol. 183, No. 2, p. 411, 15 July 1973.

32. Arp, H., "Radio Maps Around Five Spiral and Peculiar Galaxies," *Astrophysical Journal*, Vol. 183, No. 3, p. 791, Aug. 1, 1973.

33. Carpenter, R. L., et al., "Search for Small-Scale Anisotropy in the 2.7°K Cosmic Background Radiation at a Wavelength of 3.56 Centimeters," *Astrophysical Journal*, Vol. 182, L61–L64, June 1, 1973.

34. Hill, J. G., and Klein, M. J., "On the Observed Deficiency of Ionized Gas in Globular Clusters and the Companions of M31," *Astrophysical Letters*, Vol. 13, pp. 65–68, 1973.

35. Evans, N. J., et al., "Formaldehyde in Dark Nebulae: Absorption of the Isotropic Background Radiation at 2 cm Wavelength," (Abstract), *Bulletin of the American Astronomical Society*, Michigan State University Meeting, 1972.

36. Klein, M., et al., "Jupiter: Secular Variations in Its Decimeter Flux," *Bulletin of the American Astronomical Society*, Vol. 3, No. 4, Part 1, p. 475, 1971.

37. Gulkis, S., et al., "Circular Polarization and Total Flux Measurements of Jupiter at 13.1 cm Wavelength," *Astronomical Journal*, Vol. 26, 1, Feb. 1971.

38. Klein, M., et al., "Observations of the Beaming of Jupiter's Emission at 12.6 cm Wavelength," *Bulletin of the American Astronomical Society*, Vol. 4, p. 359, 1972.

39. Klein, M. J., et al., "Jupiter: New Evidence of Long-Term Variations of its Decimeter Flux Density," *Astrophysical Journal*, Vol. 176, L85–L88, Sept. 1, 1972.

40. Gulkis, S., et al., "Observations of Jupiter at 13 cm Wavelength During 1969 and 1971," *Icarus*, Vol. 18, 181–191, 1973.

41. Goldstein, R. A., et al., "Radar Observations of the Rings of Saturn," *Icarus*, Vol. 20, 1973.

Table 1. DSN support to radio science experiments—FY 1973

Month	Support time, h, for radio science experiments				Total
	RAES	OSS	OA	OTDA (DSN development)	
July	46	64	–	16	126
August	49	86	15	18	168
September	–	89.5	–	–	89.5
October	32	108	15	–	155
November	46.5	103	16	–	165.5
December	17	76.5	–	47.5	141
January	–	26.5	–	20	46.5
February	48	16.5	–	–	64.5
March	25	8	–	–	33
April	29	73	–	8.5	111.5
May	25	95.5	–	25.5	146
June	44	80	–	8	132
Totals	362	826.5	46	143.5	1378

Table 2a. Radio science experiments involving 64-m and 26-m antenna facilities—RAES Panel

Experiment	Purpose	Experimenter	DSN facility	Dates
Quasar Patrol	To make detailed measurements on radio galaxies and quasars at 2.3, 7.8 and 15.6 GHz; to search for weak compact sources in the nucleus of extended radio galaxies and quasars; to monitor time variations in fine structure and apparent positions of quasars	Group A D. S. Robertson, WRE[a] A. J. Legg, WRE J. Gubbay, WRE A. T. Moffet, Caltech G. Nicholson, CSIR[b]	DSS 43 (64-m antenna in Australia) and 26-m antenna at Goldstone	April 2, 1973
		Group B J. J. Broderick, NAIC[c] B. G. Clark, NRAO[d] M. H. Cohen, Caltech D. L. Jauncey, Cornell Univ. K. I. Kellerman, NRAO G. H. Purcell, Caltech D. B. Shaffer, Caltech	DSS 14 (used with MIT Haystack and NRAO 42-m antenna)	October 23, 1972 November 25, 1972 February 4, 1973 April 26, 1973 June 22, 1973 September 17, 1973
		Group C T. A. Clark, GSFC[e] R. M. Goldstein, JPL H. J. Hinteregger, MIT C. A. Knight, MIT G. E. Marandino, Univ. of Maryland G. Resch, Univ. of Maryland A. E. Rogers, Haystack Observatory I. I. Shapiro, MIT A. R. Whitney, MIT	DSS 14 (used with MIT Haystack and NRAO 42-m antenna)	November 7, 1972 February 3, 1973 March 31, 1973 May 17, 1973 August 13, 1973 October 14, 1973
Very Long Baseline Interferometry (medium data bandwidth, S-band)	To determine angular size of radio sources	J. Gubbay, Univ. of Adelaide A. Legg (Space Research Group, WRE) D. Robertson (Space Research Group, WRE) A. Moffett, Caltech B. Seidel, JPL	DSS 14 (64-m antenna) and DSS 41 (26-m antenna)	June 12, 1971 January 25, 1972 February 21, 1972 June 19, 1972
Weak radio source observations	To measure the "confusion distribution" of weak radio sources at 2.3 GHz	D. L. Jauncey, Cornell Univ. M. J. Yerbury, Cornell Univ. J. J. Condon, Cornell Univ. D. J. Spitzmesser, JPL	DSS 14	June 5, 12–1972 July 5, 13–1972 December 6, 18–1972 April 13, 1973
Very Long Baseline Interferometry (2295 MHz, NRAO recording terminals)	High-resolution studies of extragalactic radio sources	J. Broderick, NRAO B. Clark, NRAO M. H. Cohen, Caltech D. Jauncey, Cornell Univ. K. Kellermann, NRAO	DSS 13 (and NRAO 43-m antenna) Plus 100-m antenna in Effelsberg, Germany	August 7, 1971 July 2, 1973 June 18, 19, 20, 21–1973
Spiral galaxy mapping	To determine population of nearby radio sources in certain spiral galaxies	H. Arp, Hale Observatories	DSS 14	October 4, 7, 13, 20, 27–1971 December 8, 1971 April 16, 1972 June 2, 14–1973 August 1, 31–1973

[a]Weapons Research Establishment.
[b]Commonwealth Scientific and Industrial Research.
[c]National Astronomy and Ionospheric Center, Arecibo, Puerto Rico.
[d]National Radio Astronomy Observatory.
[e]Goddard Space Flight Center.

Table 2b. Radio science experiments involving 64-m and 26-m antenna facilities—OSS experiments

Experiment	Purpose	Experimenter	DSN facility	Dates
Interstellar microwave low-noise spectroscopy	To search for interstellar molecules at 14 GHz	S. Gulkis, JPL T. Sato, JPL B. Zuckerman, Univ. of Maryland D. Cesarsky, Caltech J. Greenstein, Caltech	DSS 14	April 2, 10, 18–1972 May 2, 6, 14, 17–1972 June 4, 19–1972 August 5, 1972 September 5, 14, 19–1972 October 10, 17, 27, 30–1972 November 2, 10, 11, 17, 23, 26, 29–1972 April 7, 16–1973 May 2, 12, 19–1973 June 3, 12, 23, 26–1973 July 12, 25–1973 August 11, 1973
Planetary radio astronomy	To study radio emissions of Uranus and Jupiter at 14 GHz	S. Gulkis, JPL B. Gary, JPL M. Klein, JPL M. Jansen, JPL Resident Research Associate E. Olsen, JPL Resident Research Associate P. Rosenkranz, JPL Resident Research Associate	DSS 14	April 29, 30–1972 July 14, 1972 August 3, 1972 September 7, 21, 28–1972 October 3, 4, 21, 28, 31–1972 December 20, 1972 April 3, 20–1973 July 5, 16–1973 August 17, 31–1973 September 11, 1973
Pulsar observations	To study emissions from various pulsars at S-, X- and K-bands	G. Downs, JPL G. Morris, JPL P. Reichley, JPL	DSS 14	November 18, 21, 30–1972 December 1, 8, 21–1972 January 6, 14–1973 February 2, 1973 April 14, 22–1973 May 4, 5, 26–1973 June 3, 4, 10, 15–1973 July 7, 8, 14–1973 August 1, 9, 20–1973 September 10, 1973
Venus/Mercury radar ranging	To provide improved ephemerides of Venus and Mercury for Mariner Venus/Mercury 1973 Project	J. Lieske, JPL R. Goldstein, JPL	DSS 14	September 1, 15, 19, 26–1972 October 3, 10–1972 November 24, 28–1972 December 1, 5, 8, 20, 26–1972 January 10, 1973 March 27, 1973 April 3, 13, 20, 27–1973 May 4, 11, 16, 25–1973 June 1, 8, 15, 22, 28–1973 July 7, 10, 13, 18, 21, 24, 27, 31–1973 August 6, 15, 20, 27–1973 September 4, 10, 24–1973 October 8, 15, 22–1973
Mars radar	To obtain surface height and roughness data of Mars in support of the Viking Mars 75 Project	R. Goldstein, JPL G. Morris, JPL	DSS 14	July 12, 18, 21, 24, 27, 29–1973 August 2, 6, 10, 15, 18, 21, 24, 28–1973 September 1, 4, 8, 12, 15, 22, 29–1973 October 4, 5, 12, 15, 19, 22, 23, 24–1973

Table 2c. Radio science experiments involving 64-m and 26-m antenna facilities—OTDA–DSN development (radio science-related)

Experiment	Purpose	Experimenter	DSN facility	Dates
Saturn radar detection	Attempt to obtain radar return from Saturn and/or its rings to demonstrate ultra-weak signal detection techniques	R. Goldstein, JPL G. Morris, JPL	DSS 14	December 4, 5, 28, 29–1972 January 4, 5–1973
Platform parameters	To investigate VLBI techniques for determining station locations, polar motion, and universal time to higher precision	J. Fanselow, JPL M. Slade, JPL J. Thomas, JPL J. Williams, JPL D. Spitzmesser, JPL	DSS 14 DSS 62	April 30, 1973 June 11, 1973 July 20, 1973 September 8, 1973
Asteroid radar detection	To attempt to obtain a radar echo from a recently discovered asteroid	R. Goldstein, JPL	DSS 14	May 21, 22, 23–1973
Jupiter radar detection	To search for radar reflection from Jupiter or its moon Ganymede	R. Goldstein, JPL G. Morris, JPL	DSS 14	July 7, 15, 26–1973 August 3, 1973 September 10, 14, 16, 20–1973

A Sequential Decoding Medium Rate Performance Model

J. W. Layland
Communications Systems Research Section

An approximate analysis of the effect of a noisy carrier reference on the performance of sequential decoding is presented. The analysis uses previously-developed techniques for analyzing noisy reference performance for medium-rate uncoded communications adapted to sequential decoding for data rates of 8 to 2048 bits/s. In estimating the 10^{-4} deletion probability thresholds for Helios, the model agrees with experimental data to within a few tenths of a dB at 8 and 2048 bits/s; the greatest error is 1.5 dB at 128 bits/s.

I. Introduction

Convolutional encoding with sequential decoding is a very powerful technique for communicating at low-error probability with deep space probes. It has been used successfully with Pioneers 9 and 10, and is planned for use on Helios. Most of the performance data for this coding technique have been developed without regard to the effects of noisy reference signals in carrier or subcarrier tracking loops. These effects must be known with fair accuracy for the optimal design of telemetry links with sequential decoding. This author (Ref. 1) previously analyzed the effect of a noisy carrier reference on sequential decoding for high data rates, and presented a general discussion of the sequential decoding noisy reference problem. This article presents a model for sequential decoding noisy reference performance that is approximately valid for the intermediate data rates of greatest interest to the DSN. The material contained herein was presented at the recent Joint Helios Working Group Splinter Session at JPL on September 27 and 28, 1973.

II. Extreme Models

At extremely high or extremely low data rates, the sequential decoding noisy reference performance is relatively well behaved. At low data rates, the time-varying carrier phase error varies rapidly enough that its effect is almost completely averaged out within one symbol

time; there is no correlation between carrier reference noise in adjacent symbols, and the resultant channel model is white and Gaussian, with a somewhat degraded signal power. At extremely high data rates, the carrier phase error can be assumed to be constant over an entire data frame; thus the approach followed by Lindsey (Ref. 2) for uncoded communications is appropriate. Specifically, performance is computed as conditioned on all feasible values of phase error, and then this result is averaged over the phase error probability distribution (Ref. 3). Ironically, the ranges of data rates for which either of these extreme models fit with exactitude is outside the range of data rates supported by the DSN. If attention is restricted to low-probability long computations (erasure causing events), the validity of the high-rate model extends down to perhaps 10^3 bits/s (Ref. 1).

III. Medium Rate Model Problems

Sequential decoding data rates between 10 and 10^3 bits/s must be categorized as medium data rates from the performance modeling standpoint. Their performance lies somewhere between the performance predicted by the high- and low-rate models. But, as observed by Stolle and Dolainsky (Ref. 4), there is a "lot of in-between." There are two primary difficulties associated with establishing an accurate performance model for these medium data rates. The first is that we do not really know over what interval of data record the sequential decoding search is defined. It could be argued that the computation distributions for most long searches are defined by a noisy "barrier" of perhaps 3 to 10 bits in length. However, the backward search depth in sequential decoding is on the order of a constraint-length, or two, and the noise at each symbol encountered within a search must necessarily affect the number of computations needed in that search. Finally, we note that individual searches can interact up to the limit of the frame length, where they are forcibly terminated. None of these correctly represents the effective memory duration of the decoder, yet all are partially correct. The second problem is that the carrier reference errors interact with the record length that defines the searches. For example, the data rate/loop bandwidth ratio δ may be such that the carrier phase reference is essentially constant over the 1 to 3 bit times that define most short searches; yet when a large carrier reference phase error occurs a long search results, with a number of computations, which is dependent not only upon the section of data over which the carrier reference is poor, but upon a long preceding section of data within which the carrier reference varies significantly. From these considerations, I do not expect that the noisy reference performance of sequential decoding can be accurately modeled with any simple technique.

IV. Medium Rate Models

Fairly tractable techniques exist for calculating the performance of uncoded telemetry at medium data rates (Ref. 5). They exist because the error probability in uncoded telemetry depends uniformly upon the signal, noise, and carrier reference statistics over a predetermined interval of the data signal, and not at all outside that interval. The approach I have been following in modeling the sequential decoding performance at medium data rates has been to use an uncoded medium rate technique to extend the validity of the high-rate model to lower data rates. This will be discussed shortly. Massey (Ref. 6) has suggested that the problem could be approached from the low-rate end, by modeling the channel statistics, and the associated Pareto exponent, using the medium rate uncoded channel techniques. The effect of carrier reference perturbations which are correlated from symbol to symbol can then be added as a perturbation term. This is quite clearly the best approach at 8 bits/s where the correlation between even adjacent symbols is relatively small. It may prove difficult with this technique to get above 30 to 50 bits/s, where significant correlations of the carrier reference error exist over more than 4 bit times.

Extension of the high-rate model into the medium-rate region involves a number of assumptions and approximations: (1) the decoding computation distribution depends predominantly upon isolated long searches that are defined in structure over some fixed length segment of the data record, called T_m; (2) the computation distribution for long searches depends uniformly upon the carrier reference noise throughout the T_m interval; (3) the correlation between T_m intervals within a frame is independent of their position within that frame. The analysis technique implied by these assumptions is as follows: the channel signal-strength statistics are computed for the signal averaged over the T_m interval using the techniques for uncoded telemetry (Ref. 5). The sequential decoding performance is computed conditioned upon the channel signal strength, and then averaged over the distribution of the channel signal strength. Specifically we compute

$$P_{\text{deletion}} = \int_0^2 \Pr\left\{\text{deletion} \,\middle|\, \text{No. of computations, SNR} = \frac{E_b}{N_0}(1 - x/2)^2\right\} h(x)\,dx + \int_2^\infty h(x)\,dx \qquad (1)$$

where

$$h(x) = \sqrt{\frac{a}{\pi}}\, e^{\sqrt{2ab}}\,(\rho'_L x)^{-1/2} \exp\{-a\rho'_L x - b/(\rho'_L x)\}\,\rho'_L$$

ρ'_L = effective loop signal-to-noise ratio (SNR)

$$a = \frac{B(\delta)}{4}\left(1 + \sqrt{1 + 4/B(\delta)}\right)$$

$$b = a - 1 + 1/4a$$

$$\delta = 1/W_L T_m$$

$$B(\delta) = 1/[\delta - (\delta^2/4)(1 - e^{-4/\delta})] \qquad (2)$$

This approximate distribution has been developed for analysis of medium-rate uncoded communications (Ref. 5), and produces more consistent results than previous medium-rate theory for uncoded communications (e.g., Refs. 7, 8). The effective loop signal-to-noise ratio ρ'_L, is determined parametrically by $\rho_L = \rho'_L \exp\{1/(2\rho'_L)\}$, where ρ_L is the true carrier loop SNR in the operating bandwidth, as computed by Lindsey (Ref. 7), and includes the effects of bandwidth expansion of the limiter-phase-locked loop.

The Pr {deletion | No. of computations, SNR} is well-approximated by

$$\Pr\{C_L > N \cdot L\} = \exp \sum_{\substack{n=-1,1 \\ r=0,2}} \{A_{n,r} R^r (\ell n N)^n\} \qquad (3)$$

where C_L is the number of computations per frame, R is bit SNR, N is the average number of computations-per-bit within a frame of length L, and $\{A_{n,r}\}$ is a coefficient matrix determined by a two-dimensional least-squares fit to experimental data. The computation distribution for the Helios frame of 1152 bits has been experimentally determined by Dolainsky (Ref. 9). Sampled points from this experimental work appear as points on Fig. 1. The coefficients $\{A_{n,r}\}$ corresponding to these data appear in Table 1. The solid lines of Fig. 1 show this approximation. The remainder of the data presented in this article were computed from these simulation data. They deviate typically by only a few tenths of a dB from data computed for the Pioneer 192-bit frame length (Ref. 1, Table 3).

The performance computed by this technique is significantly dependent upon the value of T_m used. The true value is, as noted above, unknown. It is clear that the effective value for T_m depends upon the number of computations in each search. If the number of computations-per-bit is very small, then all decoding decisions are made on the basis of very short pieces of the received data, and $T_m = 1$ is appropriate. On the other hand, when the number of computations-per-bit is large, at least some of the decoding decisions must be made over long segments of the received data, and T_m may be much greater than one. For the purposes of evaluating the dependence of T_m upon number of computations, the decoding search process has been roughly modeled as a full tree of "b" branches per node. The average search length, T_m, within a search of N steps is thus approximated as the average branch length in a tree of N edges.

$$T_m \approx \left(\frac{b}{b-1}\right)\left(1 - \frac{1}{N}\,\ell n\left[1 + N\frac{b-1}{b}\right] \Big/ \ell n\,[b]\right) \cdot T_b \qquad (4)$$

In Eq. (4), T_b is bit duration. This expression is strictly valid only for integer $b > 1$, and for $N = b^\ell$, all ℓ. It should be used for other values of b and N only with the caveat that it may be a very rough approximation. The sequential decoding tree can have at most two branches per node; numerical results in the remainder of this article have been computed with $b = 2$. It would, of course, be much more correct to compute the numerical sequential decoding model using the true joint distribution of T_m and N, but such would require much more computing time than is used by the current model, and the needed statistics are not currently available.

V. Modeled Decoding Performance

The modeled decoding performance estimate is perhaps best displayed graphically. Figures 2a and 2b show the deletion probability as a function of the total-power-to-noise-density ratio (P_T/N_0) for the Helios modulation indices (MI) and data rates. A 12-Hz carrier-tracking loop is assumed in the DSN receiver. Figures 3a through 3c show the modeled computational distribution function for 2048 bits/s, for three power levels that differ by 0.5 dB, and for several modulation indices. A comparison of these curves with real-time[1] and nonreal-time (Ref. 10) experimental results reveals that the modeled curves agree, within experimental tolerances, with the experimental curves. Figures 4a through 4c show the modeled computation distribution function for 128 bits/s. Here, modeled and experimental results agree suitably for low

[1]Real-time tests of sequential decoding performance in Helios configuration have been initiated at DSS 71, and will be reported in a future issue.

modulation indices, but disagree at the high modulation indices where the noisy carrier reference is the dominant effect. For modulation indices of 50 to 60 deg, the model predicts significantly more degradation than is observed experimentally. Figures 5a through 5c show the modeled computation distribution function for 8 bits/s. Again, at this low data rate, the model agrees with the experiment to within experimental tolerance.

Figure 6 (solid lines) shows the modeled threshold total-power-to-noise density ratio required to achieve a 10^{-4} deletion probability for the Helios data rates and modulation indices. The corresponding experimentally determined threshold (Ref. 10) is also shown for comparison. Model inaccuracies at 128 bits/s have resulted in a statistically-significant 1.5-dB separation between model computations, and extrapolation of the experimental data at this data rate.

VI. Commentary and Future Work

At this point, modeling of the sequential decoding noisy reference performance by the techniques described here appears to be at, or near, a dead-end. The results are close, and perhaps usable for system design, but they are not exact. There is no obvious physically-justifiable change to the modeling technique or parameters that can be applied with assurance of improving the result, or of representing more exactly the physical process of sequential decoding.

The choice of T_m is perhaps the weakest link within the model. T_m has been used by Stolle (Ref. 11) as a free parameter to manipulate a model similar to the one presented here[2] into agreement with experimental data. The approach is successful, and clearly a good one for improving the model with experimental data. However, the effective T_m/T_b ratio determined this way is largest at 128 bits/s, and the physical interpretation of that fact is not clear at this time. A physical explanation of this behavior may appear after the technique has been applied to a large data set.

Two approaches are known at this time that may be followed to develop an improved model of sequential decoding noisy reference performance. Both represent greater computational work than the present model. One approach is channel modeling (Ref. 6). The other is to use the joint distribution of N and T_m, and integrate over T_m as well as over the noisy reference loss distribution at fixed T_m. For this to work, we must experimentally determine the joint distribution, or hypothesize a form for it if the performance results are suitably insensitive to the detailed form of the distribution. Neither approach is assured of success, and, until success is obtained by an alternate technique, the model approach described here, with its known biases, provides a useful (conservative) approximation to sequential decoding performance in the DSN.

[2]E. Stolle's noisy reference model basis corresponds to Eqs. 4 and 5 of Ref. 5, and Eq. 3, Table 3 of Ref. 1.

References

1. Layland, J. W., "Sequential Decoding with a Noisy Carrier Reference," in *The Deep Space Network Progress Report*, Technical Report 32-1526, Vol. XII, pp. 167–175. Jet Propulsion Laboratory, Pasadena, Calif., Dec. 15, 1972.
2. Lindsey, W. C., *Performance of Phase-Coherent Receivers Preceded by Bandpass Limiters*, Technical Report 32-1162. Jet Propulsion Laboratory, Pasadena, Calif., Sept. 15, 1967.
3. Viterbi, A. J., *Principles of Coherent Communication*, pp. 86–90 and p. 198. McGraw-Hill Book Co., Inc., New York, 1966.
4. Dolainsky, F., and Stolle, E., "Note on Effect of Noisy Carrier Reference on Frame Deletion Probability for Helios," *Satellitenelektronik*, TN-180. Deutsche Forschungs Versuchsanstalt für Luft und Raumfahrt, Linder Höhe 505, Porz-Wahn, Germany, F.R., June 30, 1972.
5. Layland, J. W., "A Note on Noisy Reference Detection," in *The Deep Space Network Progress Report*, Technical Report 32-1526, Vol. XVII, pp. 83–88. Jet Propulsion Laboratory, Pasadena, Calif., Oct. 15, 1973.

References (contd)

6. Massey, J. L., University of Notre Dame, private communication given at Helios Working Group Splinter Session, May 22, 1973.

7. Lindsey, W. C., and Blake, I. F., "Effects of Phase Locked Loop Dynamics on Phase-Coherent Communications," in *Supporting Research and Advanced Development*, Space Programs Summary 37-54, Vol. III, pp. 192–195. Jet Propulsion Laboratory, Pasadena, Calif., Dec. 31, 1968.

8. Tausworthe, R. C., "Efficiency of Noisy Reference Detection," in *Supporting Research and Advanced Development*, Space Programs Summary 37-54, Vol. III, pp. 195–201. Jet Propulsion Laboratory, Pasadena, Calif., Dec. 31, 1968.

9. Dolainsky, F., "Simulation Eines Sequentiallen Decoders," *Satellitenelektronik*, TN-154. Deutsche Forschungs Versuchsanstalt für Luft und Raumfahrt, Linder Höhe 505, Porz-Wahn, Germany, F.R., April 1972.

10. Lumb, D., NASA Ames Research Center, private communication given at Helios Working Group Splinter Session, Sept. 27, 1973.

11. Stolle, E., Deutsche Forschungs Versuchsanstalt für Luft und Raumfahrt, private communication given at Helios Working Group Splinter Session, Sept. 27, 1973.

Table 1. $A_{n,r}$ for Helios frame

r \ n	−1	0	1
0	2.397	8.824	−0.9887
1	−0.5331	−6.788	1.569
2	0.02303	0.8848	−0.8543

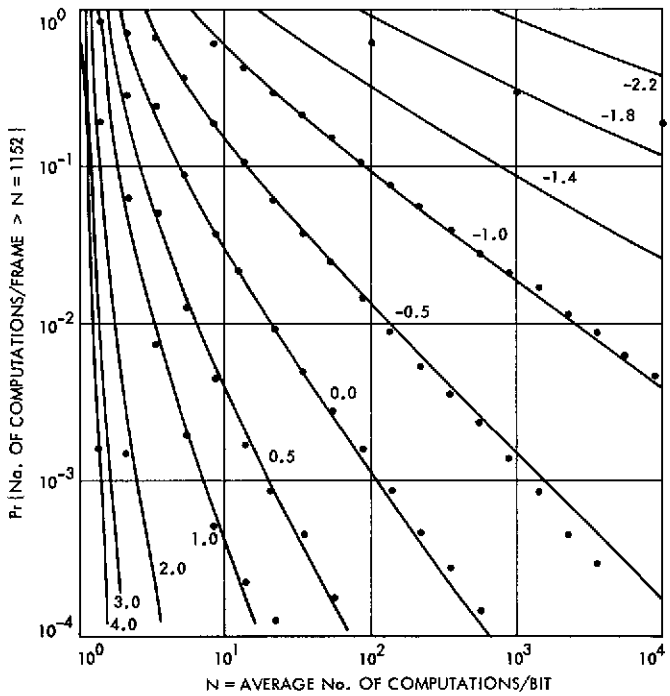

Fig. 1. Distribution of computations for sequential decoding of Helios frame

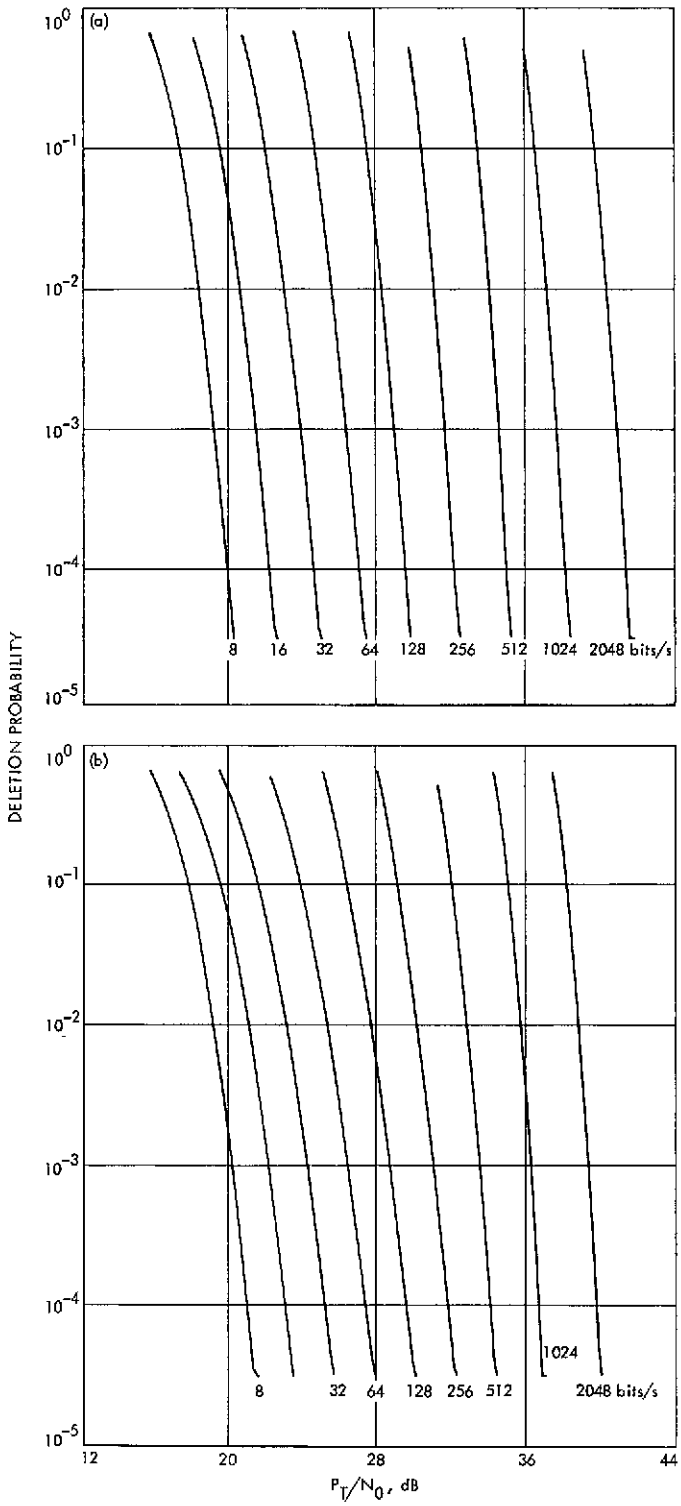

Fig. 2. Modeled deletion probability for Helios; (a) MI = 42 deg, (b) MI = 55 deg

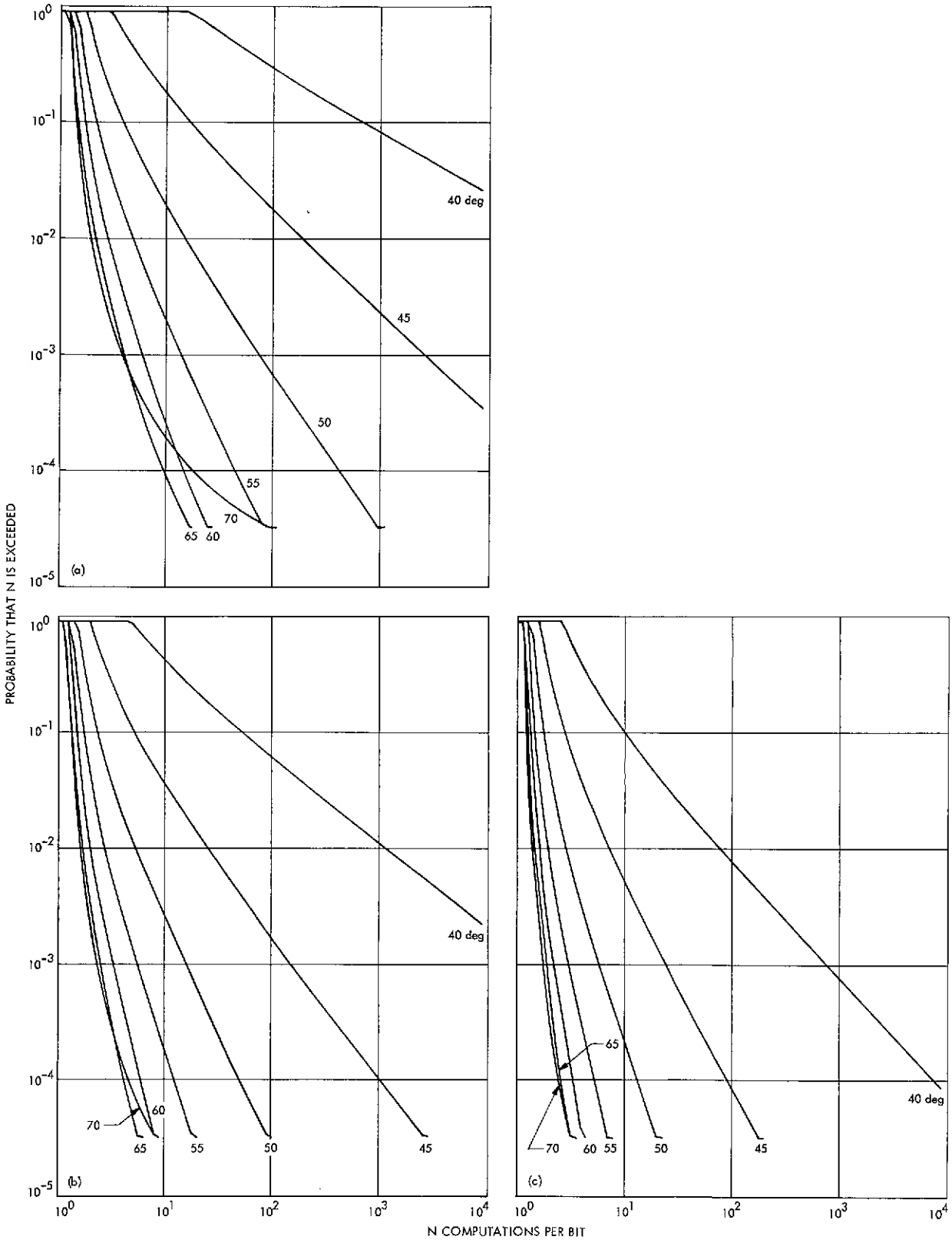

Fig. 3. Modeled distribution of computations for Helios decoding at 2048 bits/s; (a) $P_T/N_0 = 39.1$ dB, (b) $P_T/N_0 = 39.6$ dB, (c) $P_T/N_0 = 40.1$ dB

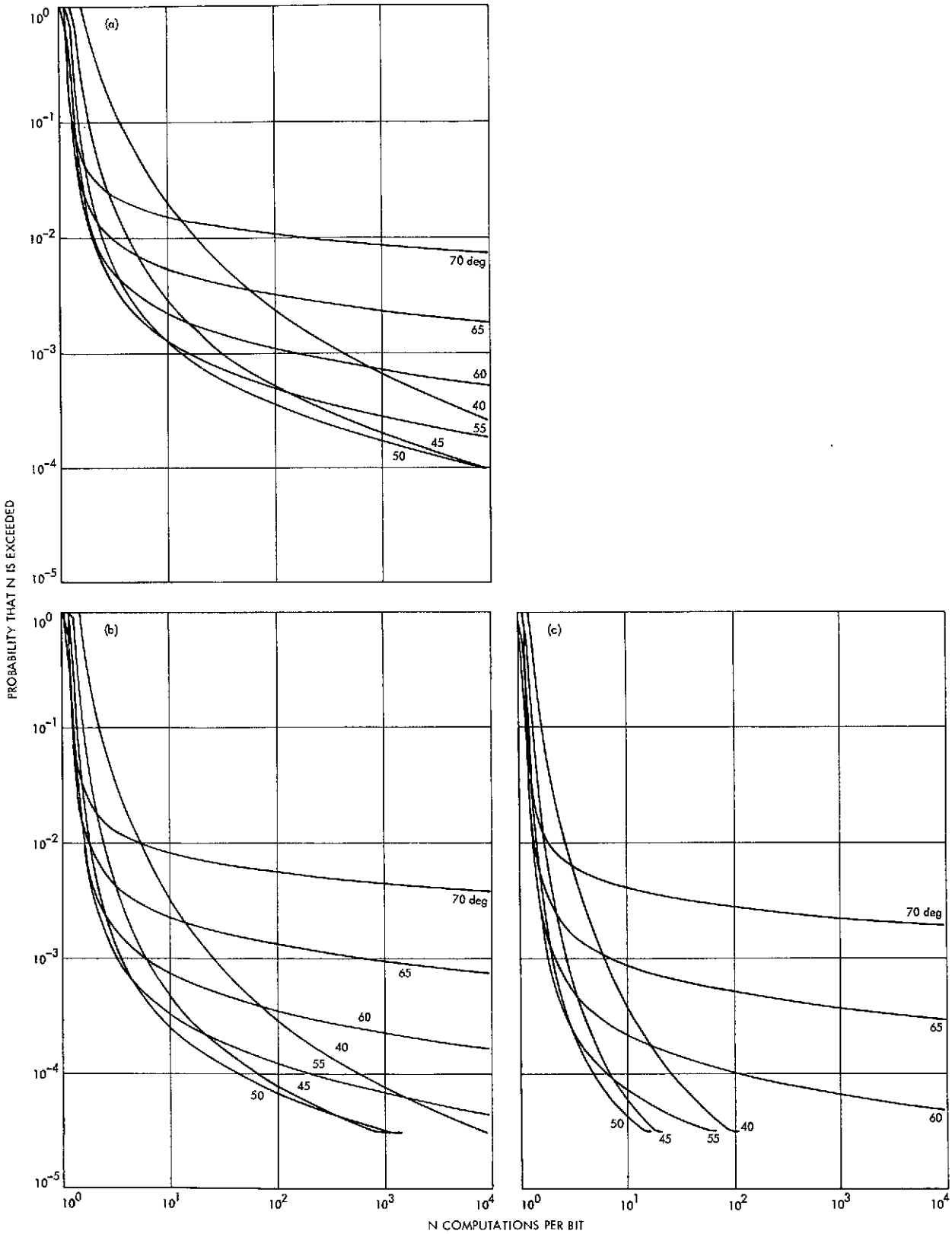

Fig. 4. Modeled distribution of computations for Helios decoding at 128 bits/s; (a) $P_T/N_0 = 29.0$ dB, (b) $P_T/N_0 = 29.5$ dB, (c) $P_T/N_0 = 30.0$ dB

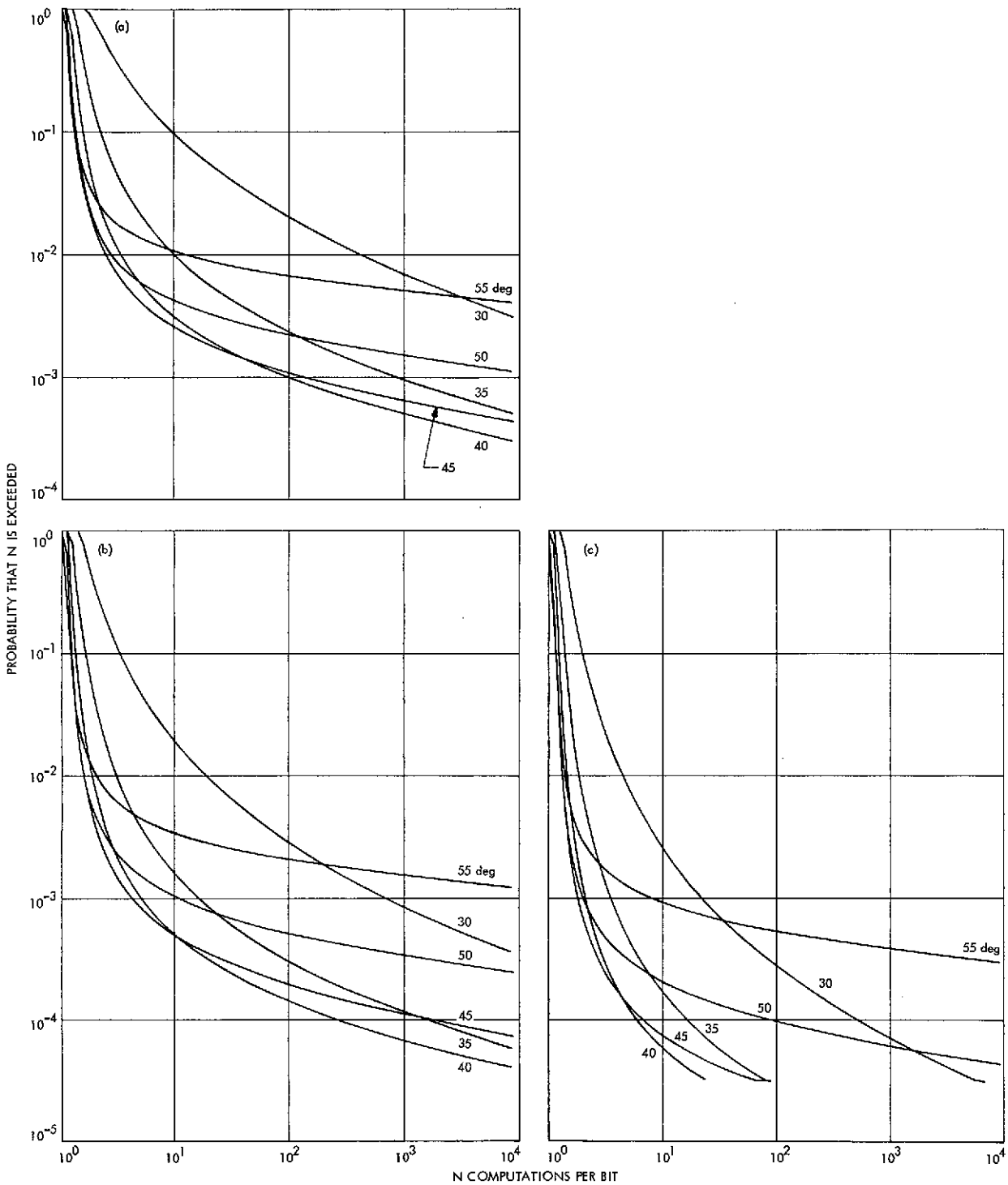

Fig. 5. Modeled distribution of computations for Helios decoding at 8 bits/s; (a) $P_T/N_0 = 19.5$ dB, (b) $P_T/N_0 = 20.0$ dB, (c) $P_T/N_0 = 20.5$ dB

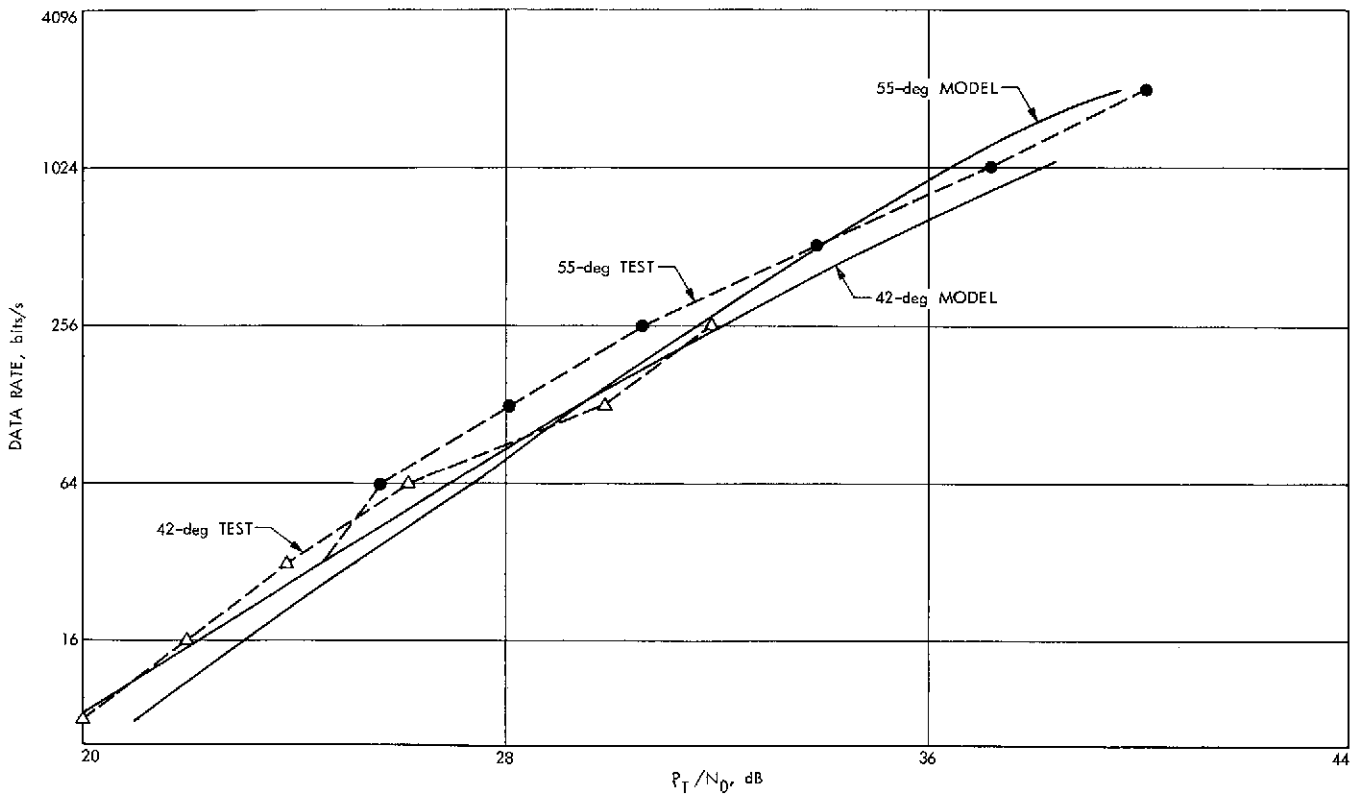

Fig. 6. P_T/N_0 thresholds for Helios for 10^{-4} deletion probability; comparison of model and extrapolated experiment

Prediction of Tropospheric Wet-Component Range Error From Surface Measurements

P. S. Callahan
Tracking and Orbit Determination Section

A new formula relating the surface temperature and water vapor pressure to the wet-component range error is found based on an empirical exponential model of the vapor pressure as a function of height. It is pointed out that wet-component models based on the hydrostatic equation are probably invalid. The range error is proportional to the first power of the surface vapor pressure. The effective scale height varies with surface temperature and vapor pressure. Models are fit to 4 months of radiosonde measurements, and agreement to 1.4 cm (1 σ) is obtained. However, in 2 of the 4 months, the standard deviation of the daily values about the observed monthly average is only slightly greater than the rms difference between the model and the measurements.

I. Introduction

The wet component of the troposphere is a relatively small, but difficult to calibrate, error source. It is particularly troublesome at low elevation angles, where the zenith value ($\Delta R_W \sim 5$–10 cm) is multiplied by a large factor. Many attempts have been made to determine the wet-component range error (see Ref. 1) from measurements made at the surface. Some progress has been made, but doppler residuals from Mariner 9 often show troposphere-like signatures (Ref. 2). Thus, it seemed useful to make another investigation of the problem.

The key element in any model of the troposphere is the distribution of water vapor with altitude. Berman (Ref. 3) assumed constant relative humidity to arrive at an expression relating the range error to the first power of the surface vapor pressure. Chao (Ref. 1) treated the water vapor as an adiabatic gas to derive $\Delta R_W \sim P_{0W}^{1.23}$. It will be shown in Section II that this derivation leads to inconsistencies. Here we follow Ref. 4 and assume that $P_W(z) = P_{0W} \exp(-az - bz^2)$, where z is distance above the ground. Using a linear temperature lapse rate, we integrate the refractivity to obtain the zenith range error.

In Section III, the new zenith range error expression is fitted to radiosonde measurements made during April, May, August, and September 1967 at Yucca Flats, Nevada. To fit the data, it is necessary to vary a and b in the above expression. The variations are correlated with temperature and surface vapor pressure: higher temperatures

result in smaller values for a and b. A linear fit for a and b is a good approximation to the data. The relationship between the parameters and the surface vapor pressure is less clear, but it appears that there is a limited range of pressures within which the exponential model applies.

In spite of the success of the model and the reasonable variation of its parameters with surface conditions, it must be noted that for April and August the rms deviation about the monthly average is only slightly greater than that about the model. Deviations of about 3 cm from both the average and the best model appear to occur at least once per month in the summer. This is consistent with the rms of 1.4 cm.

II. Refractivity Model Based on an Exponential Water Vapor Profile

The distribution of water vapor in the atmosphere is difficult to determine (Ref. 4). Theoretically, it obeys a turbulent diffusion equation with complicated boundary conditions, depending on the local surface conditions. The turbulent diffusion coefficient depends on wind velocity and other factors. Despairing of computing the water distribution from first principles, Ref. 4 states that the water vapor pressure distribution in western Europe has been found empirically to obey

$$P_w(z) = P_{0w} \exp(-az - bz^2) \tag{1}$$

where z is height above the ground, P_{0w} is the surface vapor pressure, and $a = 0.288, b = 0.0480$. Below, we will speak of the parameters a and b in terms of scale heights—their inverses. The effective scale height ($P \propto \exp(-z/d)$) corresponding to the above a and b is $d \sim 3.7$ km.

In view of the supposed difficulty in calculating the water vapor distribution, a comment on the work of Chao (Ref. 1) is needed. Chao used the hydrostatic equation

$$\frac{dP_w}{dz} = -\rho_w g \tag{2}$$

where g is the gravitational acceleration and ρ_w is the density of water vapor; a linear temperature lapse rate α, so that

$$T(z) = T_0(1 - \alpha z) \tag{3}$$

and the adiabatic law

$$P_w = D\rho_w^\gamma \tag{4}$$

where γ is the ratio of specific heats, to derive a relation between ΔR_w and P_{0w}. He used the measured value of the lapse rate α ($\alpha = 6$–8 K/km) with the measured value of γ for water ($\gamma = 1.3$), and D as an empirical parameter to fit data.

However, it is possible to derive γ and D in terms of α, so the above procedure is not internally consistent. A simple calculation for dry air using the adiabatic law and the measured γ for air (1.4) leads to a computed lapse rate of about 10 K/km, much higher than observed. Thus, the atmosphere does not behave in an adiabatic way. If one uses Eqs. (2) and (3), and the ideal gas law, a relation of the form of Eq. (4) can be obtained, with an effective γ expressed in terms of α. First, one derives (Ref. 3)

$$P(z) = P_0[T(z)]^{g/\alpha R} \tag{5}$$

where R is the universal gas constant divided by the molecular weight of the gas. Then the ideal gas law is used again to eliminate T from Eq. (6) and give

$$P = \left(\frac{P_0}{R^{g/\alpha R}}\right)^{1/(1-g/\alpha R)} \rho^{1/(\alpha R/g-1)} \tag{6}$$

Now D is a derived quantity and cannot be adjusted to fit data. The effective γ is 1.4–1.6 for water, much in excess of the true adiabatic index 1.3.

The real culprit in the above derivations is probably Eq. (2). While the dry part of the atmosphere ($\sim 99\%$) is in hydrostatic equilibrium, the partial pressure of water vapor is controlled by the local number density of water molecules. This quantity is determined by convection (wind) and need not be in hydrostatic equilibrium. Thus, Eq. (2) does not give the correct vapor pressure as a function of height, and derivations based upon it should be viewed with suspicion.

The pressure model of Eq. (1) is empirical, and the parameters given are for Europe, but it was thought useful to use it to compute the wet-component range error and test whether the form is valid. Comparison with data from various places and times could then be used to obtain the appropriate values of a and b for DSN stations.

The range error due to water vapor is given by (Ref. 1):

$$\Delta R_w = A \int_0^H \frac{P_w(z)}{T^2(z)} dz \tag{7}$$

where $P_w(z)$ is the partial pressure of the water vapor and $A = 0.373 \times 10^{-2}$ if ΔR_w is in centimeters and P_w in New-

tons per square meter; H is the height at which the water vapor vanishes. Empirically, H is in the range 7–10 km, but the exact value used makes no difference to the result. A linear temperature lapse rate is a good approximation to the observed temperature profile up to 7–10 km. Thus, the range error is given by

$$\Delta R_W = A \int_0^H \frac{P_{0W} \exp(-az - bz^2)}{T_0^2 [1 - (\alpha z/T_0)]^2} \, dz \tag{8}$$

Since $\alpha z/T_0 \lesssim 0.2$ up to 10 km, the denominator may be expanded. The resulting expression can be integrated easily to give the relation between P_{0W}, T_0, and ΔR_W, viz.,

$$\begin{aligned} \Delta R_W = {} & \frac{A P_{0W} \exp(a^2/4b)}{T_0^2 \sqrt{b}} \\ & \times \left\{ \left(1 + \frac{\alpha a}{2 T_0 b}\right) \frac{\sqrt{\pi}}{2} \left[\operatorname{erf}\left(\sqrt{b} H + \frac{a}{2\sqrt{b}}\right) \right.\right. \\ & \left. - \operatorname{erf}\left(\frac{a}{2\sqrt{b}}\right) \right] + \frac{\alpha}{T_0 \sqrt{b}} \left[\exp\left(-\frac{a^2}{4b}\right) \right. \\ & \left.\left. - \exp - \left(\sqrt{b} H + \frac{a}{2\sqrt{b}}\right)^2 \right] \right\} \end{aligned} \tag{9}$$

where erf is the error function

$$\operatorname{erf}(x) = \frac{2}{\sqrt{\pi}} \int_0^x \exp(-y^2) \, dy$$

which may be looked up in mathematical tables.

The sensitivity of Eq. (9) to a and b cannot be computed analytically because of the error functions. However, computer runs show that it is not overly sensitive and that $d\Delta R_W/\Delta R_W \cong 1/2\,(da/a)$ or $\cong 1/2\,(db/b)$, i.e., percentage changes map less than 1 to 1. Equation (9) allows a, b, and H to be functions of P_0 and T_0. Analytical fits are, of course, impossible, but comparisons of many different evaluations of Eq. (9) to observations allow the trends to be established.

For the nominal values of a (0.248 km^{-1}), b (0.048 km^{-2}), α (7 K/km), H (10 km), and T_0 (300 K), Eq. (9) reduces to

$$\Delta R_W = \frac{1.15 \times 10^{-2} \, P_{0W} \, (\mathrm{N/m^2})}{(T_0/300 \, \mathrm{K})^2} \ \mathrm{cm} \tag{10}$$

Typical water vapor pressures are in the range 4–15 $\times 10^2$ N/m^2, and temperatures range from 290–310 K. Zenith wet-component range errors are typically 4–15 cm, in agreement with Eq. (10).

III. Comparison of Model to Radiosonde Observations

Radiosonde measurements of the troposphere were obtained twice daily, at 0000 and 1200 UT, during most of 1967 at Yucca Flats, Nevada. Instruments carried aloft by a balloon measured the temperature and relative humidity as a function of height (pressure). The data were numerically integrated using Eq. (7) to find the wet-component range error.

Chao (Ref. 1) found that data obtained at 1200 UT (0400 local) do not give good results when used for surface predictions of ΔR_W. He points out that a temperature inversion invalidates the linear temperature lapse in Eq. (3). Thus, only data at 0000 UT (1600 local) were used. Two 7-week segments were found for comparison purposes. The first segment extends from April 10 to May 29; data for April 19 and May 4 and 21 are missing. The second segment, shown in Fig. 1, extends from August 6 to September 23; data for August 9 and 18 are missing. The figure contains the wet-component range error (ΔR_W, cm), the ground-level water vapor pressure (P_{0W}, N/m^2), the ground-level temperature (T_0, °C), the relative humidity (RH, %), and the height at which the contributions to ΔR_W cease ($H_{\max}$, km) plotted against date.

Table 1 lists the runs used to compare to the data and the temperature and pressure ranges in which they were found to apply. Two models are plotted with the data in Fig. 1—the best run for each month individually and the overall combination model given by the temperature and pressure ranges in Table 1.

The temperature and pressure ranges were found by a trial and error fit of a number of runs with different values for the parameters a and b to the 4 months of data described above. Recall that Run I was suggested to fit data in Western Europe; note that the temperature range in which it applies is probably typical of summer in Europe. The temperatures given in Table 1 are accurate to only about ±2°C. However, except for the special cases involving very high and low vapor pressures (Runs VIII and XII), the parameters $1/a$ and $1/b$ are well represented by linear functions of temperature. These functions are

$$\begin{aligned} \frac{1}{a} &= 1.4 + 0.078T \ (^\circ\mathrm{C}) \\ \frac{1}{b} &= 8.7 + 0.43T \ (^\circ\mathrm{C}) \end{aligned} \tag{11}$$

Equation (9) and Eqs. (11), with the two exceptions noted above, form a simple and accurate model of the wet-component zenith range error.

The accuracy of the tropospheric model is summarized in Table 2. Each month's data are given individually along with statistics of the run which best fits that month and the combination model given by all of Table 1. Table 2 shows that the combination model is superior to any single run. Note that in April and August the monthly average is a better fit than a single run, and the combination model is barely better than the average in April. The work of Thuleen and Ondrasik (Ref. 5) shows that the monthly average should provide as good calibrations as the model for the months of December through April at the Goldstone stations. Models are the most useful in the spring and fall, when tropospheric conditions fluctuate a good deal. If the April data are ignored, the combination model has an rms deviation from the data of 1.52 cm.

The variation of the model parameters with temperature and pressure is interesting. As the temperature increases, so does the effective scale height, from about 2.6 km at 10°C to about 4.2 km at 35°C. Such a variation is expected for a gas in thermal equilibrium under the influence of gravity. However, the measured values of H_{max} (the height at which the contributions to ΔR_W cease) show only a rough winter–summer correlation with temperature. Furthermore, the special Model XII needed for low surface vapor pressures has by far the highest scale height, but the data of Fig. 1 show lower values of H_{max} at the times when this model applies. Thus, while the model deals well with the integrated effect of the distribution of the water vapor in the region up to ~10 km, it may not accurately model the *local* density of water vapor. This problem may be investigated by using Eq. (1) in the analysis of sky temperature measurements (Ref. 6).

IV. Summary and Conclusions

An exponential model of the water vapor pressure, $P_W(z) = P_{oW} \exp(-az - bz^2)$, has been shown to provide a good fit to radiosonde measurements of the wet-component tropospheric range error if a and b are functions of the surface temperature and pressure. The preliminary dependence of a and b on temperature and pressure has been deduced from 4 months of observations (Table 1 and Eq. 11). When the model of Table 1 is applied to the 4 months' data, the rms difference between the model and data is 1.4 cm. In the winter (December to April), when the wet component varies little, the monthly average should provide as good a fit to the data as the model.

References

1. Chao, C. C., 1972, "A New Method to Predict Zenith Range Correction From Surface Measurements," in *The Deep Space Network Progress Report*, Technical Report 32-1526, Vol. XIV, Jet Propulsion Laboratory, Apr. 15, 1973.
2. Winn, F. B., Montez, M., and Smock, G., *For MM71 Heliocentric Cruise: Tropospheric Refraction Models, Errors, Sensitivities as They Pertain to Radio Metric Doppler Fits*, TM 391-376, October 16, 1972 (JPL internal document).
3. Berman, A. L., "A New Tropospheric Range Refraction Model," in *The Deep Space Network*, Space Programs Summary 37-65, Vol. II, Nov. 30, 1970, p. 140.
4. Tverskoi, P. N., *Physics of the Atmosphere*, NASA Translation, U.S. Dept. of Commerce, Clearinghouse for Federal Scientific and Technical Information, Springfield, Va., 1962 (trans. 1965).
5. Thuleen, K. L., and Ondrasik, V. J., "The Repetition of Seasonal Variations in the Tropospheric Zenith Range Effect," in *The Deep Space Network Progress Report*, Technical Report 32-1526, Vol. VI, Jet Propulsion Laboratory, Dec. 15, 1971.
6. von Roos, O. H., *Preliminary Investigation of the Significance of Sky Temperature Measurements on the Determination of Water Vapor Properties in the Troposphere*, TM 391-418, March 2, 1973 (JPL internal document).

Table 1. Variation of model parameters *a* and *b* with surface temperature and pressure

Run	a, km^{-1}	b, km^{-2}	Effective scale height, km	Temperature range, °C	Pressure restrictions
XI	0.461	0.0768	2.61	0–13.0	–
IX	0.419	0.0658	2.85	13.1–18.5	–
VIII	0.329	0.0535	3.39	18.6–25.0	–
VIII	0.307	0.0502	3.54	25.0–30.0	$P_{0W} > 16.0 \times 10^2$ N/m^2
I	0.289	0.0480	3.71	25.1–32.4	$5.5 < P_{0W} \leq 16.0 \times 10^2$ N/m^2
VI	0.256	0.0461	3.96	32.5–35.0	$P_{0W} > 5.5 \times 10^2$ N/m^2
X	0.242	0.0404	4.21	35.1 up	$P_{0W} > 5.5 \times 10^2$ N/m^2
XII	0.200	0.0329	4.84	25.0 up	$P_{0W} \leq 5.5 \times 10^2$ N/m^2

Table 2. Summary of fit of model to radiosonde data

Data (1967)	Average ΔR_W, cm	Rms from average	Run	Bias[a], cm	Rms from model	Number of days	Temperature range, °C
April	3.55	0.76	IX	−0.30	0.92	20	1–20
			Combined	−0.22	0.72		
May	6.20	2.19	VIII	+0.41	1.91	27	12–32
			Combined	−0.06	1.32		
August	11.8	1.88	VI	+0.09	1.89	24	31–37
			Combined	−0.02	1.51		
September	10.8	3.60	I	+0.50	2.49	23	20–32
			Combined	+0.05	1.73		
All	–	–	Combined	−0.06	1.40	94	–
All, except April	–	–	Combined	−0.03	1.52	74	–

[a]Observed − computed.

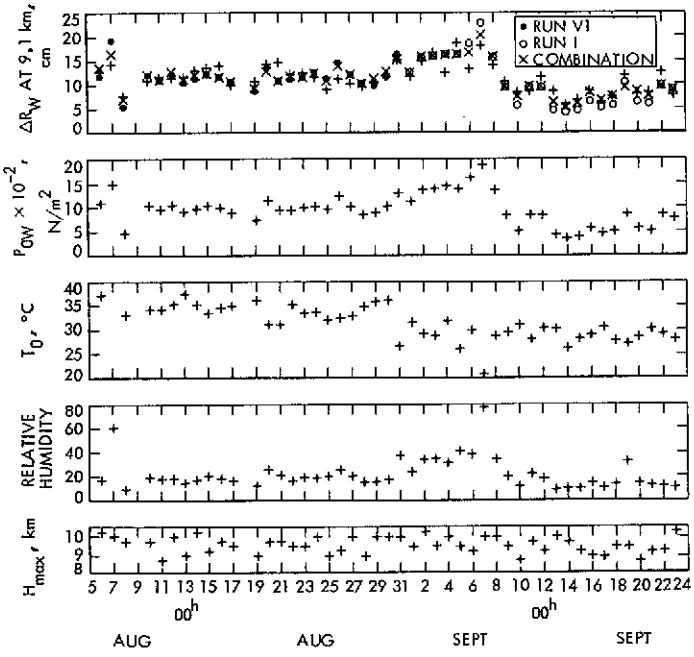

Fig. 1. Tropospheric data vs. date for August and September, 1967, Yucca Flats, Nevada; ΔR_W at 9.1 km, plotted with two models—best for each individual month and combination

Short Baseline QVLBI Demonstrations—Part I

C. C. Chao and S. K. Wong
Tracking and Orbit Determination Section

A. Lubeley
Philco-Ford Corporation

During the period between February 16 and April 11, 1973, three passes of simultaneous two-way and three-way doppler from Pioneers 10 and 11 were obtained from DSSs 11, 12, and 14 at the Goldstone complex. The residuals of the differenced doppler (quasi-very long baseline interferometry—QVLBI) which are free from process noises and effects of transmission media provide a good way to check the stabilities of the tracking system using new rubidium standards (HP 5065) for two-station tracking demonstrations.

Results indicate that the short-term (minute) and medium-term (hour) stabilities agree with expected values (specifications) of about 7 and 3 parts in 10^{13}, respectively. The long-term (month) stability, which is computed from the last two passes of data, exceeds the limited level ($\Delta f/f < 10^{-12}$) required for two-station tracking demonstrations. There are not enough data for a conclusive statement about whether the current system is capable of supporting two-station tracking demonstrations. Further investigation with more data is proposed.

I. Introduction

The new HP5065 rubidium standards which are now in operation at each tracking station have a claimed stability of $\Delta f/f = 7 \times 10^{-13}$ at a 60-s sample rate (Ref. 1). The adequacy of the frequency system using the new standards for QVLBI techniques has not been verified. Simulation studies of MVM'73 and Pioneer 10 indicate that frequency offsets between station frequency systems seriously degrade the potential accuracy of QVLBI doppler data. The desired level of long-term frequency drift is $\Delta f/f = 2 \times 10^{-14}$ (10–30 days) in order to keep the station location errors below the meter level. In Refs. 2 and 3, methods were developed for estimating the frequency offset within required accuracy in the orbit determination (OD) program. Then the tolerance for the long-term offset between frequency systems may be increased to $\Delta f/f = 10^{-12}$. However, these methods assume that the frequency offsets stay constant or vary slowly and linearly with time. To determine whether the systems with the new standard (HP 5065) satisfy these assumptions, a short baseline QVLBI demonstration based on real tracking data from Pioneers 10 and 11 was initiated.

When the simultaneous two-way and three-way data from two stations are differenced, geocentric range rate, together with errors related to the spacecraft process noise (gas leaks, solar pressure), is mostly canceled. Because of the short baseline, the differenced data become very insensitive to transmission media effects, the spacecraft position uncertainty, and errors in the baseline vector. Thus, the residuals of the differenced doppler provide a good way to check the stabilities of the new rubidium standards (HP 5065) in particular, and the entire doppler tracking system in general.

Between February 16 and April 11, 1973, three passes of simultaneous two-way and three-way doppler were obtained from DSSs 11, 12, and 14 at the Goldstone complex. The aim of this demonstration is to analyze these three passes of QVLBI data and to determine the level of

stabilities of the frequency system in supporting two-station tracking demonstrations.

II. Background

As shown in Fig. 1, station 1 and station 2 are receiving two-way and three-way doppler, respectively. From Ref. 4, the two observables can be expressed as

$$f_2 = C_3\left[f_q(t_1)\left(1 - \frac{f_R}{f_T}\right) + f_q(t_3) - f(t_1)\right] \quad (1)$$

$$f_3 = C_3\left[f_q(t_1)\left(1 - \frac{f_R^*}{f_T}\right) + f_q^*(t_3) - f(t_1)\right] \quad (2)$$

where

$f_q(t)$ = reference frequency at station 1 at time t

f_R/f_T = received frequency/transmitted frequency at station 1

$C_3 = 96\dfrac{240}{221}$

f_R^*, f_q^* = received frequency and reference frequency at station 2

The QVLBI doppler data are the differenced two-way and three-way doppler as

$$f_3 - f_2 = C_3\left[f_q(t_1)\left(\frac{f_R - f_R^*}{f_T}\right) + f_q^*(t_3) - f_q(t_3)\right] \quad (3)$$

The above equation indicates that QVLBI doppler is sensitive to the bias between two station frequency standards. If we ignore terms higher than $1/C^2$, the above equation can be given in Hamilton and Melbourne's form (Refs. 5 and 6):

$$\begin{aligned} f_3 - f_2 &= K(\dot\rho_1 - \dot\rho_2) + f_q^*(t_3) - f_q(t_3) \\ &= a + b\sin\omega t + c\cos\omega t + n(t) \end{aligned} \quad (4)$$

where

a = constant part of the error in measuring $f_q^*(t_3) - f_q(t_3)$ over one pass

$b = \dfrac{\omega}{\lambda}\Delta\alpha r_b\cos\delta$

$c = \dfrac{\omega}{\lambda} r_b\cos\delta$

λ = wavelength (λ = 13 cm at S-band)

r_b = baseline projection length

$\Delta\alpha$ = longitude error

$n(t)$ = data noise

A regression is performed on Eq. (4), and the information content of the differenced doppler is expressed in terms of the ability to determine the three coefficients a, b, and c. Quoting Hamilton and Melbourne, Table 1 gives the precision of these estimates for a 4-hour pass of QVLBI doppler with a 1-min sample rate and $\sigma_{\dot\rho}$ = 0.4 mm/s (0.003 Hz).

From Table 1, the precision of the parameter c, which contains r_b and cos δ, has been increased by almost 40 times if the constant frequency offset a is known perfectly. This strongly suggests that a careful examination of the stability of the reference frequency system at the two participating stations should be made before doing QVLBI demonstrations.

There are several ways to examine the stabilities between two frequency systems. The most reliable method is to analyze the short baseline QVLBI doppler residuals which contain the information of the overall stabilities of the entire tracking system. After the differencing of simultaneous two-way and three-way doppler from two closely located stations, most of the process noises and transmission media effects should be canceled. The residual of differenced doppler for a single pass can be written as

$$\Delta(f_3 - f_2) = \Delta a + \Delta b\sin\omega t + \Delta c\cos\omega t + n(t) \quad (5)$$

where Δa is the frequency offset, Δb and Δc are the errors due to uncertainties of baseline projection length Δr_b, baseline longitude $\Delta\alpha$, and spacecraft position $\Delta\alpha$, $\Delta\delta$:

$$\begin{aligned} \Delta b &= \left(\frac{\omega}{\lambda} r_b\cos\delta\right)\Delta\alpha + \left(\frac{\omega}{\lambda}\Delta\alpha\cos\delta\right)\Delta r_b \\ &\quad + \left(\frac{\omega}{\lambda} r_b\Delta\alpha\sin\delta\right)\Delta\delta \\ \Delta c &= \left(\frac{\omega}{\lambda}\cos\delta\right)\Delta r_b + \left(\frac{\omega}{\lambda}\sin\delta\right)\Delta\delta \end{aligned} \quad (6)$$

For reasonable values of $\Delta\alpha$, Δr_b, $\Delta\delta$, we found that

$$\Delta b \approx 0.4 \times 10^{-5}\ \text{Hz}$$

$$\Delta c \approx 0.2 \times 10^{-4}\ \text{Hz}$$

both of which are much smaller than the noise level of the frequency systems.

Thus, the residuals of differenced doppler from two close stations reveal the stabilities of the frequency system.

A criterion for the required long-term stability of the frequency system is established based on simulation studies of long baseline QVLBI doppler. The results of these simulations, which include Pioneer 10 and MVM'73, indicate the desired performance of the station frequency system (standard) for required accuracies of estimated spacecraft position and station location parameters (Fig. 2). To meet the meter level precision in station location, the long-term stability of the frequency standard must be within 2 parts in 10^{14}. If the drift between two frequency standards is constant or slowly varying, it may be estimated in the orbit determination program. Then the tolerance for the frequency stability may be increased to one part in 10^{12} with the help of the closed-loop three-station tracking (Ref. 7). Because a large portion of QVLBI data is at low elevations, refraction effects due to the atmosphere become important. The estimated effect from the uncalibrated atmospheric refraction is also shown in Fig. 2.

III. Data Acquisition and Processing

Three passes of simultaneous two-way (F2) and three-way (F3) doppler data at S-band were obtained from Pioneers 10 and 11 through the stations in the Goldstone complex. The first pass, which was made on February 16, 1973, had 6-h continuous F2 and F3 data at a 1-min sample rate. The two participating stations were DSS 11 and 12. A handover of transmitting station took place in the middle of the pass as requested. The second pass was on March 26, 1973; the two stations were DSS 12 and 14. Only 3 h of data with 1-min count time were taken, and there was no handover of transmitting station. Both the first and second passes of the simultaneous two-way and three-way doppler were obtained from Pioneer 10. The third pass was obtained from Pioneer 11 on April 11, 1973, through the same two stations as the second pass, with about 6 h of 1-min data. A data summary of these three passes is listed in Table 2. The three passes were processed by the current orbit determination program (Ref. 4), and then the two-way and three-way data were differenced by a special program (DIFFER) (Ref. 8). The output of DIFFER, which consists of the residuals (observed − computed) of differenced two-way and three-way doppler data containing the information of frequency stabilities, will be discussed next.

The station standards were measured independently against a reference clock by microwave technique for later comparison.

IV. Results and Discussion

We have shown in Section II that the short baseline QVLBI data are insensitive to both spacecraft position and baseline vector. The completeness of the cancellation of transmission media effects needs to be checked before the results are discussed. For elevation angles higher than 15 deg, the error induced in QVLBI doppler due to an equivalent zenith range error caused by the horizontal gradient and inhomogeneities in the atmosphere (troposphere and ionosphere) can be approximated by the simple relation

$$\Delta\dot{\rho} \cong \frac{\epsilon_{\rho_z} \cos\dot{\gamma}}{\sin^2\gamma}\,\gamma \tag{7}$$

where

ϵ_{ρ_z} = difference in zenith range corrections between two close stations

$\gamma, \dot{\gamma}$ = elevation angle and angle rate (nearly the same at both stations)

For a 16-km baseline (DSSs 12–14), at the same instant, the difference in zenith range effects due to troposphere and ionosphere should be no greater than a few centimeters. This gives an error less than 0.1 mHz ($\Delta\rho \leq 10^{-4}$ Hz). The estimated error is about the same order of magnitude for space plasma, except when it is very active (Ref. 9). Thus, the residuals of QVLBI data are relatively free from effects of transmission media. According to the results of a short baseline VLBI demonstration (Ref. 10) using the same baseline (DSSs 12–14), 0.1- to 0.2-mHz noises in the data residuals are believed to be due to transmission media. This agrees with the estimated value from Eq. (6).

Data from the first pass were taken on February 16, 1973, at DSS 11 and DSS 12. The two-way and three-way doppler residuals may be due to a series of unmodeled accelerations 3×10^{-9} km/s^2 in magnitude. This type of noise, which was also found in the MM'71 doppler data, is too large to be due to the solar plasma effect and gas leaks (Pioneer 10 is a spinning spacecraft). It might be caused by impacts with small meteorites. Nevertheless, it gives us an additional opportunity to demonstrate the advantage of differenced data types. Figure 3 clearly indicates that the process noise and effects due to transmission have been taken out after the differencing of F2 and F3 data. The statistics of the residuals over this 6-h pass are listed in Table 3. The residuals of F3 − F2 have mean values of −0.0436 Hz in the first 3 h and 0.0423 Hz in the second 3 h of the pass after the handover of transmitting

stations. From Eq. (3), this change of sign strongly indicates that a frequency offset existed between the two-station frequency system. The standard deviation of the residuals of F3 − F2 from the mean is 0.0027 Hz, which is consistent with the stability of the new rubidium standards, $\Delta f/f \simeq 10^{-12}$ (Ref. 1).

The second pass, on March 26, was acquired from a different pair of tracking stations (DSSs 12 and 14). As indicated in Fig. 4, this pass of data exhibited low process noise. The data noise of the differenced doppler did not show much improvement over that of the F2 and F3 data (Table 4). A bias of −0.0079 Hz exists in the F3 − F2 data, with a smaller deviation, $\sigma = 0.0018$ Hz.

The third pass was obtained from Pioneer 11 on April 11 at DSSs 12 and 14. During this pass, the spacecraft was executing a midcourse correction of 38 m/s in velocity change, consisting of one long continuous burn and several small jet pulses. The two-way and three-way doppler data were received 10 to 20 s out of synchronization during half of the 6-h pass. The estimated error in QVLBI doppler data induced by this and the 38-m/s change in velocity is around 0.015 Hz. The midcourse correction and the out-of-synchronization receiving time provide an explanation for the much noisier F2, F3, and F3 − F2 residuals compared to those of the preceding two passes.

Table 5 shows a bias of −0.0189 in F3 − F2 residuals with a large deviation ($\sigma = 0.0079$ Hz). The noise can be seen in the scattering of two-way, three-way, and differenced doppler data presented in Fig. 5. No handover of transmitting stations took place.

To check the medium-term drift in frequency, a straight line was fitted to the F3 − F2 residuals of each of the three passes. The values of the constant offsets and slopes are shown in Table 6. Because of the short data length (3 to 6 h), the time $t = 0$ is picked up at the midpoint of each pass to minimize the correlation between the constant and the slope of a straight line. The constant terms or the means of the offset can be determined with uncertainties from 0.13 to 0.5 mHz. The slope of the first pass is the largest, with 0.47 ±0.28 mHz/h. For the last two passes, the values are smaller than their uncertainties (see Table 6). The long-term drift can be seen from the means of the last two passes, which were obtained from the same two stations. A change of 11.2 ±0.63 mHz in 16 days is found; this corresponds to a slope of 0.7 ±0.04 mHz/day.[1]

[1]There was no reset of frequency standards during this interval.

When we compared the short-term (minutes) stabilities obtained from this demonstration with the specifications of frequency standards, we found that the expected value of HP 5065 rubidium is about 1.4 times smaller than our results from differenced doppler data (Fig. 6). The discrepancy can be explained by the fact that the QVLBI residuals contain the noise from two rubidium standards. The medium-term (hours) stabilities estimated from the values of the slopes of fitted straight lines agree with the results of a similar short baseline VLBI demonstration (Ref. 10). The results of QVLBI data provided some new information on the long-term (days) performance of one frequency system relative to another. Figure 6 shows the long-term relative stability to be around 5 parts in 10^{12}, which apparently exceeds the desired level for orbit determination as shown in Fig. 2.

During the first two passes, microwave measurements were made (Ref. 11). The values of the relative frequency offsets between two station standards are:

(1) First pass, 3-h interval: $f_{11} - f_{12} = -0.036 \pm 0.02$ Hz.

(2) Second pass, 10-h interval: $f_{14} - f_{12} = -0.015 \pm 0.01$ Hz.

The relative frequency offsets measured by microwave agree with the values determined from differenced doppler data even though the microwave measurements have a large uncertainty.

V. Concluding Remarks and Proposed Studies

The results from differencing three passes of simultaneous two-way and three-way doppler data show that the short-term (1-min averaging time) relative stability between two tracking systems using HP 5065 frequency standards is around 1 part in 10^{12}. The medium-term (hours) and long-term (days) stabilities are about 3 parts in 10^{13} and 5 parts in 10^{12}, respectively. The long-term stability, which is based on only two passes of data, exceeds the desired level for two-station tracking demonstrations. In order to enhance our understanding of the long-term performance of the frequency systems and their stabilities, excluding the frequency standards (HP 5065), more passes of short baseline QVLBI data are needed. The required tracking patterns for continued short baseline QVLBI doppler demonstrations are proposed in Table 7.

Acknowledgments

The authors wish to thank Jay Curtright for conducting the microwave measurement and for his helpful discussions. Thanks are also given to David Farless and Robert Ryan for scheduling the two-station tracking. Special appreciation is due to D. W. Trask for his thorough review of this article and useful suggestions.

References

1. *Hewlett-Packard Rubidium Frequency Standard 5065A*, Technical Data, Apr. 15, 1971, p. 283.
2. Ondrasik, V. J., and Rourke, K. H., "Applications of Quasi-VLBI Tracking Data Types to the Zero Declination and Process Noise Problems," in *The Deep Space Network Progress Report*, Technical Report 32-1526, Vol. IV, Jet Propulsion Laboratory, Pasadena, Calif., Aug. 15, 1971.
3. Mulhall, B. D., et al., *Report on the Two-Station Doppler (QVLBI) Demonstrations Conducted with Mariner IX, Part 1, Batch Filtering*, TM 391-413, 1973 (JPL internal document).
4. Moyer, T. D., *Mathematical Formulation of the Double Precision Orbit Determination Program*, Technical Report 32-1527, Jet Propulsion Laboratory, Pasadena, Calif., May 15, 1971.
5. Hamilton, T. W., and Melbourne, W. G., "Information Content of a Single Pass of Range Rate Observables," in *The Deep Space Network*, Space Programs Summary 37-39, Vol. III, Jet Propulsion Laboratory, Pasadena, Calif., May 31, 1966, p. 18.
6. Chao, C. C., *A Preliminary Comparison of Two-Station Tracking Data Types*, TM 391-262, Dec. 8, 1971 (JPL internal document).
7. Chao, C. C., *A Simple Analysis of QVLBI Data Obtained from Three Widely Separated Stations*, TM 391-440, Apr. 1973 (JPL internal document).
8. Johnson, D. E., *User's Guide to Differenced Partial Program*, TM 391-333, June 9, 1972 (JPL internal document).
9. von Roos, O. H., private communication.
10. Thomas, J. B., et al., "Radio Interferometry Measurements of a 16-km Baseline with 4-cm Precision," paper presented at the American Geophysical Union Annual Meeting, 1972.
11. Curtright, Jay, private communication.

Table 1. Precision of coefficient estimates, $\sigma_\rho = 0.4$ mm/s, 1-min samples

Estimated coefficients	σ_a/ω, m (σ_a, mHz)	σ_b/ω, m	σ_c/ω, m
a, b, c	6.8 (3.4)	1.2	7.6
b, c	–	1.2	0.2

Table 2. Tracking data summary

Pass	Date	Participating DSSs	Simultaneous doppler data distribution (1-min sample rate), h		Spacecraft
			Two-way	Three-way	
1	Feb. 16, 1973	11	3	3	Pioneer 10
		12	3	3	
2	Mar. 26, 1973	12	3		Pioneer 10
		14		3	
3	Apr. 11, 1973	12	6		Pioneer 11
		14		6	

Table 3. Statistics of residuals (February 16, 1973)

	Mean, Hz		σ, Hz		rms		Number of data points	
	DSS 11	DSS 12	DSS 11	DSS 12	DSS 11	DSS 12	DSS 11	DSS 12
F2	−0.0828	−0.0773	0.00605	0.0070	0.0829	0.0776	219	121
F3	−0.1210	−0.0405	0.0071	0.0059	0.1212	0.0409	121	221
F3 − F2	−0.0436	−0.0423	0.0027	0.0027	0.0437	0.0424	119	217

Table 4. Statistics of residuals (March 26, 1973)

	Mean, Hz	σ, Hz	rms	Number of data points
F2 DSS 12	0.01079	0.00214	0.01099	231
F3 DSS 14	0.00273	0.00226	0.00355	187
F3 − F2	−0.00786	0.00184	0.00807	184

Table 5. Statistics of residuals (April 11, 1973)

	Mean, Hz	σ, Hz	rms	Number of data points
F2 DSS 12	1.003	0.029	1.0035	319
F3 DSS 14	0.985	0.030	0.9855	333
F3 − F2	−0.0189	0.0079	0.0204	313

Table 6. A straight line[a] fitted to F3 − F2 residuals

Pass	Date	a, mHz	b, mHz/h
1	February 16, 1973	−42.26 ±0.18	0.467 ±0.276
2	March 26, 1973	−7.85 ±0.13	−0.097 ±0.125
3	April 11, 1973	−19.03 ±0.50	−0.055 ±0.320

[a] $\Delta(\text{F3} - \text{F2}) = a + bt$

Table 7. Accomplished and proposed short baseline QVLBI demonstrations

	Accomplished demonstration	Proposed demonstration
Data length	Three passes in 52 days, with 3–6 h data in each pass. (Only two passes can provide long-term stability.)	Ten passes in 30 days (evenly distributed), with 6 to 10 h of data in each pass. (This will give a clear picture of the long-term performance.)
Participating stations	DSSs 11, 12, and 14.	DSSs 12 and 14 (entire frequency system). DSSs 42 and 43. (Because they use a common frequency standard, the differenced data will show the stabilities of other parts of the system.)
Frequency standards	HP 5065A.	HP 5065A. (No reset should take place during the period of tracking.)
Simultaneous two-way and three-way	10 and 20 s off synchronization during the last pass.	Maintain synchronization of time tag throughout the tracking period.
Independent measurement	Microwave measurements were made for the first two passes.	Continuous microwave measurement.
Spacecraft	Pioneers 10 and 11, with one pass during midcourse maneuver.	Pioneer 10 only, with no midcourse maneuver during the tracking period.

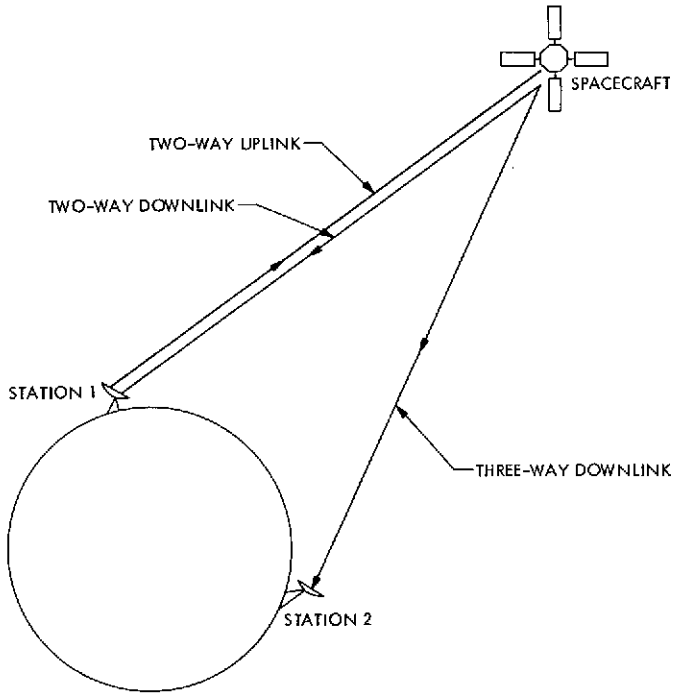

Fig. 1. Geometry of two-way and three-way doppler tracking

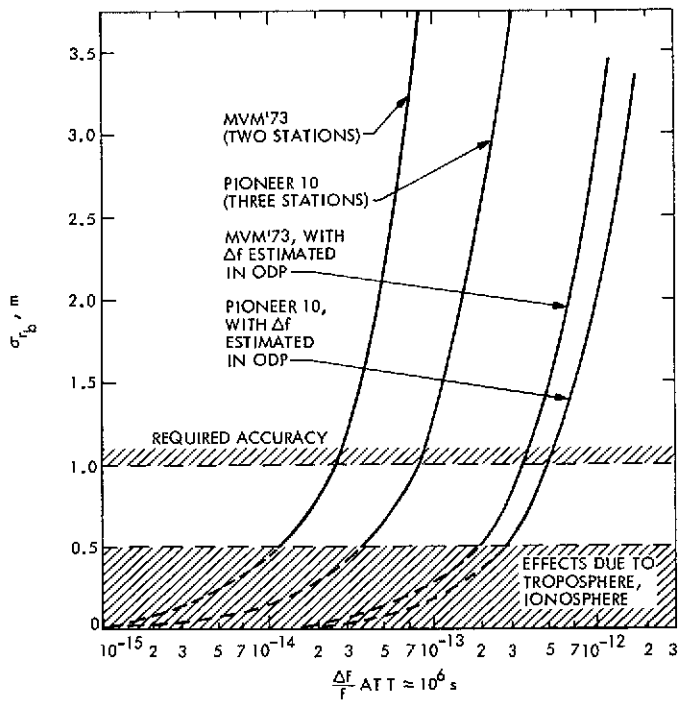

Fig. 2. Estimated effect of frequency offset on relative station location r_b uncertainties

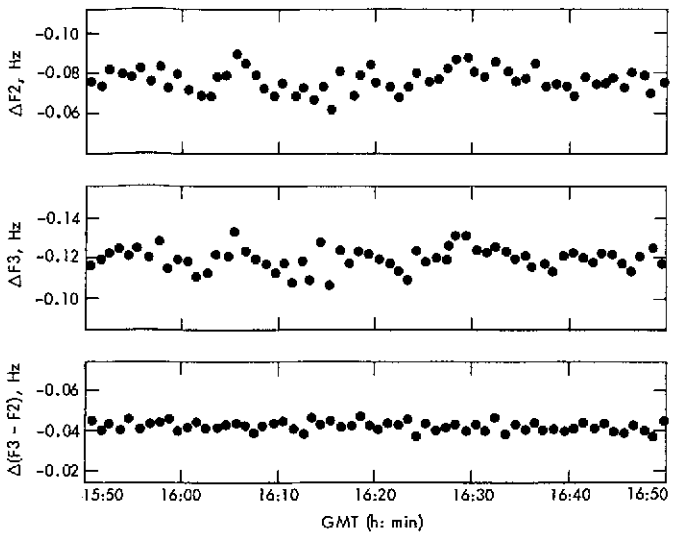

Fig. 3. Residuals of two-way, three-way, and differenced doppler on February 16, 1973 (DSSs 11, 12)

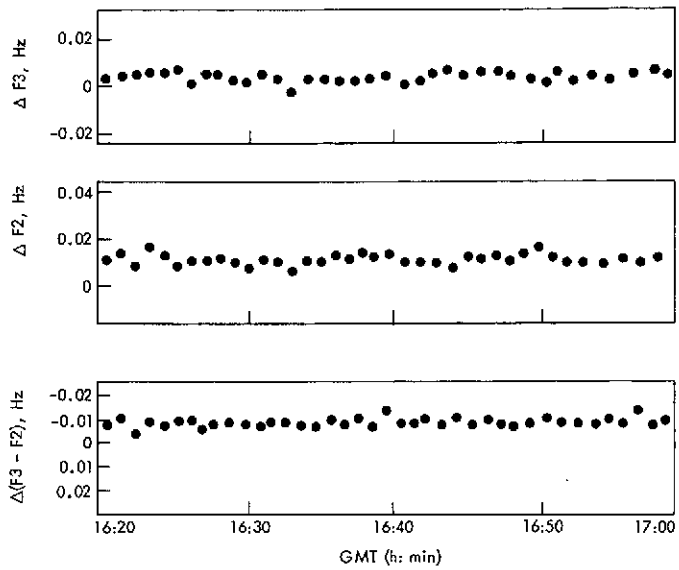

Fig. 4. Residuals of two-way, three-way, and differenced doppler on March 26, 1973 (DSSs 12, 14)

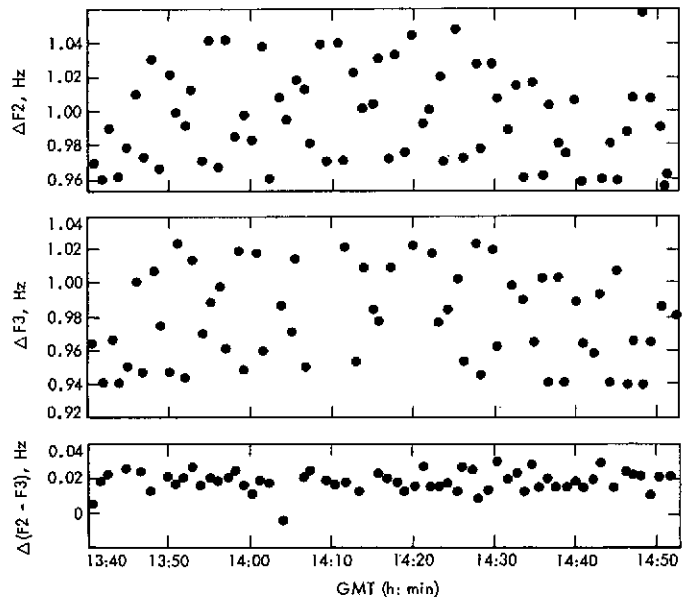

Fig. 5. Residuals of two-way, three-way, and differenced doppler on April 11, 1973 (DSSs 12, 14)

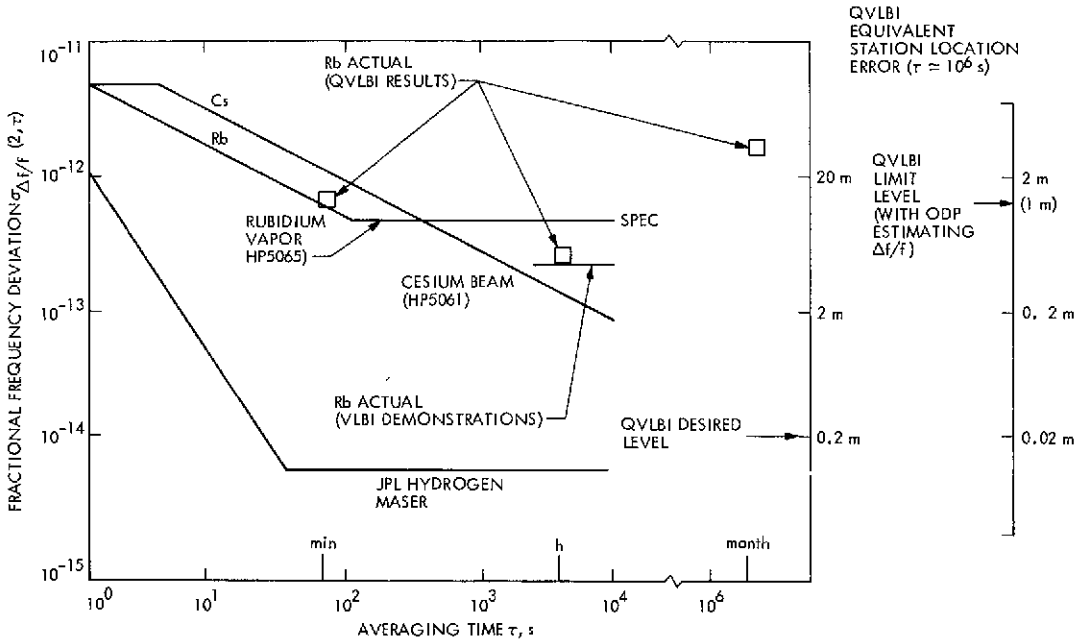

Fig. 6. Short baseline QVLBI demonstration—frequency system

Spacecraft Orbit Determination Using Long Tracking Arcs

J. K. Campbell and K. H. Rourke
Tracking and Orbit Determination Section

This article summarizes a study of the accuracy of planetary approach orbit determination based on long, 100-day arcs. Long arc orbit determination is an attractive means for improving the accuracy of radio metric based navigation in situations when conventional, 30-day "short arc" orbit determination strategies are particularly sensitive to bias deep space station (DSS) location errors. The accuracy analysis is based on the Viking Mission A and B trajectories; nevertheless, the results that are presented can be interpreted in a general way. Several error sources which are not usually included in short arc orbit determination analysis have been evaluated in the study, namely, randomly time-varying (stochastic) DSS location errors, Earth–Moon barycenter ephemeris errors, and spacecraft maneuver errors. The stochastic DSS location errors are included to model error effects arising from imperfect calibration of measurement system errors, e.g., troposphere, ionosphere, space plasma, timing, and polar motion. The inclusion of stochastic station errors in the orbit estimation strategies presented proved to be significant; these errors are shown to limit determination of the spacecraft orbit when the bias components of the station location error are also estimated. Example results using the two Viking trajectories nevertheless indicate that long arc radio orbit determination performs favorably in the presence of these and other errors, including conservative station location bias errors.

I. Introduction

Uncertainties in the deep space station (DSS) locations often produce the principal error source affecting the accuracy of radio metric based interplanetary navigation. DSS location error is used as a somewhat loose term, referring to not only Earth-fixed station coordinate uncertainties, but in addition uncertainties in the Earth's rotational dynamics, i.e., universal time (UT) and polar motion. Location errors may also include "effective" location errors arising from transmission media and instrumentation calibration errors that manifest themselves as apparent location errors in the orbit determination process. The collective radio metric "location error" is sometimes referred to as equivalent station location error.

Techniques for improving interplanetary navigation accuracy usually involve means for reducing the equivalent station location errors themselves, for instance,

improved transmission media and Earth rotation calibrations as well as improved determinations of the Earth-fixed DSS coordinates. Subjects related to this effort are found in numerous *Deep Space Network Progress Report* articles.

An alternate approach to improving navigation accuracy is the development of orbit determination techniques that exhibit reduced sensitivity to DSS location errors. A technique of this type, orbit determination based on long arcs of radio metric data, is discussed in this article. The term "long arc" refers to a span of radio metric data that is considerably longer than that necessary to minimally determine a spacecraft orbit. Thus, long arcs usually can be assumed to extend 100 days or more, as opposed to the conventional short arc, extending usually no more than 30 days. The motivation for long arcs rests in the interest in shifting from the short arc (essentially geocentric determination of the spacecraft motion) to the long arc (heliocentric determination of the spacecraft motion). This shift of radio metric information content is provided by the "heliocentric bending" due to solar gravitation that can be observed with the longer data arc. This property is somewhat in analogy to the accurate planet-centered determinations of spacecraft motion available during planetary flybys and orbiter phases. Consideration of navigation techniques that are less sensitive to DSS location errors does not suggest that improvements in DSS location accuracies (using the "location" in its general sense) are not necessarily warranted. Any improvements in navigation accuracy should be pursued whenever attractive.

Radio orbit determination based on long data arcs, although usually considered less sensitive to station location errors, is not as yet a widely accepted orbit determination technique despite some favorable operational experiences during the Mariner Mars 1969 and 1971 Missions (see Ref. 1, for example). The principal inhibition in processing long data arcs is a lack of sufficient understanding regarding the effects of major error sources on the estimation parameters. Another disadvantage cited is the assumed requirement that the radio data arc cover an interval of time that is as free as possible from major orbit perturbations, such as midcourse maneuvers. The possibility of significantly reducing the sensitivity of orbit estimates to station location errors is an attractive one, however, and hence the continued interest in long data arc processing techniques for navigation applications. In the following, orbit determination accuracies using long data spans are examined for two Viking trajectories. The data arc is arbitrarily defined to span from 100 days prior to the spacecraft's encounter with the target planet Mars.

II. Error Models for Long Arc Analysis

As pointed out, the accuracy characteristics of long arc orbit determination are not as completely understood as those for the short arc. Hence, a rather complete approach in analyzing long arc accuracies is called for. In particular, special care should be taken to include error sources which may significantly corrupt the characteristically different information inherent in the long data arc. Two error sources of this type have been included in this study. These are Earth–Moon barycenter ephemeris errors and also nonconstant (stochastic) station location errors produced by uncertainties in the polar motion, universal time, and transmission media calibrations. In the subsequent discussion, the expression "Earth–Moon barycenter" will be abbreviated as simply "Earth."

In short arc analyses, the short-term Earth ephemeris errors are found to be similar in character to the target planet ephemeris errors, and hence are usually represented as effective target planet ephemeris errors. In processing long data arcs, however, it is to be expected that long-term spacecraft orbit effects can only be poorly distinguished from long-term Earth orbit effects, and thus Earth ephemeris errors must be explicitly modeled for the long arc analysis. An assumption that is made in modeling the Earth and Mars ephemeris errors is that the heliocentric ephemeris errors of the target planet and the Earth can be expected to be strongly interrelated; this is the case since planetary ephemerides are determined from Earth-based observations. The interrelation is accounted for by a complete (12×12) position and velocity covariance describing the correlated Earth–Moon barycenter and target planet position and velocity errors. The ephemeris errors are resolved into an (inertial) plane-of-sky type cartesian coordinate system defined as follows (see Fig. 1):

z-axis: points toward Earth from target planet at spacecraft encounter time T

x-axis: points in direction of increasing target planet right ascension at time T

y-axis: points in direction of decreasing target planet declination at time T

Station location errors are representative of physical DSS station location errors plus "equivalent" station location errors that may be attributed to uncalibrated instrumentation and transmission effects. (Reference 2 discusses the concept of equivalent station location errors.) The station location error model assumed for the long arc analysis has both constant and stochastic components. This is in

contrast to the more common approach taken in short arc analysis of assuming the errors to be of a bias nature only; in fact, the station location error has a significant stochastic component (see, for example, Ref. 3). Stochastic station location errors refer to errors that can be adequately represented as randomly time-varying station location parameters (in particular, longitude and distance from the spin axis). In processing short arcs, station location parameters are generally not estimated, but the effect of the station location errors is included in the orbit accuracy determination; in this case, the stochastic error effects are negligible (see Chapter 4 of Ref. 4).

The specific DSS location error model is defined as follows: each station location is assumed to have both bias and stochastic errors in longitude and distance from the spin axis. (Preliminary work showed the tracking station distance from the equatorial plane to be inconsequential; this error source was eliminated in the subsequent study.) It is assumed that each station's constant longitude error $\bar{\epsilon}_\lambda$ is composed of an absolute component $\epsilon_{\bar{\lambda}}$ and a relative component $\epsilon_{\Delta\lambda}$, i.e.,

$$\bar{\epsilon}_\lambda = \epsilon_{\bar{\lambda}} + \epsilon_{\Delta\lambda}$$

for each station, where each $\epsilon_{\Delta\lambda}$ is independent from station to station. The absolute component $\epsilon_{\bar{\lambda}}$ represents an error common to all tracking stations (e.g., universal time and polar motion errors). The total longitude error ϵ_λ is composed of the bias term $\bar{\epsilon}_\lambda$ and the stochastic component $\epsilon_{\delta\lambda}$, i.e.,

$$\epsilon_\lambda = \bar{\epsilon}_\lambda + \epsilon_{\delta\lambda}$$

for each station. The distance from the spin axis ϵ_{r_s} has a bias component $\epsilon_{\bar{r}_s}$ and a stochastic component $\epsilon_{\delta r_s}$:

$$\epsilon_{r_s} = \epsilon_{\bar{r}_s} + \epsilon_{\delta r_s}$$

The stochastic station location parameters are modeled as first-order stationary Markov processes with correlation R of the form

$$R = \sigma^2 \exp\left[-a|\Delta t|\right]$$

The correlation time $1/a$ is set at two days.

Consideration of spacecraft maneuver errors can usually be avoided when analyzing short arc orbit accuracies by choosing data arcs which are free of maneuver perturbations. In this long arc study, however, midcourse maneuvers are assumed to occur at several points during the 100-day data span; this requires the inclusion of the maneuver error effects in the analysis of the data arc. The maneuver motor burn is of relatively short duration and is effectively modeled as a trajectory position and velocity discontinuity.

III. Orbit Determination Filter Strategy

In this section, we discuss the attempt to choose an appropriate procedure for processing the long data arc: which parameters affecting the data should be estimated, and which, although not estimated, should be considered in the accuracy analysis as affecting the orbit estimate obtained from the data. To arrive at a proper data filtering model, we first list the parameters and error sources affecting the data and spacecraft dynamics:

(1) Spacecraft trajectory (position and velocity), as determined by gravitational motion.

(2) Nongravitational spacecraft accelerations, caused by solar pressure and attitude control (constant and stochastic components).

(3) Spacecraft midcourse maneuver errors (motor pointing and shutoff).

(4) Target planet ephemeris errors.

(5) Earth ephemeris errors, and station location errors (constant and stochastic component).

A batch sequential filter is available to evaluate the effects of the nonconstant parameters (Ref. 5). The idea is to choose a set of parameters which can be effectively estimated from the long arc data, in the presence of errors modelable in terms of parameters whose values are not accurately known. In this light, the approach taken was to postulate, evaluate, and compare the following two filters:

(1) *Filter 1* (station location errors not explicitly estimated)

   (a) *Estimated parameters*
   Spacecraft state errors (position and velocity)
   Constant nongravitational acceleration errors
   Spacecraft midcourse maneuver errors

   (b) *"Considered" parameters*
   (parameters not estimated but whose error covariance degrades error covariance of estimated parameters)
   Target planet ephemeris errors
   Earth ephemeris errors
   Station location errors (constant and stochastic)

(2) *Filter 2* (constant station location errors estimated)

   (a) *Estimated parameters*
   Spacecraft state errors

Constant nongravitational acceleration errors
Spacecraft midcourse maneuver errors
Absolute component of constant station longitude error
Constant component of station spin axis error

(b) *"Considered" parameters*
Target planet ephemeris errors
Earth ephemeris errors
Constant relative component and stochastic component of station longitude error
Stochastic component of station spin axis error

We have assumed for each filter a stochastic component of nongravitational acceleration, postulated in order to model such random spacecraft perturbations as attitude control gas leakage and unpredictable fluctuations in the solar constant. These small random forces are also modeled as stationary stochastic processes, acting along each spacecraft axis; since relatively little is known of the dynamics involved, the acceleration processes are assumed to be uncorrelated between batches. These acceleration uncertainties, often referred to as process noise, are included because, although they have a negligible direct effect on the spacecraft orbit, they can, if improperly accounted for, limit the capability to actually estimate the orbit. Earth ephemeris errors essentially affect only the data, while the target ephemeris errors are felt only shortly before spacecraft encounter. These variables are strongly correlated and are not estimated. Midcourse maneuver velocity errors can significantly affect the orbit accuracies, and are estimated in each filter. The 3-axis constant components of nongravitational acceleration are easily modeled, and are also estimated in each filter.

Thus, two distinct solution strategies are hypothesized; both explicitly estimate the nongravitational acceleration effects and the spacecraft maneuvers. The performance of the two filters is compared on the basis of the estimates obtained when constant station locations are not included among the estimated parameters (filter 1), and in filter 2, which solves for constant errors in the station's absolute longitudes and distance from the spin axis. Both station location parameters are estimated, since it has been determined that the orbit solution errors become increasingly sensitive to spin axis errors, if the longitudes alone are estimated.

IV. Numerical Examples

The performance of the long arc data filters described above is evaluated using two example Viking trajectories. Trajectory A is representative of the Viking Mission A trajectories, encountering Mars early in the 1976 arrival period; the orbit determination geometry is favorable throughout the heliocentric cruise and encounter period. Trajectory B is representative of the Viking Mission B trajectories, encountering Mars later in the arrival period; its orbit determination performance is known to be degraded, due to low spacecraft declination geometry.

The data types assumed for the sample trajectories are the standard range and range rate. The data pattern takes every other pass of range rate data from DSSs 14, 42, and 61, from encounter minus 100 days ($E-100$) to encounter minus 3 days ($E-3$). Continuous range rate data are assumed from $E-3$ days to encounter, when the spacecraft dynamics begin to change more rapidly. The range datum consists of a single point from DSS 14, taken at $E-30$ days. Table 1 summarizes the data accuracy levels assumed. Note from Table 1 that the range datum is deweighted in the filters from its nominal expected value (in the vicinity of 50 m). This artifice allows Earth-based spacecraft position determinations to be consistent with target planet-centered position determinations, when the target planet ephemeris errors are included. Tables 2 and 3 summarize the parameter *a priori* error levels. The nongravitational acceleration levels and spacecraft maneuver errors are characteristic of the expected magnitudes. Two maneuvers are assumed to occur, at $E-30$ days and $E-10$ days. With regard to the station location *a priori* errors, the assumed 10-m absolute longitude error is postulated to conservatively reflect longitude knowledge degradation. Spin axis error has a nominal level of 1.5 m. The stochastic station error standard deviations are somewhat arbitrarily assigned to be 2 m for both longitude and spin axis, with correlation times set at 2 days, roughly corresponding to the intervals at which data are received from each station. The ephemeris errors accurately reflect the expected levels and are delineated separately in Table 3.

The numerical results of the study are shown in Figs. 2–6, for trajectories A and B, filters 1 and 2. Figures 2–5 show time histories of accuracy prediction in the usual B-plane; the estimate sensitivity to the individual error sources is also given. For the example trajectories, $\mathbf{B}\cdot\mathbf{R}$ errors generally predominate, and the solution time histories are shown in terms of the behavior of only the $\mathbf{B}\cdot\mathbf{R}$ coordinate.

In the case of solved-for parameters, the sensitivity that is presented is the sensitivity to an actual *a priori* error. A special convention is taken regarding the maneuver errors: although the data are filtered assuming that a 0.1-m/s per axis error existed, actual errors are not included in the overall error predictions. The effects of

actual maneuver errors can be ascertained from the ΔV curves shown in Figs. 2–5, however. These curves permit an evaluation of the effects of nominal maneuver errors and also allow an assessment of the effects of maneuver errors that are larger or smaller than the nominal 0.1-m/s error.

Note from Figs. 2 and 3 that the limiting error source, when station locations are not estimated (filter 1), is the absolute longitude component of the longitude bias. Figures 4 and 5 show that the inclusion of the constant tracking station location parameters as solve-for parameters is preferable, given that large station longitude errors are expected. In this case, the errors limiting the determination of the spacecraft orbits are the randomly time-varying (2-m) station location errors.

Perhaps the most significant results of this study are found in the curves which show the effects of station locations for each trajectory/filter case. These results indicate that (1) long arcs are strongly degraded by (10-m) longitude errors if station parameters are not estimated (filter 1); and (2) if station parameters are estimated (filter 2), the stochastic station effects (at 2 m) become the dominant error source.

Figure 6 shows the individual effects of Earth–Moon barycenter ephemeris errors. The effect of Mars ephemeris errors on $\mathbf{B} \cdot \mathbf{R}$ is relatively smaller and somewhat constant at the 100–200-km level (not shown). The implication is clear when comparing these curves to the curves in Figs. 2–5, showing the full Earth/Mars effects: that the detailed relationship between ephemeris errors (principally the Earth), as specified by the full 12×12 covariance, strongly affects the expected orbit accuracy. In particular, when estimating stations, the combined Mars–Earth effects (shown in Figs. 4 and 5) produce a smaller effect than either their effect when considering stations or the effect of the Mars ephemeris error model. This implies that special care must accompany the specification of the full covariances in subsequent long arc analysis and further effort should be directed toward better understanding the input covariances to assure that they truly reflect the expected planetary errors. Figure 7 gives the time history of the station parameters estimated using filter 2.

V. Conclusions

The universality of the above results is difficult to determine for different mission applications with different geometries. Nevertheless, several salient points present themselves:

(1) Estimation strategies that include tracking station locations as solution parameters are preferable to those that do not solve for location parameters, given that large station longitude errors are expected. Indeed, for the 100-day data arcs, the orbit determination errors still show considerable sensitivity to station location errors, if station locations are not estimated.

(2) When station locations are estimated, the dominant error source is stochastic station location errors. In the case of trajectory B, the effect of stochastic station location errors actually becomes magnified as station location parameters are solved for.

(3) Coupled Earth ephemeris and planetary (Mars) ephemeris errors do not produce large estimation errors, given that highly correlated errors (obtained from planetary ephemeris solutions) are assumed. Preliminary work has shown that use of uncorrelated ephemeris errors leads to the prediction of catastrophic orbit determination errors, principally through Earth ephemeris errors.

(4) Spacecraft maneuvers can be estimated without difficulty, given that maneuver errors do not greatly exceed assumed magnitudes (e.g., greater than 6σ; $\sigma = 0.1$ m/s).

Also, as an outcome of this analysis, the following two basic recommendations can be made:

(1) Long arc techniques are a feasible and attractive means for alleviating orbit accuracy sensitivity to station locations errors. The techniques of long arc orbit determination differ somewhat from those that have been developed for the short arc. The long arc technology requires further development to assure reliable and economical performance, particularly in the areas of:

   (a) Filter procedure development, to determine the critical parameters of filter design for the long arc methods.

   (b) Data processing economization, particularly in the areas of data compression and data batching techniques, to remove the somewhat unwieldy character of long arc data processing.

   (c) Strategy testing using past mission tracking data, to insure that techniques deemed attractive by general analyses do perform as expected.

(2) The analysis identified stochastic station location errors and barycentric ephemeris errors as major error sources for long arc orbit determination. The understanding of these errors requires further development, in particular:

(a) Simplified, conservative and yet representative models should be developed for describing the barycentric errors. As long as formal and complex error models, such as 12×12 error covariances, are used for these analyses the reliability of their predicted accuracies shall remain questionable to some degree.

(b) The actual stochastic station location error levels (i.e., rms magnitude) should be assessed rather than just hypothesized, as done in this study. This should be done on an analytical as well as an empirical basis, i.e., estimates could be derived from measurement systems analysis and analysis of past mission tracking data.

References

1. Gordon, H. J., et al., *The Mariner VI and VII Flight Paths and Their Determination from Tracking Data*, Technical Memorandum 33-469, Jet Propulsion Laboratory, Pasadena, Calif., Dec. 1, 1970.
2. Jordan, J. F., et al., "The Effects of Major Error Sources on Planetary Spacecraft Navigation Accuracies," AIAA Paper 70-1077, presented at the AAS/AIAA Astrodynamics Conference, Santa Barbara, California, August 19–21, 1970.
3. Madrid, G. A., et al., *Tracking System Analytic Calibration Activities for the Mariner Mars 1971 Mission*, Technical Report 32-1587, Jet Propulsion Laboratory, Pasadena, Calif., Dec. 15, 1973.
4. Curkendall, D. W., *Problems in Estimation Theory with Applications to Orbit Determination*, Report 7275, UCLA Department of Engineering, Sept. 1972.
5. Nishimura, T., and Nead, M., *ATHENA Filter Sequential Orbit Determination with General Evaluation Capability*, document 900-605, Mar. 8, 1973 (JPL internal document).

Table 1. Data assumptions

Range Rate:
(1) DSSs 14, 42, and 61
(2) Every second pass from each station, from $E-100$ days to $E-3$ days
(3) Continuous data from $E-3$ days to encounter
(4) Assumed measurement accuracy is 1 mm/s
Range:
(1) One point at $E-30$ days from DSS 14
(2) Range point artificially deweighted by assuming a 20-km measurement error

Table 2. *A priori* parameter errors

1. Initial state	10^5-km position
	1-km/s velocity
2. Nongravitational acceleration	1.2×10^{-12}-km/s^2 per axis bias error
3. Spacecraft maneuvers (assumed to occur at $E-30$ days and $E-10$ days)	0.1 m/s per axis for each of two maneuvers
4. Equivalent station location errors	(a) *Bias* Absolute longitude $\epsilon_{\bar{\lambda}} = 10$ m Relative longitude $\epsilon_{\Delta\lambda} = 0.95$ m Spin axis $\epsilon_{\bar{r}_s} = 1.5$ m
	(b) *Stochastic* (correlation time 2 days) Relative longitude $\epsilon_{\delta\lambda} = 2$ m Spin axis $\epsilon_{\delta r_s} = 2$ m
5. Ephemerides	See Table 3

Table 3. Ephemeris errors

Trajectory A: Encounter 6/23/76		Trajectory B: Encounter 8/21/76	
Earth–Moon barycenter	Mars	Earth–Moon barycenter	Mars
Heliocentric errors			
$\sigma_x = 43$	$\sigma_x = 92$	$\sigma_x = 57$	$\sigma_x = 98$
$\sigma_y = 43$	$\sigma_y = 77$	$\sigma_y = 45$	$\sigma_y = 84$
$\sigma_z = 52$	$\sigma_z = 51$	$\sigma_z = 34$	$\sigma_z = 36$
$\sigma_{\dot{x}} = 1.0 \times 10^{-5}$	$\sigma_{\dot{x}} = 5.1 \times 10^{-6}$	$\sigma_{\dot{x}} = 6.9 \times 10^{-6}$	$\sigma_{\dot{x}} = 4.5 \times 10^{-6}$
$\sigma_{\dot{y}} = 8.2 \times 10^{-6}$	$\sigma_{\dot{y}} = 7.9 \times 10^{-6}$	$\sigma_{\dot{y}} = 7.9 \times 10^{-6}$	$\sigma_{\dot{y}} = 7.1 \times 10^{-6}$
$\sigma_{\dot{z}} = 8.5 \times 10^{-6}$	$\sigma_{\dot{z}} = 8.5 \times 10^{-6}$	$\sigma_{\dot{z}} = 1.2 \times 10^{-5}$	$\sigma_{\dot{z}} = 9.4 \times 10^{-6}$
Earth–Moon barycentric errors			
	$\sigma_x = 133$		$\sigma_x = 158$
	$\sigma_y = 100$		$\sigma_y = 118$
	$\sigma_z = 10$		$\sigma_z = 7$
	$\sigma_{\dot{x}} = 6.6 \times 10^{-6}$		$\sigma_{\dot{x}} = 6.3 \times 10^{-6}$
	$\sigma_{\dot{y}} = 1.1 \times 10^{-5}$		$\sigma_{\dot{y}} = 1.2 \times 10^{-5}$
	$\sigma_{\dot{z}} = 1.7 \times 10^{-5}$		$\sigma_{\dot{z}} = 2.1 \times 10^{-5}$

Assumed: Full (12 × 12) covariance of Earth–Moon barycenter and Mars plane-of-sky cartesian state errors. The corresponding heliocentric and barycentric position and velocity in km, km/s, are given, using encounter dates for trajectories A and B as reference times.

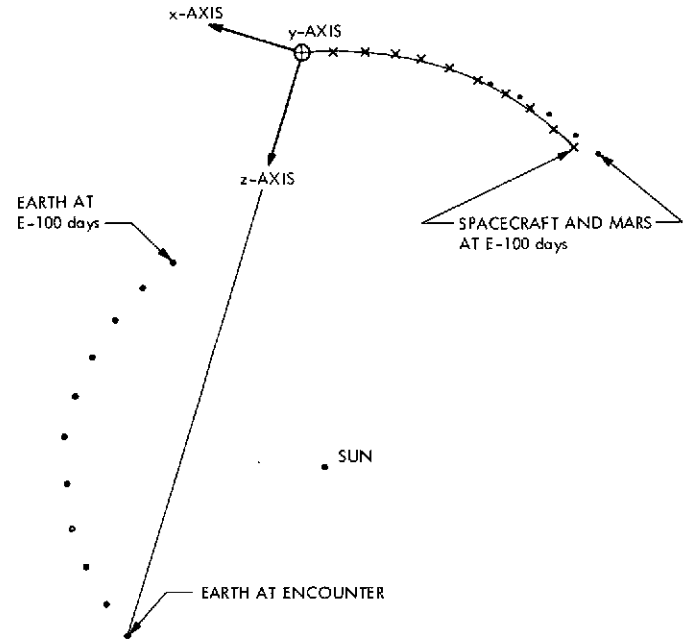

Fig. 1. Plane-of-sky ephemeris coordinates and trajectory geometry (trajectory A) example

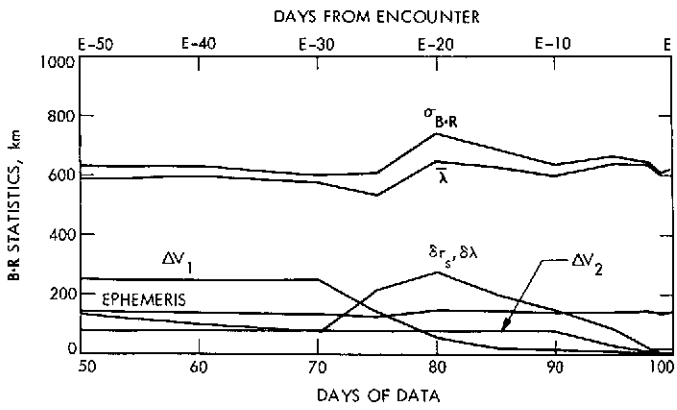

Fig. 2. Trajectory A, filter 1 error source comparison

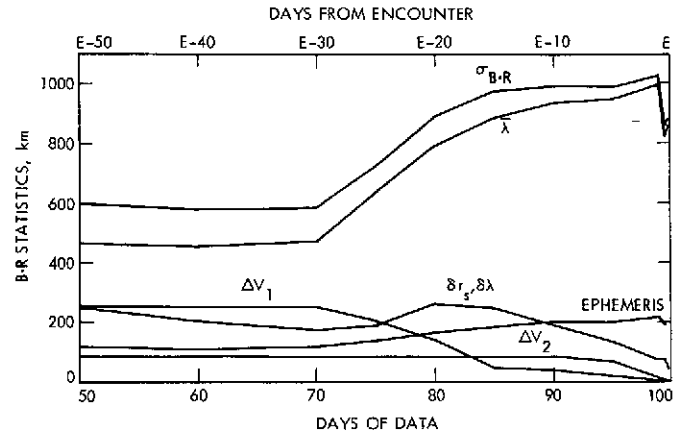

Fig. 3. Trajectory B, filter 1 error source comparison

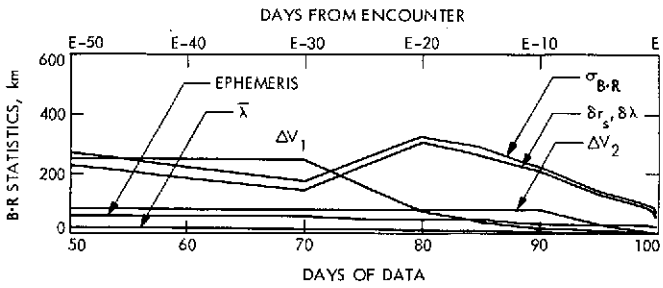

Fig. 4. Trajectory A, filter 2 error source comparison

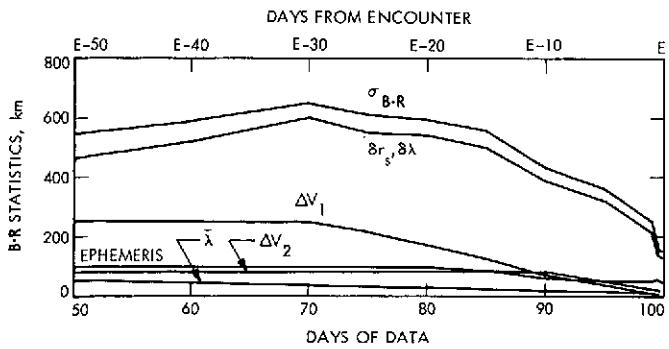

Fig. 5. Trajectory B, filter 2 error source comparison

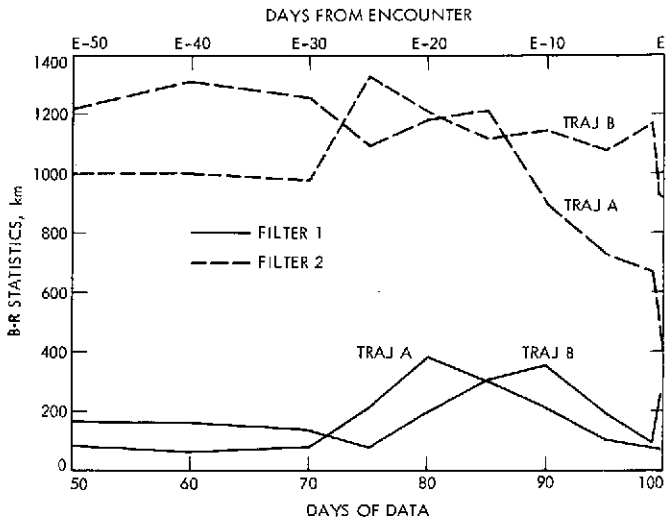

Fig. 6. Earth–Moon barycenter perturbations

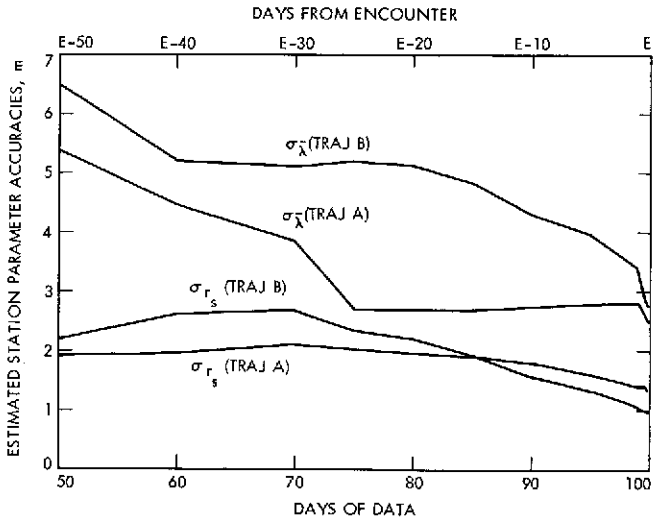

Fig. 7. Time history of station parameter accuracies from filter 2

Hydrogen Maser Frequency Standard: Receiver Configuration and Stability Requirements

R. F. Meyer
Communications Systems Research Section

The final receiver configuration and current status of the Jet Propulsion Laboratory hydrogen maser is discussed along with the phase noise and stability requirements for the various receiver modules.

I. Introduction

This is one of a continuing series of articles discussing the development of a hydrogen maser for use as a station standard in the DSN. The major objectives of this project are to develop a frequency standard that can: (1) guarantee a long-term frequency stability of at least 6×10^{-15}, (2) be reproduced on a semi-production basis from minimal documentation by non research and development (R&D) personnel, (3) be easily operated by site personnel and calibrated at station depots, and (4) operate on a one- to two-year major service interval.

II. Mechanical Configuration and Operation

The JPL hydrogen maser consists of two assemblies, the physics unit and the receiver unit, which are connected by cables. The physics unit must reside in an area free of magnetic interference, while the receiver, which is housed in a standard DSIF rack, is normally placed in the control room. A 120-Vac 15-A line powers the entire system which can be supplied through a 2-kW uninterruptible power supply (UPS) if uninterrupted operation is desired.

The receiver-control rack uses a modular approach to facilitate maintenance and future upgrading. The rack houses three power supplies and a synthesizer with the control section packaged in two cages of Nim-Bin modules and the receiver-synthesizer occupying three cages of the new DSIF standard radio-frequency (RF) module type B. All the receiver modules except the front end, which is mounted on the RF oven plate in the physics unit, are located in the rack and are easily replaceable. Each of the 18 modules is preadjusted during assembly and the entire receiver can be calibrated in one step by the operator without auxiliary equipment.

A number of self-testing features are built into the maser for ease of post-assembly calibration and maintenance in the field. The receiver contains a test oscillator

that synthesizes the maser frequency from an external 5-MHz reference and is used any time the maser signal is absent. Also included is an audio oscillator that measures the Zeeman frequency of the cavity and a multiple function digital panel meter that indicates various operating parameters, including the maser output power.

III. Physics Unit

A long-standing problem of hydrogen masers has been hard starting and low output power (−95 dBmW). A unique bulb coating (Ref. 1) has improved this situation by raising the output by 10 dB, thereby directly improving short-term stability due to a better signal-to-noise ratio. An added advantage is that full power can be obtained after about 30 min of pumping down the vacuum. Another difficulty with previous masers is the perturbation of the maser's phase by the vacuum pump at high flux levels. The traditional solution has been to lower the maser's output, but attention is presently focused on modifying the pump elements to withstand higher flux levels without disturbing the maser's output (Refs. 2, 3). In addition, mechanical reliability is being stressed and a special container has been fabricated for shipping the relatively delicate physics unit over common carriers.

The problem of maintaining cavity tuning over long periods of time has been greatly simplified. A method of automatic tuning (Refs. 4, 5, 6, 7) operates two masers in a master-slave mode whereby the first maser varies its flux to detect a tuning error, while the second maser tunes its varactor-controlled cavity to match the averaged frequency of the first. The difference in frequency of the two masers is generated by the zero crossing detector module which compares each of the 100-MHz outputs from the masers and sends the error information on a 0.01-Hz carrier to the auto-tuner control module which, in turn, applies the required cavity correction.

IV. Receiver

Some hydrogen masers fall short of expectations in the area of long-term stability simply because so much effort is expended on the complex physics unit that receiver performance is degraded through lack of development. One of the major challenges of the JPL hydrogen maser has been to design a receiver that can translate the maser's long-term stability directly into usable output frequencies. To achieve a "useable" output frequency distribution system, every standard frequency is provided with multiple outputs at a high power level and high isolation. This is necessary since the use of supplementary amplifiers, multipliers, and dividers can degrade performance by over two orders of magnitude. Table 1 lists the outputs that are available at the interface panel located on the bottom of the receiver rack. Also each of these frequencies (except 1400 MHz) has one additional output that is available on the front of the receiver.

The final configuration of the receiver-synthesizer (shown in the simplified block diagram of Fig. 1) is a triple conversion phase-lock receiver with a divider chain providing the standard distribution frequencies. Although the receiver appears rather conventional, a great deal of effort was expended in researching a configuration that could meet the stability and phase noise requirements of the maser with present state-of-the-art techniques. For example, the prototype masers that are currently operating at DSS 14 use a substantially more complex quadruple conversion receiver simply because the earlier model synthesizer lacks the resolution required to set the output frequencies within the required tolerances. The new receiver employs a synthesizer (Refs. 8, 9) with a resolution of 1 μHz which allows the output to be accurately set to within 7 parts in 10^{16}. Other areas of development include front end isolators with highly stable input VSWRs and magnetic shielding to prevent cavity detuning, a 0.02% bandwidth crystal filter in the first intermediate frequency (IF) that can meet the required phase stability without an oven, a sampling phase locked loop $\times 14$ multiplier (Refs. 10, 11) that achieves a 10-dB reduction in phase noise over conventional circuits, a 100-MHz VCO (Ref. 12) with low phase noise that requires retuning only once a year, and finally a divider-distribution amplifier (Refs. 13, 14, 15) chain with extremely low phase noise, 100-dB isolation between outputs, and meeting stringent stability requirements without the use of ovens.

V. Stability and Phase Noise Requirements

In view of the performance of the present hydrogen masers a long-term stability requirement of 10^{-15} was chosen for the overall receiver when operating in a control room environment. Since the stability requirements are severe it is important that the test conditions simulate the actual operational environment in order to avoid overly restrictive specifications. Investigation in this area revealed that most of the phase drift in the receiver is caused by temperature variations in the plenum air that cools the rack. A one-week monitor of the plenum air at DSS 14 showed a 2°C variation in temperature with a maximum short-term perturbation of 0.5°C lasting about 400 s. These data became the basis for the test conditions stated in *Footnote a* of Table 2. For the receiver modules

listed in Table 2 the phase drift rates were assumed to be cumulative, i.e., none of the phase drifts canceled each other. All the modules within the loop receive phase correction equal to the ratio of the maser frequency to the voltage-controlled oscillator (VCO) frequency, excepting the VCO and the 100-MHz distribution amplifier which theoretically receive almost infinite correction. In practice however, these two modules require a minimum amount of stability to prevent adverse effects on acquisition and hold-in performance of the loop. The fact that fractional frequency stability depends only upon phase drift *rate* (radians/second) implies that a module may have a very large phase drift provided it is slow in responding. This is harmless to the receiver loop but can have a disruptive effect on systems that use several of the hydrogen maser outputs simultaneously and are dependent on the relative phase between the outputs remaining constant. Therefore, all the outputs of the maser have a requirement holding the phase to within 5° over a 0 to 50°C temperature range.

Since most of the modules exhibit a $1/f$ phase noise spectral characteristic below 1 kHz, a noise reading at 10 Hz has been chosen as the standard measure of performance within the receiver loop bandwidth of 100 Hz. At an output of −85 dBmW the power spectral density of phase for the hydrogen maser at 10 Hz is about −109 dB rad²/Hz (Ref. 16). Ten percent of this noise was chosen as the maximum allowable contribution by the receiver loop and is the basis for the noise requirements in Table 2. However, as the maser noise progresses through the divider chain outside the loop, it is successively divided until it is reduced to −169 dB at the 100-kHz output. Even the best amplifiers (Ref. 17) as yet do not have noise levels below −150 dB and substantial problems exist in measuring phase noise performance below −140 dB due to the difficulty in eliminating amplitude modulation (AM) to phase modulation (PM) conversion in the test configurations. Since phase noise is additve rather than multiplicative, the desirability of achieving low phase noise while retaining high isolation in the distribution amplifiers has brought about an important compromise, for high isolation requires many stages, yet each additional stage will increase the phase noise by 6 dB (assuming identical stages).

One final consideration in the design of the hydrogen maser has been the stability of the coaxial cable (Refs. 18, 19) that interconnects the various components. To achieve sufficient stability, short lengths of semirigid, solid dielectric cable are used in the receiver rack and a 1.5-cm (½ in.) corrugated foam dielectric line is used for the microwave cables from the physics unit. Preserving the stability of a reference frequency over a long distance cannot be done with any presently available cable; however, currently under development is a pneumatic controlled form of active phase compensation wherein the electrical length of the cable is varied by adjusting the air pressure within the line.

VI. Conclusion

Although the hydrogen maser has demonstrated the capability of generating highly stable reference frequencies, new techniques will be needed to distribute this stability to the user destinations. This will require advanced development in the areas of station distribution amplifier banks, control room cabling, and intersite microwave links.

References

1. Erpenbach, H., Finnie, C., "High Output Power for Hydrogen Maser Frequency Standards," *The Deep Space Network Progress Report*, Technical Report 32-1526, Vol. VII, pp. 106–108. Jet Propulsion Laboratory, Pasadena, Calif., Feb. 15, 1972.
2. Erpenbach, H., Finnie, C., Petty, S., "Frequency Generation and Control: Atomic Hydrogen Frequency Standard," *The Deep Space Network*, Space Programs Summary 37-59, Vol. II, pp. 54–56. Jet Propulsion Laboratory, Pasadena, Calif., Sept. 30, 1969.
3. Erpenbach, H., Dachel, P., "Frequency Generation and Control: Improved Vacuum Pump for the Atomic Hydrogen Frequency Standard," *The Deep Space Network Progress Report*, Technical Report 32-1526, Vol. XVI, pp. 69–71. Jet Propulsion Laboratory, Pasadena, Calif., Aug. 15, 1973.

References (contd)

4. Finnie, C., "Frequency Generation and Control: Atomic Hydrogen Maser Frequency Standard," *The Deep Space Progress Report*, Technical Report 32-1526, Vol. I, pp. 73–75. Jet Propulsion Laboratory, Pasadena, Calif., Feb. 15, 1971.

5. Finnie, C., "Design of Hydrogen Maser Cavity Tuning Servo," *The Deep Space Progress Report*, Technical Report 32-1526, Vol. II, pp. 86–88. Jet Propulsion Laboratory, Pasadena, Calif., April 15, 1971.

6. Finnie, C., "Tracking and Ground-Based Navigation: Hydrogen Maser Frequency Standard Automatic Cavity Tuning Servo," *The Deep Space Network Progress Report*, Technical Report 32-1526, Vol. XIV, pp. 56–59. Jet Propulsion Laboratory, Pasadena, Calif., April 15, 1973.

7. Finnie, C., Norris, D. A., "Hydrogen Maser Frequency Standard Automatic Tuning Servo," *The Deep Space Network Progress Report*, Technical Report 32-1526, Vol. XVI, pp. 72–77. Jet Propulsion Laboratory, Pasadena, Calif., Aug. 15, 1973.

8. Wick, M. R., "Programmed Oscillator Development," *The Deep Space Network*, Space Programs Summary 37-66, Vol. II, pp. 127–132. Jet Propulsion Laboratory, Pasadena, Calif., Nov. 30, 1970.

9. Wick, M. R., "DSN Programmed Oscillator Development," *The Deep Space Network Progress Report*, Technical Report 32-1526, Vol. VII, pp. 111–124. Jet Propulsion Laboratory, Pasadena, Calif., April 15, 1972.

10. Lutes, G., MacConnell, J., and Meyer, R., "Hydrogen Maser: Low Phase Noise, L-Band Frequency Multiplier," *The Deep Space Network Progress Report*, Technical Report 32-1526, Vol. VII, pp. 81–83. Jet Propulsion Laboratory, Pasadena, Calif., Feb. 15, 1972.

11. MacConnell, J., Meyer, R., "L-Band Frequency Multipliers: Phase Noise, Stability, and Group Delay," *The Deep Space Network Progress Report*, Technical Report 32-1526, Vol. X, pp. 104–109. Jet Propulsion Laboratory, Pasadena, Calif., Aug. 15, 1972.

12. Sward, A., "Frequency Generation and Control: Performance and Analysis of a 100 MHz VCXO," *The Deep Space Network*, Space Programs Summary 37-51, Vol. II, pp. 56–61. Jet Propulsion Laboratory, Pasadena, Calif., May 31, 1968.

13. Lutes, G., "Frequency Generation and Control: Distribution Amplifiers for the Hydrogen Maser Frequency Standard," *The Deep Space Network*, Space Programs Summary 37-61, Vol. II, pp. 68–72. Jet Propulsion Laboratory, Pasadena, Calif., Jan. 31, 1970.

14. Lutes, G., "Improved Frequency Dividers," *The Deep Space Network*, Progress Report 32-1526, Vol. II, pp. 56–58. Jet Propulsion Laboratory, Pasadena, Calif., April 15, 1971.

15. Lutes, G., "Phase-Stable, Low-Phase-Noise Filters for Reference Signals," *The Deep Space Network Progress Report*, Technical Report 32-1526, Vol. XII, pp. 44–46. Jet Propulsion Laboratory, Pasadena, Calif., Dec. 15, 1972.

16. Sward, A., "Measurement of the Power Spectral Density of Phase of the Hydrogen Maser," *JPL Quarterly Technical Review*, Vol. I, No. 4, pp. 30–33. Jet Propulsion Laboratory, Pasadena, Calif., January 1972.

References (contd)

17. Meyer, R., and Sward, A., "Frequency Generation and Control: The Measurement of Phase Jitter," *The Deep Space Network*, Space Programs Summary 37-64, Vol. II, pp. 55–58. Jet Propulsion Laboratory, Pasadena, Calif., Aug. 31, 1970.

18. Clements, P., "Frequency Generation and Control: A Method for Temperature Stabilization of Cables Transmitting Standard Frequencies," *The Deep Space Network*, Space Programs Summary 37-62, Vol. II, pp. 70–71. Jet Propulsion Laboratory, Pasadena, Calif., March 31, 1970.

19. Clements, P. A., "Electrical Length Stability of Coaxial Cable in a Field Environment," *The Deep Space Network Progress Report*, Technical Report 32-1526, Vol. VII, pp. 97–99. Jet Propulsion Laboratory, Pasadena, Calif., Feb. 15, 1972.

Table 1. Frequencies available from the hydrogen maser

Frequency	1400	100	20	10	5	1	0.1	MHz
Number of outputs available	1	3	2	3	3	3	2	–
Level	+13	+13	+13	+13	+13	+13	+5V[a]	dBmW
Isolation	75	100	100	100	100	100	60	dB

[a]TTL level

Table 2. Hydrogen maser receiver modules: stability and noise requirements

Module output	Stability[a]	Correction[b]	Phase[c] noise, dB	Correction,[d] dB	Temperature coefficient[e] of phase, deg/°C
Front end	1×10^{-14}	1	−124	23	–
X14 multiplier	1×10^{-16}	1.02	−124	23	–
First IF	7×10^{-15}	69.6	−124	23	–
Second IF	3.5×10^{-13}	3501	−124	23	–
Phase detector	3.5×10^{-13}	3501	−124	23	–
VCO	2×10^{-12}	>20,000	−104	>43	–
100-MHz DA[f]	2×10^{-12}	>20,000	−104	>43	0.1
20-MHz DA & ÷5	7×10^{-15}	71	−124	23	0.1
10-MHz DA & ÷ 10	1×10^{-16}	1	−139	0	0.1
5-MHz DA & ÷ 2	1×10^{-16}	1	−145	0	0.1
1-MHz DA & ÷ 10	1×10^{-16}	1	−145	0	0.1
0.1 MHz DA & ÷ 100	1×10^{-16}	1	−145	0	0.1
Synthesizer	3.5×10^{-13}	3501	−124	23	–

[a]The fractional frequency deviation $\Delta f/f$, for averaging times between 100 and 10,000 s, resulting from a step change of 5°C in the ambient temperature of a module within the range of 0 to 50°C.

[b]The factor of improvement applied to a module's stability when the module is operating in the receiver.

[c]The one-sided power spectral density of phase noise (in rad²/Hz) measured at 10 Hz away from the center frequency.

[d]The factor of improvement in a module's phase noise when the module is operating in the receiver.

[e]Over a temperature range of 0 to 50°C.

[f]DA = distribution amplifier

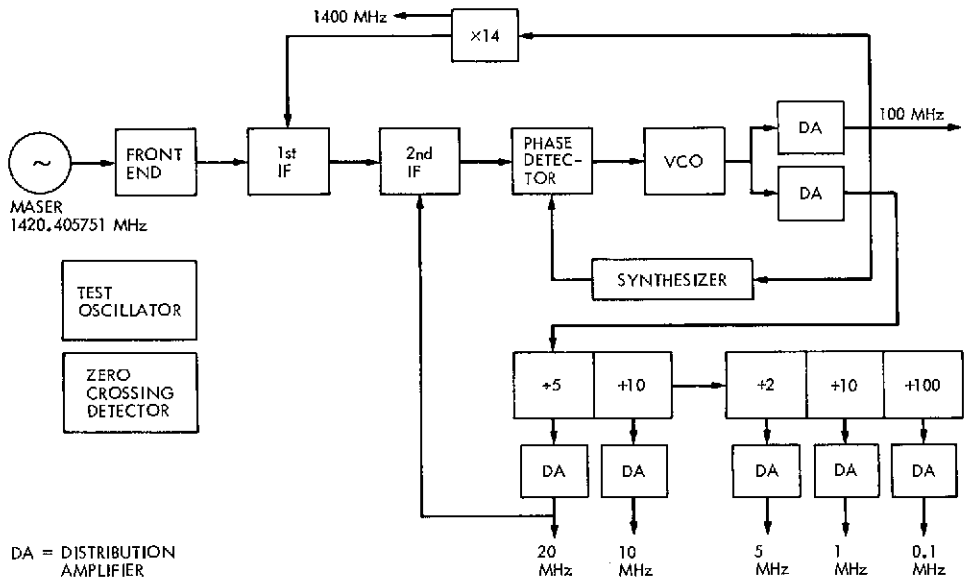

Fig. 1. Hydrogen maser receiver block diagram

Coded Interleaving for Burst Error Correction

L. R. Welch
University of Southern California

The concept of code interleaving has proved to be a very useful technique for dealing with complicated communications channels. One of the most recent applications of this concept is the Golay-Viterbi concatenation scheme proposed for use on the Mariner Jupiter/Saturn 1977 Mission. In this paper a generalization of interleaving is introduced. When two or more codes are suitably combined using this idea, the decoding algorithm for the first code can supply information about the location of errors for the remaining codes, thereby reducing the redundancy requirements for these codes.

I. Introduction

The concept of code interleaving has proved to be a very useful technique for dealing with complicated communications channels. One of the most recent applications of this concept is the Golay-Viterbi concatenation scheme proposed for use on Mariner Jupiter/Saturn 1977 (Ref. 1). In this paper a generalization of interleaving is introduced. When two or more codes are suitably combined using this idea, the decoding algorithm for the first code can supply information about the location of errors for the remaining codes, thereby reducing the redundancy requirements for these codes.

We begin with a somewhat abstract definition of interleaved codes. Let C_i be a block code of length N_i over an alphabet V_i, a vector space of dimension k_i over $GF(p)$. Let

$$V = \sum_{i=1}^{M} \oplus V_i$$

the direct sum space whose elements are represented by M-tuples $(v_1, \cdots, v_m)$ where $v_i \in V_i$. V has dimension $k = \sum k_i$ over $GF(p)$.

If $\{c_i(t)\}$ is the sequence of symbols formed by encoding a sequence of symbols from source S_i using code C_i, then the *interleaved code* is the block code of length $N = LCM(N_1, \cdots, N_M)$ whose code words are of the form

$$\{c(t)\}_1^N = \{(c_1(t), \cdots, c_m(t))\}_1^N$$

The code is *interleaved to depth M*.

When the size of the symbol alphabet of a code C is different from the size of the channel alphabet, coding of the alphabet is necessary. When the channel has p symbols and the code alphabet is a k-dimensional vector space over $GF(p)$, the coding can be achieved by selecting a basis for the vector space and transmitting the k coefficients $(a_1, \cdots, a_k)$ of a vector relative to the basis. The resulting sequence of kN terms from $GF(p)$ will be called the channel code representing C. For example, if $V_1, \cdots, V_m$ are 1-dimensional in the above definition of interleaved codes and the basis for V is

$$\{(1, 0, \cdots, 0), (0, 1, 0, \cdots, 0), \cdots, (0, \cdots, 0, 1)\}$$

then the channel code representing C is the usual definition of interleaved codes. That is, the subsequence $\{a(j), a(j+k), a(j+2k) \cdots\}$ is just a sequence obtained from the jth code used in the interleaving. In general, let $U_1, \cdots, U_k$ be a basis for V and

$$c(t) = \sum_{i=1}^{k} a_i(t)\, U_i$$

where $(c(1), \cdots, c(N))$ is a codeword in C. The set of kN-tuples $\{(a_1(1), \cdots, a_k(1), a_1(2), \cdots, a_k(N))\}$ is the *coded interleaved* code formed from $\{C_1, \cdots, C_M\}$.

II. Analysis

The question arises as to the choice of basis for V. This depends on the channel error statistics and the mode of decoding.

Let P_i be the projection of V onto V_i; that is

$$P_i(v_1, \cdots, v_m) = v_i$$

and let $u_1, \cdots, u_k$ be a basis for V. Then the mapping

$$(a_1, \cdots, a_k) \xrightarrow{L_i} \sum_j a_j P_i u_j$$

is a linear mapping from the set of k-tuples to V_i and the M-tuple $(L_1, \cdots, L_m)$ is the inverse of the coded interleaving mapping. If the component codes are to be decoded independently from a received sequence $\{r_i(t)\}$, then clearly the sequence $v_j(t) = L_j(r_1(t), \cdots, r_k(t))$ should be the input to the decoder for the jth code. The criterion for the choice of basis should be to minimize the error rate in as many component codes as possible. This choice depends on channel statistics. For example, let $(a_1(t), \cdots, a_k(t))$ and $(\bar{a}_1(t), \cdots, \bar{a}_k(t))$ be the only possibilities for $(r_1(t), \cdots, r_k(t))$, where bar denotes complementation. Then the basis should be chosen so that $L_j(1, \cdots, 1) = 0$ for all but one choice of j. M-1 codes would then be error free.

Another channel extreme occurs when

$$\text{Prob}\,((r_1 \cdots r_k) = (a_1, \cdots, a_k)) = 1 - P$$

$$\text{Prob}\,((r_1 \cdots r_k) = (b_1, \cdots, b_k)) = P/(p^k - 1)$$

$$\text{for } (b_1, \cdots, b_k) \neq (a_1, \cdots, a_k)$$

In this case, if an error occurs, it causes errors in each component code with high probability. Thus, if the decoding algorithm for one code detects an error in a given symbol, the corresponding forms in the other codes might just as well be erased and their decoding algorithm attempt to correct erasures.

The above example suggests that the following strategy may be useful for a large class of channels: use code C_1 as an error correcting code. If it is decided that symbol $c_1(t)$ is in error, erase $c_j(t)$ for $j = 2, \cdots, M$. Decode $C_2, \cdots, C_m$ as erasure channels.

It may happen that errors occur which do not affect C_1 and, therefore, are not erased in $C_2, \cdots, C_M$. The following theorem is useful in this context.

THEOREM. *Let the probability of error in a channel have the property*

$$\text{Prob}\,[(r_1 \cdots r_k) = (a_1 \cdots a_k) + (e_1 \cdots e_k)] = P(e_1 \cdots e_k)$$

For each $k_1 < k$ there exists a linear transformation L_1 from k-tuples onto $V^{k_1}(p)$ for which

$$P_{L_1} = \text{Prob}\,[L_1(e_1, \cdots e_k) = 0 \mid (e_1 \cdots e_k) \neq (0, \cdots, 0)] \leq \frac{1}{p^{k_1}}$$

Proof: Let $\delta(0) = 1$ and $\delta(v) = 0$ for $0 \neq v \in V^{k_1}(p)$

$$P = \text{Prob}\,[L_1(e_1, \cdots, e_k) = 0 \mid (e_1, \cdots, e_k) \neq (0, \cdots, 0)]$$

$$= \frac{1}{1 - P(0, \cdots, 0)} \cdot \sum_{(e_1 \cdots e_k) \neq 0} P(e_1 \cdots e_k) \times \delta(L_1(e_1, \cdots, e_k))$$

If we choose a basis for V^{k_1} and for the space of k-tuples, L_1 is represented by a k_1 by k matrix whose k_1 rows are linearly independent. There are

$$(p^k - 1)(p^k - p) \cdots (p^k - p^{k_1-1})$$

such matrices. We average the above equation over all such linear mappings.

$$\prod_{j=0}^{k_1-1} (p^k - p^j)^{-1} \sum_{L_1} P_{L_1} =$$

$$\frac{1}{1 - P(0, \cdots, 0)} \cdot \sum_{(e_1 \cdots e_k) \neq 0} P(e_1, \cdots, e_k)$$

$$\times \sum_{L_1} \prod_{j=0}^{k_1-1} (p^k - p^j)^{-1} \delta(L_1(e_1, \cdots, e_k))$$

The innermost sum is nonzero only if $L_1(e_1, \cdots, e_k) = 0$. If we choose as our basis for k-tuples one such that $(e_1, \cdots, e_k)$ is the first basis vector then L_1 with $L_1(e) = 0$ is described by a k_1 by k matrix whose first column is zero and whose rows are linearly independent. The number of such is

$$\prod_{j=0}^{k_1-1} (p^{k-1} - p^j)$$

The above equation then reduces to

$$\text{Ave}(P_{L_1}) = \frac{1 - P(0, \cdots, 0)}{1 - P(0, \cdots, 0)} \cdot \frac{\prod_{j=0}^{k_1-1} (p^{k-1} - p^j)}{\prod_{j=0}^{k-1} (p^k - p^j)}$$

$$= \frac{1}{p^{k_1}} \cdot \frac{p^k - p^{k_1}}{p^k - 1} \leq \frac{1}{p^{k_1}}$$

Since the average of P_{L_1} is less than or equal to $1/p^{k_1}$, there exists an L_1 such that $P_{L_1} \leq 1/p^{k_1}$.

Q.E.D.

The theorem can be applied to the above decoding strategy as follows: If P_E is the probability of a k-tuple error in the channel and C_1 is capable of correctly decoding all errors "seen" by it. Then the other component codes will have an erasure rate of P_E and an additional error rate of $P_E \cdot 1/p^{k_1}$. For reasonable values of k_1 the other codes need be capable of finding few errors in addition to the erasures.

A variant of the above is that the extra errors found by C_2 be used to insert extra erasures in C_3, etc. The design problem is not of finding the best L_1 then the best L_2, etc., but finding the best sequence $(L_1, L_2, \cdots, L_M)$.

III. Conclusion

The concept of coded interleaving provides a richer class of codes than simple interleaving. It provides the ability to match the interleaving process to the channel statistics, thus allowing lower redundancy codes.

Reference

1. Baumert, L. D., and McEliece, R. J., "A Golay-Viterbi Concatenation Scheme," in this issue.

A Golay-Viterbi Concatenated Coding Scheme for MJS'77

L. D. Baumert and R. J. McEliece
Communications Systems Research Section

This article describes in some detail a proposed method of delivering the nonimaging science data on the Mariner Jupiter/Saturn (MJS) mission at a bit error probability which is substantially lower than the bit error probability required for the imaging data. The method is a "pre-coding" of the nonimaging data with an interleaved (24, 12) Golay code.

I. Introduction

It is well known that deep-space telemetry encoded with a (32, 6) biorthogonal block code and decoded with a maximum-likelihood decoder requires considerably less energy to achieve a given bit error probability than telemetry that has not been encoded. Since 1969, all of JPL's Mariner-class spacecraft have been equipped with such a coding system.

It is, however, also well known that short-constraint-length *convolutional* encoding, coupled with Viterbi decoding, is superior to biorthogonal coding. Thus, current plans call for the replacement of the biorthogonal code with a convolutional code on the Mariner Jupiter/Saturn 1977 and later JPL deep-space missions. This convolutional code will probably be either constraint length 7, rate 1/2, or constraint length 6, rate 1/3. Table 1 contains the bit signal-to-noise ratio E_b/N_0, required to obtain the bit error probabilities 0.01, 0.005, and 0.001 for uncoded, biorthogonally encoded, and convolutionally encoded telemetry.

(It is seen from Table 1 that the (6, 1/3) convolutional code is about 0.5 dB better than the (7, 1/2) code. However, future NASA deep-space telemetry will be transmitted at rates on the order of 10^5 bits/s, and at such rates the (6, 1/3) code will generate 3×10^5 symbols/s as compared to only 2×10^5 for the (7, 1/2) code. The extra bandwidth requirements and implementation difficulties of handling such high symbol rates may force the adoption of the (7, 1/2) code in spite of its theoretically inferior performance.)

As has been the case on previous Mariner-class missions, the minimum bit error probability required for the imaging data (i.e., the television coverage of the planets) on MJS is in the vicinity of 0.01–0.005. However, the nonimaging data turn out to be much more susceptible to noise than the TV. Final minimum bit error probabilities required by the nonimaging scientific experiments have not yet been set, but a commonly quoted upper bound is 5×10^{-5}.

Since the TV data will comprise over 95% of the total MJS telemetry, it would obviously be wasteful to deliver the entire telemetry stream at a bit error probability of 5×10^{-5}; in fact, it would require about 1.6 dB more energy per transmitted bit to accomplish this. In this article, we will document one feasible method of delivering the nonimaging MJS telemetry at the lower bit error probability at a cost of only about 0.2 dB in signal power. This is the method of *concatenated*, or *nested*, coding. Specifically, the scheme we propose is the concatenation of the short-constraint-length convolutional code with an interleaved (24, 12) Golay code.

It should be mentioned that there are at least two other possible ways of efficiently delivering the nonimaging data more reliably than the TV. The first is the use of dual-channel telemetry, wherein the imaging and nonimaging data streams are encoded independently and frequency-multiplexed together. The second is the use of *lengthened-symbol* encoding, in which the nonimaging data bits are encoded into symbols which have, say, twice the duration of the corresponding encoded TV bits. It is not, however, our objective to weigh the relative merits of these techniques against those of our concatenation scheme.

II. Description of the Concatenation Scheme

Figure 1 is a gross block diagram of the Viterbi convolutional coded telemetry system which is to be used on MJS. The output of the Viterbi decoder is an imperfect, time-delayed version of the output of the data source. According to Table 1, this system requires 0.3–0.8 less energy per transmitted bit to achieve a bit error probability of 0.005 than does the (32, 6) biorthogonal coding system.

Now let us regard the encoder–channel–decoder ensemble of Fig. 1 as a single block, and call it the *superchannel*. From this viewpoint, the superchannel is a block which accepts binary data and expels a noisy version of those data. The idea of concatenated coding, as it applies to our problem, is to combat the noise of the superchannel with coding; i.e., to insert a suitably chosen encoder–decoder pair into the block diagram of Fig. 1, as shown in Fig. 2.

It remains, of course, to describe in detail the contents of the blocks labeled "superencoder" and "superdecoder." The code to be used on the Viterbi superchannel cannot be expected to be a simple one, since the statistics of that channel are very complicated. Indeed, no satisfactory mathematical model for this channel exists at present, and so, in order to verify that a particular coding scheme actually performs adequately, extensive computer simulation is necessary. Basically, however, what is needed is a code which is capable of correcting relatively infrequent bursts of errors, since experience has taught us that, at a bit signal-to-noise ratio adequate to drive the Viterbi decoder's bit error probability down to 5×10^{-3}, the errors, when they do occur, cluster in bursts of length 10–20 or so.

As mentioned in the introduction, we propose an interleaved version of the (24, 12) Golay code. If the "depth of interleaving" (an integer defined precisely below) is denoted by k, then the supercode will be a $(24k, 12k)$ block code. That is, the nonimaging data stream will be partitioned into blocks of size $12k$, and to each such block will be adjoined an additional $12k$ parity-check bits. Thus, the superencoder of Fig. 2 will emit binary codewords of length $24k$. The description of the actual implementation of the encoder will be deferred to Section V; here, it will suffice to point out that if a $24k$-bit codeword is denoted by $(x_0, x_1, x_2, \cdots, x_{24k-1})$, each of the k 24-bit subsequences $(x_0, x_k, x_{2k}, \cdots, x_{23k})$, $(x_1, x_{k+1}, x_{2k+1}, \cdots, x_{23k+1})$, $\cdots$, $(x_{k-1}, x_{2k-1}, \cdots, x_{24k-1})$ will turn out to be a codeword of the basic (24, 12) Golay code. Thus, the big $24k$-bit codeword consists of k Golay codewords which are "interleaved."

Now the (24, 12) Golay code, when decoded optimally, is capable of correcting any pattern of three or fewer errors, and many patterns of four errors. This fact makes the overall $(24k, 12k)$ an extremely powerful code for correcting multiple bursts of bit errors: any pattern of bit errors in a block of length $24k$ can be completely corrected so long as none of the k 24-bit Golay codewords out of which the overall codeword has been constructed contains more than three of the bit errors. Thus, in particular, if all the bit errors are confined to a "burst" of length $3k$ or less, no individual Golay codeword can contain more than three of the errors, and so all of the errors will be corrected. Of course, many other more complex patterns of bit errors will be corrected also.

Thus, the Viterbi decoder produces many complex combinations of bursts of errors, and the interleaved Golay code is capable of correcting many complex combinations of bursts of errors. The next section presents quantitative verification that the code and the channel are indeed well matched.

III. Simulation Results

We have simulated the performance of our concatenation scheme with the aid of bit error statistics obtained from a commercially manufactured (7, 1/2) Viterbi decoder, and from a software (6, 1/3) Viterbi decoder. The (7, 1/2) statistics were stored on two reels of magnetic tape. One reel contained 1.3×10^8 bits which were decoded at an E_b/N_0 of 2.5 dB, and a resulting bit error probability of 6.2×10^{-3}. The other reel had 9.9×10^7 bits, $E_b/N_0 = 2.0$ dB, P_E (bit) $= 1.8 \times 10^{-2}$. The (6, 1/3) statistics were stored on one reel of magnetic tape containing 6.4×10^6 bits decoded with $E_b/N_0 = 1.9$ dB, P_E (bit) $= 5 \times 10^{-3}$, and 6.4×10^6 bits with $E_b/N_0 = 1.5$ dB, P_E (bit) $= 10^{-2}$.[1] The interleaving depths $k = 12$, 16, 20, and 24 were all tested.

In addition, four different versions of the decoding algorithm were tested. The reason we did not settle on one decoding algorithm is that the Golay code is, in fact, a (23, 12) rather than a (24, 12) code. The 24th bit of each codeword is merely an overall parity-check bit. And while, for the (23, 12) code, an algorithm which corrects any pattern of three or fewer errors can neither correct nor detect any error pattern of more than three errors, the extended (24, 12) code has the ability to detect and correct many patterns of four errors. It was our desire to test several combinations of detection and correction which are possible with the extended code.

The four decoding rules will be denoted by A1, A2, B1, B2. Roughly speaking, A denotes an algorithm which only corrects patterns of up to three errors, and B denotes an algorithm which corrects not only all patterns of three or fewer errors but also many likely patterns of four errors. The algorithms labeled 1, when confronted with an error pattern that cannot be corrected, make no change in the received bits but merely pass them along unprocessed. Those labeled 2 "erase" all the bits in a codeword which appears to have suffered an uncorrectable error pattern. Details of these algorithms will be given in the next section; we conclude this section with performance tables of algorithms A1, A2, B1, and B2 for the interleaving depths $k = 12$, 16, 20, and 24.

There are two sets of numbers for each algorithm: those labeled (0.0062, 0.005) and those labeled "(0.018, 0.01)". The first entry in a pair under a (0.0062, 0.005) rubric represents an error or erasure probability for the concatenation scheme combined with the (7, 1/2) Viterbi decoder with bit error probability 6.2×10^{-3}; the second entry gives the same probability for the scheme combined with the (6, 1/3) decoder with a raw bit error probability of 5×10^{-3}. The entries under (0.018, 0.01) have the same significance for the higher bit error probabilities 1.8×10^{-2} for the (7, 1/2) code and 1.0×10^{-2} for the (6, 1/3) code. A condensed exponential notation is used; e.g., 1.7E-2 denotes 1.7×10^{-2}. Error probability is denoted by P_E and erasure probability by P_{ER}. Probabilities marked with an asterisk (*) were computed from less than 10 error events and so may not be reliable.

Algorithm A1

	k	P_E (bit)	P_E (block)
(0.0062, 0.005)	12	(1.8E-4, 1.4E-4)	(5.8E-3, 2.9E-3)
	16	(6.9E-5, 4.7E-5)	(3.4E-3, 2.1E-3)
	20	(3.3E-5, 1.7E-5)	(2.2E-3, 1.5E-3)
	24	(1.9E-5, 8.1E-6)	(1.7E-3, 9.0E-4)
(0.018, 0.01)	12	(1.5E-3, 6.8E-4)	(3.6E-2, 1.2E-2)
	16	(8.0E-4, 3.4E-4)	(3.0E-2, 1.0E-2)
	20	(4.9E-4, 1.6E-4)	(2.5E-2, 8.4E-3)
	24	(3.5E-4, 8.0E-5)	(2.4E-2, 6.3E-3)

Algorithm B1

	k	P_E (bit)	P_E (block)
(0.0062, 0.005)	12	(1.0E-4, 6.7E-5)	(2.5E-3, 1.4E-3)
	16	(3.9E-5, 2.3E-5)	(1.5E-3, 9.6E-4)
	20	(2.3E-5, 8.7E-6)	(1.2E-3, 4.5E-4*)
	24	(1.4E-5, 4.4E-6)	(1.0E-3, 3.6E-4*)
(0.018, 0.01)	12	(1.0E-3, 4.3E-4)	(2.1E-2, 7.3E-3)
	16	(6.0E-4, 1.9E-4)	(1.8E-2, 5.7E-3)
	20	(3.9E-4, 1.0E-4)	(1.7E-2, 5.1E-3)
	24	(3.1E-4, 5.5E-5)	(1.8E-2, 3.8E-3)

[1]There is a small discrepancy between these figures and those of Table 1 because it is not feasible to implement maximum-likelihood survivor selection at high bit rates. The faster, suboptimum Viterbi decoder is slightly less efficient. The reader interested in details should consult Ref. 1.

Algorithm A2

	k	P_E (bit)	P_E (block)	P_{ER} (block)
(0.0062, 0.005)	12	(1.1E-5, 7.5E-6)	(2.8E-4, 1.8E-4*)	(5.5E-3, 2.7E-3)
	16	(2.5E-6, <E-7*)	(1.0E-4, <E-5*)	(3.3E-3, 2.1E-3)
	20	(1.3E-6, <E-7*)	(6.9E-4, <E-5*)	(2.2E-3, 1.5E-3)
	24	(6.6E-7, <E-7*)	(4.8E-5, <E-5*)	(1.7E-3, 9.0E-4)
(0.018, 0.01)	12	(7.9E-5, 1.4E-5)	(2.1E-3, 3.6E-4*)	(3.5E-2, 1.2E-2)
	16	(3.6E-5, 1.3E-6*)	(1.4E-3, 6.0E-5*)	(2.8E-2, 1.0E-2)
	20	(1.8E-5, 5.0E-6)	(9.4E-4, 3.0E-4*)	(2.4E-2, 8.1E-3)
	24	(1.3E-5, 1.3E-6*)	(9.1E-4, 9.0E-5*)	(2.3E-2, 6.2E-3)

Algorithm B2

	k	P_E (bit)	P_E (block)	P_{ER} (block)
(0.0062, 0.005)	12	(5.0E-5, 4.1E-5)	(1.3E-3, 9.0E-4)	(1.2E-3, 4.9E-4)
	16	(2.1E-5, 1.1E-5)	(7.5E-4, 3.6E-4*)	(7.1E-4, 6.0E-4)
	20	(1.2E-5, 3.7E-6)	(5.8E-4, 1.5E-4*)	(6.3E-4, 3.0E-4)
	24	(6.2E-6, 2.5E-6)	(4.1E-4, 1.8E-4*)	(6.3E-4, 1.8E-4)
(0.018, 0.01)	12	(3.6E-4, 1.6E-4)	(9.4E-3, 3.3E-3)	(1.2E-2, 4.0E-3)
	16	(2.0E-4, 5.3E-5)	(7.3E-3, 2.0E-3)	(1.1E-2, 3.8E-3)
	20	(1.3E-4, 4.6E-5)	(6.1E-3, 2.1E-3)	(1.1E-2, 3.0E-3)
	24	(1.1E-4, 1.9E-5)	(6.4E-3, 1.3E-3)	(1.1E-2, 2.6E-3)

IV. Conceptual Description of the Decoding Algorithm

All of our decoding algorithms for the (24, 12) extended Golay code can be summarized as follows:

(1) Accept new 24-bit word.

(2) Calculate the 12-bit syndrome s for the received 24-bit word.

(3) Find the entry opposite s in the (previously calculated) syndrome table.

(4) If this entry is a 24-bit error pattern, add (mod 2) this pattern to the received word, and output the resulting 24-bit word. If the entry is the special symbol *, output the received word unprocessed for algorithms A1 and B1, or erase all 24 bits of the received word for algorithms A2 and B2.

(5) Go to step 1.

The above skeleton completely describes the algorithms, except for the syndrome table. The rest of this section will be devoted to a description of this table. We will begin with an outline of the theory of decoding a general linear code, and then specialize to the extended Golay code.

Any (n, k) linear code can be characterized as the set of binary n-tuples $c = (c_0, c_1, \cdots, c_{n-1})$ which satisfy the matrix equation

$$cH = 0$$

where H is a fixed $n \times (n-k)$ binary matrix of rank $n-k$. Now we define the *syndrome* s for an arbitrary binary vector v of length n by the equation

$$vH = s \tag{1}$$

The syndrome s is an $n-k$ dimensional binary vector. For a fixed syndrome s, the set of vectors v which satisfy (1) is called a *coset* of the code C; each such coset contains 2^k n-dimensional vectors. It turns out that if a codeword c is transmitted over a noisy channel, and if v is received, the error pattern, i.e., the difference $v - c$, must lie in the coset defined by (1). For any coset of the code, certain vectors in that coset are at least as likely to turn up as

error patterns as any of the others. In such a case, one of these likely vectors may be designated as a *coset leader*; in most applications, the coset leader is chosen from among the vectors of least weight in the coset. In the decoding algorithm, when a vector is received whose coset has a leader, that leader is added modulo 2 to the received vector, and the resulting vector is the output of the decoder. If the received vector belongs to a coset without a designated leader, the received bits are either unprocessed or are erased by the decoder. These two alternative ways of handling the leaderless cosets correspond to the algorithms of types 1 and 2 described in the last section.

To complete the description of our decoding algorithms for the (24, 12) extended Golay code, then, we must indicate how the coset leaders were chosen.

The first step was to ensure that all error patterns of weight 0, 1, 2, or 3 would be corrected. Thus, each of these

$$\binom{24}{0}+\binom{24}{1}+\binom{24}{2}+\binom{24}{3}=2325$$

low-weight error patterns was designated as a coset leader. (It is a fundamental fact about the Golay code that no two of these vectors lie in the same coset.) For the algorithms labeled A, no other cosets were given leaders.

For the algorithms labeled B, however, we used some of the remaining 1771 cosets to correct certain common error patterns of weight 4. Since

$$1771=\frac{1}{6}\binom{24}{4}$$

it is clear that we could hope to correct at most one-sixth of all patterns of weight 4. Indeed, each of the 1771 remaining cosets contains exactly six vectors of weight 4, and those six vectors are "disjoint" in the sense that their modulo-2 sum is 111111111111111111111111. Fortunately, however, it turns out that among the 10626 weight-4 error patterns that appear in the interleaved Golay code in the presence of "Viterbi noise," only a small fraction occur with substantial probability. These are the "tame" patterns, in which the four ones are confined to one or two short bursts; i.e., the 651 patterns of the form $\ldots1\ldots111\ldots$, $\ldots111\ldots1\ldots$, and $\ldots11\ldots11\ldots$

For example, for the twelve-fold interleaved Golay code, and the tape of (7, 1/2) Viterbi noise at a bit error probability of 6.2×10^{-3}, 4030 of the 5529504 processed Golay codewords suffered exactly four bit errors, and 3187 of these were of the tame variety described above. (In fact, pattern 1111 occurred 1322 times, 33% of the total; and the tame patterns of overall burst length ≤ 7 accounted for 58% of the total.)

Thus, in the B algorithms, we wanted as many of the tame weight-4 error patterns to be coset leaders as possible. This was done (by computer) by generating the 651 tame patterns sequentially, in order of increasing burst length, computing the syndromes, and making the pattern a coset leader if its coset was leaderless at the time it was being examined. It turned out that we could make 542 of the 651 tame patterns coset leaders. (The shortest tame pattern which belongs to the same coset as an even shorter tame pattern, and so cannot be corrected, is 1000111. Thus, the probability of a tame pattern being corrected is substantially higher than $542/651 = 0.833$).

Finally, a further study of the weight-4 error patterns failed to reveal any particular class of patterns which occurred a disproportionate number of times, and so we chose no other coset leaders. Hence, in the B algorithms, 2867 of the cosets had leaders, and 1229 did not.

V. Implementation—Encoding

It is possible to take advantage of the fact that the basic (23, 12) Golay code is cyclic to design a very simple encoding circuitry for the k-fold interleaving of the extended (24, 12) Golay code. Figure 3 is a diagram of one possible encoding configuration. The $12k$ data bits are sent down the channel and into the shift register, with the four switches in the "up" position as shown. The switches are then put in the "down" position, the $12k$ parity-check bits are sent down the channel, and the shift register is filled with zeros. The switches are then returned to the "up" position, and the transmission of a new block begins.

For k in the range 12–24, the circuit of Fig. 3 could be built with 20 or so standard metal oxide semiconductor (MOS) integrated circuits at a cost of less than $100; alternatively, it could be put on one specially ordered integrated circuit, although this would increase the cost considerably.

Finally, let us note one very important feature of the encoder of Fig. 3: Although the overall $24k$-bit codewords consist of k interleaved 24-bit codewords, *the data bits are not interleaved* but appear serially in the encoded stream in blocks of $12k$ separated by blocks of $12k$ parity-check bits.

VI. Implementation—Decoding

The decoding algorithms we used were software algorithms, written for an SDS 930 computer. However, we shall argue at the end of this section that at least some of the computation would be better done with relatively inexpensive special-purpose hardware.

We assume that the $24k$-bit word which is to be decoded has somehow been loaded into the computer. The decoder's first task is to "de-interleave" the k component Golay codewords. Thus, if $(y_0, y_1, y_2, \cdots, y_{24k-1})$ is the received word, the first decoding step is to arrange the bits into k 24-bit words, as follows:

Word 1	$y_0, y_k, y_{2k}, \cdots, y_{23k}$
Word 2	$y_1, y_{k+1}, y_{2k+1}, \cdots, y_{23k+1}$
.	
.	
.	
Word k	$y_{k-1}, y_{2k-1}, y_{3k-1}, \cdots, y_{24k-1}$

(Notice that at this stage, the data bits have been scrambled.) Next, each of the k 12-bit words is decoded, as indicated in Section IV; i.e., the syndromes are calculated, and the error patterns (coset leaders) corresponding to each syndrome are added modulo 2 to the received words. For the B algorithms, this will require a stored table of 4096 12-bit words (12 rather than 24, because the last 12 bits of each Golay codeword are not carrying information, only noise-combating parity). However, for the A algorithms, we need only a syndrome table of 2048 12-bit words, since a word from the (24, 12) code is merely a word from the (23, 12) code to which has been appended an overall parity check. Thus, every codeword in the (24, 12) code has even weight (i.e., an even number of ones), and so the parity of the number of errors that have occurred in a 24-bit word is the same as the parity of the number of ones in that word. This leads us to the following modified version of the decoding algorithms:

A1. Compute the 11-bit syndrome for the first 23 bits, regarded as a noisy version of a codeword from the (23, 12) code.

A2. Find the 23-bit error pattern of weight 0, 1, 2, or 3 corresponding to the syndrome calculated in A2.

A3. If the error pattern found in A3 has the same parity as the received 24-bit word, add the error pattern to the first 23 bits. Otherwise, the decoding algorithm has detected four or more errors.

This version of the algorithm requires the storage of only 2048 13-bit words (12 bits of the error pattern and one extra bit which gives the parity of the complete 23-bit error pattern). Thus, if computer storage is at a premium, the A algorithms enjoy a considerable advantage over the B algorithms.

In any event, when the k 24-bit words have been decoded, the result will be k blocks of corrected data:

Corrected word 1	$X_0, X_k, \cdots, X_{11k}$
Corrected word 2	$X_1, X_{k+1}, \cdots, X_{11k+1}$
.	
.	
.	
Corrected word k	$X_{k-1}, X_{2k-1}, \cdots, X_{12k-1}$

Each X_i is the decoder's estimate of the corresponding transmitted bit X_i, or a special erasure symbol. The final decoding step is the re-interleaving of the k words to get the corrected data stream $X_0, X_1, \cdots, X_{12k-1}$.

The program we have written to do this decoding on the SDS 930 reads the incoming codewords from magnetic tape, and can process the data at a rate of 6000 (information) bits/s. This rate is well in excess of the currently estimated nonimaging science encounter data rate of 4500 bits/s.

Although current plans call for software implementation of the decoding algorithm, we cannot conclude this report without making some mention of the advantages of hardware decoding. We have found that over 70% of the decoding time in our program is devoted to the de-interleaving and re-interleaving of the k 24-bit Golay codewords, and that most of the remainder of the decoding time is consumed in computing the k 12-bit syndromes. Both of these operations are quite awkward in most assembly languages but could be implemented almost trivially with a handful of standard MOS integrated circuits. If outboard circuitry for performing these two functions became available, the entire decoding algorithm would make a negligible demand on the computer's central processing unit (CPU) time. The only remaining burden would be the large table of 2048 or 4096 13- or 12-bit words. This table could easily be stored on a special-purpose read-only memory (ROM), making the entire decoder disjoint from the main computer.

However, a final decision on the software–hardware question must be deferred until a careful study of the various tradeoffs (available computing power, reliability, expense, etc.) involved can be made.

Reference

1. Gilhousen, K. S., Heller, J. A., Jacobs, I. M., and Viterbi, A. J., *Coding Systems Study for High Data Rate Telemetry Links*, NASA CR 114278, prepared by Linkabit Corporation, 1972.

Table 1. E_b/N_0 (in dB) required to produce certain bit error probabilities for four telemetry systems

Bit error probabilities	Uncoded	(32, 6) biorthogonal	(7, 1/2) convolutional	(6, 1/3) convolutional
0.01	4.3	2.3	2.3	1.7
0.005	5.2	2.9	2.6	2.1
0.001	6.8	4.0	3.2	2.7

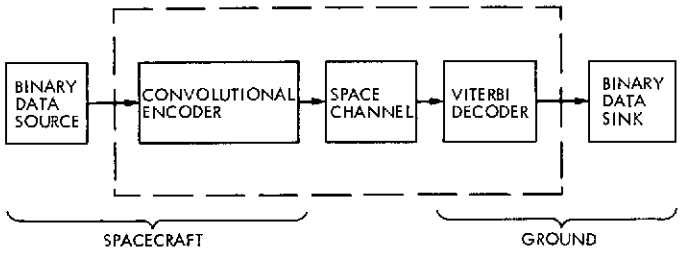

Fig. 1. Viterbi convolutional coded telemetry system for MJS

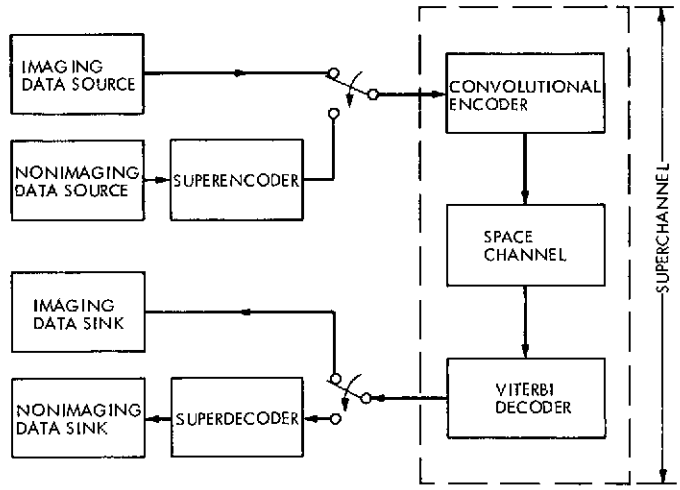

Fig. 2. Viterbi system with encoder–decoder pair

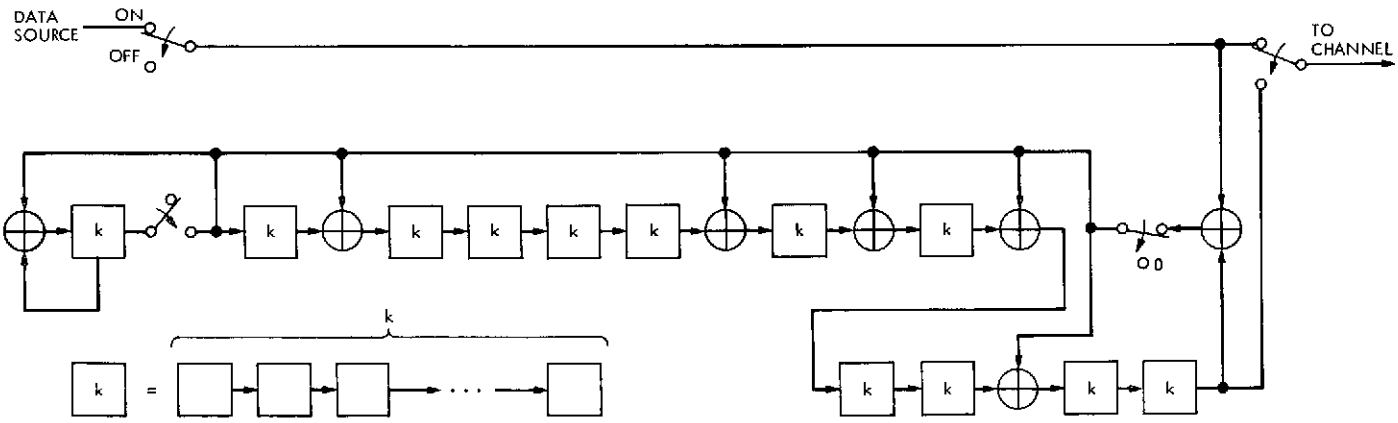

Fig. 3. Encoder for *k*-fold interleaving of Golay (24, 12) code

Capacity of Noncoherent Channels

S. Butman
Communications System Research Section
M. J. Klass
California Institute of Technology

This article determines the wideband capacity limit for noncoherent Gaussian channels which are constrained to radiate signals with peak power equal to the average power. The capacity is a function of only two parameters, the predetection signal-to-noise ratio ST/N_0 and the number of signals M. It is shown that the capacity increases monotonically to a wideband limit as M increases. The role played by this limit for noncoherent Gaussian channels is similar to that played by the famous Shannon limit, S/N_0, for coherent channels. Numerical and graphical results are presented for parameters of interest. It was found that an excellent approximation to the wideband noncoherent limit is $S/N_0 \cdot ST/N_0/(2 + ST/N_0)$.

I. Introduction

Multi-frequency-shift-keying (MFSK) is a well-known communications technique (Ref. 1) which is particularly suited for channels with rapid random variations of the phase of the carrier signal. Phase instabilities of this kind are often due to turbulence in the electromagnetic propagation medium through which the signals pass, as, for example, the solar corona and the atmospheres of Venus, Jupiter, and Saturn. A useful parameter for characterizing the degree of phase instability is the predetection signal-to-noise ratio $\alpha^2/2 = ST/N_0$, where S is the received signal power, N_0 is the one-sided spectral density of the Gaussian noise in the system, and T is the predetection correlation time used by the receiver. The critical quantity here is the predetection correlation time, which is a measure of the rapidity with which the carrier phase varies. A receiver, in order to average out or filter the received noise, will correlate for as long as possible, provided the carrier phase is constant. However, if the correlation time exceeds T, a random phase change in the carrier will

result in an averaging out of the desired signal as well as the noise.

The purpose of this article is to determine the ultimate, theoretical performance of MFSK systems in terms of the basic constraints required by practical engineering design. There are two: one is the already-mentioned predetection signal-to-noise ratio imposed by the channel; the other is that the peak power be equal to the average power S, as required by current transmitter technology. A subsidiary constraint is the system bandwidth W, which is determined, ultimately, by the complexity permitted in the receiver and the data rate of the system. Apart from these considerations, the bandwidth of an MFSK system determines the maximum number M of orthogonal signals that can be distinguished in time T, and the bandwidth is, by definition,

$$M = 2WT$$

Furthermore, the question of when an MFSK system may be considered "wideband," i.e., when the assumption that $W = \infty$ is a good approximation, depends on the predetection signal-to-noise ratio. It is shown that the wideband approximation is valid if $M \approx T \exp(ST/N_0)$ for $ST/N_0 >> 1$, which is not surprising to those familiar with MFSK. However, an $M = 16$ suffices when $ST/N_0 < 1$.

The main result is a proof that the wideband MFSK capacity, normalized to the famous wideband capacity of the coherent Gaussian channel $C_\infty = S/N_0 \log_2 e$ bits/s, where $e = 2.718 \cdots$ is the base of natural logarithms, is

$$C(\alpha)/C_\infty = 2\alpha^{-2} \int_0^\infty x \exp\left[-\frac{1}{2}(x^2 + \alpha^2)\right] I_0(\alpha x) \ln I_0(\alpha x)\, dx - 1 \tag{1}$$

where $\alpha^2/2 = ST/N_0$ is the predetection signal-to-noise ratio, and

$$I_0(\alpha x) = \frac{1}{\pi} \int_0^\pi e^{\alpha x \cos\theta}\, d\theta \tag{2}$$

The capacity is plotted as a function of the predetection signal-to-noise ratio in Fig. 2, together with a useful curve-fitting approximation:

$$C(\alpha)/C_\infty > \frac{\alpha^2/2}{2 + \alpha^2/2} = \frac{ST/N_0}{2 + ST/N_0} \tag{3}$$

Figure 3 exhibits capacity for finite bandwidths.

In terms of the minimum energy-to-noise ratio per bit $(E_b/N_0)_{\min}$, the results are simply

$$(E_b/N_0)_{\min} = [C(\alpha)\, C_\infty]^{-1} \log_e 2 \approx 0.7\,(ST/N_0)/(2 + ST/N_0) \tag{4}$$

The theoretical results are corroborated by experience at both high and low values of the predetection signal-to-noise ratio. As the predetection signal-to-noise increases, the wideband MFSK capacity approaches C_∞. This is as it should be, because, at high enough ST/N_0, it is possible to estimate and track out the random phase process and to use coherent signaling techniques. However, although MFSK signaling can achieve (in theory) the coherent limit as $ST/N_0 \to \infty$, coherent techniques (Ref. 1) become more practical since they do not require the exponential rise in bandwidth.

II. Formulation

A block diagram of an MFSK system is illustrated in Fig. 1. From a channel capacity point of view, the MFSK channel is characterized by transmission of one of M discrete inputs numbered $1, 2, \cdots, M$, and M continuous outputs $r_1, r_2, \cdots, r_M$, received every T seconds, which have the following probability distribution:

$$p(r_k \mid m) = \begin{cases} r_k \exp\left(-\frac{1}{2} r_k^2\right) & \text{for } k \neq m \\ r_k \exp\left[-\frac{1}{2}(r_k^2 + \alpha^2)\right] I_0(\alpha r_k) & \text{for } k = m \end{cases} \tag{5}$$

where $p(r_k \mid m)$ is the conditional probability density of r_k given m (Ref. 2). The probability density of the M-vector $\mathbf{r} = (r_1, r_2, \cdots, r_M)$ is then

$$p(\mathbf{r} \mid m) = g(\mathbf{r}) \exp\left(-\frac{1}{2}\alpha^2\right) I_0(\alpha r_m) \tag{6}$$

where

$$g(\mathbf{R}) = \prod_{k=1}^{M} R_k \exp\left(-\frac{1}{2} R_k^2\right) \tag{7}$$

The term $g(\mathbf{R})$ may be regarded as a joint probability density of M independent identically distributed random variables $R_1, R_2, \cdots, R_M$.

III. Information and Capacity

The channel capacity is

$$C_M(\alpha) = \frac{1}{T} \max_{\mathbf{P}} I_M(\alpha, \mathbf{P}) \log_2 e \quad \text{bits/second} \tag{8}$$

where

$$I_M(\alpha, \mathbf{P}) = \int \sum_{m=1}^{M} P_m p(\mathbf{r} \mid m) \ln \left[\frac{p(\mathbf{r} \mid m)}{\sum_{j=1}^{M} P_j p(\mathbf{r} \mid j)} \right] d\mathbf{r} \tag{9}$$

and $\mathbf{P} = (P_1, P_2, \cdots, P_M)$ is the probability assignment on the input alphabet. After substitution for $P(\mathbf{r} \mid m)$ from Eq. (6) into Eq. (9), we have

$$I_M(\alpha, \mathbf{P}) = \exp\left(-\frac{1}{2}\alpha^2\right) \times \int_{\substack{r_i > 0 \\ i=1,\cdots,M}} g(\mathbf{R}) \sum_{m=1}^{M} P_m I_0(\alpha R_m) \ln \frac{I_0(\alpha R_m)}{\sum_{k=1}^{M} P_k I_0(\alpha R_k)} d\mathbf{R} \tag{10}$$

Since $g(\mathbf{R})$ is a probability density, we can write, after splitting up the logarithm,

$$I_M(\alpha, \mathbf{P}) = \exp\left(-\frac{1}{2}\alpha^2\right) E\left[\sum_{m=1}^{M} P_m I_0(\alpha R_m) \ln I_0(\alpha R_m)\right] - \exp\left(-\frac{1}{2}\alpha^2\right) E\left[\sum_{m=1}^{M} P_m I_0(\alpha R_m) \ln \sum_{k=1}^{M} P_k I_0(\alpha R_k)\right] \tag{11}$$

where $E[\ ]$ denotes expectation with respect to the probability density $g(\mathbf{R})$. We can further simplify the expression above by noting that the first term in Eq. (11) is independent of $\mathbf{P}$, because

$$\begin{aligned} \exp\left(-\frac{1}{2}\alpha^2\right) E\left[\sum_{m=1}^{M} P_m I_0(\alpha R_m) \ln I_0(\alpha R_m)\right] &= \exp\left(-\frac{1}{2}\alpha^2\right) E[I_0(\alpha R_1) \ln I_0(\alpha R_1)] \sum_{m=1}^{M} P_m \\ &= \exp\left(-\frac{1}{2}\alpha^2\right) E[I_0(\alpha R_1) \ln I_0(\alpha R_1)] \\ &= \int_0^\infty r \exp\left[-\frac{1}{2}(r^2 + \alpha^2)\right] I_0(\alpha r) \ln I_0(\alpha r)\, dr \end{aligned} \tag{12}$$

We are now ready to maximize the information $I_M(\alpha, \mathbf{P})$ and thereby to determine the capacity of the MFSK channel.

IV. Maximization of Information and Wideband Capacity

All of the results of this section are summarized in Theorem 1. Let

$$I_M(\alpha) \triangleq \sup_{\mathbf{P}} I_M(\alpha, P)$$

$$S_M = \sum_{m=1}^{M} I_0(\alpha R_M)$$

Note that $E[I_0(\alpha R_m)] = \mu$ for all $m = 1, 2, \cdots, M$, where

$$\mu = \int_0^\infty x \exp(-x^2/2) I_0(\alpha x)\, dx = \exp(\alpha^2/2) \tag{13}$$

THEOREM 1.

(a) $$I_M(\alpha) = \exp(-\alpha^2/2) \times \left\{ E[I_0(\alpha R_1) \ln I_0(\alpha R_1)] - E\left[\frac{S_M}{M} \ln \frac{S_M}{M}\right] \right\} \tag{14}$$

(b) $$I_M(\alpha) \geqq I_{M-1}(\alpha) \tag{15}$$

(c) $$I(\alpha) = \lim_{M \to \infty} I_M(\alpha) = \exp(-\alpha^2) \{E[I_0(\alpha R_1) \ln I_0(\alpha R_1)] - \mu \ln \mu\} \tag{16}$$

$$\equiv \int_0^\infty r \exp\left(-\frac{r^2 + \alpha^2}{2}\right) I_0(\alpha r) \ln I_0(\alpha r)\, dr - \frac{\alpha^2}{2} \tag{17}$$

Division of Eq. (17) by T and $C_\infty = S/N_0$ nats[1]/second yields the wideband capacity result stated in Eq. (1).

Proof:

(a) Maximization. Since the first term in Eq. (11) is independent of P, we maximize $I_M(\alpha, \mathbf{P})$ by minimizing the second term

$$G(\mathbf{P}) = E\left[\sum_{m=1}^{M} P_m I_0(\alpha R_M) \ln \sum_{k=1}^{M} P_k I_0(\alpha R_k)\right] \tag{18}$$

[1]One bit = 0.693 nats.

We observe that $G(\mathbf{P})$ is the expectation of the convex function $x \ln x$; therefore, $G(\mathbf{P})$ is also convex, and so any critical point $\mathbf{P}_0$ will produce the global minimum. To determine such a critical point, we set

$$\frac{\partial}{\partial P_i}\left[G(\mathbf{P}) - \lambda\left(\sum_{m=1}^{M} P_m - 1 \right)\right] = 0 \tag{19}$$

where λ is a Lagrange multiplier accounting for the constraint on the sum of the probabilities being unity. The result is

$$E\left[I_0(\alpha R_i) \ln \sum_{m=1}^{M} P_m I_0(\alpha R_m) + I_0(\alpha R_i)\right] = \lambda$$

or

$$E\left[I_0(\alpha R_i) \ln \sum_{m=1}^{M} P_m I_0(\alpha R_m)\right] \equiv \text{constant for } i \leq M \tag{20}$$

Setting

$$P_1 = P_2 = \cdots = P_M = \frac{1}{M}$$

produces a probability vector which does the job.

(b) Monotonicity. By the foregoing, $G(\mathbf{P}_0) \leq G(\mathbf{P}')$. Take P' such that

$$P'_1 = P'_2 = \cdots = P'_{M-1} = \frac{1}{M-1}$$

and $P'_M = 0$. Obviously P' is a critical point for I_{M-1} but not necessarily for I_M; consequently,

$$I_M(\alpha) \equiv I_M(\alpha, \mathbf{P}_0) \geq I_M(\alpha, \mathbf{P}') \equiv I_{M-1}(\alpha) \tag{21}$$

(c) Wideband capacity. Here we must prove that

$$\lim_{M\to\infty} E\left[\frac{S_M}{M} \ln \frac{S_M}{M}\right] = \mu \ln \mu$$

Since S_M is the sum of M identically distributed random variables

$$I_0(\alpha R_1), I_0(\alpha R_2) \cdots I_0(\alpha R_M)$$

we have, by the strong law of large numbers (Ref. 3),

$$\lim_{M\to\infty} \frac{S_M}{M} = \mu \qquad \text{a.e.}$$

and also

$$\lim_{M\to\infty} \frac{S_M}{M} \ln \frac{S_M}{M} = \mu \ln \mu \qquad \text{a.e.}$$

Consequently, one is inclined to conjecture that

$$\lim_{M\to\infty} E\left[\frac{S_M(\alpha)}{M} \ln \frac{S_M(\alpha)}{M}\right] = \mu \ln \mu = \frac{\alpha^2}{2} \exp(\alpha^2/2)$$

We use martingale theory (Ref. 3) to establish this.

Definition:

A sequence of random variables $V_1, V_2, \cdots$ forms a (sub-) martingale with respect to the increasing sequence of Borel fields $\mathcal{F}_1 \subset \mathcal{F}_2 \subset \cdots$ if and only if

(i) V_n is measurable with respect to $\mathcal{F}_n$.

(ii) $E[|V_n|] < \infty$.

(iii) $E[V_n | \mathcal{F}_{n-1}] (\geq) = V_n$. a.e.

Let $X_1, X_2, \cdots$ be identically distributed random variables having finite mean. Let $S_n = X_1 + \cdots X_n$. Let $\beta_n = \beta(S_n, S_{n+1}, \cdots)$, the Borel field generated by $S_n, S_{n+1}, \cdots$. Let $Z_n = S_n/n$. The term Z_n is measurable with respect to β_n, while $\{\cdots, \beta_n, \beta_{n-1}, \cdots, \beta_1\}$ is a sequence of increasing Borel fields.

LEMMA 1.

$\{\cdots, Z_n, Z_{n-1}, \cdots, Z_1\}$ is a martingale with respect to $\{\cdots, \beta_n, \beta_{n-1}, \cdots, \beta_1\}$.

Proof:

(i) By construction, Z_n is measurable with respect to β_n.

(ii) $$E[|Z_n|] = E\left[\frac{|S_n|}{n}\right] \leq \sum_{j=1}^{n} E\left[\frac{|X_j|}{n}\right]$$
$$= E[|X_1|] < \infty.$$

(iii) By permutability of the X_j's,

$$E[X_j | S_n] = E[X_1 | S_n] \qquad \text{a.e.}$$

Thus

$$S_n = E[S_n | S_n] = E\left[\sum_{j=1}^{n} X_j | S_n\right]$$
$$= \sum_{i=1}^{n} E[X_j | S_n] = nE[X_1 | S_n] \qquad \text{a.e.}$$

or

$$E[X_1 | S_n] = S_n/n \qquad \text{a.e.}$$

Now consider

$$E[Z_{n-1} \mid Z_n] = E\left[\frac{S_{n-1}}{n-1} \middle| S_n\right] = \frac{1}{n-1} E\left[\sum_{j=1}^{n-1} X_j \mid S_n\right]$$

$$= \frac{1}{n-1} \sum_{j=1}^{n-1} E[X_j \mid S_n]$$

$$= \frac{1}{n-1} \sum_{j=1}^{n-1} \frac{S_n}{n} = \frac{S_n}{n} = Z_n \qquad \text{a.e.}$$

Equivalently,

$$E[Z_{n-1} \mid \beta_n] = Z_n \qquad \text{a.e.}$$

and so the lemma holds.

COROLLARY 1.

If ϕ is a function which is convex and continuous on a convex set containing the range of X_1 and if

$$E[|\phi(X_1)|] < \infty$$

then $\{\phi(S_n/n)\}_\infty$ is a submartingale and

$$E\left[\phi\left(\frac{S_n}{n}\right)\right] \text{ decreases monotonically to } \phi(E[X_1])$$

Applying this to the function $\phi(X) = X \ln X$ with $X = I_0(\alpha r_1)$ yields the result desired in Theorem 1(c).

Proof:

Since

$$\left\{\cdots, \frac{S_n}{n}, \frac{S_{n-1}}{n-1}, \cdots, S_1\right\}$$

is a martingale,

$$\left\{\cdots, \phi\left(\frac{S_n}{n}\right), \phi\left(\frac{S_{n-1}}{n-1}\right), \cdots, \phi(S_1)\right\}$$

is a submartingale. By the martingale convergence theorem, there exists a unique random variable w, measurable with respect to $\beta_\infty = \bigcap_n \beta_n$, such that

$$\lim_{n\to\infty} \phi\left(\frac{S_n}{n}\right) = w \qquad \text{a.e.}$$

and

$$\lim_{n\to\infty} E\,\phi\left(\frac{S_n}{n}\right) = E[w]$$

By the strong law of large numbers,

$$\lim_{n\to\infty} \frac{S_n}{n} = E[X_1] \qquad \text{a.e.}$$

Since ϕ is continuous,

$$\lim_{n\to\infty} \phi\left(\frac{S_n}{n}\right) = \phi\left(\lim_{n\to\infty} \frac{S_n}{n}\right) = \phi(E[X_1]) \qquad \text{a.e.}$$

Hence

$$E\left[\phi\left(\frac{S_n}{n}\right)\right] \to E[\phi(E[X_1])] = \phi(E[X_1])$$

Moreover, since

$$\left\{\cdots, \phi\left(\frac{S_n}{n}\right), \cdots, \phi(S_1)\right\}$$

is a submartingale,

$$E\,\phi\left(\frac{S_n}{n}\right) \leq E\left[\phi\left(\frac{S_{n-1}}{n-1}\right)\right]$$

Therefore

$$E\left[\phi\left(\frac{S_n}{n}\right)\right]$$

downverges to $\phi(E[x_1])$.

V. Selection of the Number of Signals *M*

In the preceding sections, it was established that the capacity $C_M(\alpha)$ of an MFSK system increases monotonically to the limit $C(\alpha)$ as the number of signals M is increased. Practical systems must utilize a finite input alphabet not only because the bandwidth $W = M/2T$ is finite, but, more important, because the system complexity, as measured by the number of arithmetical operations, must be kept small. Since $C(\alpha)$ is finite, we know that $C_M(\alpha)$ can be pushed as close to this limit as necessary. For all practical purposes, however, it is sufficient to determine an M such that $C_M/C(\alpha)$ is near 100%. The purpose of this section is to determine useful analytical

bounds on M. It is necessary to consider the case when $\alpha^2/2 = ST/N_0$ is small separately from the case when ST/N_0 becomes large.

A. Behavior of $C_M(\alpha)$ vs M when ST/N_0 is small

Subtracting Eq. (14) from Eq. (16) yields

$$I(\alpha) - I_M(\alpha) = \frac{1}{\mu}\left\{E\left[\frac{S_M}{M}\ln\frac{S_M}{M}\right] - \mu\ln\mu\right\}$$

$$= \frac{1}{\mu}\left\{E\left[\frac{S_M}{M}\ln\frac{S_M}{M} - \frac{1}{2}\left(\frac{S_M}{M}\right)^2 + \frac{1}{2}\left(\frac{S_M}{M}\right)^2\right] - \mu\ln\mu\right\} \tag{22}$$

But

$$\phi(x) = x\ln x - \frac{1}{2}x^2$$

is convex and continuous for $x > 1$; consequently,

$$E[\phi(x)] \leq \phi(E[x])$$

Applying this result to the equation above produces

$$I(\alpha) - I_M(\alpha) \leq \frac{1}{\mu}\left\{\mu\ln\mu - \frac{1}{2}\mu^2 + \frac{1}{2M^2}E[S_M^2] - \mu\ln\mu\right\}$$

But the expected value of the square of a sum of identically distributed random variables is

$$E[S_M^2] = M\sigma^2 + M^2\mu^2$$

where

$$\sigma^2 = E[I_0^2(\alpha r)] - \mu^2 = \int_0^\infty I_0^2(\alpha r)\, r\exp\left(-\frac{r^2}{2}\right)dr - \exp\alpha^2$$

$$= \sum_{n=0}^{\infty}\frac{(\alpha^2/2)^n}{n!}\left[\binom{2n}{n} - 2^n\right]$$

$$= \frac{\alpha^4}{4}\left(1 + \alpha^2 + \frac{9}{10}\alpha^4 + \cdots\right)$$

Therefore,

$$I(\alpha) - I_M(\alpha) \leq \frac{\sigma^2}{2\mu M} \tag{23}$$

Finally, since

$$C_M(\alpha)/C(\alpha) = I_M(\alpha)/I(\alpha)$$

we obtain

$$1 \geqq \frac{C_M(\alpha)}{C(\alpha)} \geqq 1 - \frac{\sigma^2}{2\mu M I(\alpha)} \tag{24}$$

Using our curve-fitting approximation

$$I(\alpha) \geq \frac{\alpha^4}{8}\frac{1}{1+\alpha^2/4}$$

and

$$\mu = \exp(\alpha^2/2) \approx 1 + \alpha^2/2 + \alpha^4/8 + \cdots$$

we obtain

$$1 \geqq \frac{C_M(\alpha)}{C(\alpha)} \geqq 1 - \frac{1 + 3/4\alpha^2 + 0(\alpha^4)}{M} \qquad \text{for } \alpha^2 < 1$$

Thus, as $\alpha^2/2 \to 0$,

$$C_M(\alpha)/C(\alpha) \to (M-1)/M$$

Achieving 99% of capacity requires an $M \geqq 100$ even when $\alpha^2/2 \to 0$.

B. Behavior of $C_M(\alpha)/C(\alpha)$ With M When ST/N_0 Is Large

The lower bound on $C_M(\alpha)/C(\alpha)$ derived for small α is inadequate when α becomes large, because σ^2 increases as $\exp 2\alpha^2$, and this would require M to grow as $\exp(1.5\alpha^2)$, which is too large. We do know, however, that $\ln M$ must grow at least as fast as $I(\alpha) \approx \alpha^2/2$ for large α because the information at the input of the channel must be at least as high as the capacity.

Rewriting Eq. (22), we have

$$I - I_M = E\left[\frac{S_M}{\mu M}\ln\frac{S_M}{\mu M}\right]$$

which, by symmetry, is

$$I - I_M = E\left[\frac{X_M}{\mu}\ln\left(\frac{S_{M-1} + X_M}{\mu M}\right)\right]\quad[X_M = I_0(\alpha r_M)]$$

By conditional expectation,

$$I - I_M = E\left[\frac{X_M}{\mu}E\left[\ln\left(\frac{S_{M-1} + X_M}{\mu M}\right)\middle| X_M\right]\right]$$

By Jensen's inequality,

$$I - I_M \leqq E\left[\frac{X_M}{\mu}\ln\left(\frac{E[S_{M-1}] + X_M}{\mu M}\right)\right] = E\left[\frac{X}{\mu}\ln\left(1 + \left(\frac{X}{\mu} - 1\right)\Big/ M\right)\right]$$

$$= \int_0^\infty r\exp\left[-\frac{1}{2}(r^2+\alpha^2)\right] I_0(\alpha r)\ln\left(1 + \frac{I_0(\alpha r)\exp(-\alpha^2/2) - 1}{M}\right) dr$$

$$< \int_0^\infty r\exp\left[-\frac{1}{2}(r^2+\alpha^2)\right] I_0(\alpha r)\ln\left[1 + I_0(\alpha r)\exp(-\alpha^2/2 - \ln M\right] \tag{25}$$

Further analytical approximation can now be used to show that

$$(I - I_M)/I = 0\left(\frac{1}{\alpha}\right)$$

as $\alpha \to \infty$ when

$$\ln M = \frac{\alpha^2}{2} + K\alpha$$

so that, ultimately, when α is very large, taking $M \approx \exp(\alpha^2/2)$ will suffice to achieve $C_M(\alpha) \approx C(\alpha)$. To demonstrate this, note that

$$I_0(\alpha r) \leqq e^{\alpha r} \tag{26}$$

and let

$$\ln M = \frac{1}{2}\alpha^2 + K\alpha \tag{27}$$

$$I - I_M < \int_0^\infty r I_0(\alpha r)\exp\left[-\frac{1}{2}(r^2+\alpha^2)\right]\ln(1 + \exp(\alpha r - \alpha^2 - K\alpha))\, dr$$

$$< \int_0^{\alpha+K} r I_0(\alpha r)\exp\left[-\frac{1}{2}(r^2+\alpha^2)\right]\ln 2\, dr$$

$$+ \int_{\alpha+K}^\infty r I_0(\alpha r)\exp\left[-\frac{1}{2}(r^2+\alpha^2)\right](\alpha r - \alpha^2 - K\alpha + \ln 2)\, dr$$

Combining the $\ln 2$ terms yields

$$I - I_M < \ln 2 + \int_{\alpha+K}^\infty r I_0(\alpha r)\exp\left[-\frac{1}{2}(r^2+\alpha^2)\right](\alpha r - \alpha^2 - K\alpha)\, dr$$

$$< \ln 2 + \alpha\int_{\alpha+K}^\infty r\exp\left[-\frac{1}{2}(r-\alpha)^2\right](r - \alpha - K)\, dr$$

$$= \ln 2 + \alpha\int_K^\infty (r+\alpha)(r-K)\exp\left[-\frac{1}{2}r^2\right] dr$$

$$\leqq \ln 2 + \frac{\alpha}{K}\left(1 + \frac{\alpha}{K}\right)\exp\left(-\frac{K^2}{2}\right) \quad \text{for } K > 1$$

$$\frac{I - I_M}{I} \leqq \left(1 + \frac{4}{\alpha^2}\right)\left[\frac{2\ln 2}{\alpha^2} + \frac{2}{\alpha K}\exp\left(-\frac{K^2}{2}\right) + \frac{2}{K^2}\exp\left(-\frac{K^2}{2}\right)\right] \tag{28}$$

Thus

$$\lim_{\alpha\to\infty}\frac{C_M}{C(\alpha)} \geqq 1 - \frac{2}{K^2}\exp(-K^2/2) \tag{29}$$

This shows that the number of signals required to achieve a $C_M(\alpha)$ close to $C(\alpha)$ when α is large grows as

$$M \sim \exp[\alpha^2/2(1 + 2K/\alpha)] \tag{30}$$

VI. Conclusion

In summary, the MFSK system capacity behaves roughly as follows:

$$C_M = \frac{S}{N_0}\left(\frac{ST/N_0}{2 + ST/N_0}\right) \times \begin{cases} 1 - \dfrac{1}{M} & \text{if } ST/N_0 < 1 \\ \dfrac{\ln M}{ST/N_0} & \text{if } ST/N_0 >> M >> 1 \\ 1 - \dfrac{\ln 2}{ST/N_0} & \text{if } M \gtrsim ST/N_0 >> 1 \end{cases} \tag{31}$$

The middle term was obtained from the fact that $I_M \approx \ln M$ for $\alpha^2/2 >> \ln M$.

We observe that MFSK systems capable of receiving a reasonably small number of orthogonal signals, such as the $M = 64$ MFSK receiver under construction for the DSN, have the potential of operating above 90% of $C(\alpha)$ at predetection signal-to-noise ratios of less than about 2. This does not mean that systems with a limited number of signals are necessarily inefficient at high ST/N_0. The efficiency can be maintained by reducing T and increasing the rate proportionately, as is common practice even in the case of coherent systems. However, it must be remembered that $C(\alpha)$ is itself an increasing function of α, and this, together with code efficiency, must be taken into account when such tradeoffs are made.

Comparing these results with the hard-decision MFSK channel of Ref. 4, we note that the unquantized capacity always increases with M as opposed to first increasing and then decreasing as in the hard-quantized channel. This leads us to conjecture that unavoidable quantization in practical receivers ultimately destroys the monotonically increasing property in $C_M(\alpha)$, as observed in Ref. 5.

References

1. Wozencraft, Z. M., and Jacobs, I. M., *Principles of Communications Engineering*, Chapters 5–7, John Wiley and Sons, Inc., New York, N.Y., 1965.
2. Viterbi, A. J., *Principles of Coherent Communications*, McGraw-Hill Book Co., New York, N.Y., 1968.
3. Loeve, M., *Probability Theory*, D. Van Nostrand Co., Princeton, New Jersey, 1963.
4. Bar-David, I., and Butman, S., "Performance of Coded, Noncoherent, Hard-Decision MFSK Systems," in *The Deep Space Network Progress Report*, Technical Report 32-1526, Vol. XIII, pp. 82–91, Jet Propulsion Laboratory, Pasadena, Calif., Feb. 1973.
5. Butman, S., and Levitt, B. K., "Capacity for Noncoherent, Soft Decision MFSK Signaling," in *The Deep Space Network Progress Report*, Technical Report 32-1526, Vol. XV, pp. 146–155, Jet Propulsion Laboratory, Pasadena, Calif., March 1973.

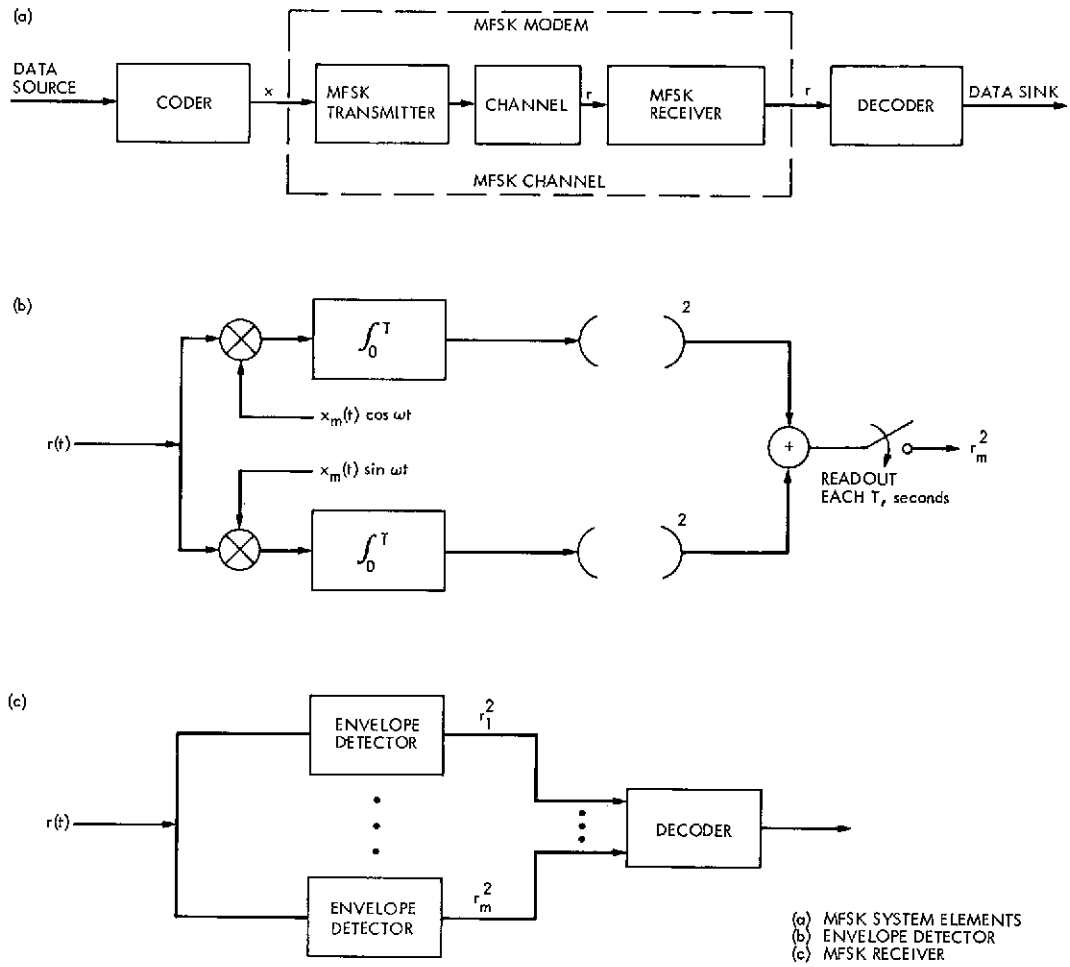

Fig. 1. MFSK channel

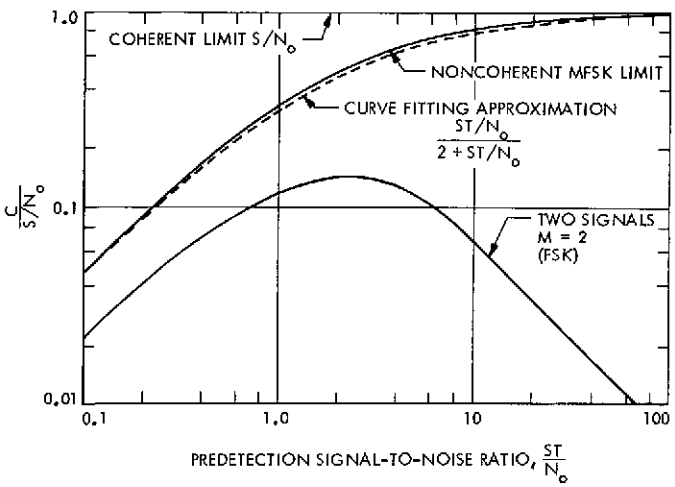

Fig. 2. Wideband MFSK capacity as a function of predetection SNR

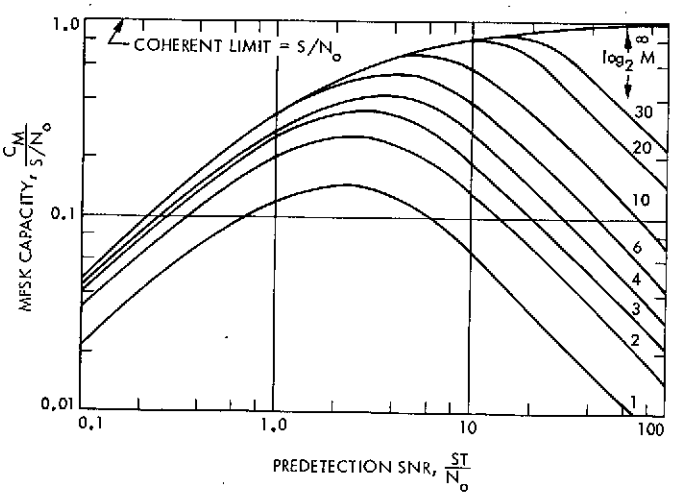

Fig. 3. Capacity of MFSK systems as a function of alphabet size (bandwidth) and predetection SNR

Improvement in the Accuracy of the New Broadband Square Law Detector

M. S. Reid, R. A. Gardner, and C. T. Stelzried
Communications Elements Research Section

Broadband square law detectors are required for precision power measurements and a wide variety of other detector applications. The new square law detector, developed and reported earlier, has a wider dynamic range and a more accurate square law response than that available in the past. Other desirable characteristics are high-level dc output with immunity to ground loop problems, fast response times, ability to insert known time constants, and good thermal stability. This article reports on further development work and shows how the new detector can be operated in a programmable system with a ten-fold increase in accuracy.

I. Introduction

Broadband square law detectors are required for precision power measurements and a wide variety of other detector applications such as the Noise-Adding Radiometer (Ref. 1), the 64-m antenna servo boresighting system, antenna gain measurements, etc. A previous article (Ref. 2) discussed the development and performance of a new constant law detector. This new detector has a wider dynamic range and a more accurate square law response than has been available in the past. Other desirable characteristics of this detector are high-level dc output with immunity to ground loop problems, fast response times, ability to insert known time constants, and good thermal stability. Conventional detectors have an accuracy on the order of 10% whereas the new detector described in Ref. 2 is a 3% instrument. This article discusses further development work which allows the operation of this detector in a programmable system that accounts for detector deviation from square law response to yield an instrument whose accuracy is better than 0.3%.

II. Calculator Applications and the Correction Factor

The increasing use of automatic machines for data acquisition, computation, control, and automation has led to a desire to adapt detectors and other instruments for operation with automatic digital equipment. Part of the development work described in the previous article

(Ref. 2), for example, fast response times and high-level dc output with immunity to ground loop problems, etc., was directed toward detector operation in computer-oriented systems. This article shows how the new detector can be operated in a programmable system with a ten-fold increase in accuracy.

The accuracy of the detector can be increased by accounting for the detector's deviation from square law. If the output voltage of the detector is designated V, then a correction factor α may be included by multiplying the square of the output voltage by the correction factor and by using this term in addition to the output voltage. Thus,

$$\text{corrected output voltage} = V + \alpha V^2 \qquad (1)$$

Nonlinearity effects, i.e., deviations from square law, can be accounted for to a large extent by using Eq. (1). With automatic digital equipment it is easily possible to determine and to use the optimum value for the correction factor.

III. Measurements

In order to make a complete set of test measurements on a detector under controlled conditions, an automatic system was designed and set up in the laboratory. The objective of these tests was to exercise the detectors over a wide dynamic range, to investigate the effects of varying correction factors, and to determine the accuracy of a (corrected) detector with the maximum possible accuracy. The test circuit was based on the measurement system of the previous article (Ref. 2), where a high-power broadband noise source was fed through a variable attenuator and a measured 1-dB step. The output from this step switch was connected to the input of the detector and the output was monitored in the usual way. The detector was taken over the whole of its output voltage range (0 to 2 V) by adjusting the variable IF attenuator. Each measurement point was determined by switching the same 1-dB step in and out. The response of a perfect detector would yield a set of points which, when plotted on a graph of deviation from square law versus output voltage, would be a line parallel to the abscissa and cutting the ordinate at the 1-dB point.

In order to avoid contaminating the data with human error and to avoid using an excessive amount of time in evaluating a detector, the measurement system was automated by using a desk calculator and a coupler/controller. The automatic measurement system is shown in Fig. 1.

The coupler was a Hewlett-Packard 2570A Coupler/Controller, which formed an output/input interface for the Hewlett-Packard 9100A calculator. The combination of the detector's voltage-to-frequency converter and the counter gave a binary coded decimal (BCD) input, as shown in the diagram. BCD output codings were then used to switch the 1-dB step pad in and out of the circuit, and also to start the motor drive on the IF attenuator.

The sequence of measurements that were made was as follows:

(1) Adjust the IF attenuator to set the noise power level to be detected.

(2) Switch the 1-dB pad out.

(3) Measure the detected output level.

(4) Switch the 1-dB pad in.

(5) Measure the detected power level.

(6) Compute the Y factor for three values of correction factor.

(7) Reset the power level and repeat the sequence.

If V_2 is equal to the averaged voltage at the detector output with the 1-dB pad out and V_1 is equal to the averaged voltage at the detector output with the 1-dB pad in, then

$$Y = \frac{V_2 + \alpha (V_2)^2}{V_1 + \alpha (V_1)^2} \qquad (2)$$

where α is the correction factor.

The Y factor was computed and plotted in dB, as shown in Fig. 2, for three values of α. The Y factor, or difference in dB between the measurement with the pad in and out of circuit, is plotted along the ordinate, and the detector output voltage is plotted along the abscissa. The dashed curve shows the detector characteristic when the correction factor is set equal to zero. The solid curve was computed for $\alpha = 0.035$, and the dots show the curve for $\alpha = 0.037$. This figure clearly shows the improvement in linearity to be obtained when a suitable correction factor is used. The figure also shows the sensitivity of the detector characteristic to small changes in the value of the correction factor.

Measurement repeatability was found to be good. If a specific pair of voltage measurements is repeated, the calculated value of the 1-dB pad repeats within ± 0.002 dB.

The Y factor on the ordinate of Fig. 2 is the measured value of the nominal 1-dB pad for various values of detector output voltage. It may be seen from the figure that with $\alpha = 0.035$ the detector unit number RFT470 measured the 1-dB pad as 0.938 dB. This step pad was checked with independent measurements against a National Bureau of Standards (NBS) attenuator (Ref. 3) and found to be 0.942 $\pm$0.001 dB. Since the NBS attenuator was calibrated with a CW signal at 50 MHz, and the input in this case was broadband noise (10-MHz bandwidth) centered at 50 MHz, it is possible that some of the discrepancy may be attributed to a frequency sensitivity in the NBS attenuator.

It may be seen from Fig. 2 that the detector linearity holds within 0.005 dB (i.e., 0.12%) from about 0.1 to about 2.6 V. This is a dynamic range of approximately 15 dB with an accuracy of 0.005 dB. The dynamic range may be extended to greater than 20 dB with a slightly reduced accuracy. On the other hand the high accuracy dynamic range may be extended at the low output level end to less than 0.05 V output without impairment to the accuracy by setting in the correct dc offset. The reason for an offset requirement is because of a small difference between the dc and the voltage-to-frequency outputs. The offset in Fig. 2 was 82 μV. Another technique is to account for the offset by adding a constant term to Eq. (1).

Figure 3 shows the effect of varying offsets and correction factors for the same detector unit as used in Fig. 2. The correction factors are 0, 0.035, and 0.07. The solid curves were computed with a dc offset of 120 μV, the dashed curves with 59-μV offset, and the dots are the points with zero offset. It may be seen from Fig. 3 that the effect of the dc offset is to change the shape and position of the curve but only at the low-voltage end of the detector's dynamic range.

IV. Conclusions

A previous article (Ref. 2) discussed the development and performance of a new constant law detector with a 3% accuracy over a dynamic range of at least 15 dB. This article has shown that when this detector is used in a system with automatic digital equipment so that a large number of calculations can be performed quickly and efficiently, the accuracy can be improved by a factor of more than 10. A subsequent article will discuss the use and performance of this detector in a noise-adding radiometer.

References

1. Batelaan, P. D., Goldstein, R. M., and Stelzried, C. T., "A Noise-Adding Radiometer for Use in the DSN," in *The Deep Space Network*, Space Programs Summary 37-65, Vol. II, pp. 66–69, Jet Propulsion Laboratory, Pasadena, Calif., Sept. 30, 1970.

2. Reid, M. S., Gardner, R. A., and Stelzried, C. T., "The Development of a New Broadband Square Law Detector," in *The Deep Space Network Progress Report*, Technical Report 32-1526, Vol. XVI, pp. 78–86, Jet Propulsion Laboratory, Pasadena, Calif., Aug. 15, 1973.

3. Stelzried, C., Seidel, B., Franco, M., and Acheson, D., "Improved RF Calibration Techniques: Commercial Precision IF Attenuator Evaluation," in *The Deep Space Network Progress Report*, Technical Report 32-1526, Vol. XII, pp. 74–82, Jet Propulsion Laboratory, Pasadena, Calif., Dec. 15, 1972.

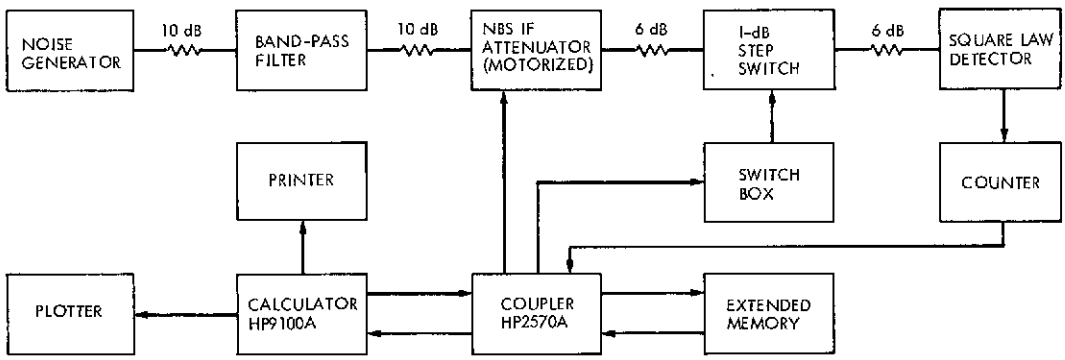

Fig. 1. Automatic measurement system

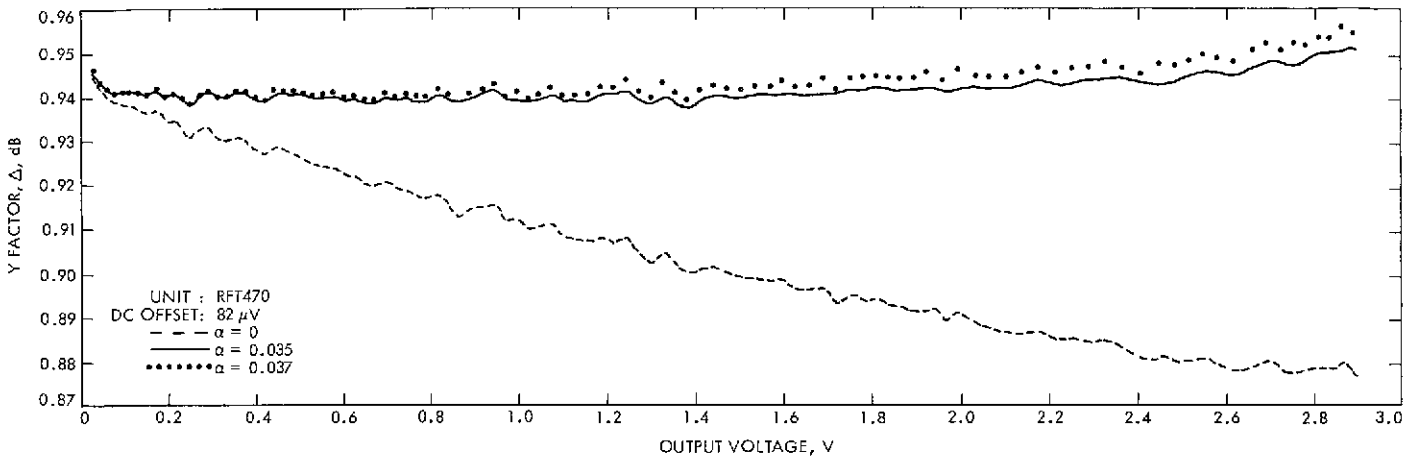

Fig. 2. Detector characteristic for three values of correction factor

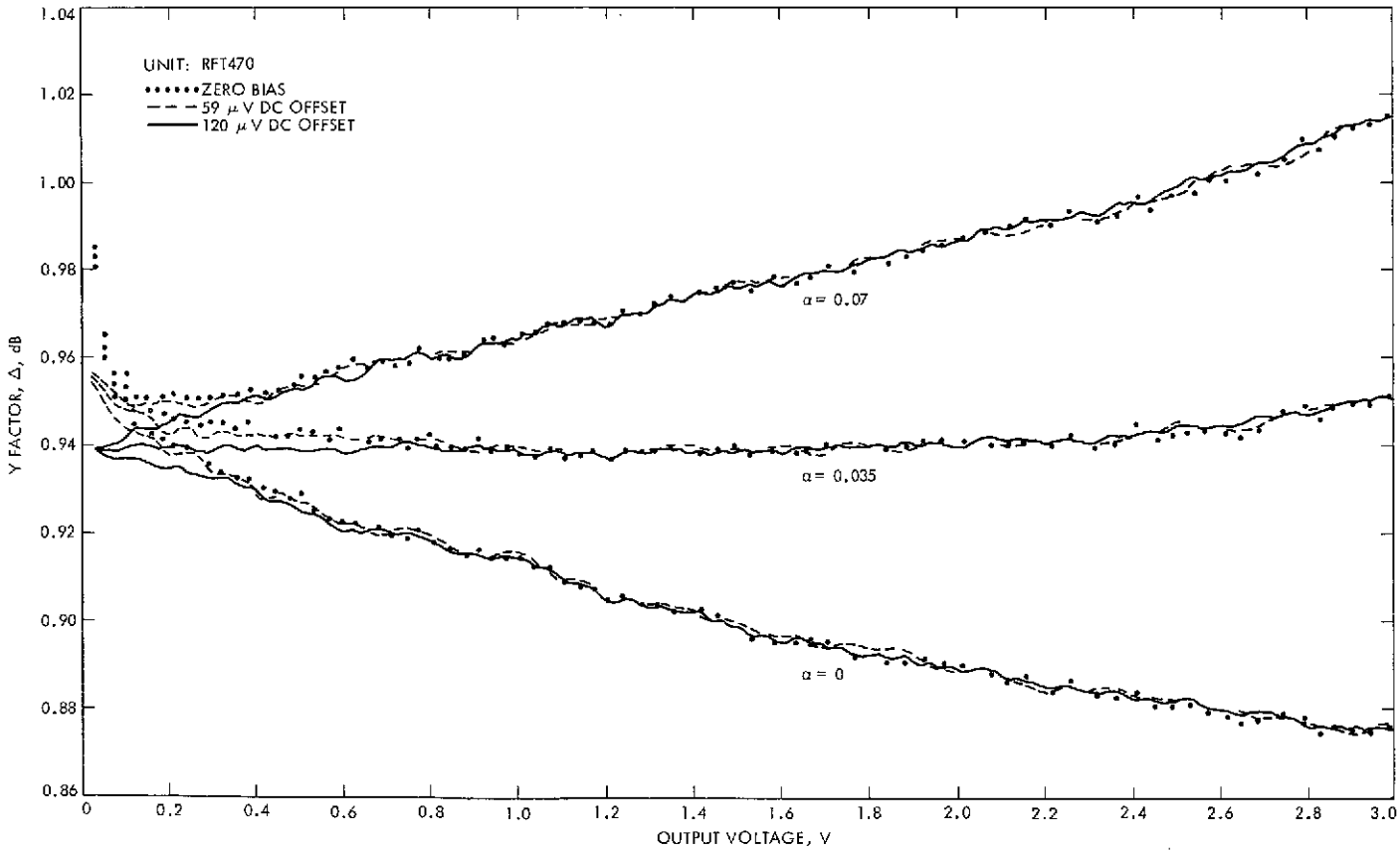

Fig. 3. Detector characteristic for various correction factors and offsets

DSN Research and Technology Support

E. B. Jackson
R. F. Systems Development Section

The activities of the Development Support Group in operating and maintaining the Venus Station (DSS 13) are discussed and progress noted. Activities covered include planetary radar, sky survey, Faraday rotation data collection, dual uplink carrier testing, X-band planetary radar developmental testing, Block IV receiver/exciter installation, equipping the 9-m antenna with a receive capability, and retrofitting the 26-m antenna with a functional planetary radar feedcone.

Activities in support of the DSS 14 high-power transmitter are also noted as are clock synchronization transmissions and Pioneer 10 science support.

During the two-month period ending October 15, 1973, the Development Support Group had the following activities in its operation of the Venus Station (DSS 13).

I. In Support of Section 331

A. Planetary Radar

For a total of 48 hours DSS 13 supported the ranging of the planet Venus to gather data for use by the MVM'73 project. Pseudonoise (PN) code and code-timing pulses were supplied, via microwave link, to DSS 14 for use as a modulating signal for the 400-kW R&D transmitter. This transmitted signal, radiated by the 64-m antenna, illuminated the planet Venus; the reflected signal was also received by the 64-m antenna at DSS 14.

B. Station Monitor and Control (RTOP-68)

As part of the work being done under Research and Technology Operating Plan 68 (RTOP-68), the SDS-930 computer and the 26-m antenna were utilized to test a developmental conical scanning program destined to be used at DSS 14.

II. In Support of Section 333

A. Sky Survey

Using the noise adding radiometer (NAR) and the 26-m antenna in a fixed position (usually 180° az and 85-87° el), data are collected on total antenna system temperature as Earth's rotation sweeps the antenna beam across the sky.

This observing is done when the station is closed for normal operation; during this period a total of 64½ hours of data were collected.

B. Faraday Rotation

Normally two receivers (the Smythe and Stanford receivers) are used for Faraday rotation data collection with their outputs being recorded on punched paper tape and returned to JPL in Pasadena for processing. However, early in this period both receivers failed and were returned to JPL and Stanford Research Institute for repair. Due to the estimated cost it was decided not to repair the Smythe receiver; Stanford Research Institute delivered a new Faraday rotation receiver late in the reporting period. This receiver, along with a new antenna, was installed and aligned to receive signals from Applications Technology Satellite 1 (ATS-1). Although only one receiver is available, the system is functioning and recording data on tape and a chart recorder. These data are, and will be, used by the MVM'73 project for correction of received doppler and range data from the spacecraft.

III. In Support of Section 335

A. Dual Uplink Carrier

Continuing with baseline testing to monitor long-term noise and intermodulation performance, 8½ hours of testing were performed before the system was made inoperative by the removal of the Cassegrain feed cone from the 26-m antenna.

B. X-Band Radar (400 kW)

A 400 kW X-band Planetary Radar system is being developed using two klystrons whose outputs are combined. During this reporting period, the "test bed" at DSS 13 was modified to accept the X-band klystrons for acceptance-type testing. One klystron has been installed into the modified test bed, and element voltages have been applied, but no radio frequency testing has been accomplished.

Various other elements of the system have been integrated, a trial layout of the feed cone has been completed, and a technical requirements document (TRD) and request for bids (RFB) have been sent out for the driver of these klystrons.

C. Block IV Receiver/Exciter

In anticipation of providing extensive support during and after installation of the Block IV Receiver/Exciter (RE) into DSS 14, four personnel from the group participated in final testing and trouble shooting at JPL in Pasadena during the last two weeks prior to shipment to Goldstone.

These same people have heavily supported the installation by fabricating and installing bracketry, terminating and installing coaxial cables, and aiding in preliminary checkout, all on a schedule determined by time available at DSS 14, usually during the midnight and weekend hours. At the end of this reporting period, the permanent cables between the DSS 14 Control Room and the tricone support structure on the 64-m antenna, which are to be manufactured and installed by the DSS 14 personnel, are not yet installed. All other cables are connected, and temporary cables are installed to allow preliminary testing to continue.

D. 9-m Antenna Receive Capability

Using available equipment wherever possible, the 9-m antenna was equipped with a capability to receive at frequencies between 8400 and 8500 MHz. The converter used on the 8448-MHz radar system of several years ago was slightly modified to handle the wider frequency range, and was installed. The standard station receiver, which operates at 30 MHz, was used to complete the system. The feed horn with which the 9-m antenna was already equipped is used at 7150 MHz, even though it is not optimum for this frequency range, but it was decided not to change feed horns since to do so would disable the capability of the 9-m antenna to transmit clock synchronization.

Due primarily to the nonoptimum feed horn, the gain of the antenna at this frequency (8450 MHz) was measured to be approximately 53.1 dB, an efficiency of only 31%. This also contributed to the overall system temperature that was measured to be approximately 2810-K single sideband.

E. 26-m Antenna Feed Cone Retrofit

Early in this reporting period, the special noise burst (NBS) feed cone, which was used for dual carrier testing, was removed from the 26-m antenna and the feed horn from this cone was returned to Section 333 for use in building a special low noise cone for DSS 43. Prior to replacing the NBS cone with the S-band radar operational (SRO) cone that had been previously used on this antenna, we decided to weld all exterior seams and perform the same "noise proofing" operations on it as had been done on the NBS cone. After completion of "noise proofing" and

repainting, the SRO cone was reinstalled on the 26-m antenna, and the maser, from which the comb section had been removed, was also reinstalled (a slightly worse-performing comb section was installed). Just prior to the end of the period, the 26-m antenna was again made operational for reception at S-band with a zenith look system temperature of approximately 29 K.

F. Microwave Test Facility Machine Shop Relocation

Since activities at the Microwave Test Facility (MTF) had been severely curtailed (Ref. 1), we decided to relocate the machine shop to DSS 13. This machine shop, consisting of a vertical mill, horizontal mill, lathe, drill presses, and belt sanders, is used for fabrication of waveguide components, developmental structural parts, and prototype fabrication. It has now been reinstalled at DSS 13 and is fully operational.

IV. In Support of Section 422

A. Clock Synchronization Transmissions

Scheduled clock synchronization transmissions have been suspended since September 1972 for lack of need by flight projects. However, the impending launch of MVM'73 has made it desirable that these scheduled transmissions be resumed. Although the system had been regularly tested, it was gone over thoroughly to ensure its readiness. These tests were completed by the beginning of September, but DSN Scheduling has not yet scheduled regular transmissions to the overseas stations. However, DSS 42 requested and received some special transmissions for a total of three hours.

B. DSS 14 High Power Transmitter Maintenance

The developmental frequency 400-kW transmitter at DSS 14 has been plagued by "kick-offs" due to higher than allowable reflected radio frequency power. Intensive testing could not isolate any one component that was the cause, although the feed cone as a whole was marginal, particularly after a period of operation at high power. It was finally concluded that the most likely cause of the difficulty was work-hardened inclusions in the wall of the waveguide which, under thermal cycling, had raised up from the walls and represented a point of localized high-voltage RF fields. These concentrated fields initiated arcing and caused the reflected RF power to become unacceptably high.

The protective circuits on the transmitter were set at higher than normal levels and an effort was made to "burn out" these suspected trouble spots by sustained high-power operation. After eight hours of high-power operation, this approach was apparently successful. After several initial kick-offs, the reflected power decreased and stabilized at an acceptable value. Some five hours of trouble-free operation were achieved at the 400-kW power level and, tentatively, the problem is assumed to be solved.

V. In Support of Section 825

Although, as mentioned earlier, the 26-m antenna's receiving capability was disabled early in this period, a total of 38½ hours of reception of the radiation from Jupiter and various radio-star calibrators was achieved. These data will be used as a comparison for the data to be telemetered back by Pioneers 10 and 11 when they encounter Jupiter.

Reference

1. Jackson, E. B., "DSN Research and Technology Support," in *The Deep Space Network Progress Report*, Technical Report 32-1526, Vol. XVI, pp. 102–104. Jet Propulsion Laboratory, Pasadena, Calif., Aug. 15, 1973.

A Preliminary Study of Spares Provisioning for the Deep Space Network

I. Eisenberger, G. Lorden, and F. Maiocco
Communications Systems Research Section

This article gives the results of a preliminary investigation into the problem of developing an efficient Initial Spares Provisioning and Spares Allocation Strategy for the Deep Space Network operational spares. A sparing procedure is given, based on failure and repair rates and specified operational requirements. The procedure was applied to several possible situations and the results are listed. The results of computer simulations of these cases are given.

I. Introduction

Reference 1 establishes the responsibilities and functions necessary to select, procure, allocate, and control spare parts for equipment used by the Deep Space Instrumentation Facility (DSIF). The cognizant operations engineer (COE), the cognizant development engineer (CDE), and a representative of the DSIF Logistics Group determine the initial complement of spare parts at a provisioning conference. This conference is also held for the purpose of identifying the funding sources to be used for procurement, the agent responsible for procurement, the delivery schedule, and the destination. Also described in Ref. 1 is the operational-spare flow of material throughout the Deep Space Network (DSN) Repair-Resupply System. However, the decision as to the number of spares to be provided for a given piece of equipment is at present apparently based solely upon engineering judgment. No systematic analytic technique is provided to determine the number of spares necessary to meet required performance criteria. Moreover, as far as we know, Ref. 2 is the only JPL document that specifies the quantity of spares for DSIF electronic equipment. The rules given in Ref. 2 are strictly rules of thumb and do not take into account such factors as failure rates, repair rates, and shipping time. Consequently, this method of sparing must in many cases result in oversparing or undersparing.

Our primary purpose is to develop efficient procedures for use by the COEs and CDEs to assist them in determining which items should be spared, how much to spare, and an optimal network allocation scheme for these spares, when applicable. Both the sparing and allocation techniques must be subject to initial funding constraints and present maintenance policies. This preliminary re-

port gives the results of our initial investigation of one aspect of the sparing problem. For an individual repairable item we determine the operational availability as a function of failure rate, repair rate, total logistic delay time, and number of spares.

II. General Assumptions

We are concerned with pieces of equipment that are removed, replaced by a spare, and repaired whenever they fail to function. To simplify the discussion we call any such piece of equipment a module. A module is assumed to be in one of three states at all times:

(1) Operating.

(2) Failed and in the repair pipeline.

(3) Spare.

While operating, it is subject to a constant failure rate λ, and while in the spares pool it is assumed not to fail. Once failed, it waits a time T to return to the operating state (or the spare state if it is not needed immediately). It is assumed that T has a fixed distribution independent of all previous waiting times for this module and other modules. The analytic model in Section III assumes T is exponentially distributed. Departures from this assumption about T, are considered in Section IV where it is shown that only the mean value of T has a significant effect on the operational availability which, in general, is defined as the stationary probability that a system is operating or operational at any given time.

III. Determination of Operational Availability

We consider a system of $N + n$ identical modules, n operating with N spares. Under the assumption that T is exponentially distributed with mean $1/\mu$, the operation of the system can be described by a so-called birth-and-death process. Detailed discussions of this process are given in Refs. 3, 4, and 5. The state of this process at any time is the number j, of failed modules among the $N + n$ modules in the system. Assuming that the system operates as long as there is at least one module unfailed, the possible values of j are $0, 1, \cdots, N + n$. The theory of Markov chains gives the result that over a long period of operation the fractions of time the system spends in the various states are given by the so-called stationary distribution $\{P_j\}, j = 0, 1, \cdots, N + n$, which can be obtained from the following formulas:

$$
\left.
\begin{aligned}
\lambda_j &= \begin{cases} n\lambda & \text{for } j = 0, 1, \cdots, N \\ (N + n - j)\lambda & \text{for } j = N + 1, N + 2, \cdots, N + n - 1 \end{cases} \\
\mu_j &= j\mu \quad \text{for } j = 0, 1, \cdots, N + n \\
q_0 &= 1 \\
q_1 &= \lambda_0/\mu_1 \\
q_{j+1} &= \mu_{j+1}^{-1}\,[q_j(\lambda_j + \mu_j) - q_{j-1}\lambda_{j-1}], \qquad j = 1, 2, \cdots, N + n - 1 \\
P_j &= \frac{q_j}{\sum_{i=0}^{N+n} q_i}, \quad j = 0, 1, \cdots, N + n
\end{aligned}
\right\} (*)
$$

The above formulas will be denoted collectively as procedure (*).

A simple way of defining operational availability for our purpose is to specify a number $k, 0 \leq k < n$, and say the system is "up" (i.e., operational) whenever $j \leq N + k$, that is, at least $n - k$ modules are operating. The operational availability is then defined by the *system* up-time ratio (UTR), which is

$$\sum_{j=0}^{N+k} P_j$$

the fraction of time with at least $n - k$ modules operating.

Another approach is to define operational availability as the fraction of time an *individual* operating location in the system is "up" (i.e., has an operating module available). This fraction is, of course, the same for all n operating locations and is obtained from the formula

$$UTR = 1 - \frac{1}{n}\,(P_{N+1} + 2P_{N+2} + \cdots + nP_{N+n}) \qquad (1)$$

This approach is applicable to the case where n independent identical modules are operating within a DSS or complex with a common pool of spares.

Whichever approach is used to define operational availability, a convenient way of determining the necessary

spares complement is to specify the minimum acceptable value, α, of the *UTR* and determine the smallest N for which the *UTR* is greater than or equal to α. Cost constraints may suggest trading off operational availability levels for different modules in such a way as to maximize the overall operational availability of the DSN. The definition and implementation of this approach will be the subject of later investigations.

To illustrate the application of procedure (*) to the problem of sparing, we first considered the case of n identical independently operating modules, for $n = 1, 3, 5, 10, 25$, and 50. Values of N were determined based on $\alpha = 0.99$. Table 1 lists the results. The first five of the six values of λ used are typical failure rates taken from Refs. 6 and 7. We used two values of $1/\mu$, 336 hours (2 weeks) and 1776 hours (two months plus two weeks). The values of N prescribed in Ref. 2 for the above values of n are, respectively, 1, 3, 4, 4, 5, 5, irrespective of failure rates, delay time, and operational availability desired.

We then considered what Rau in Ref. 3 calls an (m, n) system, $0 < m \leq n$. In this special case, n identical modules are normally in operation, with N spares, and the system requirement is that a minimum of m of them must be in operation at a given time for adequate performance. The definition of this system also assumes that whenever the system is in state $N + n - m + 1$, it is shut down and reactivated only when a spare is available. Procedure (*) can also be applied to this case with a slight modification. In the formulas comprising procedure (*) the possible values of j should be truncated at $N + n - m + 1$ because of the shutdown rule. Then, with $k = n - m$,

$$UTR = \sum_{j=0}^{N+n-m} P_j$$

or, in terms of the downtime ratio (DTR), ($DTR = 1 - UTR$), $UTR = 1 - P_{N+n-m+1}$.

Table 2 gives some of the results of this analysis for an $(m, 5)$ and $(m, 10)$ system.

Procedure (*) gives one the capability of seeing the effect on the *UTR* of increasing N. Putting N successively equal to $0, 1, 2, \cdots$, corresponding values of *UTR* can be computed. Thus one can observe the increments of *UTR* that result from each additional spare. A decision can then be made as to whether a given increment is worth the cost of the extra spare. This flexibility is illustrated in Figs. 1 and 2. In both, *UTR* is plotted against successive values of N for $\lambda = 150.45 \times 10^{-6}$. In Fig. 1, $1/\mu = 336$ hours and in Fig. 2, $1/\mu = 1776$ hours. In each figure, graphs are given for $n = 1, 3, 5$, and 10. The graphs also illustrate the importance of delay time.

IV. Computer Simulations of the Sparing Procedures

Even if the actual repair time were exponentially distributed, it is unlikely that our assumption of exponentiality for the total time between the failure of a module and its return to the spares pool is valid. To compare the theoretical *UTR*s obtained using this dubious assumption with those likely to be achieved in a real-life situation, we decided to simulate the cases under consideration. In each case, we generated random failure times that were exponentially distributed with mean $1/\lambda$ and, to make the comparison as stringent as possible, we held the repair time *constant* and equal to $1/\mu$, which means that whenever a module failed, it was assumed that it was returned to the spares pool in exactly 336 or 1776 hours. In view of the fact that the standard deviation of an exponentially distributed random variable with parameter μ is $1/\mu$, this is indeed a rigorous test of how sensitive the *UTR* is to the distribution of the return time of a failed module.

In the case of a single operating module ($n = 1$), we kept track of those intervals of time that began with the failure of the operating module with no spare available for replacement and ended with the return of the next repaired module. We will refer to these intervals as down time. The *DTR* was then defined as the ratio of the sum of the length of these intervals to the total elapsed operating time of the system (including the down time).

For $n > 1$, we kept track of the sum of the lengths of the intervals of time when exactly j of the n operating modules were down simultaneously with no spares, for $j = 1, 2, \cdots, n$. Denoting the jth sum by D_j and the total elapsed time of operation by t, the average *DTR* for each operating module was defined as

$$DTR = \sum_{j=1}^{n} jD_j/nt$$

Table 3 gives the results of the simulation for sparing a single module. The values of the parameters were chosen so that examples would be given for *DTR*s falling within each of the intervals $(0.01, 0.05)$, $(0.001, 0.01)$, and $(0, 0.001)$, corresponding to *UTR*s > 0.95, 0.99, and 0.999. Table 4 gives the results when replacements for any of n independently operating modules are taken from a common spares pool, for $n = 3, 5, 10, 25$, and 50.

For the (m, n) system case, we kept track of the intervals of time when $N + n - m + 1$ of the operating modules were in a failed state. During these intervals of down time we assumed that the system was shut down and hence no additional failures could occur until a spare was available. The *DTR* was defined as the ratio of the total down time to the sum of the total down time and the up time. Table 5 gives the results for various (m, n) systems.

V. Conclusion

The consistency of the results of all three simulations with respect to the close agreement between the simulated *DTR*s and those arrived at by theoretical considerations is, in our opinion, impressive. It strongly indicates that to determine the number of spares necessary to achieve a given *UTR*, all that is needed are reasonably accurate estimates of the failure rate of the module and the average time it takes to return a repaired module to the spares pool once it has failed. How this time interval is subdivided and the nature of the probability distributions of the subintervals of time are, within limits, unimportant. In other words, the simulation results show that the state probabilities obtained from procedure (*) are not sensitive to the actual distribution of the return time. Thus, procedure (*) can be used as a bases for determining a spares complement in many, if not all, practical situations.

Tables 1 and 2 show that the *length* of the return time is important, especially for high failure rates. The establishment of a systematic method for sparing has the added advantage that one can easily consider trade-offs between the number of spares needed and hence their cost, and the cost of shipping them to and from a repair facility. A reduction in the shipping time may result in a smaller number of spares needed and consequently justify a change in the shipping procedure for a particular module.

From our initial investigation we learned that some modules may spend anywhere from two to six weeks at the repair facility waiting for repair and that the basic repair philosophy is "first come first serve." It is our contention that some sort of priority scheme should be implemented for two reasons. First, an efficient sparing procedure that is based on valid statistical considerations must at some time or other result in a dangerously low level of spares. If this never happens, we have overspared. If it happens too often then either our estimates of the parameters are off or the specified *UTR* is too low. However, assuming that the occurrence of this phenomenon is consistent with our spares philosophy for a particular module, a priority scheme that takes into account this level of spares and extends priority to a failed module whenever this level is critical will have a direct impact on station operational availability. Second, reducing the repair time significantly has the same effect as reducing the shipping time. If a trade-off study, particularly for expensive items, shows that less spares are needed if priority is given during repair, a worthwhile cost savings may result by doing so.

The point is that an efficient method for spares provisioning gives us the capability of making sensible decisions based on valid information. Engineering judgment, as valuable as it is in many situations, is just not precise enough for this purpose. The drastic consequences that may result from either undersparing or oversparing can be avoided only by applying an acceptable scientific method to the problem of sparing. Moreover, in one sense, a priority scheme at the repair facilities can be considered as a hedge against undersparing due to underestimating a failure rate. In another sense, it can be considered as yet another possible means of saving money. Both are consequences devoutly to be wished.

It is our intention to pursue further the development of an optimum spares provisioning procedure for the DSN, incorporating the results already obtained and outlined in this report. Our future investigations will include the problem of spares provisioning with cost constraints and the allocation of spares for modules that are used in more than one DSS. Priority maintenance schemes will be investigated at a later date.

References

1. *Management of DSIF Spare Parts Program,* DSIF Operations Section M & O Document 337S-2B1. Jet Propulsion Laboratory, Pasadena, Calif., July 14, 1972 (JPL internal document).
2. *DSIF General Specification; General Requirements for DSIF Equipment,* Specification 8907A. Jet Propulsion Laboratory, Pasadena, Calif., Oct. 11, 1962 (JPL internal document).
3. Rau, J. G., *Optimization and Probability in Systems Engineering.* Van Nostrand Reinhold Co., New York, 1970.
4. Feller, W., *An Introduction to Probability Theory and Its Applications,* Second Edition, 10th Printing. John Wiley & Sons, Inc., New York, Mar. 1965.
5. Wagner, H. M., *Principles of Operations Research With Applications to Managerial Decisions.* Prentice Hall, New York, 1969.
6. *Reliability Report: Prediction of Data Decoder Assembly Mean Time Between Failure,* DSIF Operations Section M & O Document 337S1-5A3. Jet Propulsion Laboratory, Pasadena, Calif., Feb. 10, 1972 (JPL internal document).
7. *Reliability Report: Prediction of Block Decoder Assembly Mean Time Between Failure,* DSIF Operations Section M & O Document 337S1-5A5. Jet Propulsion Laboratory, Pasadena, Calif., July 25, 1972 (JPL internal document).

Table 1. Number of pooled spares, N, necessary to insure a $UTR \geq 0.99$ for each of n identical modules when they are operating independently[a]

$\lambda/10^{-6}$	$\mu = 1/336$						$\mu = 1/1776$					
	$n = 1$	$n = 3$	$n = 5$	$n = 10$	$n = 25$	$n = 50$	$n = 1$	$n = 3$	$n = 5$	$n = 10$	$n = 25$	$n = 50$
	N	N	N	N	N	N	N	N	N	N	N	N
2.72	0	0	0	0	0	0	0	0	0	0	0	0
47.85	1	1	1	1	1	1	1	1	2	2	3	5
150.44	1	1	1	2	2	3	2	3	4	5	10	16
481.07	2	2	3	4	6	10	3	6	8	13	27	49
791.14	2	3	4	5	9	16	5	8	12	20	42	78
1000.00	2	3	4	6	12	20	5	10	14	24	53	98

[a]Assuming exponentially distributed times to failure and repair; the unit of time is one hour.

Table 2. Number of spares, N, necessary to ensure a $UTR \geq 0.99$ for an $(m, 5)$ and an $(m, 10)$ system[a]

$\lambda/10^{-6}$	$n = 5$						$n = 10$							
	$\mu = 1/336$			$\mu = 1/1776$			$\mu = 1/336$				$\mu = 1/1776$			
	$m = 1$	$m = 3$	$m = 5$	$m = 1$	$m = 3$	$m = 5$	$m = 1$	$m = 4$	$m = 7$	$m = 10$	$m = 1$	$m = 4$	$m = 7$	$m = 10$
	N	N	N	N	N	N	N	N	N	N	N	N	N	N
2.72	0	0	0	0	0	1	0	0	0	0	0	0	0	1
47.85	0	0	1	0	0	2	0	0	0	2	0	0	0	3
150.44	0	0	2	0	2	4	0	0	0	3	0	0	3	7
481.07	0	1	3	1	6	9	0	0	1	5	0	5	11	15
791.14	0	2	4	4	10	13	0	0	3	7	0	10	18	22
1000.00	0	3	5	6	12	16	0	0	4	8	1	14	22	26

[a]Assuming exponentially distributed times to failure and repair; the unit of time is one hour.

Table 3. Results of simulating sparing for a single module[a]

$\lambda/10^{-6}$	$1/\mu$	N	Theoretical DTR	Actual simulated DTR	% difference	Years operated
2.72	336	0	0.00091	0.00099	−8.8	10138
2.72	1776	0	0.0048	0.0048	0	2740
47.85	336	0	0.0158	0.0158	0	556
47.85	336	1	0.00013	0.00015	−15.4	5946
47.85	1776	1	0.0033	0.0033	0	1845
150.44	336	0	0.0481	0.0498	−3.5	1424
150.44	336	1	0.0012	0.0013	−8.3	980
150.44	1776	1	0.0274	0.0267	+2.6	570
150.44	1776	2	0.0024	0.0027	−12.5	960
481.07	336	1	0.0111	0.0109	+1.8	433
481.07	336	2	0.00060	0.00064	−6.7	425
481.07	1776	2	0.0447	0.0484	−8.3	70
481.07	1776	3	0.0095	0.0077	+18.9	440
791.14	336	1	0.0272	0.0261	+4.0	118
791.14	336	2	0.0024	0.0027	−12.5	423
791.14	1776	3	0.0404	0.0403	+0.2	455
1000.00	336	1	0.0405	0.0416	−2.7	59
1000.00	1776	4	0.0252	0.0251	+0.4	216

[a]Return time for repaired modules is constant and equal to $1/\mu$; N denotes number of spares.

Table 4. Results of simulating pooled sparing for n independent modules[a]

n	$\lambda/10^{-6}$	$1/\mu$	N	Theoretical DTR	Actual simulated DTR	% difference	Years operated
3	2.72	1776	0	0.0048	0.0050	−4.2	6753
	47.85	1776	1	0.0094	0.0104	−10.6	367
	150.45	1776	2	0.0166	0.0148	+10.8	264
	481.07	336	2	0.0046	0.0050	−8.7	122
	481.07	1776	4	0.0406	0.0409	−0.7	123
	791.14	336	2	0.0164	0.0170	−3.7	70
	791.14	1776	7	0.0217	0.0235	−8.3	99
	1000.00	336	2	0.0287	0.0303	−5.6	116
5	2.72	1776	0	0.0048	0.0046	+4.2	4365
	47.85	1776	2	0.0020	0.0024	−20.0	219
	150.45	336	0	0.0481	0.0464	+3.5	165
	150.45	1776	3	0.0107	0.0113	−5.6	152
	481.07	1776	6	0.0342	0.0310	+9.4	100
	1000.00	1776	13	0.0158	0.0150	+5.1	69
10	2.72	1776	0	0.0048	0.0049	−2.1	4167
	47.85	1776	3	0.0013	0.0010	+23.1	239
	150.45	1776	4	0.0183	0.0183	0	78
	481.07	1776	10	0.0384	0.0428	−11.5	61
	791.14	1776	16	0.0396	0.0342	+13.6	62
	1000.00	336	4	0.0370	0.0385	−4.1	59
25	47.85	1776	1	0.0460	0.0460	0	100
	150.45	336	0	0.0481	0.0469	+2.5	65
	150.45	1776	10	0.0053	0.0043	+18.9	91
	481.07	1776	21	0.0490	0.0479	+2.2	16
50	2.72	1776	1	0.00054	0.00057	−5.6	877
	47.85	336	1	0.0050	0.0051	−2.0	48
	47.85	1776	2	0.0432	0.0399	+7.6	52
	150.45	1776	11	0.0467	0.0452	+3.2	48

[a]Return time for repaired modules is constant and equal to $1/\mu$; N denotes the number of pooled spares.

Table 5. Results of simulating sparing for an (m, n) system[a]

n	m	$\lambda/10^{-6}$	$1/\mu$	N	Theoretical DTR	Actual simulated DTR	% differenced	Years operated
10	10	2.72	336	0	0.0090	0.0084	+6.7	2271
5	5	2.72	1776	0	0.0236	0.0256	−8.5	3946
5	4	47.85	1776	0	0.0482	0.0464	+3.7	270
10	9	47.85	1776	1	0.0400	0.0402	−0.5	124
25	21	47.85	1776	2	0.0031	0.0031	0	100
5	4	150.45	336	0	0.0200	0.0221	−10.5	157
5	3	150.45	1776	1	0.0177	0.0179	−1.1	84
10	8	150.45	1776	3	0.0261	0.0241	+7.7	118
25	18	150.45	1776	1	0.0475	0.0468	+1.5	112
5	5	481.07	336	2	0.0396	0.0393	+0.8	49
5	3	481.07	1776	4	0.0397	0.0421	−6.0	55
10	7	481.07	336	1	0.0096	0.0078	+18.8	79
10	3	481.07	1776	0	0.0267	0.0289	−8.2	44
10	7	481.07	1776	11	0.0073	0.0064	+12.3	95
5	1	791.14	1776	1	0.0397	0.0325	+18.1	116
5	3	791.14	336	1	0.0174	0.0173	+0.6	32
5	2	791.14	1776	4	0.0490	0.0461	+5.9	61
5	5	791.14	1776	13	0.0073	0.0068	+6.8	113
5	1	1000.00	336	0	0.0010	0.00087	+13.0	92
5	1	1000.00	1776	2	0.0438	0.0462	−5.5	90
5	2	1000.00	336	1	0.0044	0.0051	−15.9	79
5	2	1000.00	1776	6	0.0423	0.0408	+3.5	59

[a]Return time for repaired modules is constant and equal to $1/\mu$; N denotes the number of spares for the system.

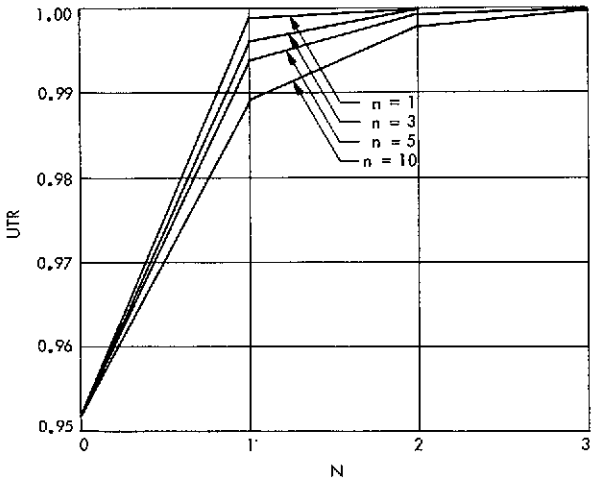

Fig. 1. *UTR* vs *N* for $\lambda = 150.45 \times 10^{-4}$/h, $1/\mu = 336$ hours

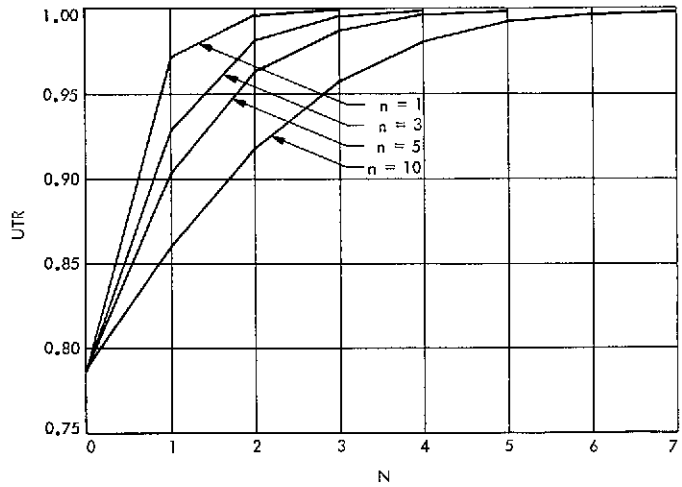

Fig. 2. *UTR* vs *N* for $\lambda = 150.45 \times 10^{-6}$/h, $1/\mu = 1776$ hours

Word Formatter for MVM'73 Real-Time High-Rate TV Data

B. K. Levitt
Communications Systems Research Section

During both MVM'73 encounters, real-time TV data at 117.6 kilobits/s will be transmitted from DSS 14 to the Space Flight Operations Facility (SFOF) along a 230.4-kilobits/s supergroup line. The reliability of this link is largely an unknown parameter, but previous experience with similar data channels suggests that random (nonbursty) bit errors may occur at rates between 1 in 10^4 and 1 in 10^7 bits. The original design of the word formatter necessitated by the discrepancy between the source and ground transmission rates is shown to be inadequate to guarantee acceptable reception of the TV data at the SFOF. An alternative formatter design is described, which alleviates this problem with minimum cost changes from the original system.

I. Introduction

Current plans call for the transmission of the 117.6-kilobits/s imaging data from the 1973 Mariner Venus/Mercury (MVM'73) probe to the Space Flight Operations Facility (SFOF) during both planetary encounters. The ground leg of this telemetry link will consist of a 230.4-kilobits/s telephone company supergroup data line between the Goldstone 64-m tracking station (DSS 14) and the SFOF. This particular data channel has not been used before, so its reliability is largely an indeterminate parameter at this stage. However, for system design purposes, it is estimated that the link will have randomly distributed bit errors at rates between 1 in 10^4 and 1 in 10^7 bits, except in those rare periods when the errors occur in bursts.

To accommodate the mismatch between the information source and ground transmission rates, a hardware device will stuff filler bits onto the data line at an average rate of 112.8 kilobits/s. The combined imaging data and filler bits will be organized into 18-bit words (bytes) prior to transmission, as described below. At the other end of the ground link, another piece of hardware will establish and maintain byte synchronization, and remove the filler bits to reconstruct the original TV data sequence. The combined hardware system for stuffing filler bits onto the ground link and then extracting them at the receive end is referred to as a "word formatter."

The purpose of this report is to analyze the original design of the word formatter, and to show that the resultant TV pictures would be likely to fall below minimum acceptable project standards. It will then be demon-

strated that a few inexpensive changes in this formatter design are sufficient to guarantee the required performance levels.

II. Original Formatter

A. Design

The transmit portion of the original formatter design is diagrammed in Fig. 1. Imaging data from the spacecraft are received at DSS 14 at 117.6 kilobits/s. The supergroup data link transmits information to the SFOF in 18-bit bytes at 230.4 kilobits/s. Because of the difference between the source and transmission rates, there are two kinds of bytes: data (D) and filler (F) bytes. The F byte is a fixed 18-bit sequence:

$$S = 001 \quad 010 \quad 000 \quad 000 \quad 000 \quad 000$$

stored in a shift register of that length. The D byte contains 16 bits of TV data, one extraneous bit which is always a 1, and a parity check bit P. In each D byte, the P bit is selected so that the 18 bits sum to 1 modulo 2; thus the D bytes have odd parity while the F bytes have even parity.

The Symbol Synchronizer Assembly (SSA) feeds imaging data in 16-bit blocks into the D-byte shift register at an average rate of 117.6 kilobits/s. Every 18/230.4 ms, an 18-bit byte is transferred to the supergroup data line for transmission. At these instants, if the data shift register is full, a D byte is sent; otherwise, the F byte is transmitted. Thus, approximately every other transmitted byte is an F byte. Furthermore, the transmitted data never contains two consecutive F or three consecutive D bytes, as emphasized in Fig. 1.

At the receive end of the ground link, the formatter must strip off the imaging data. This involves the acquisition and maintenance of byte synchronization, and the correct identification of D and F bytes. Acquiring byte synchronization is not a problem because almost every other transmitter byte is a known 18-bit filler sequence. Shifting one bit at a time, the synchronizer searches for an 18-bit received sequence that is identical to the transmitted F byte. Once this initial search is consummated, byte synchronization can be verified by checking successive F bytes.

To distinguish between D and F bytes, the formatter determines the parity of each received byte. This parity-check algorithm is also used to detect loss of byte synchronization resulting from the random deletion of data or insertion of extraneous bits in the ground link. For a particular received byte, the algorithm operates as follows:

$$\text{odd parity} \Rightarrow \text{D byte}$$

$$\text{even parity} \begin{cases} \text{identical with F byte} \Rightarrow \text{F byte} \\ \text{does not agree with F byte} \Rightarrow \text{loss of byte sync} \end{cases}$$

When the algorithm decides byte synchronization is lost, the formatter reenters the byte sync acquisition (BSA) mode.

B. Performance

The imaging data extracted by the receive portion of the formatter are fed to a Univac 1230 computer that acquires and maintains frame synchronization. A frame of TV data contains 7056 bits, which translates into 1 line of video. Any time the formatter parity-check algorithm misinterprets a received F byte to be a D byte, the corresponding received frame of imaging data is augmented by 16 bits. This usually causes the frame synchronizer to drop lock, resulting in the loss of at least 1 line of video. Similarly, if a received D byte is judged to be an F byte, the frame is shortened by 16 bits, leading to a minimum loss of 1 line of video. Finally, there is a loss of at least 1 frame of TV data any time the formatter reverts to the BSA mode.

A "byte error" is defined as the event that a particular received byte is misinterpreted or causes the formatter to reenter the BSA mode, due only to bit crossovers in the ground link. (We are not attempting to include the effects of random bit insertions or deletions in our model of the supergroup line.) The ground link can be regarded as a binary symmetric channel with unknown crossover probability p. Because p is thought to lie in the approximate range $10^{-4} \gtrsim p \gtrsim 10^{-7}$, all computations below are to lowest order in p. The parity-check algorithm commits a byte error whenever the parity of a received byte is incorrect: a single bit crossover anywhere within a given received byte is sufficient to cause such an error. For a particular received byte, the probability ϵ_B of making a byte error is therefore given by

$$\epsilon_B \equiv \Pr[\text{byte error}] = 18p \tag{1}$$

to lowest order in p. Furthermore, these errors are independent from byte to byte.

A byte error anywhere within a frame of imaging data results in the loss of the corresponding line of video, but

α bytes are transmitted over the ground link for each frame of TV data, where

$$\alpha = \frac{230.4 \times 7056}{117.6 \times 18} \text{ bytes/frame} \tag{2}$$

Therefore the probability of ϵ_L of losing a given line of a TV picture is specified by

$$\epsilon_L \equiv \Pr[\text{lose 1 line}] = \alpha\epsilon_B = \frac{230.4 \times 7056}{117.6} p \tag{3}$$

to lowest order in p. Since there are 700 lines in each picture, we can expect to lose 700 ϵ_L lines in every picture received at the SFOF. This expected loss of video is tabulated in Table 1 as a function of p.

An acceptable performance level is the loss of 1 or 2 lines of a given TV picture. To achieve this fidelity with the original formatter design, p would have to be of the order of 10^{-7} or better. Since we cannot guarantee that the supergroup channel will meet this criterion, the formatter design must be improved. The suggested changes are outlined below.

III. Improved Formatter

A. Design

The limiting problem inherent in the original formatter design is that ϵ_B is of order p. To realize any significant improvement in performance, we must change the design so that ϵ_B is of order p^2. Because of cost considerations, the ground rules are that we can only change the last 2 bits in the D-byte shift register, the contents of the F-byte shift register, and the formatting algorithm.

Starting with the least important change, it is recommended that the original filler word be replaced by the 18-bit Neuman-Hofman sequence (Ref. 1):

$$S = 001 \quad 100 \quad 111 \quad 110 \quad 100 \quad 101$$

This word has correlation properties that are particularly suited for synchronization applications, although byte synchronization is not really a problem since about half of the transmitted bytes are F bytes. The byte synchronization acquisition procedure described earlier should be retained in the new design.

Once byte synchronization is established, the receive portion of the formatter must decide whether each byte contains data or filler. This is a standard binary hypothesis decision problem in information theory. It is assumed that the 16-bit blocks of TV data in each D byte are independent and uniformly distributed. To minimize the probability of error in deciding between F and D bytes, we want to maximize the expected Hamming distance between them. As shown in Fig. 2, this requires that the last two bits of the F and D bytes be complementary. This precludes the use of the parity-check scheme in the original formatter design.

To distinguish between D and F bytes, the receive portion of the formatter computes the Hamming distance d_H between each received byte and the known F byte. The binary decision for a given received byte is then specified by the algorithm

$$\boxed{\begin{aligned} d_H &= 0 \text{ or } 1 \Rightarrow \text{F byte} \\ d_H &> 1 \quad\;\; \Rightarrow \text{D byte} \end{aligned}}$$

The algorithm must also decide when byte synchronization is lost. We know that we can lose synchronization only because of the random deletion or insertion of bits over the ground channel. If we actually do lose byte synchronization, the binary decision procedure above will interpret almost every received byte to be a D byte. But we know we can never have more than two consecutive D bytes. Therefore, the recommended byte synchronization maintenance scheme is to reenter the BSA mode if, and only if, three consecutive received bytes are declared to be D bytes.

B. Performance

We will now compute the probability ϵ_B of making a byte error on a given received byte, due only to random bit crossovers with probability p. An F byte is misinterpreted as a D byte if two or more bits are in error; the probability of this occurrence is given by

$$\Pr[\text{D} \mid \text{F}] = \binom{18}{2} p^2 \tag{4}$$

to lowest order in p. The most likely way that a received D byte will be misinterpreted as an F byte is when the received 16-bit data block is identical to the first 16 bits of the filler sequence, and one of the last two bits is in error:

$$\Pr[\text{F} \mid \text{D}] = 2^{-16}\binom{2}{1} p \tag{5}$$

If a received F byte between two D bytes is misinterpreted while the received D bytes are correctly detected,

we will reenter the BSA mode. This is the most probable circumstance under which the BSA mode is invoked. The probability of this event is given by Eq. 4 to lowest order in p.

The fraction of transmitted bytes containing TV data is given by

$$\Pr[D] = \frac{18 \times 117.6}{16 \times 230.4} \tag{6}$$

Conversely,

$$\Pr[F] = 1 - \Pr[D] \tag{7}$$

Therefore, we conclude that

$$\begin{aligned} \epsilon_B &= \Pr[D \mid F] \Pr[F] + \Pr[F \mid D] \Pr[D] \\ &= 153p^2 + p(2^{-15} - 153p)\left(\frac{18 \times 117.6}{16 \times 230.4}\right) \end{aligned} \tag{8}$$

Since 2^{-15} is of the order of p, ϵ_B is now of the order of p^2 as desired. The probability of losing a particular line of video is again specified by $\epsilon_L = \alpha\epsilon_B$, where α is defined in Eq. 2, and the expected video loss is 700 ϵ_L lines per TV picture.

The expected loss of video for the new formatter design is compared with the performance of the original system in the table of Fig. 3. We see that we can now anticipate the loss of less than 1 line every 3 pictures on the average, provided the ground channel exceeds its minimum estimated reliability, $p = 10^{-4}$. Since p had to be less than 10^{-7} to guarantee this performance in the original formatter, this implies a design advantage of 3 orders of magnitude with respect to the maximum acceptable crossover probability of the ground link.

IV. Conclusion

The conclusions of this report are self-evident. The original formatter design could not ensure adequate performance levels; the recommended design does. At a meeting held on May 18, 1973, the project ratified the proposed formatter design changes, and these have subsequently been implemented.

Reference

1. Neuman, F., and Hofman, L., "New Pulse Sequences with Desirable Correlation Properties," in *Proceedings of the National Telemetry Conference, Washington, D.C., April 14, 1971*, pp. 272–282.

Table 1. Performance comparison of original and new word formatter designs versus bit crossover probability p of ground link

Bit error rate, p	Expected number of lines lost per TV picture	
	Original design	Proposed Design
1 in 10^4	700	1 in 3
1 in 10^5	100	1 in 280
1 in 10^6	10	1 in 2.2×10^4
1 in 10^7	1	1 in 7.8×10^5

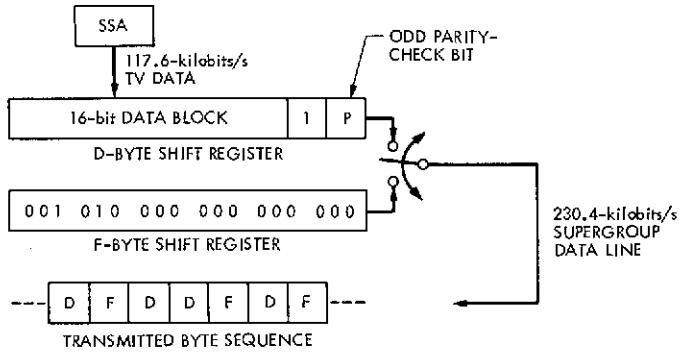

Fig. 1. Transmit portion of original word formatter design

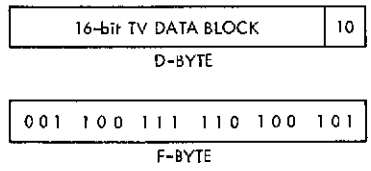

Fig. 2. Recommended formats of D- and F-byte shift registers

GCF Wideband Switch Subassembly—Requirements and Design Concept

E. F. Bird
DSN Data Systems Development Section

Basic requirements and design approach for the wideband switch subassembly (WBSS) are presented. The WBSS is a part of the Ground Communication Facility's wideband subsystem located in the Central Communications Terminal at the Jet Propulsion Laboratory. It is used to support the Mariner-Venus-Mercury 1973 and Viking operations. The WBSS is a complex switching unit that provides for simple control by the operator for effecting the many interconnect configurations of various data sets, coded multiplexers/demultiplexers, and computer systems.

I. Introduction

Among other communications capabilities, the Ground Communications Facility provides for the interchange of wideband data between the Mission Control and Computing Center and deep space stations or Project locations. The hub of this activity is located within the Central Communications Terminal (CCT) at JPL.

The functional operations requirements established by the Deep Space Network for the necessary capabilities to support the Mariner-Venus-Mercury 1973 and Viking Flight Projects specify complete versatility in providing interchange configurations for wideband data.

This article discusses the basic requirements set forth as design criterion for that part of the wideband subsystem (WBS) which is to accomplish this multifaceted switching of wideband data and control signals—the wideband switch subassembly (WBSS).

II. Capabilities Requirements

The WBSS is required to provide real-time switching (interconnection) of equipments in the WBS with a minimum of operator actions. It is required to be capable of handling data rates of up to 250 kilobits/s in a high (electrical) noise environment without adding to that noise.

Its minimum switching capacity is that which is sufficient to interconnect 10 data sets (DSs), 3 coded multiplexers/demultiplexers (CMDs), and 6 local computer

systems, herein referred to as on-site computers (OSCs). These interconnections are further subdivided as to direction of data flow relative to OSCs.

III. Design Requirements

The WBSS is required to utilize no more than two full 61-cm (24-in.) equipment bays with each bay being fully connectorized at its external interfaces. Any individual rack-mounted assemblies must also be connectorized at their external interfaces.

To meet the frequency/noise specifications it is required to use coaxial cabling. This cabling is required to be so arranged as to prevent clock-to-data skew of greater than 1% of a bit period.

The WBSS is required to have a readout display which is continuous and allows easy interpretation of switched path configurations. It must have redundant power supplies with automatic cross-over in the event of power supply failure. It must have configuration-memory as a precaution against commercial power failure.

IV. Design Concept

The basic functions of the WBSS are depicted in Fig. 1. Superficially it appears as a fairly straightforward design. Challenges are then brought to the fore when the various types of interconnection are investigated and especially when the transmit/receive functions of each piece of equipment are to be controlled separately.

It is possible, for example, to route nonmultiplexed (uncoded) inbound data directly from DS No. 1 (receive) to OSC No. 3 (via the DS/OSC matrix) and simultaneously route outbound data from OSC No. 5 through CMD No. 2 (via the CMD/OSC and then the DS/CMD matrices) to DS No. 1 (transmit).

This is not a common operations configuration, but it does indicate how versatile the WBSS can be. Unique provisions are made for allowing the multiple connection of DSs to a single CMD. This permits outbound (only) data to be routed to more than one distant location from the same CMD.

Crossbar switches are utilized for two reasons. First, they have a high switch-contact density—about 37,500 contacts per cubic meter (1,250 per cubic foot). Secondly, they are capable of "latching" a crosspoint and thus retaining it through a power failure.

Integrated circuits are utilized to provide an uncomplicated interface for the operator at the control and display panels. All aspects must be considered to minimize those factors which could confuse an operator during a critical or busy period.

V. Conclusion

The requirements set forth describe a complex switching unit. A detailed calculation reveals a requirement of 626 specific configurations of from 3 to 6 signal lines per configuration. The human-factors requirements of the WBSS are nearly as involved as those of the configuration switching.

Reference

1. McClure, J. P., "Ground Communications Facility Functional Design for 1973–1974," Technical Report 32-1526, Vol. XI, pp. 124–131, Jet Propulsion Laboratory, Pasadena, Calif., Oct. 15, 1972.

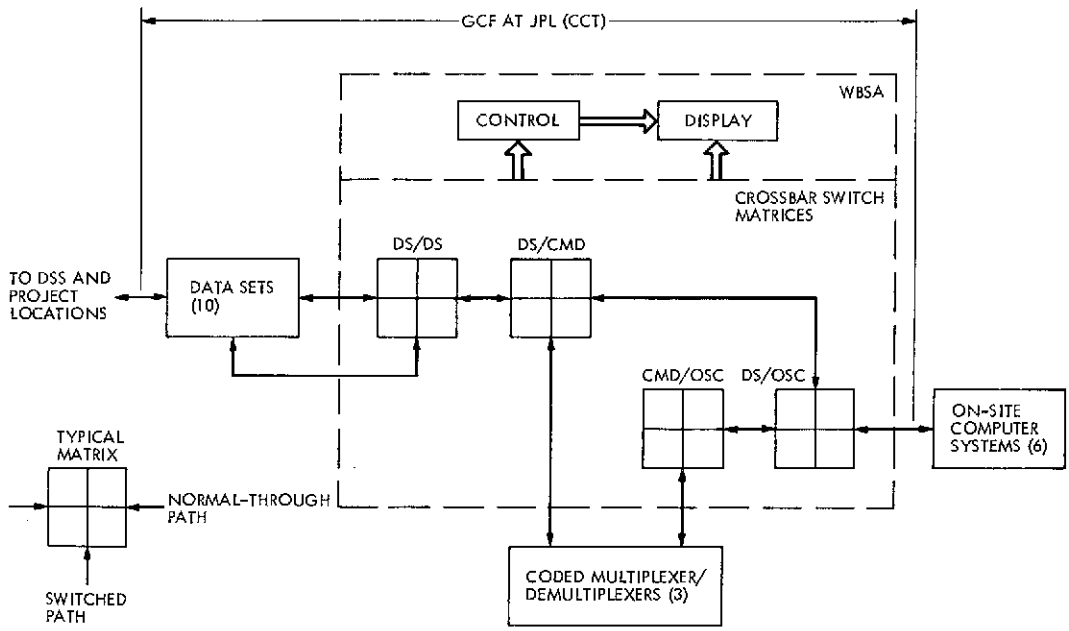

Fig. 1. GCF wideband switch subassembly

Integral Modulating Anode Resistor

R. H. Smith
R.F. Systems Development Section

The klystron in the Deep Space Network 400-kW transmitter subsystem uses a resistor to hold the modulating anode at ground potential. The resistor is connected to the klystron modulating anode through a high-voltage connector; in the past this resistor has been mounted in an air dielectric environment and has been subject to physical damage. If a cathode arc occurs, the arc forms between the cathode and modulating anode, the modulating anode potential is biased to the potential of the cathode by the arc current in the modulating anode resistor, and the arc is extinguished. The modulating anode resistor will have high-voltage (65 kV) across it during an arc.

This article describes a new method in which the resistor is mounted in an enclosed cap on the side of the klystron socket tank, eliminating the above problem.

I. Introduction

The 400-kW DSN transmitter klystron requires a resistive path to ground for the modulating anode. The modulating anode being at ground potential via the resistive path causes the electrons leaving the cathode to be accelerated toward the anode. The physical construction of the cathode (Fig. 1) causes the electrons to converge into a very narrow beam as they pass through the modulating anode ring. When an arc occurs in the cathode region, the electrons intercept the modulating anode. The voltage generated across the resistors is a function of the electron current which is a function of the energy in the electron beam at the time of intercept. As the modulating anode's potential approaches that of the cathode, the electron emissions from the cathode will stop, and the arc will be suppressed. The resistive path has been provided in the past by two resistors in series mounted on the wall of the transmitter cabinet (Fig. 2). The volume of space required for the resistor in free air is in excess of 57,365 cm^3 (3,500 $in.^3$). The resistors were connected to the klystron socket tank by a short section of high-voltage cable and a high-voltage connector in the side of the klystron socket tank.

Two major problems exist with this method: (1) the high-voltage connector has a history of leaking the insulating oil in the socket tank, and (2) the resistors are exposed to mechanical damage. The new integral modulating anode resistor is mounted in a simple casing that is mounted with a reliable O-ring seal to the side of

the socket tank where the high-voltage connector was mounted for the external resistors. The integral modulating anode resistor uses only 1,033 cm^3 (63 $in.^3$) of space, part of which was used by the high-voltage connector. The unit is immersed in the high-voltage insulating oil which also cools the resistor. There is no high voltage present—no personnel hazard; there is a more reliable oil seal, and a protective seal cover over the resistor.

II. Description

The integral modulating resistor (Fig. 3) consists of a single 33-kΩ, 200-W resistor. The resistor is attached at one end to an insulating phenolic disk with a stud extending to the outside of the housing. This stud is then grounded to a second stud attached to the housing with a short jumper. This jumper can be used to monitor the current in the modulating anode for sensing internal arcing. The resistor extends beyond the housing and is insulated from the housing via a ceramic disk that has several openings so that the insulating oil can flow freely in and out of the housing. A contact clip is on the end of the resistor to make contact with modulating anode contact ring of the klystron. The oil which surrounds the resistor is water cooled so that the resistor can dissipate a very large amount of energy (heat) compared to the same resistor in free air. The dielectric strength of the oil is six times higher than that of air so that smaller space can be used for the same potential.

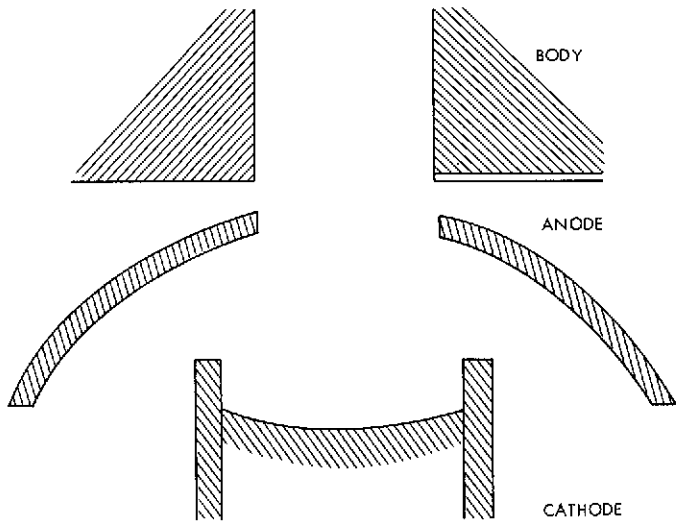

Fig. 1. Cathode-anode construction

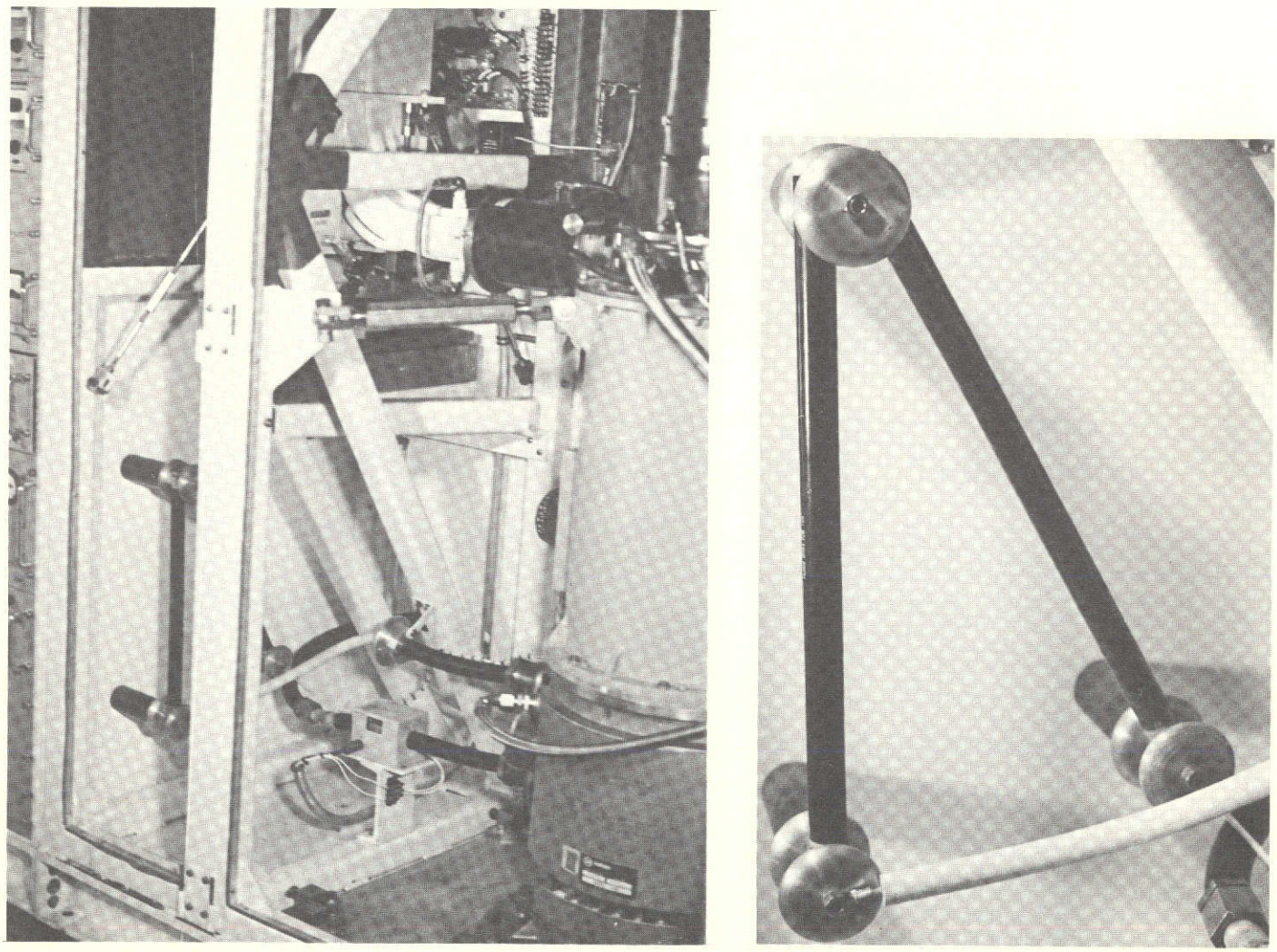

Fig. 2. Modulating anode resistor: (a) resistor mounted on wall (b) resistor and klystron connection

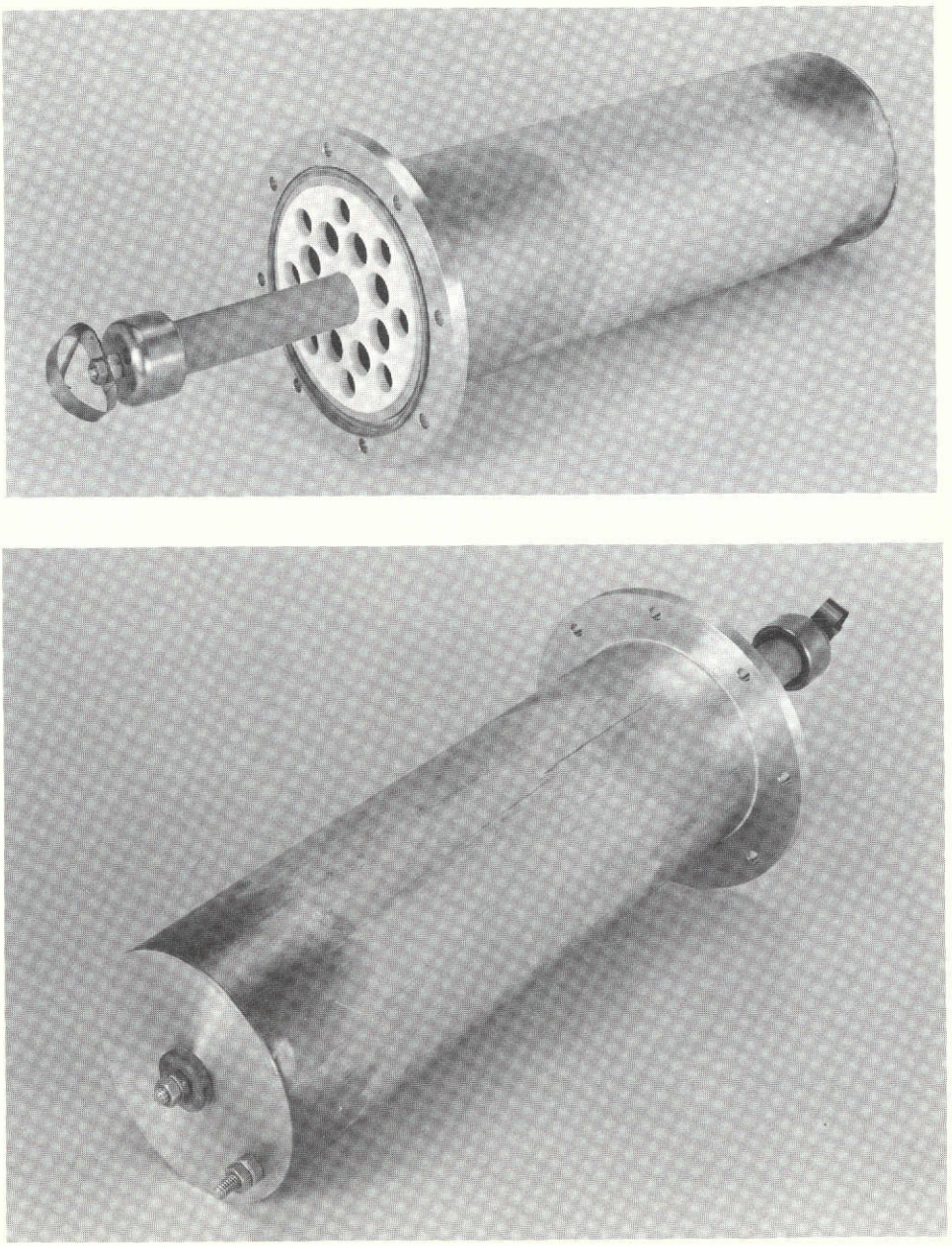

Fig. 3. Integral modulating anode resistor: (a) resistor end (b) grounding end

Sharing Range Capability at the Conjoint Stations

W. J. Blandford
R.F. Systems Development Section

Enhancement of 26-m subnet ranging coverage by sharing 64-m ranging capability has been proposed in order to improve tracking capability. An analysis of the error sources contributing to the ranging system accuracy indicates that high-frequency noise and range-modulation group-delay instability are of primary concern but that the overall result is that the range error is virtually unaffected by the additional cabling.

I. Introduction

Currently, three sets of planetary ranging equipment are available to be located at one of the 26-m stations as well as at the 64-m stations. Considering the Viking Operations Mission A recommended prime landing site (A-1), the requirements for tracking and commanding of the Mission A orbiter and lander and the approaching Mission B spacecraft during the critical period in which spacecraft B is 10–3 days from Mars orbit insertion can be met if the planetary ranging equipment is located at the Madrid 26-m station. If, for some reason, the Mission A prime site is unacceptable and landing occurs at the backup site (A-2), then it would be necessary to locate the planetary ranging equipment at the Goldstone 26-m station. Since changing the Mission A site from A-1 to A-2 is a real-time decision, there would not be time to move the planetary ranging equipment from the Madrid station to the Goldstone station; therefore, tracking and commanding requirements would not be met (Ref. 1).

One possible solution to this problem is that since the overseas 26-m stations are located conjointly with the 64-m stations, it may be possible to share the ranging capability of the 64-m stations with the 26-m stations. Then by locating one set of planetary ranging equipment at the Goldstone 26-m station, it would be possible to give planetary ranging capability to all three 26-m stations and provide full flexibility in mission planning. The purpose

of this report is to provide information on the feasibility of the proposed solution.

II. System Performance

Table 1, derived from Ref. 2, is a list of the system error sources contributing to the planetary ranging system accuracy for both the 64-m and 26-m stations at the conjoint sites. The effect of low input signal margin or signal-to-noise ratio is to introduce a variance (high-frequency noise) in the measured value of range, which is a function of the integration time. A system analysis (Ref. 3) has shown that the integration time required to achieve an acceptable variance σ_τ^2 is given by

$$t_i = \frac{T^2 No}{32\sigma_\tau^2 S}$$

where

T = period of the highest frequency component, 2×10^{-6} s

No = system noise spectral density

S = power in the ranging signal

Assuming that an uncertainty of ± 5 m would be acceptable, and employing the highest frequency component C_1, the equation simplifies to

$$t_i = 112.5 \frac{No}{S}$$

Figure 1, which is derived from data in Ref. 4, shows a plot of ranging signal performance margin vs time (GMT) for the Viking Orbiter with the S-Band discrete ranging system. Integration time for a 1σ instability of 5 m is shown along the right-hand margin.

The other ranging system error source in Table 1 affected by sharing range capability is instability in range modulation group delay. Figure 2 is a sketch of cabling affected by the change, with switching and dimensions indicated. The portion of the cabling that is delay sensitive is, for the 64-m station, an additional 15 m between the exciter and the planetary ranging assembly and, for the 26-m station, an additional 76 m between the exciter and the planetary ranging equipment. If polyethelene-insulated coaxial cable is used, there is a delay of 0.001 ns/100 m/10°C. The additional range error for group delay instability in Table 1 is 0.0045 m for the 64-m station and 0.0225 m for the 26-m station.

III. Results

The DSS planetary ranging system error is primarily dependent on the high-frequency noise. When switched from the 64-m station to the 26-m station, the planetary ranging system suffers a loss in signal-to-noise ratio but may be compensated to a certain extent by allowing a longer integration time.

The additional cabling affects primarily range-modulation group-delay instability. Some of the signals are compensated for by the fact that the reference for these signals also shifts by the same amount of range delay, the overall result being that the error is virtually unaffected by the additional cabling.

References

1. Boyer, W. J., NASA Letter 159 (PL-6267-THS), to D. J. Mudgway, Apr. 20, 1973.
2. Brockman, M. H., IOM 3300-73-70, Jet Propulsion Laboratory, Pasadena, Calif., Mar. 7, 1973 (JPL internal document).
3. Martin, W. L., "A Binary-Coded Sequential Acquisition Ranging System," in *The Deep Space Network*, JPL Space Programs Summary 37-57, Vol. II, Jet Propulsion Laboratory, Pasadena, Calif., May 31, 1969.
4. "Viking Orbiter System to Deep Space Network," ID-370311, Vol. II, Jet Propulsion Laboratory, Pasadena, Calif., Dec. 19, 1972 (JPL internal document).

Table 1. Planetary ranging performance

Ranging system accuracy due to error sources, 1σ	10^8-s round-trip light time			
	1973		1975	
	64-m	26-m	64-m	26-m
High frequency noise, m rms[a]	5.0	5.0	5.0	5.0
Instability in range modulation group delay, m/12 h	2.0	2.0	1.0[b]	2.0
Uncertainty in knowledge of frequency, m	1.5	1.5	1.5	1.5
Station calibration error, m	2.5	2.5	1.0[b]	2.5
Time of measurement error, m (35 km/s)	0.7	0.7	0.7	0.7
RSS total (m, 1σ)	7.0	7.0	6.0	7.0

[a]Can be reduced below 5 m rms by selection of integration time.
[b]Operation with Block IV receiver/exciter.

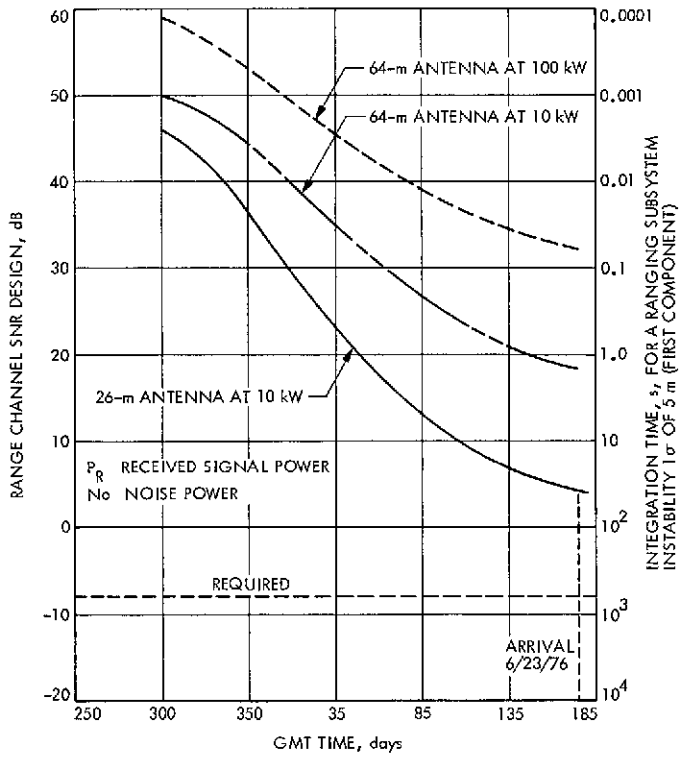

Fig. 1. Ranging P_R/No vs time for Viking Orbiter S-band ranging, discrete spectrum, command on, high-gain antenna, in cruise mode.

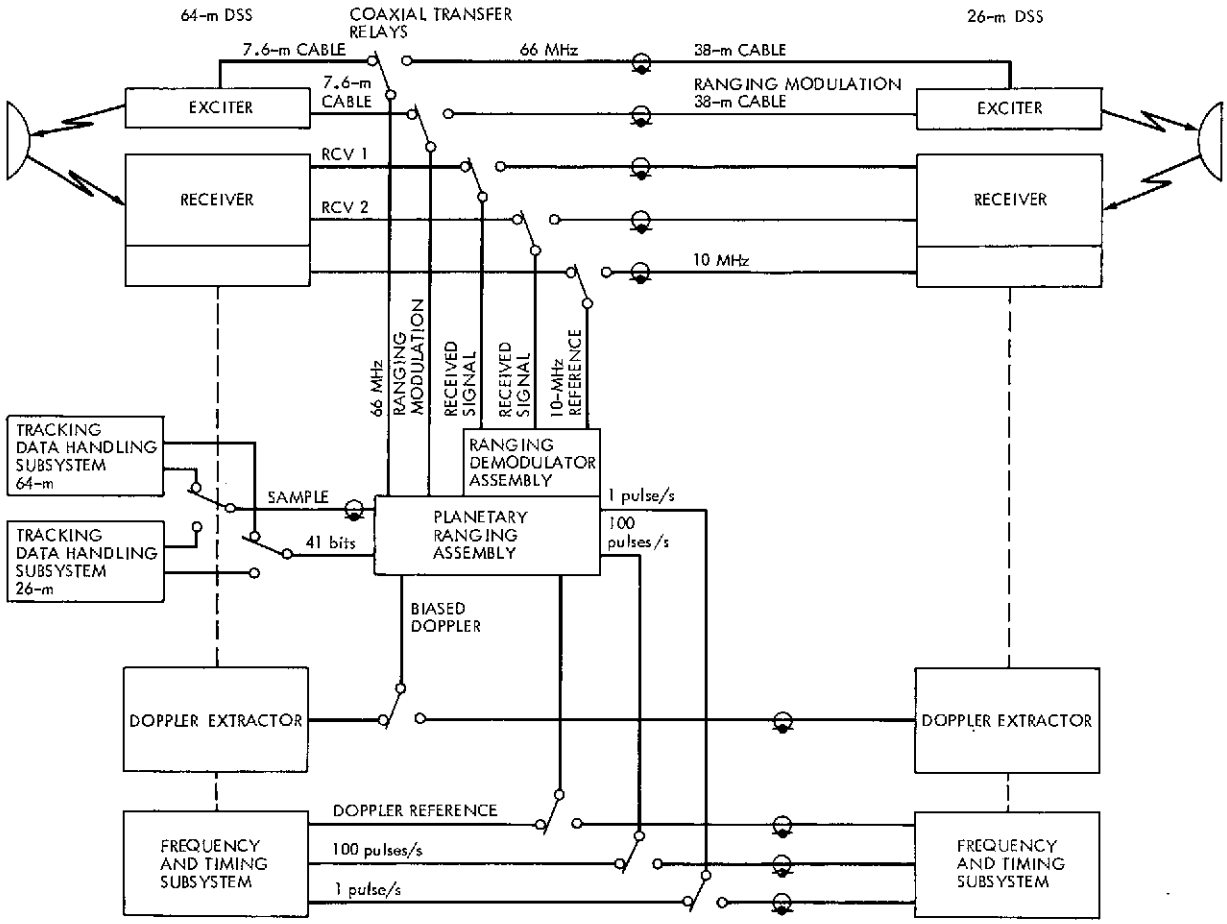

Fig. 2. Switching and cabling modifications required.

Block III Maser Implementation Program

D. L. Trowbridge
R.F. Systems Development Section

The implementation of the Block III Maser System into the 64-m and 26-m antenna Deep Space Stations has recently been completed. The Block III maser system has improved the reliability and microwave performance over that of the previous Block II maser system.

The Block III traveling wave maser amplifier has 45 ±1 dB gain at a center frequency of 2285 MHz, with an instantaneous 1-dB bandwidth of 30 MHz minimum. The higher gain and lower noise temperature of the Block III maser system have lowered the overall system temperature approximately 10 K.

I. Introduction

The implementation of the Block III maser system into the 64-m and 26-m antenna stations of the Deep Space Network (DSN) has recently been completed. Block III maser equipment has also been delivered to the Spaceflight Tracking and Data Network (STDN).

The Block I maser system originally installed in the DSN was designed to operate as described in Table 1, DSN mode. The equipment was later changed to the Block II configuration, which allowed remote tuning to either the DSN mode or the Manned Space Flight Network (MSFN) mode as described in Table 1[1]. The Block II maser system included two traveling wave maser amplifiers. Three stations in the DSN were implemented with Block II maser systems to support the Apollo program.

[1]The MSFN is now a part of the STDN.

Following the Block II maser implementation, the development of an improved closed cycle refrigeration (CCR) system and an S-band traveling wave maser amplifier with improved performance characteristics took place at JPL (Refs. 1 and 2). These developments provided the basis for a new maser system design featuring increased refrigeration system reliability and substantially improved microwave performance. This availability of improved performance and the desire to implement all DSN stations with dual maser amplifiers led to the Block III maser implementation program. This report covers the maser amplifier and associated assemblies portion of the implementation program.

II. Program Description

The objective of the Block III maser implementation program was to produce maser systems which met the performance characteristics listed in Table 1 in a field

operational environment and which provided interchangeability of major subassemblies and components to facilitate field maintenance. The program included the development, design, documentation, fabrication, and testing of 27 Block III maser amplifier assemblies, of which four were delivered to the STDN.

The initial effort in the program was to produce manufacturing documentation, fabrication drawings, and procedures, based on a detailed review of the maser development work previously mentioned (Ref. 2). Additional design work was required to produce an operational Block III maser assembly which would meet the program objectives with repeatability.

The fabrication and testing phases of the program were divided into two parts. Complete subassemblies and piece parts were procured to specified documentation from outside sources where possible. JPL's effort was used for only those areas, such as the following, where special techniques were involved:

(1) Isolator fabrication and testing.

(2) Maser slow-wave structure assembly and testing.

(3) Magnet assembly charging process.

(4) Maser and refrigerator integration with adjustment and alignment to meet performance characteristics specified.

(5) Final acceptance testing of the maser assembly in the final package configuration.

III. Maser Description

The Block III maser assembly is shown in Fig. 1 with the major subassemblies indicated. The majority of the subassemblies are similar in function to those used on the development maser (Ref. 2).

The input signal is coupled to the maser amplifier thru a 30-dB crossguide coupler, end-on waveguide transition and 22-mm coaxial line which extends through the refrigerator to the input of the maser amplifier. Input match tuning is provided at the waveguide transition for interface match adjustments between the maser amplifier, coaxial line and waveguide transition. The coaxial input line extends through the refrigerator and is cooled by a quarter wave thermal short (Ref. 3) to reduce its noise contribution.

The output signal is coupled through the refrigerator with a 22-mm coaxial line, similar to the input line, to a 12.7-GHz reject filter and is then connected to the coupler panel assembly with a semirigid cable. The 12.7-GHz filter provides a minimum of 80 dB rejection over the pump frequency range of 12.66 to 12.72 GHz and has a maximum of 0.2 dB loss at the signal frequency.

The klystron assembly provides approximately 100 mW power in a pump frequency range of 12.66 to 12.72 GHz. A variable attenuator for setting the proper pump saturation level is used. The noise calibration and coupler panel assemblies provide noise injection and the necessary switching for gain calibration of the maser assembly. The magnet assembly is mounted in the lower portion of the frame and provides the maser slow-wave structure with a uniform field strength of approximately 2500 gauss. A field-aiding trim coil, mounted on each pole piece, provides the required field strength adjustment.

Proper ruby c-axis alignment with respect to the magnet assembly involved the accumulated tolerances of many interfaces. The interface surfaces between the maser slow-wave structure, refrigerator, frame, and magnet assembly were designed to maintain the magnetic field perpendicular to the c-axis of the ruby, in the slow-wave structure, within ± 0.5 deg. It has been found at S-band frequencies that a c-axis misalignment of 1.0 deg to the magnet field causes a gain degradation of 5 dB in the Block III masers.

The maser slow-wave structure containing the ruby bars and isolators is shown in Fig. 2. The ruby bars and ruby isolator mounting strips were procured from Union Carbide with the c-axis alignment specified to be accurate within ± 0.25 deg. The typical ruby bar c-axis alignment was accurate within ± 0.1 deg. The isolators were fabricated at JPL and improvements in the fabricating, sorting, and assembling techniques produced reverse-to-forward loss ratios in excess of 200 to 1. The isolators are capable of ± 2 deg rotation in the magnet field without detectable performance degradation.

Magnetic field shape adjustment is required to set the gain and bandwidth of the maser to the proper values. Field spreading adjustment to achieve the required bandwidth is accomplished with two coils connected in a figure-eight manner with one aiding and one bucking the main magnetic field. Initial field spreading is achieved with a soft iron shim mounted under the aiding coil. The maser is adjusted for proper gain with a second iron shim which is mounted on the maser cover.

IV. Maser Performance

The gain vs frequency response of a typical Block III maser assembly is shown in Fig. 3. The gain was adjusted to the specified 45 dB at the peaks, and the bandwidth easily met the required 30 MHz at the 1-dB points. During preshipment acceptance tests, when the response curve was drawn, the magnet current, field spreading current, vapor pressure gauge reading, and klystron frequency were recorded on the graph. By comparing these values with those obtained after installation, the slightest performance variation can be detected. The Block III maser performance at the DSN stations was found to be in close agreement with preshipment test data.

The noise temperature was measured prior to shipment, using an ambient termination and calibrated nitrogen-cooled waveguide termination, at 2270 MHz, 2285 MHz, and 2300 MHz. The noise temperature distribution as a function of frequency and maser assembly quantity is shown in Fig. 4.

Figure 5 is a bar graph which shows the reported system temperatures for both masers (dual installation) at the 26-m antenna Deep Space Stations indicated. The results indicate an approximate 10 K lower noise temperature than the previous Block I maser systems. Two of the 64-m antenna Deep Space Stations have reported the following system noise temperatures:

Station	43	63
Maser 1	22 K	26 K
Maser 2	26 K	30 K

The DSN stations have reported a typical gain stability of ± 0.02 dB for durations of 10 s and ± 0.3 dB for durations of 12 h.

V. Conclusion

Performance results indicate that the Block III maser assemblies have met the performance requirements with considerable margin. The Block III masers have reduced the overall system equivalent noise temperature by 10 K and provided bandwidths exceeding that required. The previously mentioned objectives of the program have been achieved. Major subassemblies are interchangeable, and additional units can be procured to meet released documentation.

Acknowledgment

The success of the Block III maser implementation program was due to the combined efforts of many people at the Jet Propulsion Laboratory. Thanks are especially due to the members of the Microwave Electronics Group, R. Clauss, E. Wiebe, R. Quinn, and D. Hofhine, under the direction of Dr. W. Higa.

References

1. Higa, W. H., and Wiebe, E., "A Simplified Approach to Heat Exchange Construction for Cryogenic Refrigerators," *Cryogenic Technology*, Mar./Apr. 1967.
2. Clauss, R., "Low Noise Receivers: Microwave Maser Development, Second Generation Masers," *The Deep Space Network*, Space Summary 37-47, Vol. II, pp. 71–73, Jet Propulsion Laboratory, Pasadena, Calif., Sept. 30, 1967.
3. Clauss, R., *A Traveling Wave Maser for Deep Space Communication at 2295 and 2388 MHz*, Technical Report 32-1072, Jet Propulsion Laboratory, Pasadena, Calif., Feb. 15, 1967.

Table 1. Maser assembly functional characteristics

Characteristic	Required performance		
	Block I/II maser		Block III maser
	DSN mode	MSFN mode	
Center frequency, MHz	2295	2280	2285
Minimum bandwidth (1 dB), MHz	10	20	30
Minimum bandwidth (3 dB), MHz	15	24	40
Gain, dB	35 ±1	27 ±1	45 ±1
Gain stability			
Short term	±0.05 dB/10 s	±0.05 dB/10 s	±0.05 dB/10 s
Long term	±0.5 dB/12 h	±0.5 dB/12 h	±0.5 dB/12 h
Maximum voltage standing wave ratio			
Input	1.3	1.3	1.3
Output	1.5	1.5	1.5
Effective input			
Maximum noise temperature, K	12	14	8

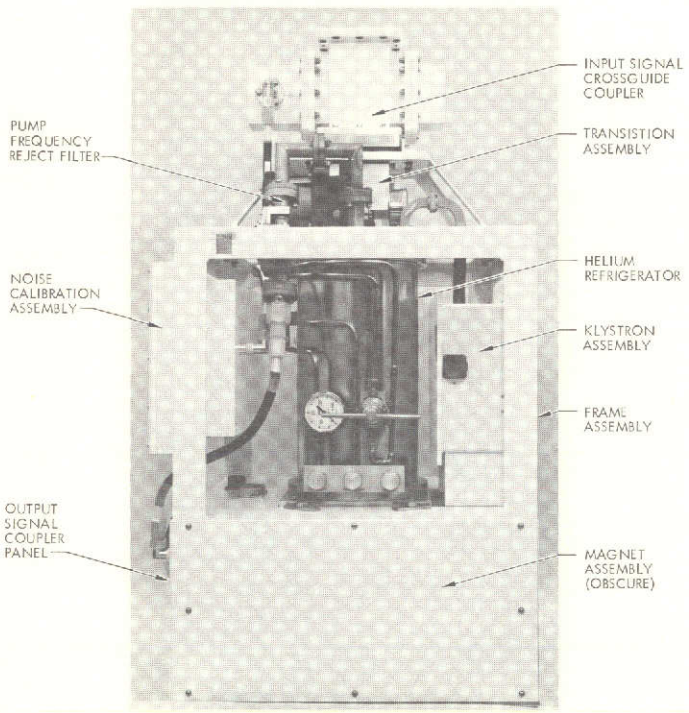

Fig. 1. Block III maser assembly

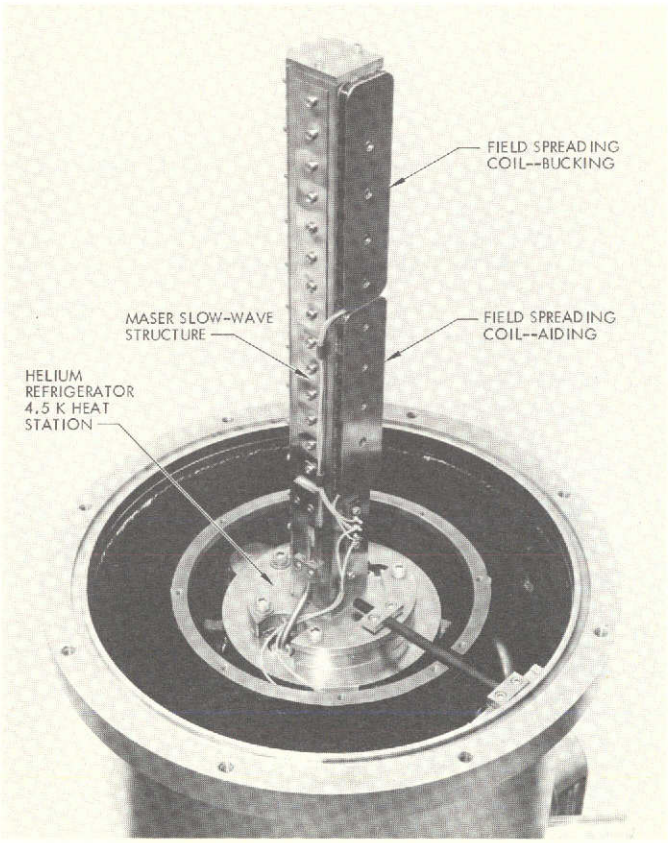

Fig. 2. Maser amplifier mounted on helium refrigerator

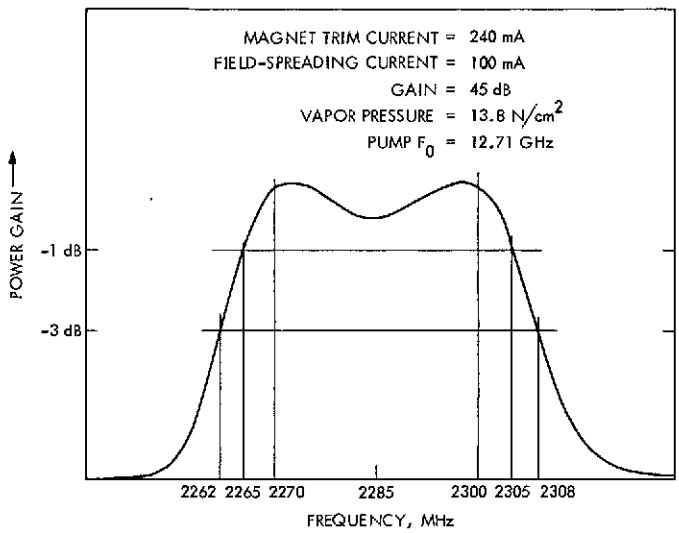

Fig. 3. Block III maser response (TWM Serial No. 018)

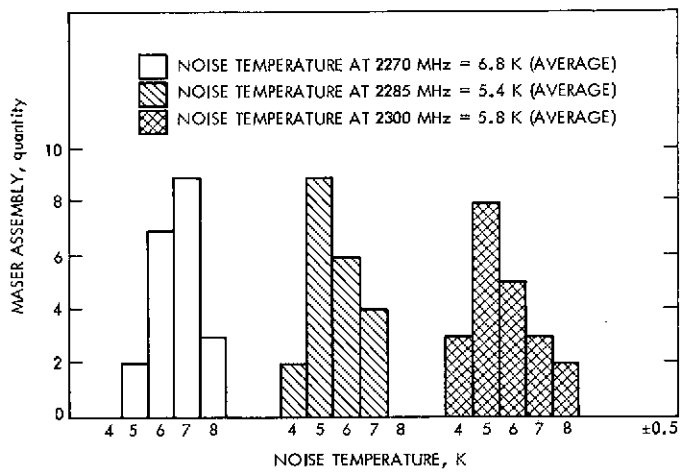

Fig. 4. Noise temperature distribution vs quantity

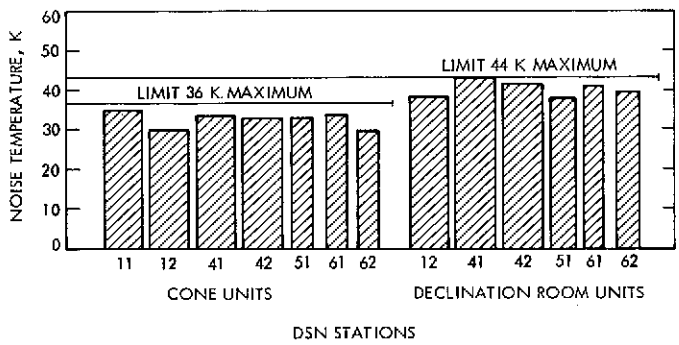

Fig. 5. System equivalent input noise temperatures

Signal Suppression in Bandpass Limiters

D. W. Brown
R.F. Systems Development Section

The results of numerous studies and applications of hard and soft limiters are compared. A unifying approach is taken, with the result that the applications considered differ only in regard to the relative level of the input signal.

I. Introduction

At least three different bandpass limiter types or applications are treated in the literature. Most familiar is the hard limiter (Refs. 1–4). Other analyses consider the general case of soft limiters by assuming an error function (erf) transfer characteristic (Refs. 5 and 6). And finally, a special application of the soft limiter appears in the DSN telemetry subcarrier demodulation equipment (Refs.7–10).

The results obtained differ rather markedly in form and perhaps more subtly in application. Is there a unity to these analyses? What differences in application underlie them? It is the purpose of this article to try to answer these questions insofar as they apply to signal suppression.

Signal suppression α is a commonly used factor in expressing the effective signal gain, as a function of input signal-to-noise ratio (SNR), for a bandpass limiter element in a communications system. More rigorous definitions will follow as required.

II. Limiter Types

The hard limiter, in which the input is usually taken as constant in amplitude, and is always in limiting, regardless of input SNR, is commonly characterized by the approximation (Refs. 1 and 2)

$$\alpha_{hl}^2 \approx \frac{1}{1 + \frac{4}{\pi}\frac{1}{\mathrm{SNR}}} \tag{1}$$

An approximate form, which will be shown to be equivalent to Eq. (19) of Ref. 5, for the general soft limiter follows:

$$\alpha_s^2 \approx \frac{1}{1 + \frac{4}{\pi}\frac{1}{(1+\nu^2)\,\mathrm{SNR}}} \tag{2}$$

where $\nu^2 = \ell^2/S_i G^2$, ℓ^2 is defined as the output power of the signal (only) saturated bandpass limiter, S_i the input signal power, and G^2 the small signal power gain. Comparing with Eq. (1), we see that Eq. (2) immediately reduces to the hard limiter case for $\nu^2 \to 0$. In discussions that follow, it will be useful to recognize the ratio ℓ^2/G^2 as the effective input limit level.

The special application referred to in the introduction utilizes the bandpass limiter *following* the loop phase detector, and since it operates at an intermediate frequency,

the limiter is in turn followed by a coherent detector. The interesting result of this mechanization is that the signal input to the bandpass limiter carries the loop phase error information as amplitude. Because the phase-locked loop in this application is designed for low tracking errors, the models (with the notable exception of Ref. 9) inherently assume that the input signal is much less than the input limit level.

One such application (Ref. 7) uses the form

$$\alpha_{il}^2 \approx \frac{1}{1 + \frac{4}{\pi}\frac{1}{\nu^2 \mathrm{SNR}}} \tag{3}$$

with definitions as above, except that S_i and SNR now both refer to the full or virtual error signal, while assuming as above that the actual signal is negligibly small. Equation (3) was originally developed empirically by applying an effective input ν^2SNR to the approximate hard limiter form. However, Ref. 7 does apply a correcting function developed by Springett (Ref. 4) to account for the effective change in output SNR vs. input SNR in hard limiters.

Before proceeding to consideration of the exact forms, it may be of interest to note that one could speculate on a general form:

$$\alpha^2 \approx \frac{1}{1 + \frac{4}{\pi}\frac{1}{(\gamma^2 + \nu^2)\,\mathrm{SNR}}} \tag{4}$$

where γ^2 relates actual input signal power to virtual signal. When γ^2 is unity, (4) becomes (2), which, as noted above, includes (1) as a special case. And when $\gamma^2 \to 0$ (negligible input signal), (4) approaches (3). We will return later to these forms as special cases of Lesh's result (Ref. 6).

III. A General Model

Equation (29) of Ref. 6 may be rewritten to express the output signal power as[1]

$$S_o = A^2G^2\frac{D}{1+D}\exp\left[-\frac{A^2}{N_oB\,(1+D)}\right] \times \left\{I_0\left[\frac{A^2}{2N_oB\,(1+D)}\right] + I_1\left[\frac{A^2}{2N_oB\,(1+D)}\right]\right\}^2$$

where

A_2 = actual input signal power

N_oB = input noise power

$D = \dfrac{2L^2}{\pi G^2 N_oB}$, a measure of noise limiting

$L^2 = \dfrac{\pi^2}{8}\ell^2$ = limiter saturation level

and I_0, I_1 are modified Bessel functions.

If we now further define γ^2 as the fractional input signal, identically equal to $A^2/S_i = A^2/\mathrm{SNR}N_oB$, then we have

$$S_o = A^2G^2\frac{D}{1+D}\exp\left(-\frac{\gamma^2\mathrm{SNR}}{1+D}\right) \times \left\{I_0\left[\frac{\gamma^2\mathrm{SNR}}{2\,(1+D)}\right] + I_1\left[\frac{\gamma^2\mathrm{SNR}}{2\,(1+D)}\right]\right\}^2 \tag{5}$$

where $D = (\pi/4)\,\nu^2\mathrm{SNR}$.

The notation in use here is somewhat redundant and has evolved from several of the references. Interchangeable forms are applied from time to time and are summarized in the Appendix.

IV. The Hard Limiter

For the ideal hard limiter, $G^2 \to \infty$, $\nu^2 \to 0$, and $D << 1$. And with $\gamma^2 = 1$, Eq. (5) becomes

$$S_o\Big|_{\substack{\text{HARD}\\ \text{LIMITER}}} = A^2G^2D\exp(-\mathrm{SNR}) \times \left\{I_0\left[\frac{\mathrm{SNR}}{2}\right] + I_1\left[\frac{\mathrm{SNR}}{2}\right]\right\}^2$$

$$\alpha_{hl}^2 = \frac{S_o}{\ell^2} = \frac{\pi}{4}\,\mathrm{SNR}\exp(-\mathrm{SNR})\left\{I_0\left[\frac{\mathrm{SNR}}{2}\right] + I_1\left[\frac{\mathrm{SNR}}{2}\right]\right\}^2$$

the exact form for the hard limiter (Ref. 3). Or, if we let

$$\exp(-\mathrm{SNR})\left\{I_0\left[\frac{\mathrm{SNR}}{2}\right] + I_1\left[\frac{\mathrm{SNR}}{2}\right]\right\}^2 \approx \frac{2/\pi}{2/\pi + \mathrm{SNR}/2} \tag{6}$$

[1]Setting to unity the $\cos\theta$ factor which applies to the coherent detection following the limiter.

Eq. (1), the approximate form, follows immediately. This approximation is asymptotically correct for large and small SNR; it is in error by a few percent when SNR is near unity.

V. The Soft Limiter—Special Application

Before continuing to the general limiter of Eqs. (2) and (4)[2], consider the exact form of Eq. (5) as applied to the $\gamma^2 \to 0$ (i.e., small signal) case:

$$S_o = A^2G^2 \frac{D}{1+D} = \gamma^2 \frac{\ell^2}{\nu^2} \frac{D}{1+D}$$

since the exponential/Bessel product approaches unity for small argument.

And if we define suppression,

$$\alpha_{sl}^2 = \frac{S_o}{\gamma^2 S_i G^2} = \frac{\text{output signal power}}{\text{fractional input signal} \times \text{unlimited virtual output signal}} \tag{7}$$

$$\alpha_{sl}^2 = \frac{D}{1+D} = \frac{1}{1+\frac{4}{\pi}\frac{1}{\nu^2 \text{SNR}}} \qquad \text{(see footnote 3)}$$

Or, if one prefers the definition of suppression to be the ratio of signal output powers with and without noise[4],

$$\alpha_{sl}^2 = \frac{\gamma^2 \ell^2 D}{\nu^2 (1+D)} \Big/ \frac{\gamma^2 \ell^2}{\nu^2} = \frac{1}{1+\frac{4}{\pi}\frac{1}{\nu^2 \text{SNR}}}$$

In any case, it is at first surprising that Eq. (3), derived as it was from the approximate hard limiter form, should turn out to be exact. A little reflection on Eqs. (5) and (6) shows, however, that no approximation is involved in the limit of $\gamma^2 << \nu^2$. In other words, Eq. (3) is correct as it stands (for the small signal case), and it is inappropriate in this application to include Springett's $(\text{SNR})_o/(\text{SNR})_i$ correction as noted above.

For this subcarrier application, Refs. 8 and 10 develop and apply a somewhat different model, with results which can differ from the above, depending upon definitions of input signals. However, the results obtained here are in agreement with Ref. (9), given the small signal assumption.

VI. The Soft Limiter—General Case

Consider now Eq. (5) and apply the approximation (6), but let γ^2 and ν^2 retain generality:

$$S_o \approx \frac{\gamma^2}{\nu^2} \ell^2 \frac{1}{1+\frac{\gamma^2}{\nu^2}+\frac{4}{\pi}\frac{1}{\nu^2 \text{SNR}}} \tag{8}$$

Defining $\alpha^2 = S_o/\ell^2$,

$$\alpha^2 \approx \frac{\gamma^2}{\gamma^2+\nu^2} \frac{1}{1+\frac{4}{\pi}\frac{1}{(\gamma^2+\nu^2)\,\text{SNR}}} \tag{9}$$

Taking into account the necessary normalization of definitions and level $\gamma^2/(\nu^2+\gamma^2)$, we see that the hypothesis of Eq. (4) has been borne out and is applicable to all cases, with small sacrifice of accuracy only when the actual signal-to-noise ratio is near unity *and* the actual input signal is not small compared to the input limit level. One other case in minor error, but seldom if ever occurring in practice, is that of high signal-to-noise ratio *and* actual input signal near the input limit level.

Applying this result to the full signal case $\gamma^2 = 1$,

$$\alpha^2 \approx \frac{1}{1+\nu^2} \frac{1}{1+\frac{4}{\pi}\frac{1}{(1+\nu^2)\,\text{SNR}}} \tag{10}$$

we see the form of Eq. (2) as well as the P_s/L^2 result (approximately) of Fig. 5 of Ref. 5. Applying Tausworthe's definition of α_s as the ratio of signal output powers with and without noise,

$$\alpha_s^2 \approx \frac{1}{1+\frac{4}{\pi}\frac{1}{(1+\nu^2)\,\text{SNR}}}$$

[2]Equations (2) and (4) can be seen to be redundant given a $\gamma^2\text{SNR} \to \text{SNR}$ transformation.

[3]In the subcarrier application, it is convenient to write

$$K_d = \frac{\text{limiter output}}{\text{phase error}} = \frac{2}{\pi}\frac{\ell}{\nu}\alpha'\alpha_{sl} \text{ V/rad}$$

where $\alpha' = (\pi/2)\,(\gamma/\text{Phase error})$ for this mechanization (Ref. 8).

[4]This definition can be misleading if neither γ^2 or ν^2 is small.

and rearranging,

$$\alpha_s^2 \approx \frac{1}{1+\frac{4}{\pi}\left(\frac{1+\frac{\pi}{4}\nu^2\mathrm{SNR}}{\mathrm{SNR}}\right)} \Bigg/ \frac{1}{1+\nu^2}$$

and noting from Eq. (1) that

$$\alpha_{hl}^2(x) \approx \frac{1}{1+\frac{4}{\pi}\left(\frac{1}{x}\right)}$$

it follows that

$$\alpha_s^2 \approx \frac{\alpha_{hl}^2\left(\frac{\mathrm{SNR}}{1+\frac{\pi}{4}\nu^2\mathrm{SNR}}\right)}{\alpha_{hl}^2\left(\frac{4}{\pi\nu^2}\right)}$$

It is readily apparent that this is Tausworthe's Eq. (19), where $\rho = \mathrm{SNR}$, since

$$\frac{\pi}{4}\nu^2 = \frac{\pi}{4}\left(\frac{8}{\pi^2}L^2\right)\frac{\gamma^2}{A^2G^2} = \frac{4}{\pi}\frac{L^2}{V^2K^2}$$

given that $V = \sqrt{2}A$, $K = G$, and $L^2 = (\pi^2/8)\,\ell^2$ and, of course, $\gamma^2 = 1$.

VII. Conclusion

It appears that there is a unity to the several treatments of hard and soft limiters, provided careful definitions are made. The significant difference in the various cases lies only in the amplitude of the input signal relative to the effective input limit level, expressed here as the γ^2/ν^2 ratio.

References

1. Rechtin, E., *Design of Phase-Lock Oscillator Circuits*, Section Report No. 8-566, Feb. 7, 1957 (JPL internal document).
2. Viterbi, A. J., *Principles of Coherent Communication*, McGraw-Hill Book Co., New York, 1966.
3. Lindsey, W. C., *Performance of Phase-Coherent Receivers Preceded by Bandpass Limiters*, Technical Report 32-1162, Jet Propulsion Laboratory, Pasadena, Calif., Sept. 15, 1967.
4. Springett, J. C., *Signal-to-Noise and Signal-to-Noise Spectral Density Ratios at the Output of a Filter-Limiter Combination*, TS 3341-65-2, July 15, 1965 (JPL internal document).
5. Tausworthe, R. C., "Analysis of Narrow-Band Signals Through the Band-Pass Soft Limiter," in *Supporting Research and Advanced Development*, Space Programs Summary 37-53, Vol. III, Jet Propulsion Laboratory, Pasadena, Calif., Dec., 1968.
6. Lesh, J. R., *Signal-to-Noise Ratios in Coherent Soft Limiters*, Technical Report 32-1589, Jet Propulsion Laboratory, Pasadena, Calif., Sept. 15, 1973.
7. Specification DM 505940, May 1971 (JPL internal document).
8. Brockman, M. H., "MMTS: Performance of the Subcarrier Demodulator," in *The Deep Space Network*, Space Programs Summary 37-52, Vol. II, Jet Propulsion Laboratory, Pasadena, Calif., July 1968.
9. Lesh, J. R., "A Re-Examination of Subcarrier Demodulator Performance," in *The Deep Space Network*, Technical Report 32-1526, Vol. XVII, Jet Propulsion Laboratory, Pasadena, Calif., Oct. 15, 1973.
10. Crow, R. B., "Block IV Subcarrier Demodulator Assembly Design," in *The Deep Space Network*, Technical Report 32-1526, Vol. XVI, Jet Propulsion Laboratory, Pasadena, Calif., Aug. 15, 1973.

Appendix

$$\mathrm{SNR} = \frac{S_i}{N_o B} = \text{virtual input signal-to-noise ratio}$$

$$\ell^2 = \frac{8}{\pi^2} L^2 = \text{maximum output signal power}$$

$$\nu^2 = \frac{\ell^2}{S_i G^2} = \frac{4}{\pi} \frac{D}{\mathrm{SNR}} = \frac{\text{input limit level}}{\text{virtual input signal}}$$

$$\nu^2 \mathrm{SNR} = \frac{\ell^2}{G^2 N_o B} = \frac{\text{input limit level}}{\text{input noise level}}$$

$$\gamma^2 = \frac{A^2}{S_i} = \frac{A^2}{\mathrm{SNR}\, N_o B} = \frac{\text{actual input signal}}{\text{virtual input signal}}$$

$$\gamma^2 \mathrm{SNR} = \frac{A^2}{N_o B} = \text{actual input signal-to-noise ratio}$$

$$\frac{\nu^2}{\gamma^2} = \frac{\ell^2}{A^2 G^2} = \frac{\text{input limit level}}{\text{actual input signal}}$$

α = signal suppression factor, general case
$0 < \gamma^2 \leqq 1, \nu^2 \geqq 0$

α_{hl} = signal suppression factor, hard limiter
$\gamma^2 = 1, \nu^2 \to 0$

α_{sl} = signal suppression factor, special case
$\gamma^2 \to 0, \nu^2 \geqq 0$

α_s = signal suppression factor, special case
$\gamma^2 = 1, \nu^2 \geqq 0$

Design of the 10-MHz IF Amplifier for the Block IV Subcarrier Demodulator Assembly

P. F. Kuhnle
R.F. Systems Development Section

The design effort was started in September 1971 to design and build the Block IV subcarrier demodulator assembly (SDA). The design goals were (1) remote control of the adjustable parameters (gain and bandwidth) to allow automatic calibration and control; (2) increased package density to reduce cabinet space over the Block III SDA and improve performance at high symbol rates; and (3) improved linear dynamic range and extended symbol rate range. This article will review the basic design and current status.

I. Introduction

The Block IV subcarrier demodulator assembly is scheduled for implementation into the DSN during the first quarter of FY'75.

The following design criteria for the 10-MHz intermediate frequency (IF) amplifier assemblies will be reviewed in this article:

(1) Required design specifications

(2) Block diagram of the 10-MHz intermediate frequency (and video) amplifier assemblies

(3) Signal and noise profile

(4) Hardware improvements over Block III SDA

(5) Current status

For a basic overall Block IV SDA design background, see Ref. 1.

II. Design Specifications

The specifications applicable to determine the IF amplifier design are shown in Table 1. These were based on a review of future missions and on previous development work on the Block III SDA.

III. Block Diagram

The block diagram of the data channel is shown in Fig. 1. This discussion will be limited to the 10-MHz channel located in the quadrature generator assembly, the selectable bandwidth filter assembly, and the 10-MHz section of the coherent amplitude detector assembly. These assemblies are standard Block IV radio frequency (RF) modules, interchangeable without operator adjustment to that module.

Controls are divided into three categories: (1) factory alignment, (2) SDA calibration, and (3) internal pro-

grammable gain and bandwidth switching. All factory alignment controls are entirely contained within the assembly and are not available to operating personnel.

The programmable calibration controls consist of two continuously adjustable analog-controlled attenuators. The quadrature channel gain balance is used to correct the gain error between the data and quadrature channels. The receiver (RCV) 1 or 2 gain control is used to correct the overall gain error between the receiver and SDA.

The gain and bandwidth switching is controlled digitally in several discrete ranges, depending on the desired symbol rate. The gain switching before and after the quadrature generator phase switch is designed in several steps, with the resultant overall gain for all steps being constant. Gain switching was required to reduce the subcarrier leakage through the phase switch. This leakage is caused by imperfections in the mixer which allow the subcarrier frequency harmonics to pass through the IF amplifier as an added signal to the expected products. The leakage becomes increasingly pronounced in the wider bandwidths at high symbol rates because the channel cannot discriminate against the unwanted subcarrier and yet pass the desired data stream.

To reduce this leakage, the gain for each gain/bandwidth step, before the subcarrier phase switch, was increased to the maximum permissible that would still maintain the design point signal-to-noise linearity. The gain, after subcarrier demodulation, is programmed to maintain constant overall IF amplifier gain.

Post-subcarrier demodulation bandwidth switching was utilized to retain the design point signal-to-noise ratio linearity of the RF amplifiers, double-balanced mixers, and video amplifiers.

It is necessary to maintain a constant 10-MHz phase shift for all the multiple gain/bandwidth steps. Phase shift due to gain switching with solid state attenuators was not a problem. Bandwidth switching required the insertion of the several bandpass filters into the amplifier. It was not economical to procure filters with the identical phase shift for all multiple steps. To correct these phase errors in the signal path, a preset factory adjustable phase shifter was inserted in the 10-MHz reference path. This was accomplished by designing a continuously adjustable, voltage-variable phase shifter programmed for the required phase shift to compensate the phase errors in the signal path. The phase shifter is located in the selectable bandwidth filter assembly, along with the multiple bandwidth filters, to preserve the module interchangeability concept.

IV. Signal and Noise Profile

The signal-to-noise power ratio, in the particular IF bandwidth, vs. symbol rate for the after subcarrier demodulation is shown in Fig. 2.

Six programmable filter bandwidths were chosen to cover the symbol rate range from 8.33 to 500K symbols per second (SPS). A margin of 7 dB minimum has been allowed between the RMS noise power and the IF amplifier 1-dB gain compression level. Gain switching is coincident with the switching of the six filter bandwidths. Two continuously variable 0- to 20-dB RF attenuators are located ahead of the subcarrier demodulator phase switch. It is necessary to maintain the maximum design point signal plus noise power into the quadrature generator to reduce the subcarrier leakage into the IF amplifier. Two additional continuously variable 0- to 20-dB RF attenuators are located after the subcarrier demodulator phase switch. These act as complementary attenuators to maintain constant gain for the complete IF amplifier channel. The signal and noise levels (referred to in Fig. 1) for the six gain/bandwidths are presented in Table 2. The noise levels shown are at the design point for the minimum symbol rate in each bandwidth.

V. Hardware Improvements

Hardware improvements in the IF amplifier (compared to the Block III SDA) include the use of wideband integrated-circuit amplifiers, solid-state RF attenuators, high-level double-balanced mixers, and greater-density packaging concepts.

The wideband RF amplifier series selection was based on (1) gain and phase-shift characteristics at 10 MHz, (2) the fact that various model amplifiers in the series could be cascaded to increase the dynamic range upper limit, and (3) the use of the same amplifier package on all applications to allow efficient design.

Solid-state RF attenuators were used in place of mechanically switched attenuators. Each attenuator is continuously adjustable and set during factory alignment with a series of potentiometers multiplexed for each programmable gain step.

The double-balanced mixers have a 10-dB greater dynamic range and lower intermodulation distortion than

units available several years ago. Each of the three module types is packaged in one of the new DSN RF modules. This high-density packaging reduces the space required to contain the same generic hardware used in the Block III SDA, thus decreasing the delay time between circuits and permitting the use of higher symbol rates.

VI. Current Status

The engineering models for the modules shown in Fig. 1 have been assembled. Initial in-process tests have indicated that the specifications in Table 1 will be met. A future report will cover the final results.

Reference

1. Crow, R. B., "Block IV Subcarrier Demodulator Assembly Design," in *The Deep Space Network*, Technical Report 32-1526, Vol. XVI, Jet Propulsion Laboratory, Pasadena, Calif., Aug. 15, 1973.

Table 1. Design specifications for Block IV SDA

Parameter	Specification[a]
Symbol rate	8.33 to 500K SPS
Subcarrier frequency range	100 Hz to 1 MHz
IF center frequency	10 MHz
Input bandwidth (prior to subcarrier demodulation)	7 MHz min. at −1 dB 11 ±1 MHz at −3 dB
Data bandwidth (after subcarrier demodulation)	Multiple, to be determined by (1) symbol rate (2) S/N_0 at design point to preserve amplifier linearity
IF system linearity (i.e., allowance made for a 7-dB noise crest factor between RMS noise power and 1-dB signal gain compression)	$\frac{ST_{sy}}{N_0} = -1$ dB $(8.33 < R_{sy} < 220$ SPS) $\frac{ST_{sy}}{N_0} = -4$ dB $(220 < R_{sy} < 500$K SPS)
Gain stability at 10 MHz	Δ1 dB max. per 12 h and/or Δ5°C
Phase stability at 10 MHz	Δ5 deg max. per 12 h and/or Δ5°C
Input/output impedance	50-Ω nominal
Input signal level	−70 ±3 dBm
Baseband output level	Signal = ±140 mV, noise = ±5 V peak

[a]S = signal power; N_0 = noise density; T_{sy} = time period for 1 symbol; R_{sy} = symbol rate.

Table 2. Signal and noise profile

		Point 1 on Fig. 1		Point 2 on Fig. 1			Point 3 on Fig. 1		
Gain/bandwidth switch position	Symbol rate range, SPS	Signal	Noise	Signal	Noise[a]	Phase switch 1-dB gain compression	Signal	Noise[b]	Coherent amplitude detector 1-dB gain compression
1	8.33–100	−70	−7	−59	+4	+13	−17	+6	+13
2	100–1000	−70	−18	−58	+4	+13	−17	+5	+13
3	1000–4800	−70	−25	−41	+4	+13	−17	+5	+13
4	4800–22K	−70	−32	−34	+4	+13	−17	+4	+13
5	22K–100K	−70	−38	−28	+4	+13	−17	+5	+13
6	100K–500K	−70	−45	−23	+2	+13	−17	+5	+13

[a]Maximum noise bandwidth = 12 MHz.
[b]Noise power in the bandwidth associated with that symbol rate range.

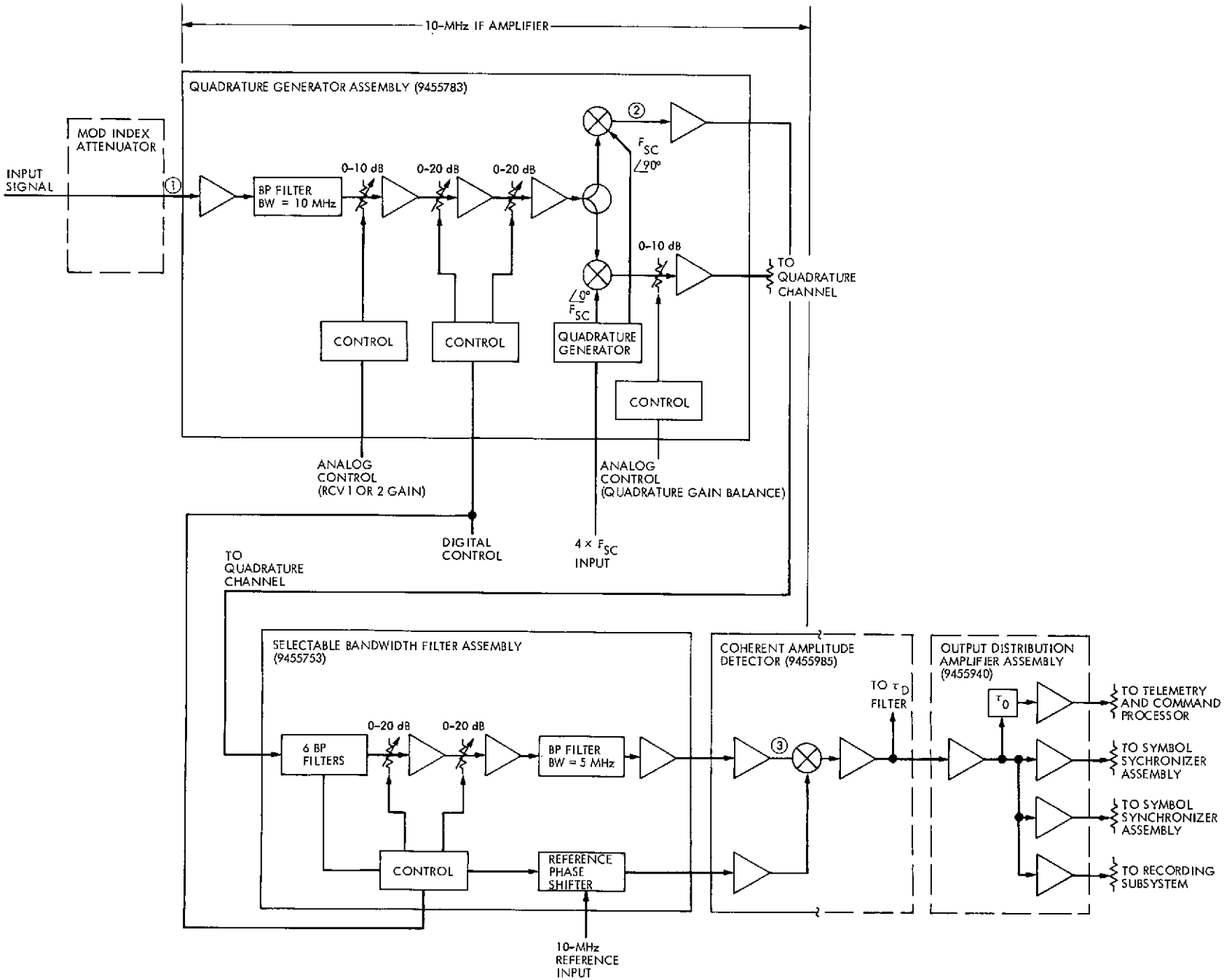

Fig. 1. Data channel block diagram

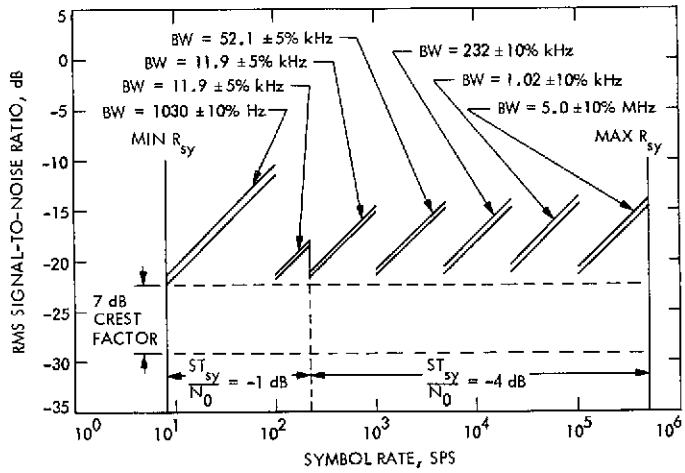

Fig. 2. Signal-to-noise ratio vs. symbol rate for six IF noise bandwidths

Helios Spacecraft Low-Gain Antenna Model

N. C. Ham
R. F. Systems Development Section

An extension of the Helios spacecraft low-gain antenna analysis has been performed with emphasis on the region of RF signal interferometry produced by the combined signals radiated from the horn and dipole antennas of like polarization. A mathematical model of the low-gain antenna model is developed and resultant computer plots compared against the amplitude and phase characteristics measured from a spacecraft antenna mockup. The model proved to correlate well with measured patterns and serves to consider major effects that may impact the telecommunications link.

I. Introduction

The preliminary investigation of the Helios low-gain antenna (LGA) effect on a telemetry link was covered by Ref. 1 with particular emphasis on the effects due to amplitude modulation and frequency modulation upon the radiated carrier signal as the Helios LGA was rotated about its spin axis.

Reference 2 was an extension of the study following receipt of preliminary spacecraft LGA patterns measured from a Helios spacecraft mockup and for the condition of right circular polarization (RCP) at the deep space stations and was analyzed that the maximum frequency deviation would be 28 Hz with a frequency rate of change of 89 Hz/s.

Figure 1 illustrates the Helios spacecraft LGA coordinate configuration showing the combined RCP horn and linear dipole antennas which comprise the LGA that produces a typical polar gain pattern.

This report is a further extension of the LGA analysis with particular emphasis on the region of signal interferometry produced by the combined horn and dipole antenna of similar polarization and develops a mathematical model of the LGA and then compares the results against the extensive antenna pattern measurements contained in Ref. 3.

II. Mathematical Model of LGA

The dimensional configuration of the Helios LGA for mathematical modeling purposes is depicted in Fig. 2 for the downlink frequency of 2295 MHz, where the aspect angle ψ is set to 45° for mathematical expediency since the slope of the signal rays, $\cos \omega_c t$ and $\cos(\omega_c t + \beta)$, are -1 and the equal wave front line is 1.

Figure 2a is the three-axis orientation illustrating the RCP horn antenna rotating around the Z-axis and the dipole antenna, with its linear polarization, coaxial to the Z-axis. The RCP horn signal linear polarization component is obtained by projection to the X–Z plane to match the polarization of the dipole antenna within this same plane.

Next the two matched polarized signals will be considered as having a common wave front for a specific aspect angle ψ and then vectorily summed as a function of the rotation angle ϕ.

As a first approximation for this model, the ratio of the radiated signal form will be used to circumvent the tedious and detailed equations to account for changing ellipticity, fringe effects, etc.

Figure 2b is the diagram used to formulate the equation for summing the linear components within the X–Z plane. Simultaneous equations are derived as follows:

$$z = x + 6.5\lambda \cos \phi$$

$$z = -x + 30\lambda$$

and are solved to determine the coordinates (x_1, z_1) with resulting values of

$$x_1 = 15\lambda - 3.25\lambda \cos \phi$$

$$z_1 = 15\lambda + 3.25\lambda \cos \phi$$

The distance L represents the phase difference between the two signal sources as a function of the rotation angle ϕ. The value L from the above equations is

$$L = [(x_2 - x_1)^2 + (z_2 - z_1)^2]^{1/2}$$

$$L = [225\lambda^2 - 97.2\lambda^2 \cos \phi + 10.5\lambda^2 \cos^2 \phi + 225\lambda^2 - 97.2\lambda^2 \cos \phi + 10.5\lambda^2 \cos^2 \phi]^{1/2}$$

$$L = 4.6\lambda\,[21.4 - 9.25 \cos \phi + \cos^2 \phi]^{1/2}, \text{ wavelengths} \quad (1)$$

To express in phase angle at the carrier frequency, where $\lambda = 360°$, the equation becomes

$$L = 1660°\,(21.4 - 9.25 \cos \phi + \cos^2 \phi)^{1/2}, \text{ degrees} \quad (2)$$

L_0 is the reference distance at $\phi = 0°$ and equals 5800°, and as ϕ increases in magnitude, when the spacecraft is rotated as shown, the signal radiated from the horn antenna begins to lead the dipole signal by the phase angle β; or $\beta' = L - L_0$. However, as the horn antenna is rotated one revolution, the radiated E vector also undergoes one revolution, thus advancing an additional λ (or 360°) modifying the phase difference to become $\beta = \beta' + \phi$; hence,

$$\beta = 1660°\,(21.4 - 9.25 \cos \phi + \cos^2 \phi)^{1/2} + \phi - 5800°, \text{ degrees} \quad (3)$$

The general expression for the ground received signal, in terms of amplitude and phase, is the sum of the signal from the two LGA sources and is derived from the following diagram:

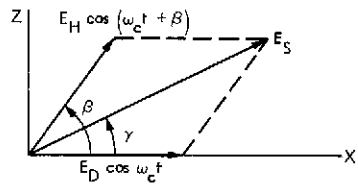

$$\mathbf{E}_S = \mathbf{E}_H + \mathbf{E}_D$$

where E_H is the horn signal and E_D the dipole signal,

$$\mathbf{E}_S = [(E_H \cos \beta + E_D)^2 + (E_H \sin \beta)^2]^{1/2}$$

and, finally, by normalizing the signal relative to the dipole antenna gain, as

$$E_S \angle \gamma = E_D \left[1 + \left(\frac{E_H}{E_D}\right)^2 + 2\left(\frac{E_H}{E_D}\right) \cos\beta \right]^{1/2} \Big/ \arctan\left(\frac{\frac{E_H}{E_D} \sin\beta}{1 + \frac{E_H}{E_D} \cos\beta} \right) \tag{4}$$

Using the value of β from Eq. (3) and trigonometric identities, the general equation becomes

$$E_S \angle \gamma = E_D \left\{ 1 + \left(\frac{E_H}{E_D}\right)^2 + 2\left(\frac{E_H}{E_D}\right) \cos\left[1660^\circ (21.4 - 9.25\cos\phi + \cos^2\phi)^{1/2} + \phi - 5800^\circ\right] \right\}^{1/2}$$

$$\Big/ \arctan\left(\frac{\frac{E_H}{E_D} \sin\left[1660^\circ (21.4 - 9.25\cos\phi + \cos^2\phi)^{1/2} + \phi - 5800^\circ\right]}{1 + \frac{E_H}{E_D} \cos\left[1660^\circ (21.4 - 9.25\cos\phi + \cos^2\phi)^{1/2} + \phi 5800^\circ\right]} \right) \tag{5}$$

for the specific aspect angle $\psi = 45^\circ$.

III. Signal Amplitude

The amplitude variation of the received signal as a function of the rotation angle ϕ, for the specific aspect angle $\psi = 45^\circ$, is the amplitude portion of the general equation (5):

$$E_S = E_D \left\{ 1 + \left(\frac{E_H}{E_D}\right)^2 + 2\left(\frac{E_H}{E_D}\right) \cos\left[1660^\circ (21.4 - 9.25\cos\phi + \cos^2\phi)^{1/2} + \phi - 5800^\circ\right] \right\}^{1/2} \tag{6}$$

Figure 3a is the computer plot of the signal amplitude for values of $E_H = E_D = 1$, where the amplitude is in volts; Fig. 3b shows the results when the amplitude scale is the logarithm or in dB.

Figures 4a, 4b, and 4c are the dB plots for the values of $E_H = 0.8$, $E_D = 1.1$; $E_H = 0.9$, $E_D = 1.05$, and $E_H = 1.1$, $E_D = 0.9$, and are estimated average antenna gain values at $\psi = 47^\circ$, 46°, and 44°, respectively.

IV. Signal Phase

The phase variation of the received signal can be obtained in a similar manner from the general equation (5):

$$\gamma = \arctan\left(\frac{\frac{E_H}{E_D} \sin\left[1660^\circ (21.4 - 9.25\cos\phi + \cos^2\phi)^{1/2} + \phi - 5800^\circ\right]}{1 + \frac{E_H}{E_D} \cos\left[1660^\circ (21.4 - 9.25\cos\phi + \cos^2\phi)^{1/2} + \phi - 5800^\circ\right]} \right) \tag{7}$$

The ideal interferometry condition, when $E_H = E_D = 1$ (i.e., equal gain pattern from the dipole and horn antenna) for all rotation angle ϕ, is shown in Fig. 5 at the aspect angle of 45°, while Fig. 6 is for the value of $E_H = 0.7$ and $E_D = 1$. Figure 7 is for $E_H = 1.08$ and $E_D = 1$.

As can be seen in Fig. 5, the phase derivation about the received signal is $\pm 90^\circ$ for the condition $E_H/E_D = 1$ since Eq. (4) becomes

$$\gamma = \arctan\frac{\sin\beta}{1 + \cos\beta} = \arctan \cdot \tan\frac{1}{2}\beta = \frac{1}{2}\beta \tag{8}$$

Thus, when $\phi = 180^\circ$, $\beta = 90^\circ$ maximum, and when $\phi \simeq 181^\circ$, $\beta = -90^\circ$ maximum.

For the condition when $E_H/E_D = 0.7$, the phase deviation is seen to be approximately $\pm 46^\circ$; while for $E_H/E_D = 1.08$, the phase deviation is approximately $\pm 150^\circ$.

V. Actual Case Versus Ideal Case

The ideal case of equal amplitude from the LGAs for every value of ϕ at any specific aspect angle ψ does not

exist for the Helios configuration due to the offset horn antenna and slight physical misalignment of the dipole antenna from the spin axis and is further compounded when viewed at various aspect angles.

Figure 8 illustrates the polar plot of the LGA in the X–Z plane for the rotation angle $\phi = 0°$, which shows that for $\psi = 0°$ to 44° the horn antenna is dominant, while for $\psi = 53°$ to 180° the dipole becomes dominant, and $\psi = 44°$ to 53° is the combined horn–dipole region.

Figure 9 illustrates the orthogonal X–Y plane conic section for $\phi = 0°$ to 360° at various aspect angles.

Figure 10 is the test measurement configuration used to obtain the amplitude and phase characteristics from a Helios spacecraft mockup, and Fig. 11 is a reproduction of a typical measurement. This illustrates that $30° > \phi > 310°$ is the dipole region, $30° < \phi < 200°$ is the horn dominant region, and $200° < \phi < 310°$ is the combined horn–dipole region.

The horn dominant region ($30° < \phi < 200°$) in this plot shows the restriction of the measuring instrument whose scale is limited to $\pm 180°$ for phase measurements; hence, the plot shows modulo 2π cuts of the total phase change of 3060°, which represents a frequency deviation about the carrier frequency of approximately 19 Hz (see Ref. 2).

Figure 12 is a comparison of the amplitude variation of the mathematical model versus the measurement data for one revolution of the spacecraft at the aspect angle of 45°. Figures 13, 14, and 15 are the comparisons of the same computer plot (at $\psi = 45°$) with measured data for $\psi = 44°$, 46°, 47°, respectively, using various values of E_H, E_D.

Using a scaled drawing of the spacecraft geometry for an aspect of $\psi = 50°$, the equation for β becomes

$$\beta_{50°} = [1820° (14.6 - 7.57 \cos\phi + \cos^2\phi)^{1/2}] + \phi - 4830° \quad (9)$$

Substitution of this value into Eq. (6) produces a computer plot as shown in Figs. 16, 17, and 18 comparing the measured plots for $\phi = 49°$, 50°, and 51°, respectively, again with various ratios of E_H/E_D.

In similar fashion Figs. 19, 20, and 21 are comparisons of the computer plot of the phase variation for $\psi = 45°$ against the measured data for $\psi = 44°$, 45°, and 46°. Figure 19 shows a frequency deviation region which is not covered by this model.

In Fig. 20, for the computer plot, the dipole antenna gain is constant ($E_D = 1$) and the horn antenna relative gain varied as a function of ϕ, i.e., $E_H = 1$ at $0° < \phi < 100°$, $E_H = 1.08$ at $100° < \phi < 190°$, $E_H = 0.7$ at $190° < \phi < 360°$ compared to the measured antenna plot. This illustrates the varying horn antenna gain versus the rotation angle ϕ (due to its offset symmetry axis) and clearly shows that the phase deviation has varying values for one spacecraft rotation. Notice the similarity to Fig. 11 for the amplitude case.

Figures 22, 23, and 24 compare the computer phase plot for $\psi = 50°$ against the measured data for $\psi = 49°$, 50°, and 51°, respectively, and, as seen in Figs. 8 and 9, the ratio of E_H/E_D is less than 1 and nearly constant.

VI. Evaluation of the Mathematical Model

If the good correlation of the mathematical model computer plots relative to the actual measurement plots is accepted as the validity of the model, to a first approximation, then an analysis of the model results should aid in the determination of the effects of the amplitude and spin modulation characteristics on the telecommunications link performance.

A study of Eq. (4) related to the carrier amplitude indicates that the coefficient to the circular function is compensating, i.e., when $E_H = E_D = 1$, the maximum peak-to-peak variation of the amplitude exists; when $E_D > E_H$, the peak variation decreases; and, similarly, when $E_H > E_D$, the peak variation also decreases. For example, Figs. 3 and 4 illustrate that the maximum peak variation exists at $E_H = E_D = 1$, and Figs. 4b and 4c show similar peak values when $E_D > E_H$ and $E_H > E_D$, respectively.

In the case of the phase function, however, the maximum phase deviation does not exist at $E_H/E_D = 1$ but does decrease at $E_H/E_D < 1$. For example, when $E_H/E_D = 0.7$, the peak-to-peak variation is $\pm 46°$ as shown in Fig. 6. The sensitivity of the peak variation as E_H/E_D becomes greater than 1 is shown in Fig. 7, where the ratio $E_H/E_D = 1.08$ can be seen to nearly double the peak variation when $E_H/E_D = 1$. This indicates the domineering influence of the rotating horn antenna to phase variation.

For the combined horn–dipole region ($44 < \psi < 53°$), the phase variation upon the carrier was seen to be a mix of frequency deviation (which was tested in Ref. 1) and phase deviation. The phase deviation as shown in Fig. 20 can be assumed to be a sawtooth waveform with an

average periodic frequency of 25 Hz (since the spacecraft rotates at 1 cycle/s) with a phase deviation of ±150° maximum.

The Fourier series of a sawtooth waveform is expressed by

$$y = \frac{2}{\pi} E \left(\sin x - \frac{1}{2} \sin 2x + \frac{1}{3} \sin 3x + \cdots - \frac{1}{n} \sin nx \right) \tag{10}$$

where E is the peak-to-peak value of the waveform.

Thus, for the periodicity of 25 Hz average, the fundamental frequency component would produce a maximum phase deviation of $\pm 150° \times 0.636 = \pm 86°$ and a corresponding deviation of ±43° for the second harmonic component and ±28.6° for the third harmonic component. This results in sideband components spaced about the carrier frequency separated by integer values of 25 Hz with decreasing amplitude.

The question arises as to what effect these components have upon the RF phase-locked loop (PLL) whose threshold loop bandwidth values are 48 and 152 Hz (two-sided). This question will be discussed later.

In the dipole dominant region it was analyzed (Ref. 3) that phase deviation was largely due to the solar panels and dipole antenna misalignment. Thus, the total effect upon the carrier can be summarized as a mixture of frequency deviation and phase deviation as a function of the aspect angle ψ, as shown in Fig. 25.

Since the model was formulated from the physical dimensions and geometry of the spacecraft, the equations are easily adaptable to the uplink conditions and applicable because of reciprocity.

VII. System Test

A possible test of the Telemetry System performance, based on the results of the mathematical model, could be structured on the technique employed previously as in Ref. 1.

An addition to the previous test would be to evaluate separately the performance of the receiver phase-locked loop when subjected to the worst-case condition from the LGA interferometry. From the computer plots it was shown that the phase deviation, or phase modulation, upon the carrier was that of a sawtooth waveform occurring at a periodic rate of 25 Hz, producing a phase deviation of ±150° peak-to-peak. However, from the Fourier series, it was shown (Eq. 10) that the fundamental frequency results in an approximate ±86° phase deviation.

Since the resulting spectrum overlaps the effective receiver loop noise bandwidths ($2B_{L_0} = 48$ and 152 Hz), a good experimental test would be to see what this spectrum does to the degradation of PLL performance as a function of carrier signal-to-noise ratio (SNR).

Figure 26 is the block diagram of a possible arrangement to evaluate the receiver PLL. The function generator with a sawtooth pattern would phase modulate the exciter only at the periodic frequency of 25 Hz and level set to deviate the carrier ±150° peak-to-peak.

The input signal level to the receiver would then be adjusted to produce a decreasing SNR and then measure the number of cycles slipped by the PLL (for a given elapsed test run time). The procedure would be to initially obtain the cycle slippage characteristics without the perturbing interferometry signal followed by the phase modulation without amplitude modulation and then a repeat with the combined PM and AM applied.

Similar to previous tests, an actual telemetry signal would be applied and a value of the resultant symbol error rate (SER) versus input ST_{s_H}/N_0 determined.

VIII. Computer Program

The MBASIC conversational computer language was used to develop the mathematical model for the LGA. The program instruction was written in sentence form and then combined into a program module that was written like a paragraph.

Equation (6) for the signal amplitude, at $\psi = 45°$, was written as

$$E_S = E_D \left\{ 1 + \left(\frac{E_H}{E_D} \right)^2 + 2 \left(\frac{E_H}{E_D} \right) \cos \left[1660° \left(21.4 - 9.25 \cos \phi + \cos^2 \phi \right)^{1/2} + \phi - 5800° \right] \right\}^{1/2} \tag{6}$$

and the resultant plot of this program is shown in Fig. 27. A comparison of this plot against Fig. 3b (or measured data as in Fig. 15) indicated that there exists a phase reference error as seen by the envelope shape at $\theta = 180°$.

This discrepancy is probably due to the initial phase relation between the horn and dipole antenna signals assumed as shown in the vector summation diagram and projection diagram of Fig. 2. Since an unknown phase shift exists within the RF cables, power splitters, etc., the initial phase condition must be more closely approximated.

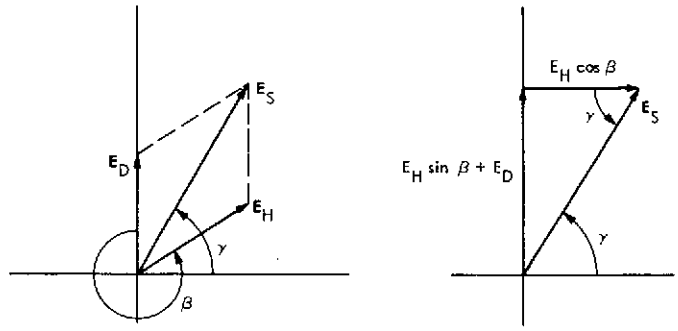

Assume then that at $\phi = 0°$ the horn phase is leading the dipole at a phase angle β greater than 270° as shown in the following diagrams:

---

then

$$\mathbf{E}_S = [(E_H \sin\beta + E_D)^2 + (E_H \cos\beta)^2]^{1/2} \tag{11}$$

and

$$E_S \angle \gamma = E_D \left[1 + \left(\frac{E_H}{E_D}\right)^2 + 2\left(\frac{E_H}{E_D}\right)\sin\beta\right]^{1/2} \Big/ \arctan\left(\frac{1 + \frac{E_H}{E_D}\sin\beta}{\frac{E_H}{E_D}\cos\beta}\right) \tag{12}$$

will be used as the general equation for the amplitude and phase relation of the summed signal.

Thus, the signal amplitude equation becomes

$$E_S = E_D\left\{1 + \left(\frac{E_H}{E_D}\right)^2 + 2\left(\frac{E_H}{E_D}\right)\sin\left[1660°\,(21.4 - 9.25\cos\phi + \cos^2\phi)^{1/2} + \phi - 5800°\right]\right\}^{1/2} \tag{13}$$

and for phase

$$\gamma = \arctan\left(\frac{1 + \frac{E_H}{E_D}\sin\left[1660°\,(21.4 - 9.25\cos\phi + \cos^2\phi)^{1/2} + \phi - 5800°\right]}{\frac{E_H}{E_D}\cos\left[1660°\,(21.4 - 9.25\cos\phi + \cos^2\phi)^{1/2} + \phi - 5800°\right]}\right) \tag{14}$$

for the aspect angle of 45°.

The final computer program for the amplitude is listed as follows:

```
55 INPUT USING 'A=#B=#C=#D=#':A,B,C,D&! ENTER COEFF FOR MODEL
60 FOR LOOP=1 UNTIL DONE WHERE DONE=0
65   INPUT USING 'MORE PLOT CASES (YES OR NO)?%':AN$
70   GO TO 170 IF DONE=1 WHERE DONE=(AN$='N')
90   INPUT USING 'ENTER VALUES FOR EH AND ED: # #':EH,ED
100  PRINT 'PLTL'
110  FOR PHI=0 TO 360 WHERE E=EH/ED
120    ES=ED*SQR(1+E**2+2*E*SIN(A*SQR(B-C*COS(PHI)+(COS(PHI))**2)-D+PHI))
130    PRINT USING '%%%% %%%%':9999*PHI/360,9999*((2+LOG10(ES))/2)*.48
```

```
140   NEXT PHI&
160   PRINT 'PLTT'
170   NEXT LOOP
```

In line 90, EH and ED are the magnitudes of the horn and dipole antenna gain respectively, with their gain ratio listed as E = EH/ED as in line 110.

The coefficients A, B, C, and D in line 120 are related to the geometrical dimensions obtained from Fig. 2b and the solution for L as explained by Eq. (2) for the case of $\psi = 45°$.

The resultant computer plots for the amplitudes are as shown in the previous figures.

The program for the resultant phase variation is listed below:

```
50  INPUT USING 'ENTER VALUES FOR EH1 AND ED1: # #':EH1,ED1
75  A1=1820,A2=14.6,A3=7.57,A4=4830
100 PRINT 'PLTL'     ! START OF PLOTTING
110 FOR PHI=0 TO 360 WHERE E=EH1/ED1
115   EN=E*COS(A1*SQR(A2-A3*COS(PHI)+COS(PHI)**2)+PHI-A4)
117   ED=1+E*SIN(A1*SQR(A2-A3*COS(PHI)+(COS(PHI))**2)+PHI-A4)
120   GAMMA=180+ATN(ED,EN) ! 180 IS ADDED FOR PLOTTING OF E>1 CASES
130   PRINT USING '%%%% %%%%':9999*PHI/360,9999*(GAMMA/180)*(2/4.25)
140   NEXT PHI
160 PRINT 'PLTT'     !TERMINATE PLOT
```

Again the gain values for the horn antenna, EH1, and dipole antenna, ED1, are entered (line 50). A1, A2, A3, A4 (line 75) are coefficients that are used in the solution for β (lines 115 and 117). These coefficients are the values obtained by scaling the diagram of Fig. 2b for $\psi = 50°$.

EN (line 115) and ED (line 117) are the numerator and denominator expressions of Eq. (14).

The general equation GAMMA = ATN (ED, EN) served when $E_H < E_D$, since by Eq. (8), the resultant angle, γ, never exceeded 90°; however, when $E_H > E_D$, gamma is greater than 90° and the program included a modifier for this condition by the prefix addition 180 as stated in line 120.

References

1. Ham, N. C., "Amplitude and Frequency Modulation Effects to Telemetry Link Reception," in *The Deep Space Network Progress Report*, Technical Report 32-1526, Vol. XIV, pp. 149–160, Jet Propulsion Laboratory, Pasadena, Calif., Apr. 15, 1973.
2. Ham, N. C., *Helios LGA Pattern Measurements*, IOM 335A-73-113, Mar. 21, 1973 (JPL internal document).
3. Zerwes, G., *Radiation Characteristics of Helios Low Gain Antenna*, Technical Memorandum RB1-6764/73 C-264, Messerschmitt-Bokow-Blohm, Ottobrunn, W. Germany, Mar. 26, 1973.

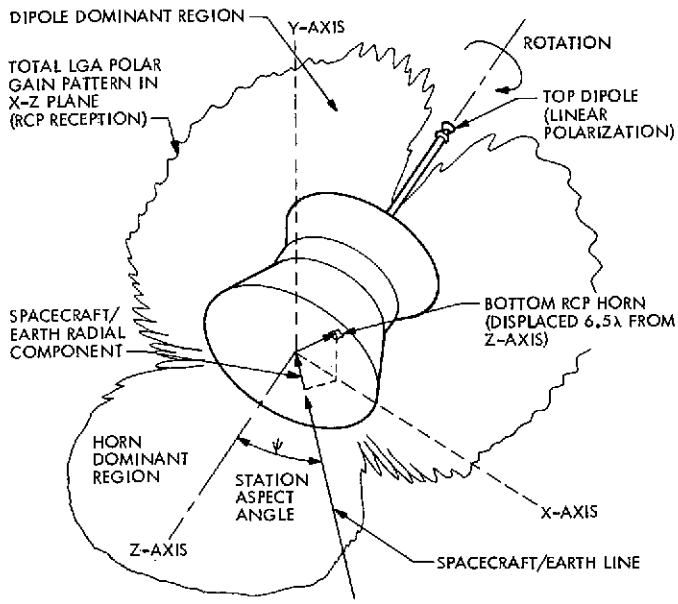

Fig. 1. Spacecraft coordinate configuration

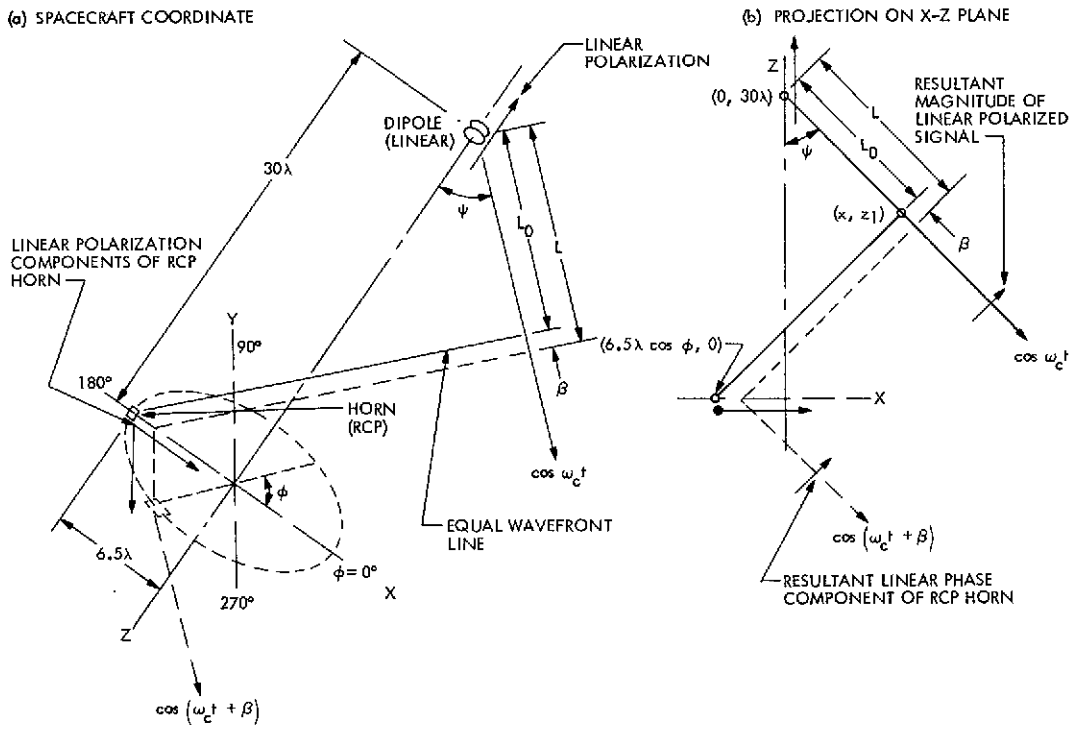

Fig. 2. Spacecraft LGA interferometry

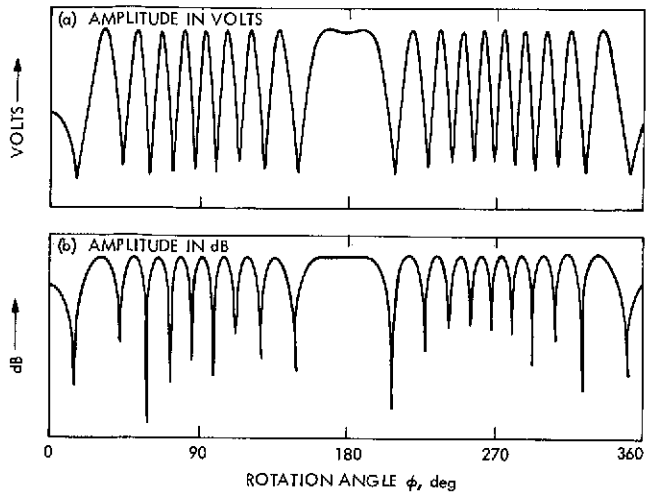

Fig. 3. Computer plots of carrier amplitude, $\psi = 45°$, $E_H = 1$, $E_D = 1$

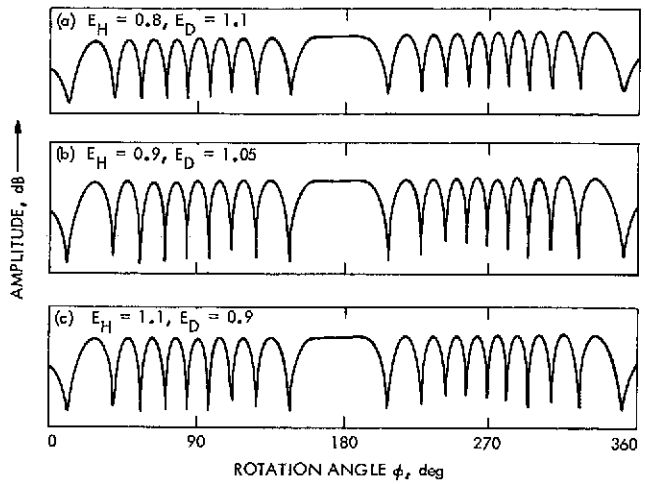

Fig. 4. Computer plots of carrier amplitude, $\psi = 45°$

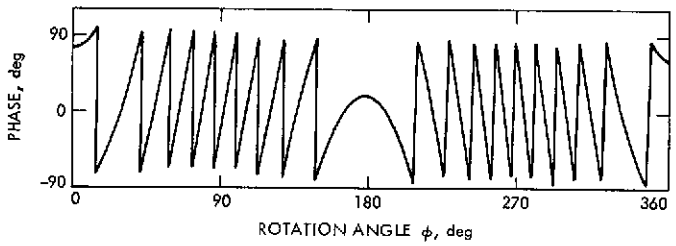

Fig. 5. Computer plot of carrier phase, $\psi = 45°$, $E_H = 1$, $E_D = 1$

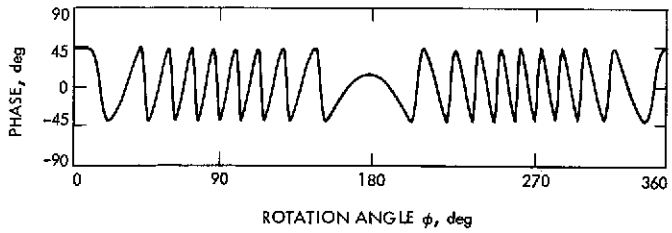

Fig. 6. Computer plot of carrier phase, $\psi = 45°$, $E_H = 0.7$, $E_D = 1$

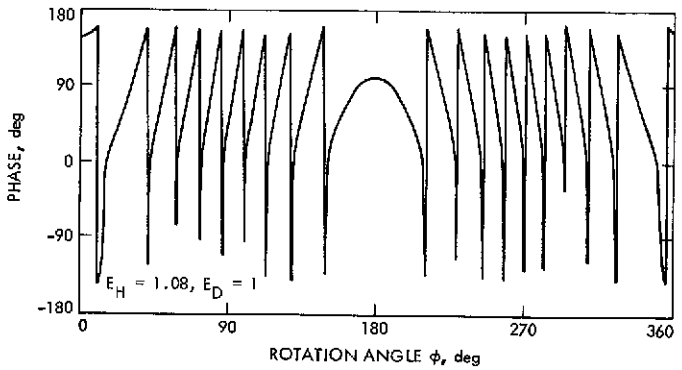

Fig. 7. Computer plot of carrier phase, $\psi = 45°$

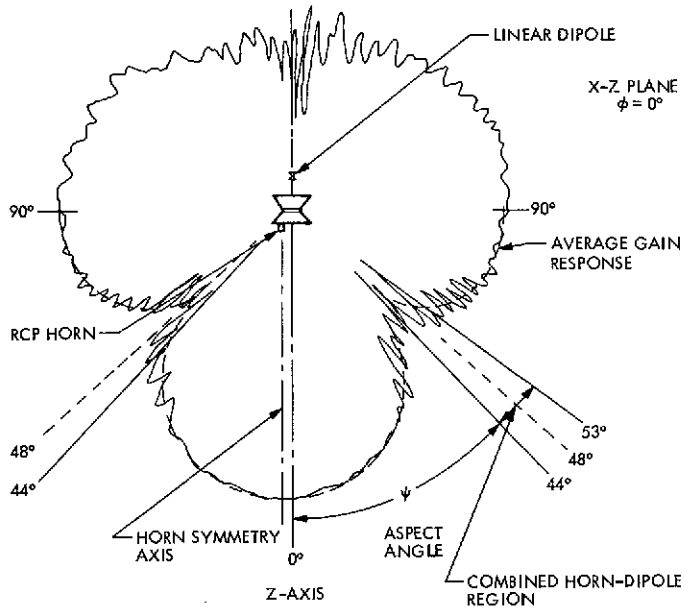

Fig. 8. Polar plot of LGA for RCP reception (downlink frequency)

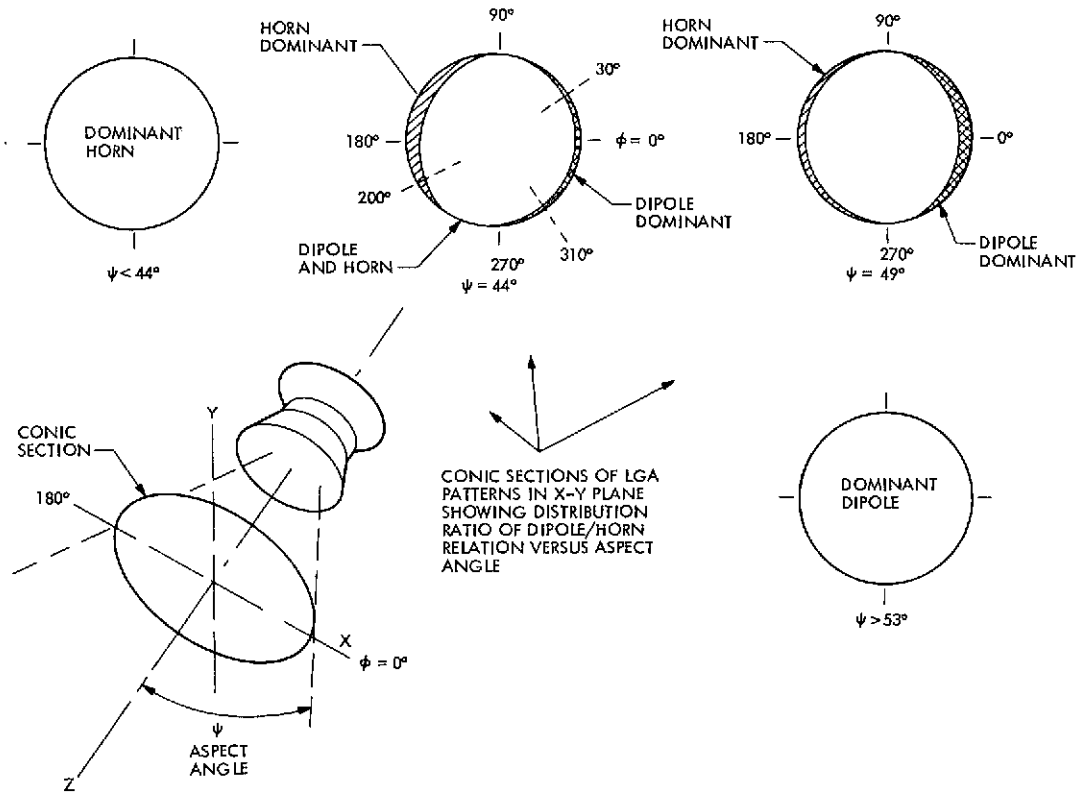

Fig. 9. LGA conic section pattern versus aspect angle

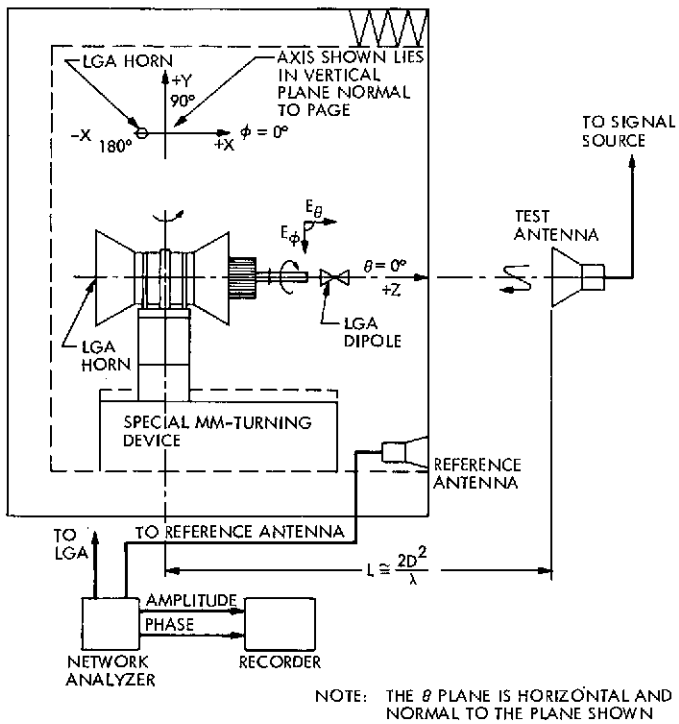

Fig. 10. Radiation pattern test setup

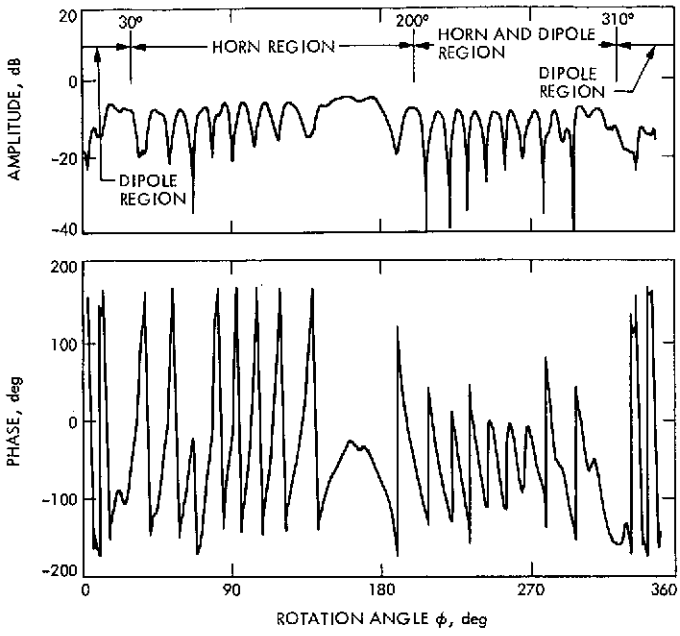

Fig. 11. Helios LGA measured data, $\psi = 44°$

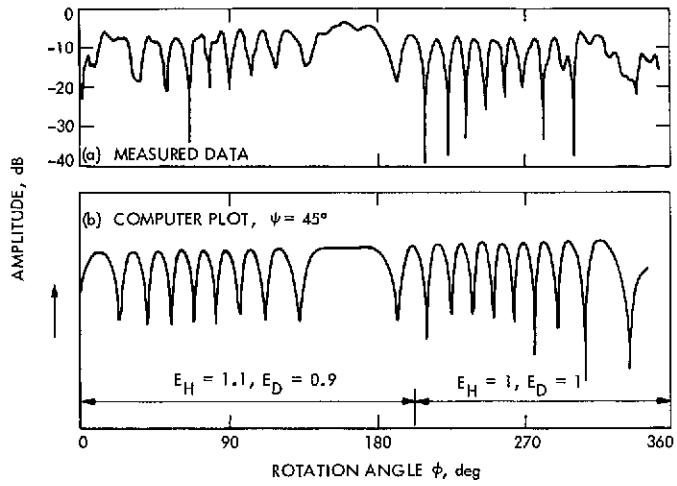

Fig. 13. Computer plot versus measured data, $\psi = 44°$

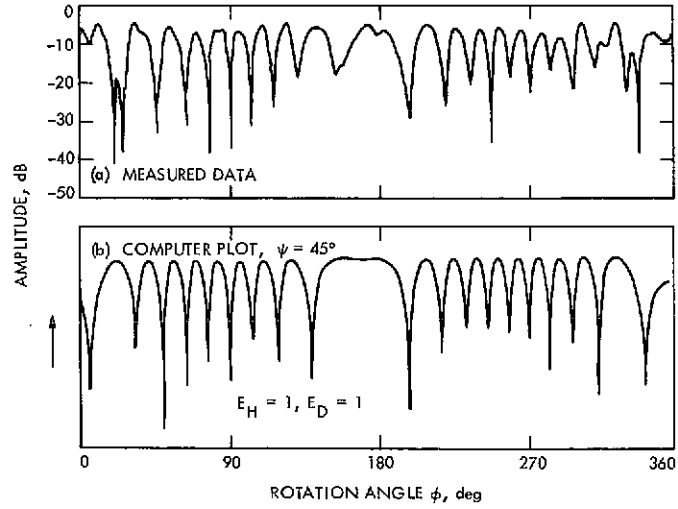

Fig. 12. Computer plot versus measured data, $\psi = 45°$

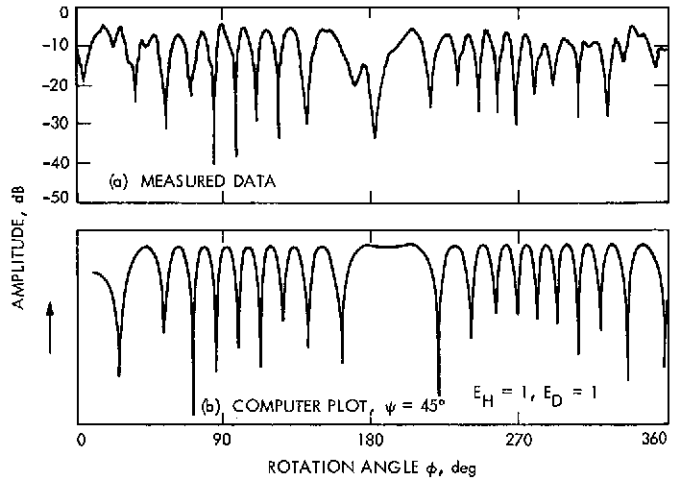

Fig. 14. Computer plot versus measured data, $\psi = 46°$

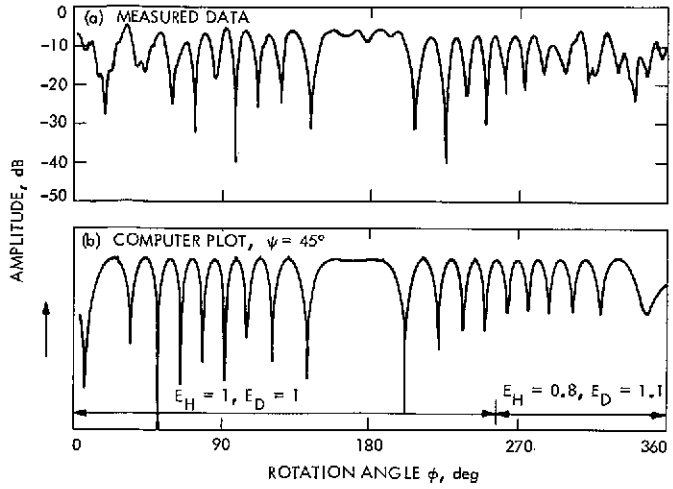

Fig. 15. Computer plot versus measured data, $\psi = 47°$

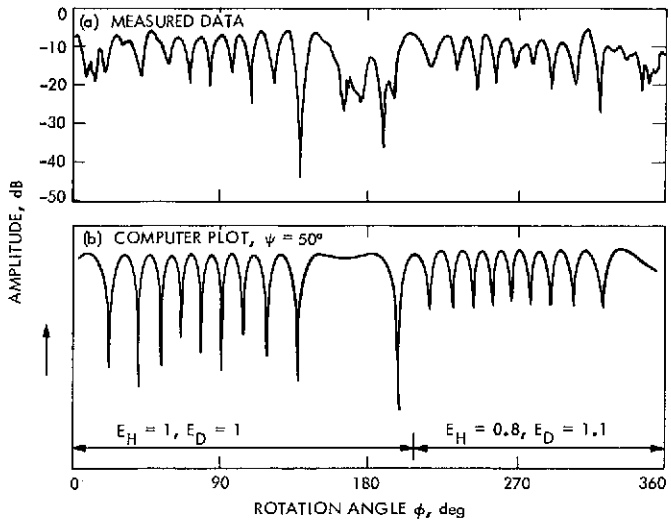

Fig. 16. Computer plot versus measured data, $\psi = 49°$

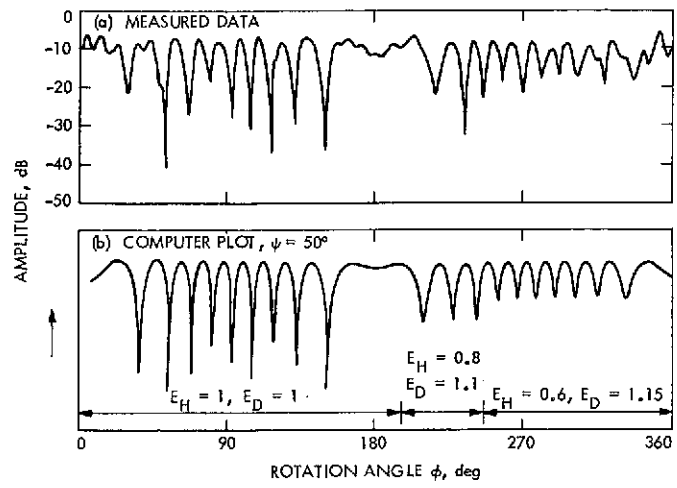

Fig. 17. Computer plot versus measured data, $\psi = 50°$

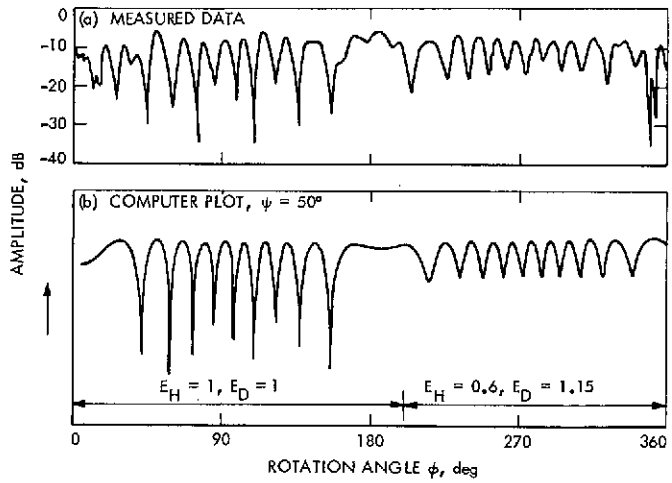

Fig. 18. Computer plot versus measured data, $\psi = 51°$

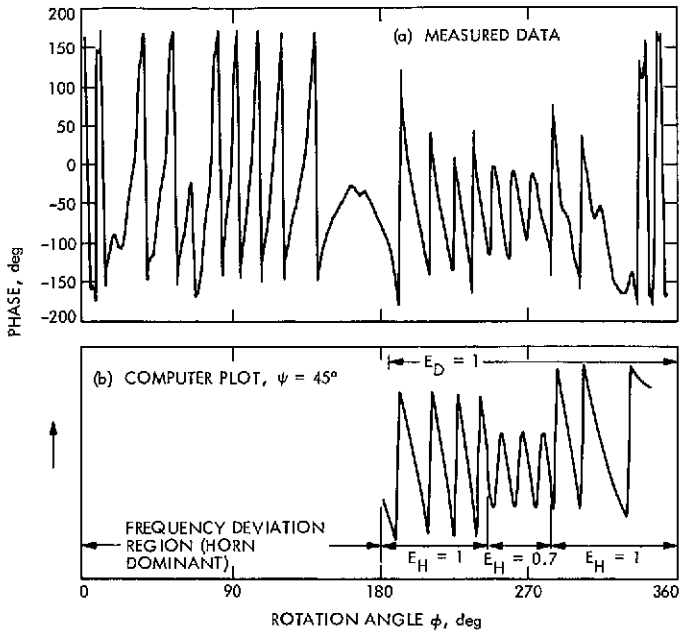

Fig. 19. Computer plot versus measured phase data, $\psi = 44°$

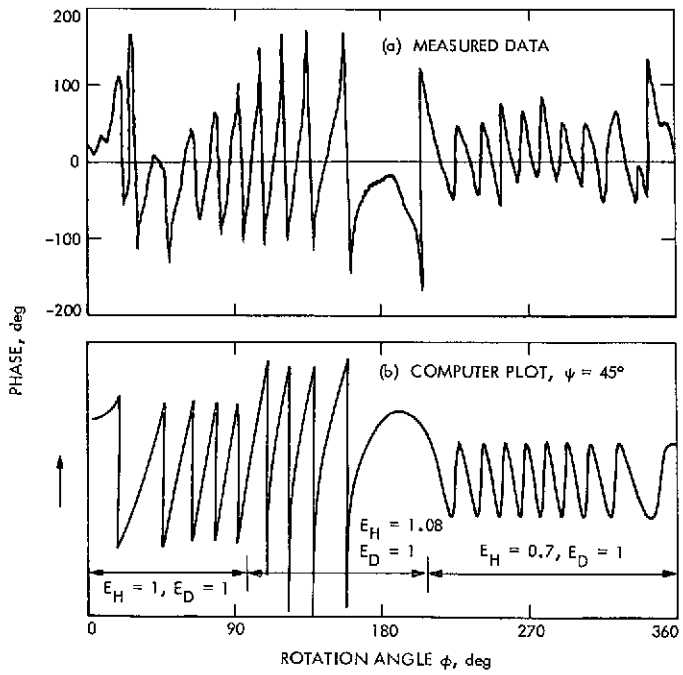

Fig. 20. Computer plot versus measured phase data, $\psi = 45°$

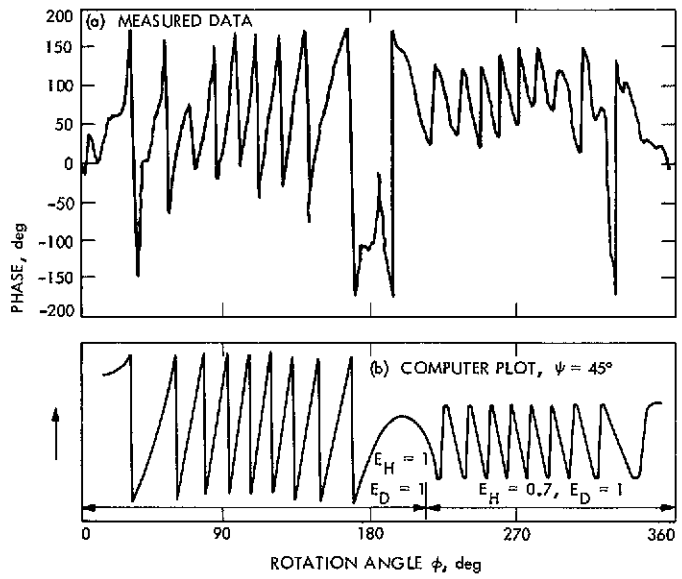

Fig. 21. Computer plot versus measured phase data, $\psi = 46°$

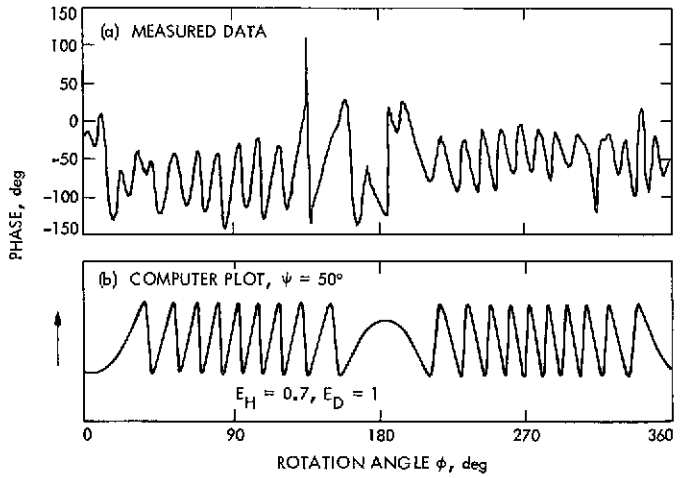

Fig. 22. Computer plot versus measured phase data, $\psi = 49°$

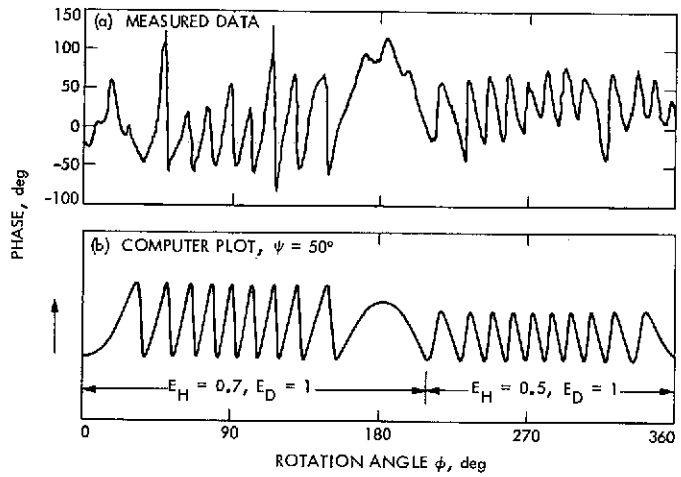

Fig. 23. Computer plot versus measured phase data, $\psi = 50°$

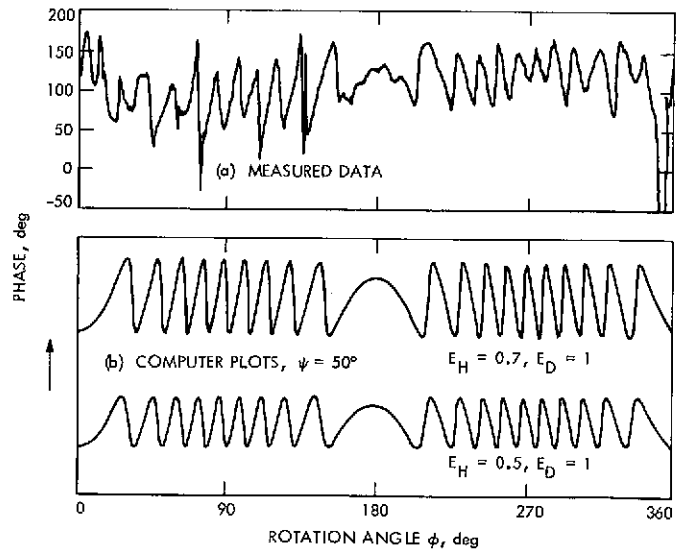

Fig. 24. Computer plots versus measured phase data, $\psi = 51°$

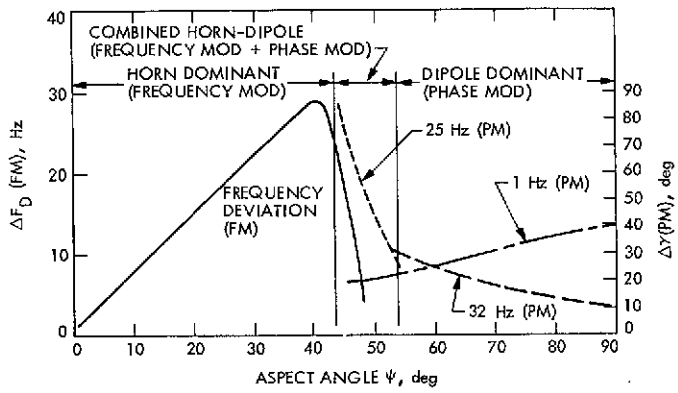

Fig. 25. Frequency deviation and PM versus aspect angle for RCP reception

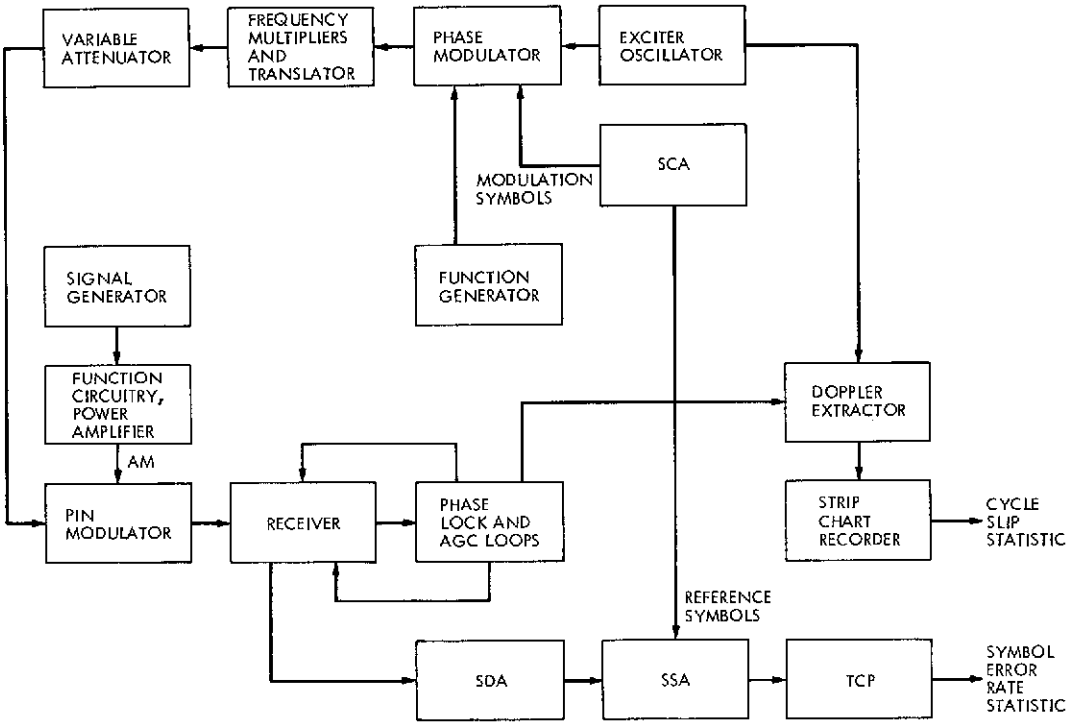

Fig. 26. Block diagram of system test configuration

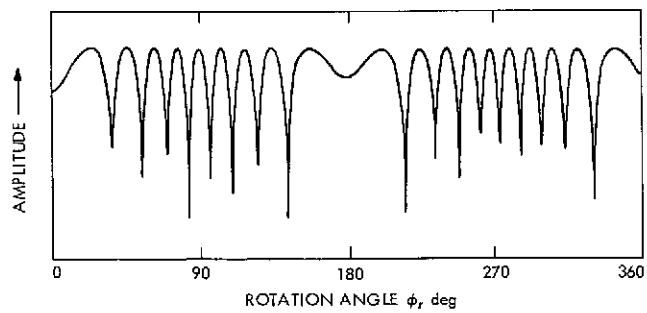

Fig. 27. Computer plot of amplitude, $\psi = 45°$

Telemetry and Command Multiple-Mission Software (Model A)

Vernon D. Jones
DSN Data Systems Development Section

This article gives the status of the Deep Space Station Telemetry and Command operational software central to the support of Mariner Venus/Mercury 1973. The program was implemented by developing mission-oriented segments and integrating with a basic software nucleus. The selected method of implementation is an outgrowth of a feasibility study, conducted by the Data Systems Development Section.

I. Introduction

This article describes the Model A version of the Telemetry and Command (TCD) operational software which supports the Mariner Venus/Mercury 1973 (MVM'73) mission. This software is multiple mission in structure and serves as the basic building block which will also support the Helios and Viking missions. Individual program elements that reside in the TCD computers (XDS 920 and ID4) form building blocks which can be selected and integrated to perform specific functions, viz., transmission of the Ground Communications Facility (GCF) blocks formatted in accordance with the Deep Space Network/Mission Control and Computing Center Interface Document (820-13). The ID4 computers are configured as a peripheral to the XDS 920, and program functions are input and controlled through the XDS 920 computer.

II. Major Categories and Support Software

The basic software categories are Executive Control, Command, Telemetry, and support programs. Each software category consists of many data sets. A brief description of functions is as follows:

(1) *Executive.* Loads all routines central to a given function, processes and routes input messages,

queues and outputs messages to the Monitor System, GCF blocks, local alarms, and logs the Telemetry and Command Processor (TCP) Digital Original Data Record (DODR) as required.

(2) *Telemetry.* Assembles newly acquired data for transmission to user in real time. Functionally, monitors all telemetry-related assemblies (subsystems) and reports their status to the user.

(3) *Command.* Dedicated to controlling, monitoring and supplying the Command Modulator Assembly (CMA) with command data for radiation.

Support software has been written to perform the following functions:

(1) *Program Tape Maintenance.* TCP resident routine which adds, deletes or replaces routines or data sets on magnetic tape—the TCD system tape.

(2) *Punched Paper Tape and Edit Routine.* Prepares paper tape with input messages for subsequent processing by the TCP Executive.

(3) *Bootstrap Loader.* Bootload (on punched paper tape) to load the controller from the system tape.

III. TCD System Tape

The system tape (program tape) houses all the data sets required for anticipated missions through 1975. A data set may be viewed as a self-contained mission-dependent routine. Each data set is characterized by a label and resident computer (TCP or Data Decoder Assembly (DDA) Central Processor). The program tape is prepared by the maintenance (update) routine.

Previous operational programs featured a program tape which contained a complete TCP memory image. To increase reliability, several images were usually written. The TCD system tape is organized so that a given data set appears only once. Each data set is preceded by a label record which provides a unique name and date. Each physical record after the label record has a checksum field which is computed at the time of the update and is recomputed by the Executive at load time. The checksum algorithm is a "folded" checksum and is compatible with the requirements of the XDS Monarch Loader. Loading is aborted whenever the checksum criterion fails.

Dummy data sets are provided in order to satisfy all references and interface requirements at load time. Finally, a terminating record is provided to signify the end of the tape.

IV. Executive Data Sets

Basically, the Executive can be partitioned into two segments. Each segment, in turn, consists of its own data sets. The partitioning of the Executive is necessary because the program has two phases of operation-loading and actual monitoring and control:

(1) Data sets for the loading phase (software configuration generator)

(a) *Configuration Monitor.* Processes and responds to manual directives and builds loading tables.

(b) *Table Module.* Pre-assembled tables which link data sets. This element may be altered without affecting the Executive. This is the "Configuration List."

(c) *General Loader.* Loads all data sets into destination computer(s) as required.

(2) Data sets for real-time phase

(a) *Supervisor.* Controls execution of subprograms queued as the result of some real-time event.

(b) *Utilities.* Magnetic tape output routines, GCF block input and output routines, monitor output and TTY output routines.

(c) *Common Data Base.* Constants and parameters available to all data sets.

V. Data Sets for Model A

The TCD software Model A is restricted to MVM'73 support. The Executive was treated separately because it must remain intact regardless of mission. The MVM'73 command format is 1 bit/s, phase-shift keying/pseudo-noise. A self-contained data set performs the command function. Due to storage limitations, the telemetry software category was subdivided into three basic software configurations or functions. These functions are (1) the internal bit synchronization algorithm, (2) processing of coded or uncoded data by the DDA, and (3) DDA processing of uncoded data and Block Decoder Assembly processing of coded data. Hence, the telemetry subdivisions correspond to the low-, medium- and high-rate channels, respectively. Data sets common to all telemetry configurations are listed in Table 1. Specialized data sets would be the GCF block formatters and interrupt processors written specifically for a given function. The low-rate channel utilizes a formatter, interrupt processor, and a routine to control and monitor the digital phase shifter. The medium- and high-rate configurations utilize for-

matters and Symbol Synchronizer Assembly and DDA control routines in addition to self-contained DDA resident programs. The high-rate DDA program logs a 9-track DODR and outputs on wideband lines when required.

VI. Summary

Mission-dependent routines or data sets may be specified in the Configuration List portion of the Executive. This allows integration of new application programs with the existing Executive. Since the Executive would not be altered by this process, previous configurations will remain valid and the total collection of program elements on a given system tape will form a multiple-mission software package.

The Model A version of this program has been implemented and transferred to the program library and will be used for MVM'73 support. This includes the additional configuration and data sets necessary for 9-track DODR replay. Model B, which adds those functions necessary to support Helios, is currently undergoing acceptance testing. The Model C version for Viking support is in the final implementation stages.

Table 1. Common telemetry data sets

Data set name	Function
DISGEN	Formats all telemetry monitor messages
SNCAL	Computes SNR whenever channel or decoder statistics are available
LOMSG	Edits all telemetry input messages entered via punched paper tape or keyboard and builds parameter tables for channel operation
TMINT	Telemetry initialization, i.e., channel start
TMRNT	Terminates telemetry
TMAGC	Processes receiver AGC
MSTAT	Monitors telemetry assemblies and initiates alarms when necessary

NASA — JPL — Coml., L.A., Calif.